Multiple ionization in strong laser fields

Dissertation

zur Erlangung des
Doktorgrades der Naturwissenschaften
(Dr. rer. nat.)

dem Fachbereich Physik
der Philipps-Universität Marburg
vorgelegt von

Jan Hendrik Thiede
aus Lich

Marburg, 2017

Vom Fachbereich Physik der Philipps-Universität Marburg
(Hochschulkennziffer 1180) als Dissertation angenommen am: 22. Januar 2018

Autor: Dipl.-Phys. Jan Hendrik Thiede
Erstgutachter: Prof. Dr. Bruno Eckhardt
Zweitgutachter: Prof. Dr. Reinhard Noack

Tag der mündlichen Prüfung: 24. Januar 2018

Für
meine Eltern
und meinen Großvater
Hermann Georg Horst Schubert

Even a vacuum arguably isn't truly empty,
but that's a question for quantum semantics.

Randall Munroe, What If?

It was then that I realized that
I must devote my life to science.

Doc Brown, Back To The Future, Part III

Zusammenfassung

Mit den heutzutage verfügbaren ultrakurzen Laserpulsen lassen sich mühelos Intensitäten erreichen, die jene eines bindenden atomaren Feldes um mehrere Größenordnungen übersteigen. Folglich ist es mit einem einzigen Laserpuls möglich, ein oder mehrere Elektronen aus einem Atom zu entfernen (zu ionisieren).

Die Intensitätsabhängigkeit der laserinduzierten Ionisation ist hochgradig nichtlinear und wird vor allem an reaktionsträgen Edelgasen untersucht, wobei meist Laserpulse mit Frequenzen im sichtbaren oder nahinfraroten Bereich zum Einsatz kommen. Für Intensitäten oberhalb von 10^{14} W/cm^2 und Pulslängen im Femtosekundenbereich lässt sich Einfachionisation ($A \rightarrow A^+$) sehr gut als Tunnelprozess mit anschließender klassischer Bewegung des Elektrons im Laserfeld beschreiben. Betrachtet man die Ionisation *zweier* Elektronen, so kann diese für genügend große Intensitäten (z. B. $I > 10^{15}$ W/cm^2 für Neon) als Abfolge von zwei unabhängigen Einfachionisationen aufgefasst werden (sequentielle Doppelionisation, $A \rightarrow A^+ \rightarrow A^{2+}$). Für kleinere Intensitäten liegen die gemessenen A^{2+}-Ionenausbeuten dagegen um mehrere Größenordnungen über den auf Basis des sequentiellen Mechanismus erwarteten Ergebnissen, wobei der Übergang zum sequentiellen Bereich in der Intensitätsabhängigkeit der Ausbeute zu einer charakteristischen Kniestruktur führt. Den für die erhöhte A^{2+}-Ionenproduktion verantwortlichen Ionisationspfad, d.h. die simultane Ionisation zweier Elektronen ($A \rightarrow A^{2+}$), bezeichnet man als nichtsequentielle Doppelionisation (NSDI). Zur qualitativen Beschreibung dieses Prozesses hat sich ein semiklassischer Rückstreumechanismus bewährt. Nach diesem tunnelt ein Elektron aus dem atomaren Potential heraus, wird im elektrischen Feld des Lasers beschleunigt und schließlich unter Energieaufnahme zum Ion zurückbeschleunigt, wo durch inelastische Kollision ein weiteres Elektron freigesetzt wird. Der Rückstreumechanismus macht auch quantitative Aussagen bezüglich der finalen Impulse der ionisierten Elektronen, welche gut mit experimentellen Messergebnissen übereinstimmen.

Die Mechanismen der Doppelionisation lassen sich auf die Ionisation einer beliebigen Zahl von Elektronen verallgemeinern, wobei man alle von der sequentiellen Vorhersage abweichenden Ionisationspfade als nichtsequentielle Mehrfachionisation bezeichnet. Ein Verständnis der Dreifachionisation ist von besonderem Interesse, da hier erstmals mehrere miteinander konkurrierende nichtsequentielle Pfade auftreten. Dies sind neben der durch den Rückstreumechanismus beschriebenen simultanen Ionisation dreier Elektronen (I: $A \rightarrow A^{3+}$) die beiden möglichen Kombinationen von Einfachionisation mit NSDI durch Rückstreuung (II: $A \rightarrow A^+ \rightarrow A^{3+}$ bzw. III: $A \rightarrow A^{2+} \rightarrow A^{3+}$). Aufgrund der nichtlinearen Abhängigkeit der Tunnelwahrscheinlichkeit von den Ionisierungsenergien der beteiligten Ladungszustände erwartet man, dass im nichtsequen-

tiellen Intensitätsbereich (z. B. $I < 10^{16}$ W/cm^2 für Neon) nur die Pfade I und II signifikant zur A^{3+}-Ionenausbeute beitragen. Des Weiteren geht man davon aus, dass die A^{3+}-Ionenausbeute zwei Kniestrukturen aufweist, die den Wechsel des dominanten Ionisationspfades von I zu II bzw. von II zur sequentiellen Dreifachionisation (IV: $A \rightarrow A^+ \rightarrow A^{2+} \rightarrow A^{3+}$) anzeigen. Diese Wechsel sollten sich nach den Vorhersagen des Rückstreumechanismus auch in der Struktur der Impulsverteilungen der A^{3+}-Ionen bemerkbar machen. Da die bisherigen Experimente die obigen Erwartungen nur teilweise bestätigen konnten, ist eine eingehende theoretische Untersuchung von Dreifachionisation sinnvoll.

In dieser Arbeit werden quantenmechanische Simulationen zur Dreifachionisation mit Laserpulsen sichtbarer und nahinfraroter Frequenz vorgestellt. Um eine effiziente numerische Umsetzung zu ermöglichen, wird die Bewegung der drei Elektronen auf einen dreidimensionalen Unterraum des vollen Konfigurationsraums eingeschränkt. Diese Art der Modellierung hat sich bereits bei der qualitativen Behandlung der Doppelionisation bewährt. Aus der quantenmechanischen Wellenfunktion des Modells werden verschiedene Größen berechnet, die auch experimentell gemessen werden können (Ionenausbeuten, Elektronen- und Ionen-Impulsverteilungen) und ihre Abhängigkeit von den Laserparametern (Intensität, Frequenz, Pulsdauer) wird untersucht. Ziel der Arbeit ist es, die Pfade und Mechanismen der Dreifachionisation in den verschiedenen Intensitätsbereichen zu verstehen. Zu diesem Zweck werden zunächst die Ionenausbeuten als Funktion der Intensität betrachtet. Mit Hilfe von Ein- und Zwei-Elektronen-Näherungen können die Ausbeuten der Pfade II - IV als Produkt der Ausbeuten der Zwischenschritte geschrieben werden. Auf diese Weise ist es möglich, die A^{3+}-Ausbeuten in einem breiten Intensitätsbereich quantitativ nachzuvollziehen. Um den verbleibenden Pfad I zu quantifizieren, wird die Rückstreuung eines Elektrons klassisch (durch Trajektorienstudien) und quantenmechanisch (mit Hilfe des zeitabhängigen Wahrscheinlichkeitsflusses) analysiert. Die gewonnenen Erkenntnisse zu Produktausbeuten und klassischer Rückstreuung werden anschließend zur Interpretation der A^{3+}-Ionenimpulsverteilungen eingesetzt, die den Wechsel des dominanten Ionisationspfades noch deutlicher zeigen als die Ausbeuten.

Eines der wesentlichen Ergebnisse der Arbeit ist die Bedeutung klassischer Schwellen für die simultanen Mehrfachionisationsprozesse. So lässt sich z. B. der Beginn des Intensitätsbereichs mit nahezu konstantem A^{3+}/A^+-Ausbeutenverhältnis mit der Schwellenintensität der simultanen Dreifachionisation identifizieren, bei der die Energie des zurückgestreuten Elektrons gerade der Summe der beiden Ionisierungsenergien des A^+-Ions entspricht. Des Weiteren legt die Untersuchung der A^{3+}-Ausbeuten nahe, dass der Pfad III im nichtsequentiellen Intensitätsbereich der Dreifachionisation eine weitaus größere Rolle spielt als bisher angenommen. Hervorzuheben ist schließlich auch die Fähigkeit des entwickelten Modells, die wesentlichen experimentellen Beobachtungen zur Dreifachionisation qualitativ zu reproduzieren.

Abstract

With the ultrashort laser pulses available today, intensities which exceed the binding electrical field of an atom by several orders of magnitude are routinely achieved. As a consequence, it is possible to remove (ionize) one electron or several electrons from an atom within one pulse.

The intensity dependence of laser-induced ionization is highly nonlinear and is mostly studied with chemically inert noble gases, using pulses with frequencies in the visible or near-infrared range. For intensities above 10^{14} W/cm^2 and femtosecond pulse durations, single ionization ($A \rightarrow A^+$) can be described very well as a tunneling process with subsequent classical motion of the electron in the laser field. Ionization of *two* electrons can be expressed in terms of two independent single ionization steps (sequential double ionization, $A \rightarrow A^+ \rightarrow A^{2+}$) if the intensity is high enough (e.g. $I > 10^{15}$ W/cm^2 for neon). However, for smaller intensities, the measured A^{2+} ion yields are several orders of magnitude larger than those expected from the sequential mechanism and the transition to the sequential regime leads to a characteristic knee structure in the intensity dependence of the yield. The ionization pathway responsible for the increased production of A^{2+} ions, i.e. the simultaneous ejection of two electrons ($A \rightarrow A^{2+}$), is called nonsequential double ionization (NSDI). For the description of this process, a semiclassical rescattering mechanism has proved successful. According to the rescattering mechanism, an electron tunnels from the atomic potential, is accelerated by the laser field and driven back to the ion where, in an inelastic collision, a second electron is released. With respect to the final momenta of the ionized electrons, the rescattering mechanism also allows for quantitative predictions which are in good agreement with experimental results.

The mechanisms of double ionization can be generalized to ionization of an arbitrary number of electrons, with all pathways deviating from the sequential one being referred to as nonsequential multiple ionization. An understanding of triple ionization is of special interest since it is the first case for which several competing nonsequential pathways exist, i.e. simultaneous ionization of three electrons described by the rescattering mechanism (I: $A \rightarrow A^{3+}$) and the two combinations of single ionization with NSDI by rescattering (II: $A \rightarrow A^+ \rightarrow A^{3+}$ and III: $A \rightarrow A^{2+} \rightarrow A^{3+}$). Considering the nonlinear dependence of the tunneling probability on the ionization energies of the participating charge states, one expects that only the pathways I and II contribute significantly to the A^{3+} yield in the nonsequential intensity regime (e.g. $I < 10^{16}$ W/cm^2 for neon). Furthermore, one expects two knee structures in the A^{3+} yield which indicate the transition from I to II and from II to sequential triple ionization (IV: $A \rightarrow A^+ \rightarrow A^{2+} \rightarrow A^{3+}$), respectively. Based on the predictions of the rescattering mechanism, these transitions

should also manifest themselves in the momentum distributions of the A^{3+} ions. Since experiments could only partially confirm the above expectations, a detailed theoretical investigation of triple ionization is desirable.

In this work, quantum mechanical simulations of triple ionization with laser pulses of visible and near-infrared frequencies are presented. To allow for efficient numerical calculations, the motion of the electrons is restricted to a three-dimensional subspace of the full configuration space. This modeling approach has already proved successful in the qualitative investigation of double ionization. From the quantum mechanical wave function of the model, several quantities are calculated which can also be measured experimentally (ion yields, electron and ion momentum distributions) and their dependence on the laser parameters (intensity, frequency, pulse duration) is studied. The main goal of this work is to understand the pathways and mechanisms of triple ionization in the different intensity regimes. For this purpose, we first study the ion yields as a function of intensity. Using one- and two-electron approximations, the yields of the pathways II - IV can be written as products of the yields of the intermediate charge states. This way, it is possible to quantitatively understand the A^{3+} yields in a wide range of intensities. To quantify the remaining pathway I, rescattering of an electron is analyzed classically (by performing trajectory studies) and quantum mechanically (by considering the time-dependent probability flux). Finally, the insights gained from the product yields and the rescattering analysis are used to interpret the A^{3+} ion momentum distributions which reflect the change of the prevalent ionization pathway more clearly than the yields.

A major result of this work is the importance of classical thresholds for simultaneous multiple ionization. For example, the onset of the regime where the intensity-dependent A^{3+}/A^{+} yield ratio is approximately constant can be identified with the threshold intensity of simultaneous triple ionization where the energy of the rescattered electron is equal to the sum of the two ionization energies of the A^{+} ion. Furthermore, the investigation of the A^{3+} yields indicates that the pathway III plays a much more important role for triple ionization in the nonsequential intensity regime than previously thought. Finally, one has to emphasize the ability of the model to qualitatively reproduce the essential experimental observations on triple ionization.

Contents

List of Figures

List of Tables

Symbols and abbreviations

Abbreviations

a.u.	atomic units	XVII
ADK	Ammosov, Delone, Krainov	36
AEM	aligned-electron model	18
arb. u.	arbitrary units	XVII
COLTRIMS	cold target recoil ion momentum spectroscopy	11
FFT	fast Fourier transform	225
FWHM	full width at half maximum	31
NSDI	nonsequential double ionization	8
OBI	over-the-barrier ionization	7
RESI	recollision-induced excitation with subsequent field ionization	9
ROBI	recollision-induced over-the-barrier ionization	9
SAE	single-active-electron	54
TAE	two-active-electron	56

Ionization pathways

0-1	single ionization	3
0-1-2	sequential double ionization	3
0-1-2-3	sequential triple ionization	3
0-1-3	single ionization followed by simultaneous double ionization	3
0-2	simultaneous double ionization	3
0-2-3	simultaneous double ionization followed by single ionization	3
0-3	simultaneous triple ionization	3

Greek symbols

Δp	momentum grid spacing	125
Δr	position grid spacing	41
Δt	time step	41
η	strength of imaginary potential for absorbing boundaries	41
γ_K	Keldysh parameter	5
ω_0	laser frequency	30
Θ	Heaviside step function	30
ε	cut-off parameter for soft-core Coulomb potentials	18
φ_0	carrier-envelope phase	30

Roman symbols

Units and notation

Hartree atomic units (a.u.) are used throughout this work, except where indicated otherwise. In Table U.1, the atomic units of several important physical quantities are listed. Atomic units are not to be confused with arbitrary units which are abbreviated as (arb. u.).

Experimentalists usually characterize a laser pulse in terms of its (peak) intensity I (measured in W/cm^2), wavelength (measured in nm) and full width at half maximum duration (measured in fs). On the theoretical side, it is more common to use the amplitude F of the electric field and the frequency ω, both in atomic units. To facilitate comparison, we give the conversion formulas

$$\lambda[\text{nm}] = \frac{45.56}{\omega[\text{a.u.}]}, \tag{U.1a}$$

$$I[\text{W/cm}^2] = 3.509 \cdot 10^{16} (F[\text{a.u.}])^2. \tag{U.1b}$$

A conversion formula for the pulse duration will derived in Section 2.3 after the shape of our theoretical laser pulse has been specified.

In mathematical expressions, a bold symbol $\boldsymbol{r}$ always denotes a vector, with the number of components evident from the context. $\widehat{f}(b)$ denotes the Fourier transform of the function $f(a)$. The conjugate variables a and b are either time and energy or position and momentum. Hats for quantum mechanical operators are completely omitted in this work since the corresponding observables are also studied classically.

Quantity	Atomic unit		SI units
Mass	m_{at}	$= 1\ m_e$	$\approx 9.109 \cdot 10^{-31}$ kg
Charge	e_{at}	$= 1\ e$	$\approx 1.602 \cdot 10^{-19}$ As
Length	x_{at}	$= 1\ a_0$	$\approx 5.292 \cdot 10^{-11}$ m
Action	S_{at}	$= 1\ \hbar$	$\approx 1.055 \cdot 10^{-34}$ Js
Energy	E_{at}	$= 1\ \frac{\hbar^2}{a_0^2 m_e}$	$\approx 4.360 \cdot 10^{-18}$ J
Time	$t_{at} = \frac{\hbar}{E_{at}}$	$= 1\ \frac{a_0^2 m_e}{\hbar}$	$\approx 2.419 \cdot 10^{-17}$ s
Momentum	$p_{at} = \sqrt{m_{at} E_{at}}$	$= 1\ \frac{\hbar}{a_0}$	$\approx 1.993 \cdot 10^{-24}$ kg m/s
Electric field	$F_{at} = \frac{E_{at}}{a_0 e}$	$= 1\ \frac{\hbar^2}{a_0^3 m_e e}$	$\approx 5.142 \cdot 10^{11}$ V/m

Table U.1. Physical quantities and their atomic units, adapted from Grossmann (2008). All quantities are expressed in terms of four fundamental constants, namely the electron mass m_e, the elementary charge e, the Bohr radius a_0 and Planck's constant $\hbar$.

1. Introduction

2017 marks the 100th anniversary of Einstein's prediction of stimulated photon emission (Einstein, 1917). The most important application of this effect is the generation of highly coherent radiation with lasers which have become indispensable tools in medicine, science and every day life. The rapid and still ongoing evolution of laser technology has made it possible to confine the emitted energy to ever shorter time and length scales (Brabec and Krausz, 2000), resulting in very high radiation intensities. While the first ruby laser constructed by Maiman (1960) delivered 1 ms (10^{-3} s) pulses with intensities around 10^9 W/cm^2 (Mourou *et al.*, 2007), modern commercially available Ti:sapphire lasers can produce ultrashort pulses with durations on the order of a few fs (10^{-15} s) and intensities larger than 10^{16} W/cm^2. If an atom is exposed to such a laser pulse, one or several electrons will be removed from it. This effect is known as laser-induced ionization.

While laser-induced single and double ionization have been thoroughly studied in the last three decades, triple ionization is still largely unexplored. In this thesis, we approach this topic from the theoretical side. To put the work in context, we briefly outline the qualitative theory of laser-induced single and double ionization for visible and near-infrared frequencies. For details, the reader is referred to the reviews of de Morisson Faria and Liu (2011), Becker *et al.* (2012) (focusing on theory), Brabec and Krausz (2000) (focusing on the evolution of laser technology) and Chin (2004) (who gives a historical account of experiments on multiphoton and tunnel ionization).

1.1. Strong short laser pulses

Due to their chemical inertness, noble gases are the preferred targets in experiments on the interaction of short laser pulses and atoms. Until the end of the eighties, ionization of noble gases was usually studied with solid-state lasers (ruby, Nd:glass, Nd:YAG) and the CO_2 gas laser (Brabec and Krausz, 2000). The corresponding pulse durations were on the order of several picoseconds. Since then, the Ti:sapphire laser has become the most popular laser since it can emit pulses which are a thousand times shorter, i.e. a few femtoseconds long[1]. With techniques such as chirped-pulse amplification (Strickland and Mourou, 1985), the emitted laser intensity can be increased to over 10^{22} W/cm^2 (Yanovsky *et al.*, 2008) which is almost six orders of magnitude larger than the intensity of the static electric field experienced by the electron in the ground

[1]For example, in a recent experiment by Kübel *et al.* (2016) on multiple ionization of argon, Ti:sapphire pulses with a duration of 4 fs were used.

state of atomic hydrogen ($3.5 \cdot 10^{16}$ W/cm^2). Therefore, it comes as no surprise that ions with very high charge states can be generated with Ti:sapphire pulses[2], e.g. Ne^{8+} (Palaniyappan *et al.*, 2005), Ar^{16+}, Kr^{19+} and Xe^{26+} (Yamakawa *et al.*, 2003). In most cases, the number of A^{i+} ions, i.e. the A^{i+} ion yield or the i-fold ionization yield (we will use both terms interchangeably), was measured as a function of intensity.

In view of the ability to remove many electrons from an atom, it is natural to speak of "strong laser fields". However, the notion of "strong" clearly depends on the point of reference. Following the literature, we will consider laser fields with intensities between 10^{14} and 10^{16} W/cm^2 as strong. For these and all other intensities considered in this work, the photon density of the radiation is so high[3] that field quantization is not necessary, i.e. one can use the classical electromagnetic fields $\boldsymbol{F}$ and $\boldsymbol{B}$ (and their potentials ϕ and $\boldsymbol{A}$) to describe the laser radiation. In this work, we exclusively consider linearly polarized fields. In this case, the laser intensity is related to the electric field as $I \propto |\boldsymbol{F}|^2$.

A common property of the solid-state lasers listed in the first paragraph is that the frequency ω_0 of the emitted radiation lies in the visible or near-infrared spectral range, i.e. roughly between 0.015 a.u. and 0.120 a.u. The corresponding wavelength is much larger than the extension of a typical atom, so the position dependence of the electromagnetic field may be neglected. This simplification is known as the electric dipole approximation (Grossmann, 2008) and will be used throughout this work. Since $\boldsymbol{B} = \nabla \times \boldsymbol{A}(t) = \boldsymbol{0}$, the magnetic field is always equal to zero. For intensities beyond 10^{18} W/cm^2, usually classified as "superstrong" or "ultrastrong", the electron motion becomes relativistic and the dipole approximation loses its validity (Chowdhury and Walker, 2003). However, since the intensities studied in this work do not exceed 10^{16} W/cm^2, relativistic effects are negligible and will therefore not be discussed.

Within the electric dipole approximation, the field interaction term H_{int} of the Hamiltonian describing the atom-laser system is obtained by using the minimal coupling formalism, i.e. by replacing the electron momenta $\boldsymbol{p}_i$ by $\boldsymbol{p}_i - \boldsymbol{A}$ and the potential V by $V + \phi$ (Friedrich, 2006). With gauge transformations, the resulting Hamiltonian can be simplified, yielding the field interaction term in length gauge

$$H_{int} = -\sum_i \boldsymbol{F}(t) \cdot \boldsymbol{r}_i \tag{1.1}$$

where the electric field couples to the electron positions $\boldsymbol{r}_i$, and in velocity gauge

$$H_{int} = -\sum_i \boldsymbol{A}(t) \cdot \boldsymbol{p}_i \tag{1.2}$$

where the vector potential couples to the electron momenta.

[2]Using X-ray free-electron laser pulses which have a much larger frequency, even more electrons can be removed, and ionization up to Kr^{21+} and Xe^{36+} has been observed (Rudek *et al.*, 2012, 2013). Note that for Xe^{36+}, the two outermost electron shells are stripped completely from the xenon atom.

[3]For example, an intensity of 10^{16} W/cm^2 corresponds to about 10^{10} photons in a cube with a side length of 800 nm (Dörner *et al.*, 2002).

1.2. Theory of laser-induced ionization

For a theoretical description of laser-induced n-fold ionization all the way from the neutral atom to the final charge state, one has to understand which intermediate charge states are visited during the ionization process (the ionization pathways) and how the transition between the charge states is accomplished (the ionization mechanisms). For double ionization, there are two pathways from the neutral atom to the doubly-charged ion, namely simultaneous ionization of two electrons (0-2) and sequential double ionization, i.e. two independent single ionization steps (0-1-2). In the labels of the pathways, the charge states are indicated by numbers and the transitions by dashes (Feuerstein *et al.*, 2000). For triple ionization, the simultaneous and the sequential pathway also exist (0-3 and 0-1-2-3), but there are two additional pathways which combine a single ionization step and a simultaneous double ionization step (0-1-3 and 0-2-3). For the general case of n-fold ionization, one can prove by mathematical induction that there are 2^{n-1} pathways.

The above examples show that there are only two types of transitions between charge states, namely single ionization (0-1, 1-2, 2-3, ...) and simultaneous ionization of two or more electrons (0-2, 0-3, 1-3, ...). To emphasize the difference to the sequential ionization pathway 0-1-...-n (which consists entirely of single ionization steps), all pathways which contain at least one simultaneous ionization step are called nonsequential. The number of nonsequential pathways for n-fold ionization is $2^{n-1} - 1$, i.e. one for double ionization (0-2) and three for triple ionization (0-3, 0-1-3, 0-2-3).

The use of the terms "sequential" and "simultaneous" in the above ionization pathways is motivated by the classical description of ionization where one can specify the ejection time of each electron. In the quantum mechanical description, the main difference between sequential and simultaneous ionization of n electrons is the role of the electron repulsion, as emphasized by Geltman (1995). For the sequential pathway, the repulsion is negligible so that each single ionization step may be considered separately. For simultaneous ionization (0-n), on the other hand, we expect some form of correlation between the outgoing electrons. As we will see below, a semiclassical description of both single ionization and simultaneous multiple ionization is possible for certain parameters of the laser pulse. Therefore, we will continue to speak of sequential and simultaneous ionization, but without insisting on perfectly synchronous electron ejection in the second case.

As discussed above, it is sufficient to work out the mechanisms of single and simultaneous multiple ionization. This is the purpose of the next sections.

1.3. Single ionization

The mechanism of single ionization varies strongly the laser frequency ω_0 and the peak amplitude F_0 of the laser electric field (Fig. 1.1). In the multiphoton regime (a), ω_0 governs the ionization process while F_0 is the crucial quantity in the tunneling regime (b and c). We consider the different mechanisms separately.

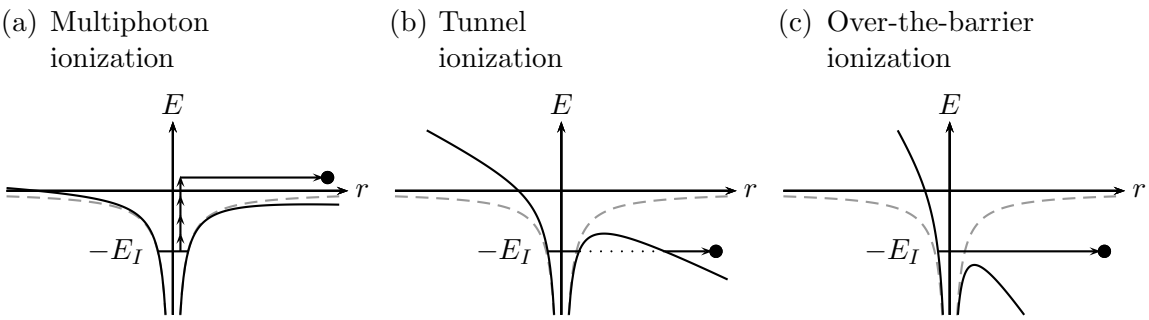

Figure 1.1. Illustration of various single ionization mechanisms, adapted from Brabec and Krausz (2000). The superposition of the atomic Coulomb potential (dashed gray curve) and the electric field of a laser creates a time-dependent, deformed potential (solid black curve). For small field amplitudes, the deformation is small and an electron (black dot) with ionization energy E_I can only reach the continuum by (a) absorbing N photons with energy ω_0 so that $N\omega_0 > E_I$. If the field amplitude is large and the laser field varies sufficiently slow, the electron can (b) tunnel through the barrier or (c) escape over it. An extended version of this figure was first presented in Thiede (2011).

1.3.1. Multiphoton ionization

If light shines on a metal surface and the frequency ω_0 exceeds a certain minimum value, electrons are set free, independent of the light field amplitude F_0. This is known as the photoelectric effect. Its explanation in terms of photons, i.e. discrete energy packets ω_0, was given by Einstein (1905) and marked one of the first successful applications of Planck's quantum hypothesis. The one-atom version of the photoelectric effect, i.e. the emission of an electron from an atom with ionization energy E_I upon light irradiation with frequency $\omega_0 > E_I$, is called single-photon ionization or simply photoionization. For a noble gas in the ground state and a laser with visible or near-infrared frequency, this process cannot occur. However, extending Einstein's explanation to the case $\omega_0 < E_I$, Göppert-Mayer (1931) proposed that two or even N photons may be absorbed simultaneously to overcome the ionization threshold ($N\omega_0 > E_I$, Fig. 1.1a), defining the mechanism of multiphoton ionization. Due to the very small probabilities of multiphoton transitions, a light source with a very high photon density is required to observe them, so it was not until the invention of the laser that the existence of multiphoton ionization could be confirmed (Voronov and Delone, 1966).

Experimentally, multiphoton ionization manifests itself in an increase of the singly-charged ion yield as F_0^{2N} (see e.g. L'Huillier *et al.* (1982, 1983a,b,c)) which is consistent with the result of high-order perturbation theory (Bebb and Gold, 1966; Lambropoulos, 1976; Mainfray and Manus, 1991). An extreme example is the observation of 22-photon ionization of helium at $\omega_0 = 0.043$ a.u. (L'Huillier *et al.*, 1983c). If the field amplitude is increased beyond the value for which the ionization probability equals one (the so-called saturation field amplitude), the F_0^{2N} power law is replaced by a universal F_0^3 power law which results from the expanding Gaussian focal volume (Chin and Isenor, 1970; Cervenan and Isenor, 1975).

1.3.2. Tunnel and over-the-barrier ionization

In order to obtain a general analytical expression for laser-induced single ionization, Keldysh (1965) calculated the transition rate from an atomic bound state to a Volkov state, e.g. the wave function of a free electron in a laser field. Keldysh's paper contained a number of groundbreaking physical predictions (see DiMauro *et al.* (2014) for an enthusiastic summary), most importantly that of tunnel ionization[4] (Fig. 1.1b): If the field amplitude of the laser is large enough, the barrier formed by the superposition of the atomic Coulomb potential and the laser field may become so narrow that an electron wave packet is more likely to escape by tunneling through the barrier than by absorbing photons. However, due to the oscillatory character of the laser field, this situation only occurs in narrow time windows near the field extrema, implying that the efficiency of tunnel ionization is determined by the ratio of the field oscillation period to the time the electron takes to reach the outside of the barrier (the tunneling time) or, equivalently, by the ratio of the respective frequencies,

$$\gamma_K = \frac{\omega_0}{\omega_{tun}}. \tag{1.3}$$

Approximating the smooth barrier in Fig. 1.1c by one with a triangular shape, we find $\omega_{tun} \approx F_0/\sqrt{2E_I}$ (Grossmann, 2008) so that

$$\gamma_K = \frac{\omega_0}{F_0}\sqrt{2E_I} = \sqrt{\frac{E_I}{2U_p}} \tag{1.4}$$

where

$$U_p = \frac{F_0^2}{4\omega_0^2} \tag{1.5}$$

is the ponderomotive energy, i.e. the mean kinetic energy of a classical electron in the periodic field $F(t) = F_0 \sin(\omega_0 t)$.

The dimensionless quantity γ_K defined by equation (1.4) is known as the Keldysh or adiabaticity parameter. Its value relative to 1 can give a first idea of the prevalent single ionization mechanism. In the limit $\gamma_K \gg 1$ (defining the multiphoton regime), the field oscillation period is small compared to the tunneling time, so tunnel ionization is suppressed compared to multiphoton ionization. For fixed ω_0 and E_I, the condition $\gamma_K \gg 1 \Leftrightarrow \omega_0 \gg F_0/\sqrt{2E_I}$ can only be fulfilled with a sufficiently small field amplitude F_0. However, a small field amplitude means that the energy levels of the atom are only slightly influenced by the laser field. Therefore, perturbation theory can be applied, yielding the previously mentioned F_0^{2N} power law for the ion yield. The perturbative description breaks down for $F_0 \approx 0.02$ a.u. (Brabec and Krausz, 2000). For the Ti:sapphire frequency $\omega_0 = 0.057$ a.u. and an ionization energy of $E_I = 1$ a.u. (appropriate for the noble gases), this field amplitude corresponds to $\gamma_K \approx 4$.

[4]For the sake of brevity, we will often refer to tunnel ionization as "tunneling".

The other extreme is $\gamma_K \ll 1$ (defining the tunneling regime) which is achieved with large field amplitudes. In this case, the tunneling time is short compared to the field oscillation period, i.e. tunnel ionization prevails. Furthermore, the barrier width is essentially constant during the tunneling process, allowing for a quasistatic description. Experience has shown that this description remains valid up to $\gamma_K \leq 0.5$ (Chin, 2004). For $\omega_0 = 0.057$ a.u. and $E_I = 1$ a.u., the upper limit corresponds to $F \approx 0.16$ a.u. In the intermediate regime of field amplitudes (0.02 a.u. $\leq F_0 \leq$ 0.16 a.u.), there is no general prediction as to which ionization mechanism dominates. Instead, one must rely on solutions of the time-dependent Schrödinger equation to identify the ionization mechanisms.

The above discussion of the regimes essentially assumes a periodic electric field. However, in a pulse, the oscillation of the field is modulated by an envelope function. If this envelope rises slowly to its maximum (as is the case for a long pulse) and the multiphoton ionization probability is non-negligible (as is the case for visible or near-infrared frequencies), multiphoton ionization in the rising part of the pulse will completely deplete the focal volume of neutral atoms before tunneling field amplitudes are reached. As a result, multiphoton ionization obscures tunnel ionization (Chin, 2004) and it was not until the availability of femtosecond Ti:sapphire pulses that tunnel ionization in the near-infrared could be observed regularly (Augst *et al.*, 1989, 1991). The first experimental observation of tunnel ionization (Chin *et al.*, 1985) was not affected by the above issue since the small mid-infrared frequency of the CO_2 gas laser ($\omega_0 = 0.004$ a.u.) makes multiphoton ionization so unlikely that tunnel ionization prevails even in a long pulse. Nevertheless, the importance of the pulse duration shows that the Keldysh parameter alone is not suitable to predict the prevalent single ionization mechanism (Reiss, 2010).

The singly-charged ion yields measured in the tunneling regime do not increase $\propto F_0^{2N}$ as in the multiphoton regime, but exhibit a more complicated nonlinear dependence on the field amplitude. Building on Keldysh's results, Perelomov *et al.* (1966) and Ammosov *et al.* (1986) derived approximate expressions for the tunnel ionization rate of general atoms with which the experimental results can be reproduced very well. The approaches of these authors are usually referred to as PPT and ADK theory, respectively. The ADK tunnel ionization rate will be introduced and discussed in Section 3.2.

An important property of the tunneling regime is that the motion of the tunneled electron wave packet can be described in good approximation with classical mechanics. The reason is that the spread of the wave packet is small compared to the oscillation amplitude of its center of mass[5] (Brabec and Krausz, 2000) so that the wave packet can be treated as a point charge. In view of this property, it is not surprising that classical trajectory simulations can qualitatively model several features of laser-induced (multiple) ionization (see part IV.B of Becker *et al.* (2012)). These simulations only require a small amount of computational resources, even if a large number of trajectories

[5]If the Coulomb potential is neglected on the outside of the barrier, the center of mass moves according to Newton's equation. This is a consequence of the Ehrenfest theorem.

is integrated. However, for physical initial conditions, one has to rely on approximate tunneling formulas (e.g. ADK) or elaborate microcanonical distributions (Zhou *et al.*, 2010b; Tang *et al.*, 2013). Moreover, quantum effects like tunneling, multiphoton transitions and wave packet interference are excluded a priori. Recently, some authors have tried to remove these drawbacks by providing initial conditions for Newton's equation based on the solution of the Schrödinger equation in a small region around the nucleus (Wang *et al.*, 2013; Tian *et al.*, 2017; Zhang *et al.*, 2017). Nevertheless, if one wants to incorporate all possible effects, the fully quantum mechanical description remains the appropriate starting point.

If the field amplitude is so large that the top of the barrier is suppressed below the ground state energy, the electron can ionize classically (Fig. 1.1c). This mechanism of single ionization is called over-the-barrier ionization[6] (OBI). For the noble gases, Augst *et al.* (1989) showed that the onset of OBI is linked to the saturation of the singly-charged ion yield in the tunneling regime. Since tunnel ionization and OBI are determined by the field amplitude, both mechanisms are also referred to as field ionization.

Having discussed single ionization, we now turn our attention to multiple ionization. We restrict ourselves to field amplitudes corresponding to the tunneling regime where the mechanism of single ionization is either tunnel ionization or OBI.

1.4. Simultaneous multiple ionization

In the tunneling regime, the F_0-dependent single ionization yields of noble gas atoms can be fitted quite well with analytical tunneling theories such as ADK. An equally successful method is the single-active-electron (SAE) approximation (Kulander, 1987, 1988), a version of time-dependent Hartree-Fock theory where the total wave function is approximated by an antisymmetrized product of single-electron wave functions. The common idea of ADK and SAE is that only one electron interacts with the laser field at a time. Applied to multiple ionization, this means that the electrons are ejected one by one and independent from each other, corresponding to the sequential ionization pathway 0-1-...-n. In the first experiments for which multiple ionization in the tunneling regime was reported, the ion count uncertainties were still so large that it was difficult to quantify the deviations from the sequential prediction (Augst *et al.*, 1991; Auguste *et al.*, 1992).

For double ionization, this situation changed with the helium yield measurements of Fittinghoff *et al.* (1992) and Walker *et al.* (1994). By using a large number of laser shots for each field amplitude (60.000 in the latter experiment), the authors could greatly reduce the ion count uncertainties. Most importantly, they found a regime of field amplitudes in which the measured He^{2+} yields exceeded the prediction of sequential double ionization by several orders of magnitude, indicating that the concept of independent electron ejection had to be abandoned there. The underlying mechanism was

[6]Synonyms include above-barrier ionization and barrier-suppression ionization.

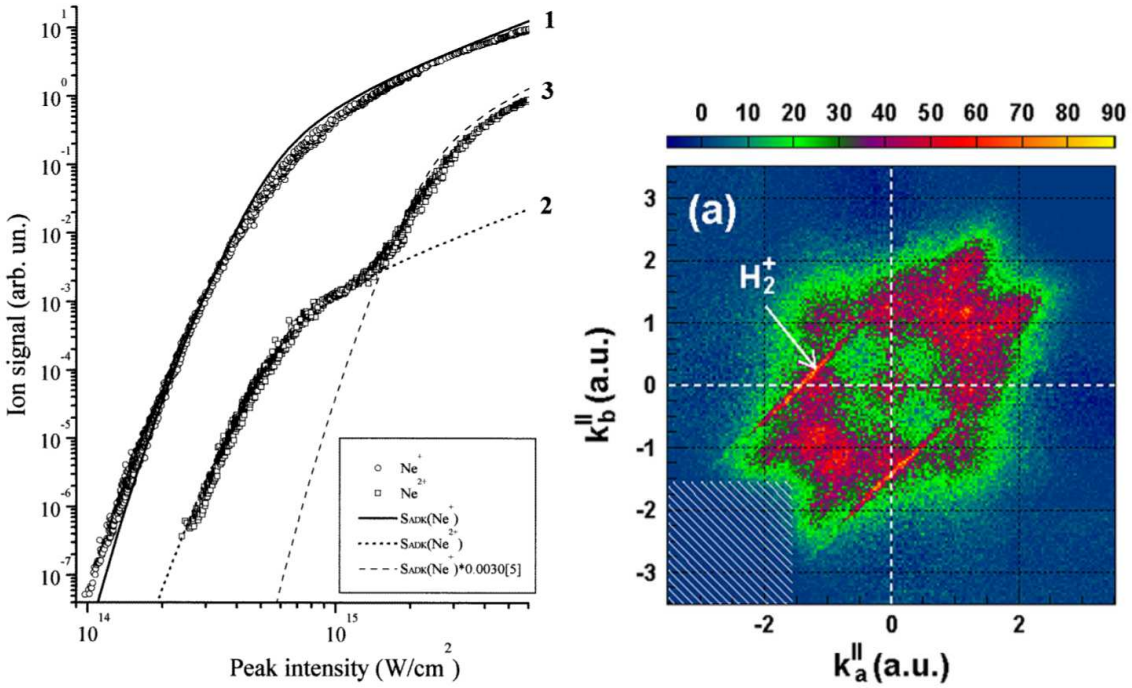

Figure 1.2. Experimental results on double ionization of noble gases. Left image: Ion yields of neon as a function of intensity, obtained with a 200 fs, 800 nm Ti:sapphire laser pulse. The solid, dashed and dotted curves were calculated with ADK tunneling theory. Reprinted from Larochelle *et al.* (1998) with permission from IOP Publishing and S. L. Chin. Right image: Distribution of parallel electron momenta for double ionization of helium, obtained with a 40 fs, 800 nm Ti:sapphire laser pulse at an intensity of $4.5 \cdot 10^{14}$ W/cm^2. Reprinted from Staudte *et al.* (2007) with permission from the American Physical Society and A. Staudte.

named nonsequential double ionization (NSDI). For larger field amplitudes, sequential double ionization was found to give a very accurate prediction of the yields. The transition from one regime to the other is accompanied by a pronounced change of slope in the He^{2+} yield, commonly known as the "knee structure". It was also found in the double ionization yields of all other noble gas atoms (for neon, see the left-hand side of Fig. 1.2), thus being recognized as a universal feature of NSDI.

By considering the He^{2+}/He^{+} yield ratio (which is nearly constant in the knee regime) and demonstrating the simultaneous saturation of the He^{+} yield and the nonsequential He^{2+} yield, Walker *et al.* showed that the excess He^{2+} ion production is due to simultaneous ionization of the two electrons, i.e. the ionization pathway 0-2. As a result, the terms NSDI and simultaneous double ionization are used synonymously.

Several mechanisms of simultaneous double ionization were discussed over the years, including a shake-off scenario (Fittinghoff *et al.*, 1992), a rescattering mechanism (Corkum, 1993) and collective two-electron tunneling (Eichmann *et al.*, 2000). However, only the rescattering mechanism has proved to be successful in both experiment and theory, so we give a brief summary of it in the following section. Mathematical details will be provided in Section 3.6.1.

1.4.1. Rescattering mechanism

The rescattering mechanism is a simple semiclassical three-step model that can consistently explain several strong-field phenomena, including simultaneous multiple ionization. Its development is commonly attributed to Corkum (1993) although the concept was outlined earlier by Kuchiev (1987).

A schematic illustration of the rescattering mechanism for simultaneous *double* ionization is shown in Fig. 1.3. In a first step, an electron wave packet leaves the atom by tunneling through the barrier formed by the superposition of the atomic Coulomb potential and the laser field. As argued above, the tunneled electron can be treated as a classical point charge which, in the second step, is accelerated by the laser field and driven back (rescattered) to the nucleus. Finally, in an inelastic collision (the recollision) with the singly-charged ion, the electron transfers some of its kinetic energy to a second electron so that both can ionize. Depending on the kinetic energy of the recolliding electron (whose maximum classical value is $3.17U_p$ (Corkum, 1993)), several situations can occur. We only treat those eventually leading to double ionization.

(a) If the kinetic energy of the recolliding electron exceeds the binding energy of the second electron (i.e. the first ionization energy of the singly-charged ion), both can escape classically. To emphasize the similarity to single-electron over-the-barrier ionization (see Section 1.3.2), this scenario will be referred to as recollision-induced over-the-barrier ionization (ROBI) in the following[7]. Within a classical calculation, it can be shown that both electrons escape in the same direction parallel to the field polarization axis (Feuerstein *et al.*, 2001).

(b) If the kinetic energy is merely sufficient to promote the second electron to an excited state of the ion, the colliding electron ionizes immediately while the second one ionizes at the next field extremum (via field ionization, i.e. tunneling or OBI). This is called recollision-induced excitation with subsequent field ionization (RESI). Due to the small time delay between recollision and the ejection of the second electron (about a quarter of a field cycle), the electrons ionize back-to-back and not strictly simultaneously.

Both scenarios can be extended to simultaneous n-fold ionization by assuming that the recolliding electron not only interacts with one, but with $n-1$ electrons. To allow for n-electron ROBI, the recollision energy must now be higher than the sum of the first $n-1$ ionization energies of the singly-charged ion.

In contrast to shake-off and collective tunneling, the rescattering mechanism can qualitatively explain the dependence of the NSDI yield on the frequency and the polarization of the laser light (Kondo *et al.*, 1993; Walker *et al.*, 1993). More conclusive evidence was provided by the momentum distributions of the ionized electrons and multiply-charged ions obtained with cold target recoil ion momentum spectroscopy

[7] A synonym which is frequently used in the literature is recollision-induced direct ionization, often abbreviated as REDI (Liu *et al.*, 2008a) or RII (Zhang *et al.*, 2014).

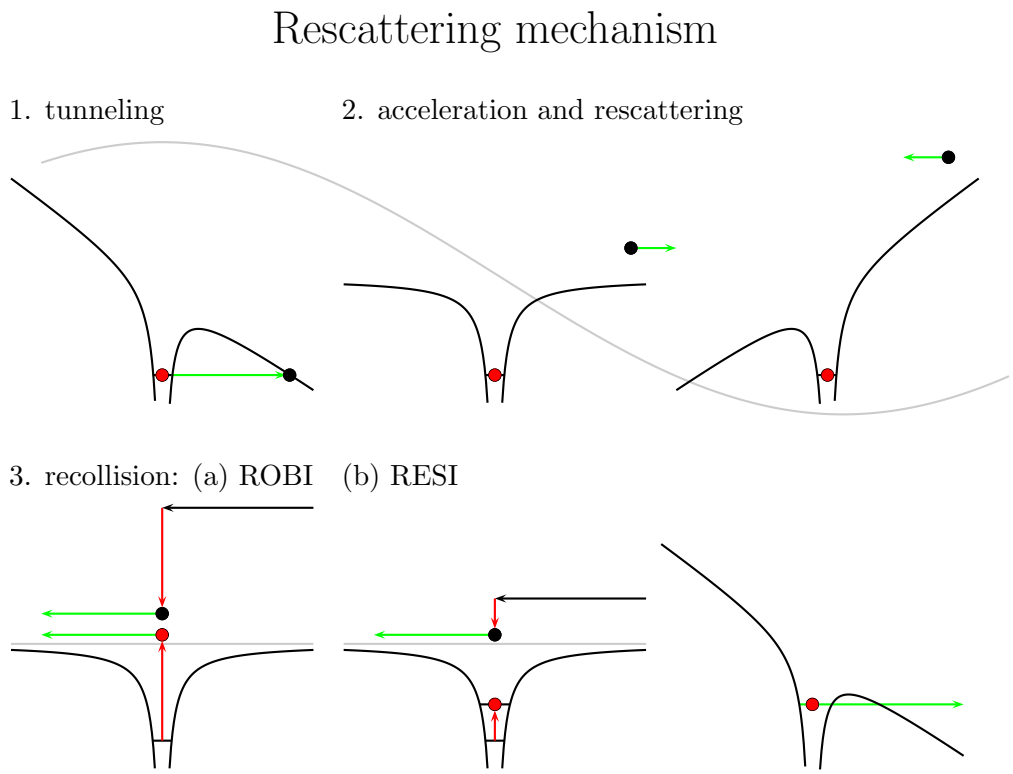

Figure 1.3. Illustration of the rescattering mechanism for simultaneous double ionization, adapted from Rudenko *et al.* (2004) and Corkum and Krausz (2007). In the first step, an electron (black dot) tunnels from the potential well near an extremum of the laser field (gray curve). In the second step, the electron is accelerated in the laser field and driven back (rescattered) to the ion. Finally, the electron collides inelastically with the ion, thereby transferring some of its kinetic energy to a second, residual electron (red dot). If the kinetic energy exceeds the ionization energy of this electron, both electrons escape classically (recollision-induced over-the-barrier ionization, ROBI) and in the same direction. If the kinetic energy is merely sufficient to promote the second electron to an excited state of the ion, the colliding electron ionizes immediately while the other electron ionizes at the next field extremum in the opposite direction (recollision-induced excitation with subsequent field ionization, RESI).

(COLTRIMS) (Weber *et al.*, 2000a,b; Moshammer *et al.*, 2000). This technique allows to measure the full momentum vector of the recoil ion and the ionized electrons in coincidence. The momentum distributions revealed that the electrons typically escape with similar nonzero momenta in NSDI (see right-hand side of Fig. 1.2). By momentum conservation, this leads to a double-maximum structure in the longitudinal momentum distribution of the doubly-charged ion. Both observations could only be explained in terms of ROBI, thereby establishing the rescattering mechanism as *the* mechanism of simultaneous double ionization in the tunneling regime.

Finally, we note that the rescattering mechanism can also explain two other prominent strong-field effects if the inelastic collision of the electron in the last step is replaced by a different scenario. On the one hand, if the returning electron collides elastically with the ion, the electron can absorb additional photons from the laser field while passing the ion (Paulus *et al.*, 1994b). This effect is known as above-threshold ionization. Its characteristic property are peaks in the electron energy distribution which are separated by the photon energy. On the other hand, if the electron recombines with the ion, a photon with frequency equal to an odd multiple of ω_0 (which, for visible or near-infrared frequencies ω_0, is typically located in the extreme ultraviolet (XUV) spectral range) can be emitted. This effect is called high harmonic generation and is used for the creation of attosecond (10^{-18} s) pulses (Paul *et al.*, 2001; Hentschel *et al.*, 2001; Goulielmakis *et al.*, 2008) which open the opportunity for imaging electron dynamics on atomic length and time scales (Corkum and Krausz, 2007). Today, attosecond XUV pulses are already used in many pump-probe experiments (see e.g. Campi *et al.* (2016) and references therein).

1.5. Triple ionization

Now we consider triple ionization in the tunneling regime. Formally, the triple ionization processes are fully specified by applying the mechanisms of tunnel ionization and rescattering to the four triple ionization pathways. Accordingly, simultaneous ionization of three electrons (0-3) is accomplished by rescattering of an electron which ionizes two other electrons. The two-step pathways (0-1-3, 0-2-3), on the other hand, combine single-electron tunnel ionization with simultaneous double ionization by rescattering. Finally, sequential triple ionization (0-1-2-3) consists of three independent tunnel ionization steps.

To estimate how the four triple ionization pathways manifest themselves in the experimental observables, one can consider the ionization energies of the intermediate charge states and the electron momenta expected from the rescattering mechanism, as done by Feuerstein *et al.* (2000). The authors proposed that the pathway 0-2-3 is suppressed compared to 0-1-3 due to the strong decrease of the single-electron tunneling probability with the ionization energy, which is larger for the doubly-charged ion than for the neutral atom (see also Rudenko *et al.* (2008a)). As a result, the yields and longitudinal momentum distributions of the triply-charged ion (Fig. 1.4) only contain

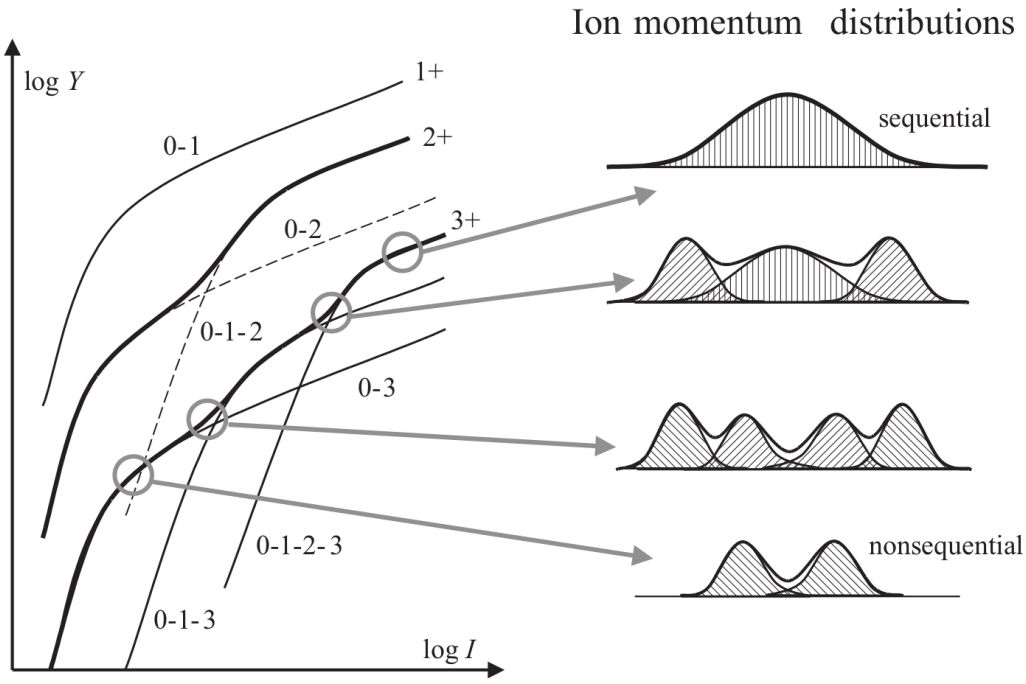

Figure 1.4. Expected intensity dependence of the ion yields (left) and the longitudinal momentum distributions of a triply-charged ion (right). The hatched areas indicate the contributions of the triple ionization pathways 0-3 (\\\), 0-1-3 (///) and 0-1-2-3 (|||). Reprinted from Feuerstein *et al.* (2000) with permission from IOP Publishing and R. Moshammer.

intensity-dependent contributions from the pathways 0-3, 0-1-3 and 0-1-2-3. Based on the natural assumption that the ion production by simultaneous ionization is coupled to the existence of the precursor species, one can predict the intensity regime in which a given pathway dominates the ion yield (left-hand side of Fig. 1.4). For intensities below saturation of the single ionization yield, the interaction volume contains a large number of neutral atoms throughout the pulse, so triple ionization is mainly accomplished on the pathway 0-3. Above saturation of single ionization, almost all atoms are singly-ionized during the pulse (by definition) so that the pathway 0-1-3 takes over. At the same intensity, the prevalent pathway of double ionization changes from 0-2 to 0-1-2. Finally, above saturation of double ionization, almost all atoms are doubly-ionized (via 0-1-2) and the prevalent triple ionization pathway therefore is 0-1-2-3. Near the saturation intensities, the competition between different charge states originating from the same precursor species forces the yields to saturate simultaneously (Walker *et al.*, 1994). As a result, one expects two knee structures in the triple ionization yield.

The longitudinal momentum distribution of the triply-charged ion mirrors the transition from one ionization pathway to another. For a start, we consider the substeps of the triple ionization pathways separately. If an electron leaves the atom via tunnel ionization, the momentum distribution of the resulting ion is a Gaussian distribution peaking at zero longitudinal ion momentum (Delone and Krainov, 1991). For n-electron ROBI ($n = 2, 3$), one expects a double-maximum distribution centered at zero, with the

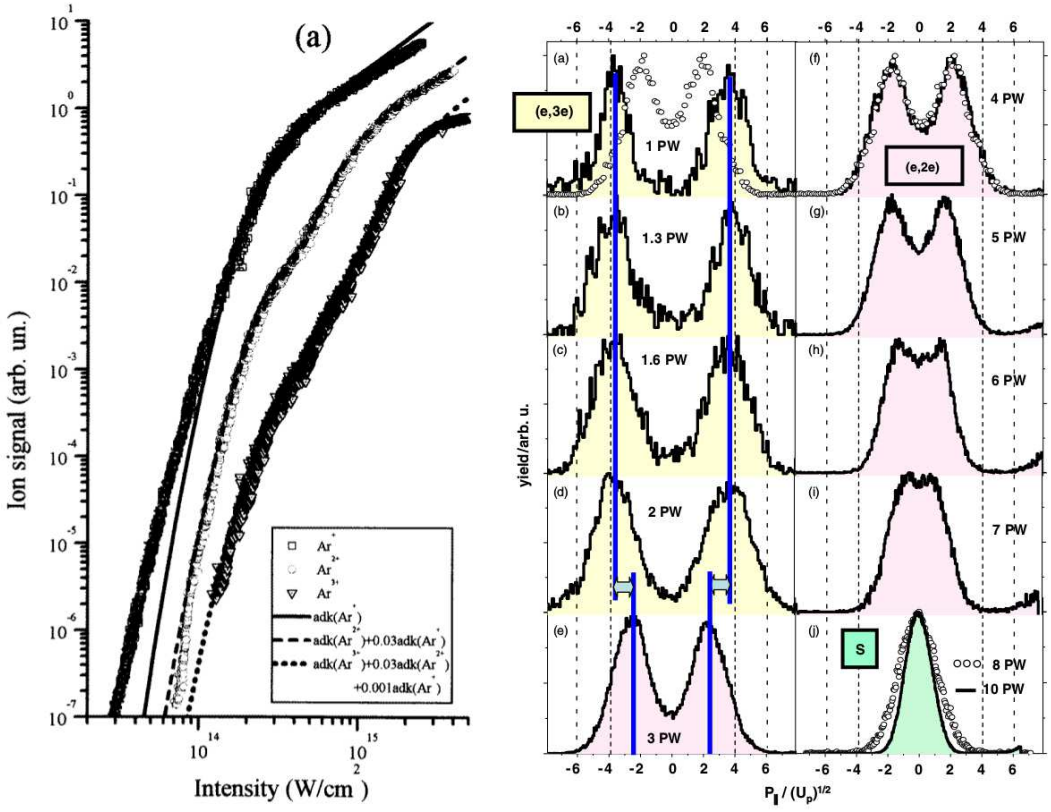

Figure 1.5. Experimental results on triple ionization of noble gases. Left image: Ion yields of argon as a function of intensity, obtained with a 200 fs, 800 nm Ti:sapphire laser pulse. The solid, dashed and dotted curves were calculated with ADK tunneling theory. Reprinted from Larochelle *et al.* (1998) with permission from IOP Publishing and S. L. Chin. Right image: Longitudinal momentum distributions of triply-charged neon ions, obtained with a 25 fs, 795 nm Ti:sapphire laser pulse at various intensities. Reprinted from Rudenko *et al.* (2008a) with permission from IOP Publishing and R. Moshammer.

separation of the maxima increasing with n and the intensity (mathematical details will be given in Section 4.2). For each pathway, the longitudinal ion momentum distribution is obtained by convolving the distributions of the substeps with each other (Zrost *et al.*, 2006). Summing up the contributions of the three pathways, one expects the following intensity dependence of the longitudinal ion momentum distribution (right-hand side of Fig. 1.4): For low intensities, the distribution displays a double-maximum structure, indicative of the ROBI scenario of 0-3. Above saturation of single ionization, a narrower double-maximum structure originating from 0-1-3 appears which eventually evolves into a Gaussian above saturation of double ionization. At the saturation intensities, the distribution may exhibit three or four maxima since the contributions of two pathways are comparable.

1.6. Goals

With the exception of the four-maximum structure, the expected intensity dependence of the longitudinal momentum distribution of the triply-charged ion was confirmed by Rudenko *et al.* (2008a), as shown on the right-hand side of Fig. 1.5. In contrast, the intensity-dependent triple ionization yields measured until now (see the left-hand side of Fig. 1.5 for argon and Palaniyappan *et al.* (2005); Ekanayake *et al.* (2012) for neon) only exhibit a faint knee structure near the saturation intensity of double ionization. For lower intensities, the ion counts drop rapidly. An accurate determination of the triple ionization yield near the saturation intensity of single ionization would require a very large number of laser shots, probably two orders of magnitude larger than in the experiment of Walker *et al.* (1994) on double ionization. Therefore, an unambiguous observation of the knee structure signifying the transition from 0-3 to 0-1-3 has not been reported until now.

This rather unsatisfactory situation on the experimental side calls for a detailed theoretical investigation of triple ionization. Until now, only isolated aspects have been studied, e.g. the ion yields (Becker and Faisal, 1999; Ho and Eberly, 2006; Guo and Liu, 2008) or the momentum distributions (Sacha and Eckhardt, 2001a; Ho and Eberly, 2007; Zhou *et al.*, 2010b; Tang *et al.*, 2013), mostly within the framework of classical mechanics. A quantum mechanical investigation of triple ionization is, however, still lacking. Filling this gap is the purpose of this work. The main goal is to understand the triple ionization pathways and mechanisms in the different regimes of field amplitudes by studying *both* the ion yields and the momentum distributions. As discussed in the previous section, there is a competition between three nonsequential pathways below the onset of sequential triple ionization. If one is able to disentangle their contributions, it may be possible to generalize the procedure to nonsequential ionization of four, five and more electrons. For double ionization with its single nonsequential pathway, such a generalization is not possible. Nevertheless, double and single ionization will be considered in detail in this work since they not only compete with triple ionization, but also provide starting points for the interpretation of the triple ionization results. This motivates the thesis title "*Multiple* ionization in strong laser fields".

1.7. Overview

The remainder of this thesis is organized as follows. In Chapter 2, a three-electron model with one degree of freedom per electron is introduced which allows for numerical calculations with manageable computational effort. The subsequent chapters are devoted to an extensive quantum mechanical study of single, double and triple ionization within the model.

Chapter 3 focuses on the ion yields at the end of the pulse. After discussing the dependence of the yields on the field amplitude for fixed frequency and pulse duration, we derive simplified one- and two-electron Hamiltonians from the model Hamiltonian. With products of the yields of these systems, we are able to approximate the yields of

the multiple ionization pathways 0-1-2, 0-1-3, 0-2-3 and 0-1-2-3. The product yields are compared to the results obtained with the three-electron model for various frequencies and pulse durations.

Next, we focus on the simultaneous multiple ionization pathways (0-2, 0-3). For this purpose, we perform a semiclassical analysis of electron rescattering in one dimension to determine typical recollision energies and times. With these, we calculate the threshold field amplitudes of two- and three-electron ROBI and discuss how they manifest themselves in the quantum mechanical ion yields. Finally, we provide a quantitative description of the simultaneous multiple ionization yields by considering the time-dependent rescattering yield.

In Chapter 4, the momentum distributions of the ions and electrons are discussed for various field amplitudes and frequencies. Based on the findings of the previous chapter and using the available experimental results, we identify the contributions of the various ionization pathways in the distributions.

Chapter 5 collects the results of this thesis with respect to triple ionization and suggests directions for future research. The Appendix not only offers supplementary results and technical details on the numerical algorithms, but also includes a self-contained chapter on Wannier theory of multiple ionization in a constant laser field.

2. Model

In strong-field multiple ionization, the electric field of the laser no longer represents the proverbial "small perturbation" familiar from textbooks, and an ab initio investigation of the problem becomes inevitable. To this end, we develop a model that captures the characteristic features of multiple ionization and is computationally accessible.

2.1. Low-dimensional models

The fundamental problem of studying strong-field multiple ionization quantum mechanically is the high dimensionality of the time-dependent Schrödinger equation

$$\mathrm{i}\frac{\partial\psi}{\partial t} = H\psi \tag{2.1}$$

describing the atom-laser system. For an atom with N electrons in a linearly polarized laser field $F(t)$ pointing in the $-z$-direction, the Hamiltonian reads, in length gauge,

$$H = \sum_{i=1}^{N}\left(\frac{\boldsymbol{p}_i^2}{2} - \frac{N}{|\boldsymbol{r}_i|} - F(t)z_i\right) + \sum_{\substack{i,j=1\\ i<j}}^{N}\frac{1}{|\boldsymbol{r}_i - \boldsymbol{r}_j|}. \tag{2.2}$$

Due to the electron repulsion, the solution ψ of (2.1) cannot be given in analytical form and has to be found numerically, e.g. by expanding ψ in a basis set of orthogonal functions and solving the coupled differential equations for the expansion coefficients (Grossmann, 2008). If the number of basis functions per dimension is M, this amounts to the calculation of M^{3N} time-dependent coefficients and M^{6N} time-dependent matrix elements. Since the computation time of each matrix element is non-negligible, a numerical solution of the Schrödinger equation (2.1) for $N > 2$ is out of reach, even if M is small (say 10). With supercomputers, helium ($N = 2$) becomes accessible for large laser frequencies (Taylor *et al.*, 1998, 2003; Dundas *et al.*, 1999; Parker *et al.*, 2003, 2006) but the requirements are enormous: For example, a high-accuracy integration of the Schrödinger equation for a laser pulse with $\omega_0 = 0.057$ a.u. and seven cycles takes about 130 hours on 16.110 processors (Taylor *et al.*, 2010). Other approaches that aim for an exact quantum mechanical treatment of the system described by (2.2), e.g. S-matrix theory or density-functional methods (Taylor and Dundas, 1999; Becker *et al.*, 2012), are equally challenging on a computer, so we look for another way to tackle the problem.

For a *qualitative* understanding of multiple ionization, it is not necessary to study the full-dimensional Hamiltonian since most of the experimental effects can be reproduced with low-dimensional models. They are found by "reducing the dimensionality" of the Hamiltonian, i.e. eliminating the degrees of freedom in (2.2) which are considered irrelevant for the processes one wants to study. In most cases, only one degree of freedom per electron is retained ("one-dimensional models"). If the total dimension does not exceed three, such a model is computationally accessible and ionization can be studied as a function of a laser parameter, e.g. the field amplitude, the frequency or the pulse duration, like it is done in an experiment. In particular, the parameter range is not as restricted as in the full-dimensional atom[1].

Reducing the position space of (2.2) to one dimension per electron produces Coulomb potentials of the form $1/|x|$. To circumvent the numerical problems associated with the singularities, one introduces a cut-off parameter[2] ε such that $1/|x|$ becomes $1/\sqrt{x^2+\varepsilon^2}$. This potential is called a soft-core Coulomb potential. Its first use in the context of strong-field ionization is due to Javanainen *et al.* (1988). Apart from its regularity, the soft-core Coulomb potential has a number of advantages – it approaches the real Coulomb potential for $x \gg \varepsilon$ and the bound-state levels show a Rydberg-like spacing. If one is solely interested in removing the singularity, the cut-off parameter can in principle be arbitrarily small, provided the potential slopes can be accurately resolved with the chosen spatial grid spacing. For reasonable resolutions, $\varepsilon = 1$ a.u. is used in many applications (Javanainen *et al.*, 1988; Grobe and Eberly, 1992, 1993). However, as shown by Eberly (1990) for one electron, a variation of ε allows to tune the ionization energy of the soft-core Coulomb potential to a desired (negative) value. The same is possible for a system of multiple, interacting electrons (Pindzola *et al.*, 1991). Even for qualitative studies, this is a useful property since the ionization energies determine the regime of field amplitudes where the interesting ionization processes take place.

For $N = 2$, the most widely used model in strong-field atomic physics is the aligned-electron model (AEM) where the electrons are restricted to move along the field polarization axis, i.e. in an invariant dynamical subspace of the full atom. The Hamiltonian reads

$$H = \sum_{i=1}^{2} \left(\frac{p_{z_i}^2}{2} - \frac{2}{\sqrt{z_i^2+\varepsilon^2}} - F(t) z_i \right) + \frac{1}{\sqrt{(z_1-z_2)^2+\varepsilon^2}}. \tag{2.3}$$

The properties of the AEM were extensively studied during the last two decades (see e.g. Grobe and Eberly (1992, 1993); Bauer (1997); Lappas and van Leeuwen (1998); Liu *et al.* (1999); Lein *et al.* (2000); Panfili and Liu (2003)). Since rescattering of an electron requires only one degree of freedom parallel to the field axis (Kästner *et al.*, 2012a), effects which are due to the rescattering mechanism, e.g. the knee structure in

[1] For example, in the Schrödinger equation of the helium-laser system, the frequencies cannot be made arbitrarily small since the effort scales as ω_0^{-3} (Parker *et al.*, 2003). Therefore, one usually studies large frequencies which, however, are hard to realize experimentally (Parker *et al.*, 2001).

[2] Synonyms include smoothing, soft-core and screening parameter.

the double ionization yield, can be qualitatively reproduced with the AEM. However, the increased Coulomb repulsion between the electrons leads to a pronounced potential ridge along $z_1 = z_2$. As a result, access to this subspace is strongly suppressed. With the advent of differential momentum distributions showing clear evidence of both electrons escaping parallel to the field axis in NSDI (Weber *et al.*, 2000a,b; Moshammer *et al.*, 2000), the AEM seemed to be stretched to its limits and the search for new models was reignited.

Based on the observation that the laser field couples to the electrons' center-of-mass coordinate $\boldsymbol{R} = \boldsymbol{r}_1 + \boldsymbol{r}_2$, Ruiz *et al.* (2006) suggested to restrict $\boldsymbol{R}$ to the field axis while keeping the full-dimensional character of the relative coordinate $\boldsymbol{r} = \boldsymbol{r}_1 - \boldsymbol{r}_2$. Since the system has a cylindrical symmetry with respect to the field axis, $\boldsymbol{r}$ can be expressed in cylindrical coordinates. The resulting Hamiltonian has three degrees of freedom and is given by (Chen *et al.*, 2010)

$$H = \frac{P_Z^2}{4} + p_\rho^2 + p_z^2 - F(t)Z - \frac{2}{\sqrt{\rho^2/4 + (Z - z/2)^2 + \varepsilon^2}} - \frac{2}{\sqrt{\rho^2/4 + (Z + z/2)^2 + \varepsilon^2}} + \frac{1}{\sqrt{\rho^2 + z^2 + \varepsilon^2}}. \tag{2.4}$$

With this model, Staudte *et al.* (2007) were able to qualitatively reproduce their measured two-electron momentum distributions for helium.

The two-electron model of Eckhardt and Sacha (2006) is based on the rescattering picture of NSDI. The basic idea is that the rescattering electron recombines with the ion to form a short-lived, doubly-excited compound state. Due to the fast electron motion and the strong interactions close to the nucleus, the compound state has no memory of the mechanism that lead to its formation, so the preparation paths can be separated from the decay paths (Sacha and Eckhardt, 2001b). Searching for the classical decay path of NSDI, a saddle point is identified in the potential of the atom which corresponds to a symmetric configuration of the electrons with respect to the field axis. This saddle can be thought of as a transition state[3] which separates the compound state (both electrons close to the nucleus) from the doubly-ionized state (both electrons far away from the nucleus). Inspired by Wannier's study of single ionization by electron impact (Wannier, 1953), it is argued that the electrons have to escape across the saddle or very close to it in NSDI since the electron repulsion will otherwise amplify the position differences, thus leading to single rather than double ionization. Following this proposition, the electrons are confined to the straight lines created by the saddle configuration as the field is varied (the "saddle tracks"). This yields the two-dimensional Hamiltonian of the Eckhardt-Sacha model

$$H = \sum_{i=1}^{2} \left(\frac{p_{r_i}^2}{2} - \frac{2}{\sqrt{r_i^2 + \varepsilon^2}} - \frac{\sqrt{3}}{2} F(t) r_i \right) + \frac{1}{\sqrt{(r_1 - r_2)^2 + r_1 r_2 + \varepsilon^2}}. \tag{2.5}$$

[3]In contrast to the transition states usually encountered in chemical reactions (Wigner, 1938), this one has two unstable directions.

It agrees with the AEM Hamiltonian (2.3) up to a factor of $\sqrt{3}/2$ in front of the field and a different electron repulsion term[4]. As shown in a number of publications (Prauzner-Bechcicki *et al.*, 2007, 2008; Eckhardt *et al.*, 2008, 2010), the Eckhardt-Sacha model can qualitatively reproduce all relevant features of NSDI. Moreover, the existence of a doubly-excited state prior to double ionization, i.e. the foundation of the model, was experimentally confirmed by Camus *et al.* (2012) for the case where the recolliding electron has not enough energy to ionize the residual one directly.

2.2. Eckhardt-Sacha model for three electrons

An extension of the AEM and the Ruiz model to three electrons is straightforward: The resulting Hamiltonian has three degrees of freedom in the AEM (Ruiz *et al.*, 2005; Ho and Eberly, 2006) but six degrees of freedom in the Ruiz model, so the latter is not computationally accessible. For the Eckhardt-Sacha model, the extension to three electrons is less clear since there are two saddle points associated with simultaneous triple ionization (Sacha and Eckhardt, 2001a, 2003). The first saddle point corresponds to the three electrons sitting on the vertices of an equilateral triangle around the field axis. In the second one, an electron is located on the field axis while the two others are arranged symmetrically with respect to it. As in the two-electron case, the electron positions move along straight lines as the field is varied, and a three-dimensional Hamiltonian can be obtained by restricting the electrons to these saddle tracks. We base our model Hamiltonian on the triangular configuration since it has the lower energy. In addition, the electrons are indistinguishable in this configuration (see Fig. B.3 in Appendix B.3.2) which is advantageous for a quantum mechanical treatment.

Fig. 2.1 shows the three saddle tracks of the triangular configuration. Each of them can be parametrized by a single coordinate $r_i \in \mathbb{R}$. In the full-dimensional space, the electron positions $\boldsymbol{r}_i$ on the saddle tracks are given by

$$\boldsymbol{r}_1 = \left(-\frac{1}{2\sqrt{3}} r_1, \quad \frac{1}{2} r_1, \sqrt{\frac{2}{3}} r_1 \right), \tag{2.6a}$$

$$\boldsymbol{r}_2 = \left(-\frac{1}{2\sqrt{3}} r_2, -\frac{1}{2} r_2, \sqrt{\frac{2}{3}} r_2 \right), \tag{2.6b}$$

$$\boldsymbol{r}_3 = \left(\frac{1}{\sqrt{3}} r_3, 0, \sqrt{\frac{2}{3}} r_3 \right). \tag{2.6c}$$

Plugging these coordinate restrictions into the full-dimensional Hamiltonian (2.2) for $N = 3$ and smoothing all Coulomb interactions ($1/|r_i| \to 1/\sqrt{r_i^2 + \varepsilon^2}$), we obtain the

[4]The main difference of the AEM and the Eckhardt-Sacha model is the behavior in the symmetric subspace of equal electron coordinates. While the electrons in the AEM have a constant repulsion potential of $1/\varepsilon$ for $z_1 = z_2$ which does not vanish for $z_1 \to \infty$, the repulsion in the Eckhardt-Sacha model decreases as $1/\sqrt{r_1^2 + \varepsilon^2}$ for $r_1 = r_2 \to \infty$, i.e. the electrons are asymptotically noninteracting.

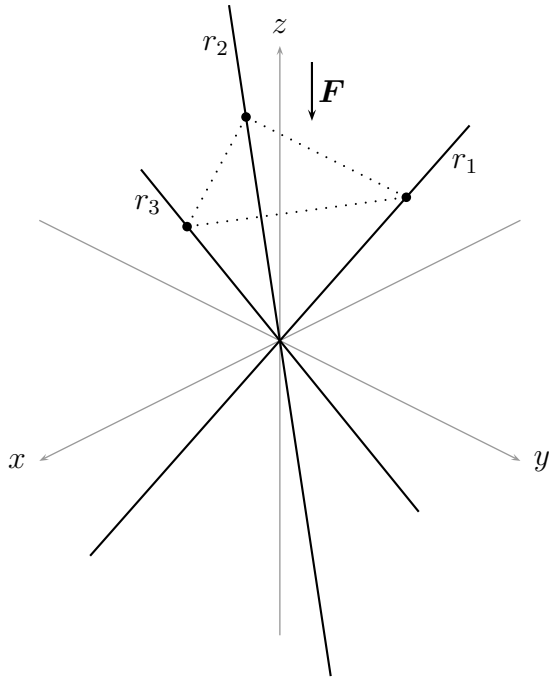

Figure 2.1. Geometry of the three-electron Eckhardt-Sacha model. For a fixed field amplitude, the triple ionization saddle corresponds to the three electrons (black dots) being located on the vertices of an equilateral triangle around the field axis, i.e. on the same side and at an equal distance from the nucleus. As the field amplitude is varied, the electrons move along straight lines (black lines) which keep a constant angle to the field axis. To each of these lines, one electron is confined, with its position parametrized by a coordinate r_i.

Hamiltonian of the three-electron Eckhardt-Sacha model

$$H = \sum_{i=1}^{3} \frac{p_i^2}{2} + V(r_1, r_2, r_3) \tag{2.7}$$

with the potential

$$V(r_1, r_2, r_3) = -\sum_{i=1}^{3} \left(\frac{3}{\sqrt{r_i^2 + \varepsilon^2}} + \sqrt{\frac{2}{3}} F(t) r_i \right) + \sum_{\substack{i,j=1 \\ i<j}}^{3} \frac{1}{\sqrt{(r_i - r_j)^2 + r_i r_j + \varepsilon^2}}. \tag{2.8}$$

The factor $\sqrt{2/3}$ in the field interaction term is due to the tilt of the saddle tracks with respect to the field axis and effectively reduces the field amplitude felt by the electrons. In this work, we will refer to $\sqrt{2/3}$ as the geometrical factor of our model. It will always appear explicitly in the quantities that are discussed in the context of the model, e.g. the ponderomotive energy.

The potential (2.8) is invariant under permutation of the three electron coordinates, meaning that the electrons are indistinguishable. Moreover, we note that the restriction

of the potential to a coordinate plane, e.g. the $r_1 r_2$-plane ($r_3 = 0$),

$$V(r_1, r_2, 0) = -\sum_{i=1}^{2} \left(\frac{2}{\sqrt{r_i^2 + \varepsilon^2}} + \sqrt{\frac{2}{3}} F(t) r_i \right) + \frac{1}{\sqrt{(r_1 - r_2)^2 + r_1 r_2 + \varepsilon^2}} - \frac{3}{\varepsilon}, \quad (2.9)$$

resembles the potential of the two-electron Eckhardt-Sacha model

$$V(r_1, r_2) = -\sum_{i=1}^{2} \left(\frac{2}{\sqrt{r_i^2 + \varepsilon^2}} + \frac{\sqrt{3}}{2} F(t) r_i \right) + \frac{1}{\sqrt{(r_1 - r_2)^2 + r_1 r_2 + \varepsilon^2}}, \quad (2.10)$$

apart from the geometrical factor in front of the field and the constant term $-3/\varepsilon$. This property will be exploited in the next chapter. Furthermore, by considering the classical equations of motion, we find that (2.8) has stationary points on the diagonal $r_1 = r_2 = r_3$ of the configuration space if the field is nonzero. These stationary points are solutions to a cubic equation and can be found with Cardano's method (see Appendix C.2). For $|F(t)|$ smaller than the critical value

$$F_{crit} := \frac{2^{3/2}}{3\varepsilon^2}, \quad (2.11)$$

we find a local maximum at

$$r_s^{TI} = \operatorname{sgn}(F(t)) 2\varepsilon \sqrt{\frac{F_{crit}}{|F(t)|}} \cos^{3/2}\left(\frac{1}{3} \arccos\left(-\frac{|F(t)|}{F_{crit}} \right) \right) \quad (2.12a)$$

$$\xrightarrow{\varepsilon \to 0} \operatorname{sgn}(F(t)) \frac{6^{1/4}}{\sqrt{|F(t)|}} \quad (2.12b)$$

(where sgn is the signum function with $\operatorname{sgn}(x) = \pm 1$ for $x > 0$ and $x < 0$, respectively) with energy

$$V(r_s^{TI}, r_s^{TI}, r_s^{TI}) = -\frac{2\sqrt{12}}{|r_s^{TI}|} \left[2\cos\left(\frac{1}{3} \arccos\left(-\frac{|F(t)|}{F_{crit}} \right) \right) - \frac{|F(t)|}{3F_{crit}} \right] \quad (2.13a)$$

$$\xrightarrow{\varepsilon \to 0} -2 \cdot 6^{3/4} \sqrt{|F(t)|}. \quad (2.13b)$$

In addition, there is a local minimum on the diagonal which merges with the maximum at $|F(t)| = F_{crit}$ to form a saddle point. For $|F(t)| > F_{crit}$, no stationary point exists on the diagonal. As shown in Fig. 2.1, the subspace containing the two stationary points corresponds to the three electrons sitting on the vertices of an equilateral triangle, i.e. the original saddle configuration.

In a Hamiltonian system with n degrees of freedom, Collins *et al.* (2011) define an index-k saddle as a stationary point of Hamilton's equations which has k unstable and $n - k$ stable directions in configuration space. In this terminology, the local maximum (2.12) corresponds to an index-3 saddle. For $\varepsilon \neq 0$, there exist three index-2

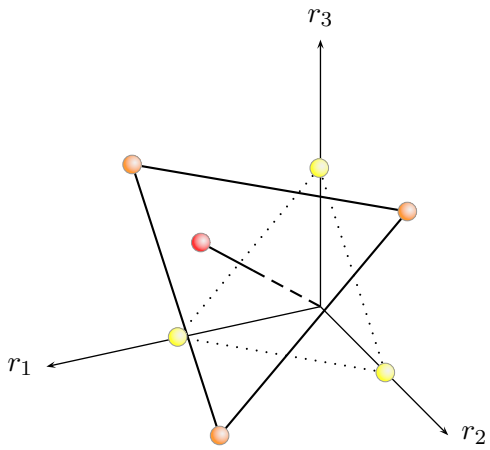

Figure 2.2. Positions of the saddles of single ionization (yellow), double ionization (orange) and triple ionization (red) for $F(t) = 0.2$ a.u. The lines connecting saddle points of the same kind are drawn to guide the eye.

saddles near the coordinate planes at $r_1 = r_2 = r_{s,1}^{DI} < r_s^{TI}$, $r_3 = r_{s,2}^{DI} \approx 0$ (plus cyclic permutations) and three index-1 saddles near the coordinate axes at $r_1 = r_{s,1}^{SI} < r_{s,1}^{DI}$, $r_2 = r_3 = r_{s,2}^{SI} \approx 0$ (plus cyclic permutations), as shown in Fig. 2.2. The fact that there are three equivalent saddles of each type is due to the indistinguishability of the electrons. To simplify the discussion, we will discuss the saddles as if there was only one of each type.

Following Wigner (1938), Sacha and Eckhardt (2001b), the above saddles can be associated with transition states for simultaneous triple ionization, simultaneous double ionization and single ionization, as indicated by the superscripts TI, DI and SI. For the saddle energies, we find

$$V(r_{s,1}^{SI}, r_{s,2}^{SI}, r_{s,2}^{SI}) < V(r_{s,1}^{DI}, r_{s,1}^{DI}, r_{s,2}^{DI}) < V(r_s^{TI}, r_s^{TI}, r_s^{TI}) \tag{2.14}$$

which means that classical single ionization sets in at a lower energy than double ionization which in turn sets in at a lower energy than triple ionization.

The triangular configuration is a special case of an escape configuration where N electrons are located on a regular N-gon around the field axis. As shown in Appendix B.3.2, this configuration can be used to obtain an N-dimensional version of the Eckhardt-Sacha model. However, the indistinguishability of electrons is lost for $N > 3$.

2.2.1. Spectrum and ionization energies

The previous section was concerned with classical and geometrical aspects of the Eckhardt-Sacha model. Now we focus on its quantum mechanical properties, starting with the energy level spectrum for vanishing field. The Hamiltonian (2.7) for $F(t) = 0$

reads

$$H = \sum_{i=1}^{3} \left(-\frac{1}{2}\frac{\partial^2}{\partial r_i^2} - \frac{3}{\sqrt{r_i^2+\varepsilon^2}} \right) + \sum_{\substack{i,j=1 \\ i<j}}^{3} \frac{1}{\sqrt{(r_i-r_j)^2 + r_i r_j + \varepsilon^2}}. \tag{2.15}$$

Ionization of an electron is equal to letting its coordinate tend to infinity. This way, one arrives at the Hamiltonians of the singly-charged ion

$$H_+ = \sum_{i=1}^{2} \left(-\frac{1}{2}\frac{\partial^2}{\partial r_i^2} - \frac{3}{\sqrt{r_i^2+\varepsilon^2}} \right) + \frac{1}{\sqrt{(r_1-r_2)^2 + r_1 r_2 + \varepsilon^2}} \tag{2.16}$$

and the doubly-charged ion

$$H_{2+} = -\frac{1}{2}\frac{\partial^2}{\partial r_1^2} - \frac{3}{\sqrt{r_1^2+\varepsilon^2}}. \tag{2.17}$$

The discrete bound-state energy levels of the Hamiltonians H, H_+ and H_{2+} depend on ε and will be denoted by E_i, E_i^+ and E_i^{2+}, respectively, with $i = 0, 1, \ldots, \infty$. An accurate calculation of the energy levels and the corresponding wave functions is possible with several methods, e.g. imaginary time evolution (Grobe and Eberly, 1993) or the spectral method (Feit *et al.*, 1982). A key ingredient of both methods is the use of operator splitting to solve the Schrödinger equation (see Appendix D).

In imaginary time evolution, the Schrödinger equation is transformed into a diffusion equation by introducing the imaginary time $\tau = \mathrm{i}t$. For $\tau \to \infty$, an arbitrary initial wave function $\psi(0)$ will relax into the ground state if it is renormalized to one in every time step. Higher-lying states can be obtained in the same way by subtracting the contributions of the previously calculated lower-lying states prior to renormalization. The wave function is assumed to be converged if the change of the energy $\langle\psi(\tau)|H|\psi(\tau)\rangle$ in one imaginary time step becomes smaller than some threshold value (here 10^{-12} a.u.). The structure of the algorithm implies that it takes a long time to obtain the excited states (at least in two and three dimensions). Therefore, we only use the method to calculate the ground state wave functions of the Hamiltonians (2.15) - (2.17) which will be needed in the following chapters.

The spectral method propagates an arbitrary initial wave function $\psi(0)$ in real time and computes the time-dependent correlation function $P(t) = \langle\psi(t)|\psi(0)\rangle$. The Fourier transform $\widehat{P}(E) = \int P(t)\exp(\mathrm{i}Et)\mathrm{d}t$ exhibits resonant peaks at the positions of the bound-state energy levels. The positions of the peaks can be determined with a line-shape fitting technique, thus dramatically improving the accuracy of the energy levels. Furthermore, the spectral method allows for a separation of the different symmetry types of the Hamiltonian, a feature which is particularly helpful when dealing with degenerate energy levels (see below). If the initial wave function is constructed without symmetries, all energy levels can be calculated simultaneously. Due to the above properties, we will use the spectral method to calculate the bound-state energy levels of the Hamiltonians.

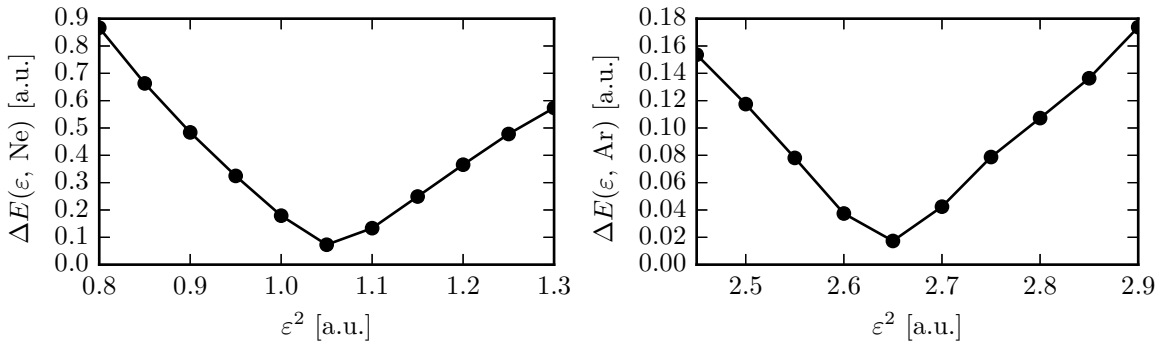

Figure 2.3. The function $\Delta E(\varepsilon, \mathrm{A})$ for neon (left) and argon (right).

	Ne	Model $\varepsilon^2 = 1.05$ a.u.	Ar	Model $\varepsilon^2 = 2.65$ a.u
E_0 [a.u.]	-4.63	-4.69	-3.09	-3.08
E_0^+ [a.u.]	-3.84	-3.83	-2.51	-2.52
E_0^{2+} [a.u.]	-2.33	-2.29	-1.50	-1.51

Table 2.1. Ground state energies of real atoms and ions (from Kramida *et al.* (2016)), compared to the ones of our model with a specific value of ε. The origin of the energy axis ($E = 0$) is equal to the ground state energy of the triply-charged ion.

By subtracting the ground state energies from each other, we obtain the three ionization energies of the model,

$$E_I = E_\infty - E_0 = E_0^+ - E_0, \tag{2.18a}$$
$$E_I^+ = E_\infty^+ - E_0^+ = E_0^{2+} - E_0^+, \tag{2.18b}$$
$$E_I^{2+} = E_\infty^{2+} - E_0^{2+} = -E_0^{2+}. \tag{2.18c}$$

Through the ground state energies, the ionization energies depend on ε. To find the value of ε for which the ionization energies are close to a given real atom, we study the Euclidian norm of the difference vector, i.e. the function

$$\Delta E(\varepsilon, \mathrm{A}) = \sqrt{(E_I(\varepsilon) - E_{I,A})^2 + (E_I^+(\varepsilon) - E_{I,A}^+)^2 + (E_I^{2+}(\varepsilon) - E_{I,A}^{2+})^2}. \tag{2.19}$$

Since all ground state energies decrease monotonically with decreasing ε, $\Delta E(\varepsilon, \mathrm{A})$ has a minimum for any atom A. Varying ε^2 in steps of 0.05 a.u., we find that $\varepsilon^2 = 1.05$ a.u. minimizes $\Delta E(\varepsilon, \mathrm{Ne})$ while $\varepsilon^2 = 2.65$ a.u. minimizes $\Delta E(\varepsilon, \mathrm{Ar})$, as shown in Fig. 2.3. The ground state energies obtained for these values of ε are compared to the ground state energies of the real atoms in Table 2.1.

The Hamiltonian (2.15) was deduced from the Hamiltonian of lithium, so one may wonder which value of ε is appropriate for this atom. To get a rough estimate, we consider the last ionization step $\mathrm{Li}^{2+} \to \mathrm{Li}^{3+} + \mathrm{e}^-$. Li^{2+} is a hydrogen-like ion, so its

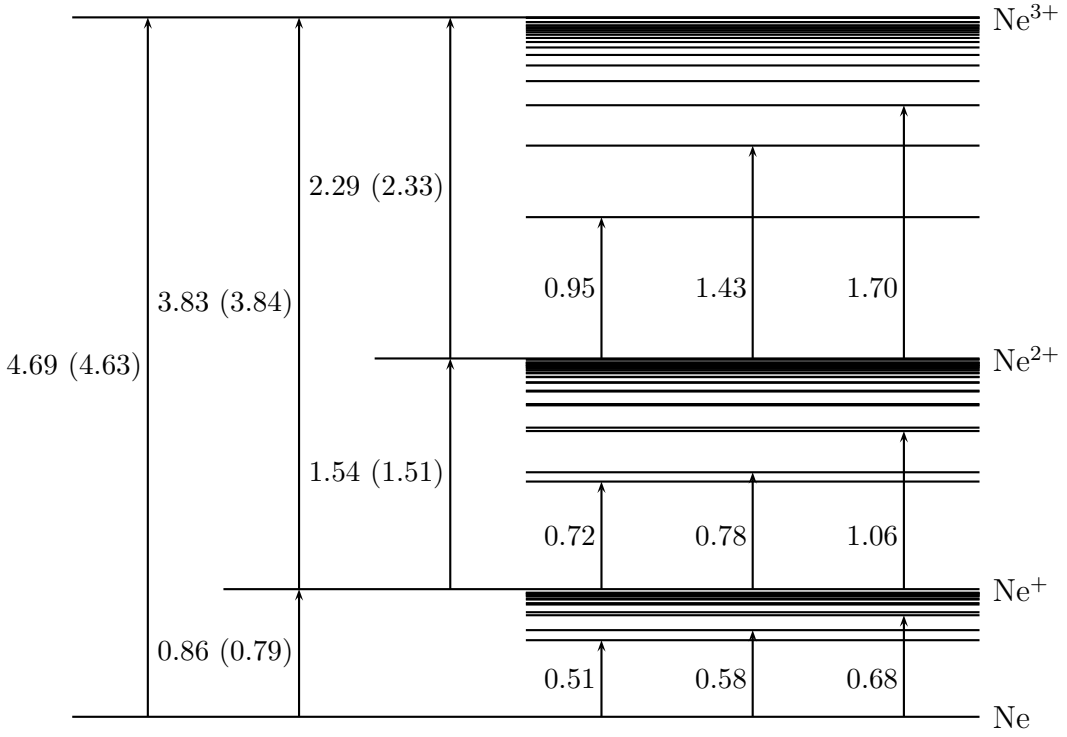

Figure 2.4. Bound-state energy levels (in a.u.) of the three-electron Eckhardt-Sacha model for $\varepsilon^2 = 1.05$ a.u. The values in parentheses are the ionization energies of the full-dimensional Ne atom. Due to the similarity, the ionization stages of the Eckhardt-Sacha model are referred to as Ne, Ne^+, Ne^{2+} and Ne^{3+}.

full-dimensional Schrödinger equation is solvable analytically which gives the ground state energy $E_0^{2+} = -4.5$ a.u. The Hamiltonian of our model Li^{2+} ion is (2.17). From the scaling law for one-dimensional soft-core Coulomb potentials (Hall *et al.*, 2009)

$$\sigma^2 E(Z, \varepsilon^2) = E(\sigma Z, \varepsilon^2/\sigma^2) \tag{2.20}$$

and the analytical result $E_0^{2+}(1, 2) = -0.5$ a.u. (Liu and Clark, 1992), it follows that

$$E_0^{2+}(Z, 2/Z^2) = Z^2 E_0^{2+}(1, 2) = -\frac{Z^2}{2} \text{ a.u.} \tag{2.21}$$

This means that the soft-core Coulomb potential $-Z/\sqrt{x^2 + \varepsilon^2}$ with $\varepsilon^2 = 2/Z^2$ has the ground state energy $-Z^2/2$ a.u. Therefore, $\varepsilon^2 = 2/9$ a.u. ≈ 0.22 a.u. should be a good starting point to minimize $\Delta E(\varepsilon, \mathrm{Li})$. This estimate is corroborated by the three-electron AEM which is structurally similar to the Eckhardt-Sacha model and whose ground state energy is equal to the one of full-dimensional lithium for $\varepsilon^2 = 0.25$ a.u. (Ruiz *et al.*, 2005).

For the further analysis of the model, we have to settle for a cut-off parameter. Clearly, the larger ε, the more shallow is the potential well and the less localized is

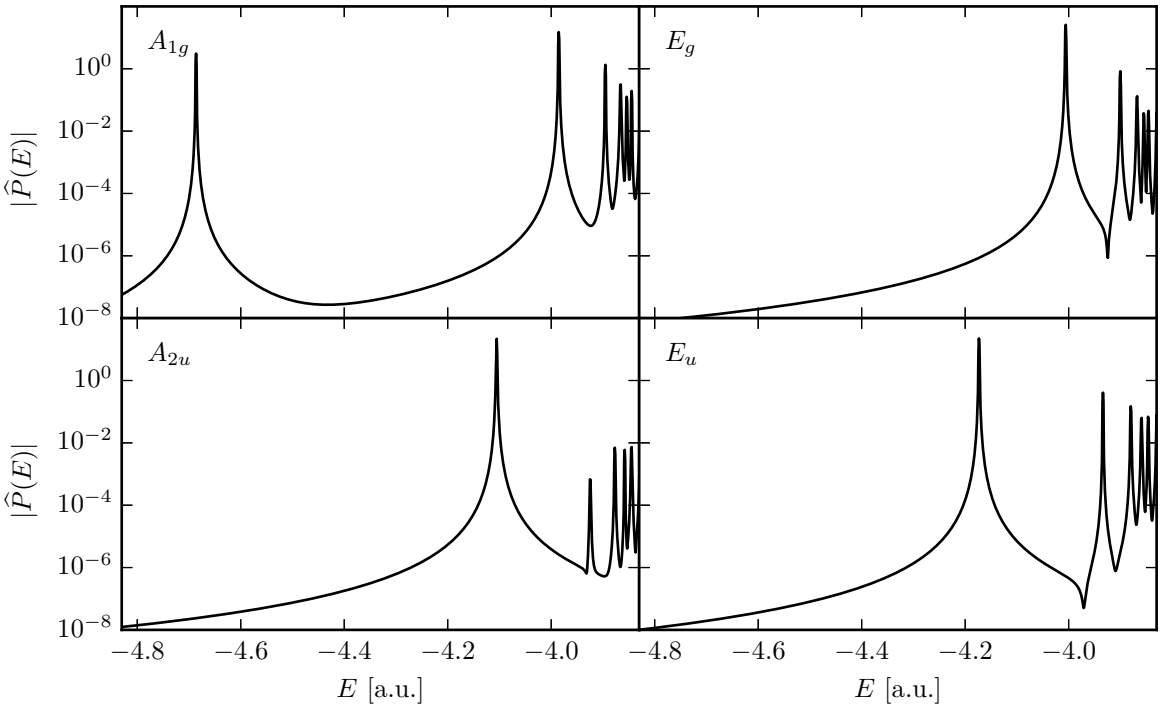

Figure 2.5. Fourier-transformed correlation functions $\widehat{P}(E) = \int \langle\psi(t)|\psi(0)\rangle \exp(\mathrm{i}Et)\mathrm{d}t$, calculated with the spectral method for the Hamiltonian (2.15) with $\varepsilon^2 = 1.05$ a.u. and initial wave functions $\psi(0)$ transforming like the indicated irreducible representation of the symmetry group D_{3d}. The resonant peaks correspond to the bound-state energy levels. The upper limit of the E-axis is equal to the ground state energy of the singly-charged ion ($E_0^+ = -3.83$ a.u.), i.e. the first ionization threshold.

the ground state wave function. However, a localization of the ground state is vital for our numerical calculations since the extension of the numerical grid must be as small as possible in order to reduce the computational effort. Therefore, we will set $\varepsilon^2 = 1.05$ a.u. in the following. Since the ground state energies of our model are close to the ones of neon in this case, we will refer to the ionization stages as Ne, Ne^+, Ne^{2+} and Ne^{3+}. We emphasize that this naming is only justified with respect to the ionization energies and should be understood as a mere notational convention.

The spectrum of our model for $\varepsilon^2 = 1.05$ a.u. is shown in Fig. 2.4. We discuss the different ionization stages separately. The symmetry group of the Ne Hamiltonian (2.15) is D_{3d} which has the six irreducible representations A_{1g}, A_{2g}, E_g, A_{1u}, A_{2u} and E_u (see Appendix C.3). Using an appropriate initial wave function $\psi(0)$, the bound-state energy levels of each symmetry type can be calculated separately with the spectral method (Fig. 2.5). For a position space grid with side length $L = N\Delta r$ a.u. (with $N = 512$ and $\Delta r = 0.2$ a.u.) and a propagation time of $T = N_t\Delta t$ (with $N_t = 2^{18}$ and $\Delta t = 0.025$ a.u.), i.e. an energy resolution of $\Delta E = \pi/T = 5 \cdot 10^{-4}$ a.u., sixteen bound states were found below the first ionization threshold $E_\infty = E_0^+ = -3.83$ a.u. As the energy is increased, we observe the recurring order A_{1g}, E_u, A_{2u}, E_g of symmetry types.

n	E_n [a.u.]	Symmetry	Degeneracy	n	E_n [a.u.]	Symmetry	Degeneracy
0	−4.6864	A_{1g}	1	8	−3.8954	A_{1g}	1
1	−4.1732	E_u	2	9	−3.8798	E_u	2
2	−4.1056	A_{2u}	1	10	−3.8770	A_{2u}	1
3	−4.0058	E_g	2	11	−3.8679	E_g	2
4	−3.9854	A_{1g}	1	12	−3.8661	A_{1g}	1
5	−3.9337	E_u	2	13	−3.8593	E_u	2
6	−3.9246	A_{2u}	1	14	−3.8580	A_{2u}	1
7	−3.9003	E_g	2	15	−3.8547	E_g	2

Table 2.2. Bound-state energy levels of the Hamiltonian (2.15) for $\varepsilon^2 = 1.05$ a.u., calculated with the spectral method. Note the recurring order of symmetry types (A_{1g}, E_u, A_{2u}, E_g).

Their energies are listed in Table 2.2. The ground state wave function ϕ_0 transforms like A_{1g}, meaning that it is even with respect to all elements of the symmetry group. The excited states which transform like E_g and E_u are doubly degenerate since these irreducible representations are two-dimensional. For A_{2g} and A_{1u}, we find that the smallest energy level lies above the first ionization threshold, i.e. in the one-electron continuum, so the energy levels are included neither in the figure nor in the table.

The Ne^+ Hamiltonian (2.16) has the symmetry group C_{2v}. Its four irreducible representations A_1, A_2, B_1 and B_2 are one-dimensional, so there are no degenerate energy levels. The recurring order of symmetry types for increasing energy is A_1, B_1, B_2 and A_2. This order was found before for a different nuclear charge and another value of ε^2 (Thiede, 2011). The Ne^{2+} Hamiltonian (2.17) has the symmetry group C_2, so states of even and odd parity alternate. The energy levels show a Rydberg-like behavior, a feature which was first observed by Singh *et al.* (1985).

2.2.2. Over-the-barrier field amplitudes

Consider the ground state wave function in the three-electron potential of (2.16) for $F(t) = 0$. If the field amplitude is increased to a constant nonzero value, the potential is deformed and saddle points emerge (see Section 2.2) close to which parts of the wave function can tunnel out. Neglecting the Stark shift of the ground state energy, one can ask for the onset of single-electron over-the-barrier ionization (OBI), i.e. the field amplitude F_{OBI}^{SI} for which an electron can escape classically over the single ionization saddle near the coordinate axis. We can estimate F_{OBI}^{SI} based on the natural assumption that only one electron coordinate (say r_1) gets large during single ionization and the other two remain small[5], i.e. $r_1 \gg r_2$ and $r_1 \gg r_3$. In this case, the Hamiltonian (2.7) separates into two independent Hamiltonians, i.e.

$$H = H_+(r_2, r_3) + H_1(r_1, F) \tag{2.22}$$

[5]This is the starting point for the single-active-electron approximation of the three-electron model which will be derived in Chapter 3.

where H_+ is the Hamiltonian (2.16) of the singly-charged ion and

$$H_1 = -\frac{1}{2}\frac{\partial^2}{\partial r_1^2} - \frac{1}{\sqrt{r_1^2+\varepsilon^2}} - \sqrt{\frac{2}{3}}Fr_1 \tag{2.23}$$

is the Hamiltonian describing the ionizing electron. Since H_+ does not depend on F, the electrons described by r_2 and r_3 remain in the ground state of the singly-charged ion ($E_0^+ = -3.83$ a.u.) during single ionization. The ionizing electron, on the other hand, sees a barrier with energy $V_s(F)$ through which it can tunnel. By equating $V_s(F)$ with the available energy $-E_I = E_0 - E_0^+ = -0.86$ a.u. and solving for F, we obtain the single-electron OBI field amplitude

$$F_{OBI}^{SI} = 0.25 \text{ a.u.} \tag{2.24}$$

In the same way, we can estimate the two-electron OBI field amplitude F_{OBI}^{DI} for which two electrons can escape over the double ionization saddle. For $r_1 \gg r_3$, $r_2 \gg r_3$, the Hamiltonian (2.7) decouples into the Hamiltonian of the doubly-charged ion (2.17) and a two-electron Hamiltonian $H_2(r_1, r_2, F)$ whose potential has a local maximum in the subspace $r_1 = r_2$. The energy available for double ionization is the sum of the first and second ionization energy, i.e. $E_I + E_I^+ = 2.40$ a.u. Equating this energy with the negative energy of the local maximum, we find

$$F_{OBI}^{DI} = 0.33 \text{ a.u.} \tag{2.25}$$

For three-electron OBI, the entire energy $E_I + E_I^+ + E_I^{2+} = -E_0 = 4.69$ a.u. is available. Equating this energy with the triple ionization saddle energy (2.13) yields the three-electron OBI field amplitude

$$F_{OBI}^{TI} = 0.41 \text{ a.u.} \tag{2.26}$$

Since $F_{OBI}^{TI} > F_{OBI}^{DI} > F_{OBI}^{SI}$, single-electron OBI becomes possible first as the field amplitude is increased from zero towards F_{OBI}^{TI}. If this increase is sufficiently slow, single-electron OBI will completely deplete the ground state population before two- and three-electron OBI become possible. Therefore, it is not very likely that the last two effects can be observed.

For the sake of completeness, we also give the OBI field amplitudes of the singly- and doubly-charged ion,

$$F_{OBI}^{SI,+} = 0.40 \text{ a.u.}, \tag{2.27a}$$

$$F_{OBI}^{DI,+} = 0.49 \text{ a.u.}, \tag{2.27b}$$

$$F_{OBI}^{SI,2+} = 0.58 \text{ a.u.} \tag{2.27c}$$

which are calculated with the same approximations as above. Note that $F_{OBI}^{SI,+}$ is smaller than F_{OBI}^{TI}.

For the estimate of the OBI field amplitudes, we assumed a constant laser field. However, the field of a real laser pulse is oscillating and nonzero only in a rather small time window. To perform simulations, we need to define the shape of the laser pulse and choose its parameters. This is the purpose of the next section.

2.3. Laser pulse shape

A strong short laser pulse[6] can be characterized by profile functions which describe how the electric and the magnetic field vary in time and space. Usually, it is assumed that the temporal and the spatial profile factorize. Since we use the electric dipole approximation, there is no magnetic field and the spatial profile of the electric field is equal to one, so it is sufficient to specify the time dependence of the electric field F. We use the one of Eckhardt *et al.* (2010) given by

$$F(t) = F_0(-1)^{n_c}\Theta(t)\Theta(T_p - t)\sin\left(\frac{\pi t}{T_p}\right)\left[\sin\left(\frac{\pi t}{T_p}\right)\cos(\omega_0 t + \varphi_0) + \frac{1}{n_c}\cos\left(\frac{\pi t}{T_p}\right)\sin(\omega_0 t + \varphi_0)\right] \tag{2.28}$$

where Θ is the Heaviside step function and F_0, ω_0, φ_0, n_c and $T_p = 2\pi n_c/\omega_0$ are the field amplitude, central frequency, carrier-envelope phase, number of field cycles and pulse duration, respectively. The vector potential of (2.28) is

$$A(t) = -\int_{-\infty}^{t} F(t')\mathrm{d}t' = \frac{F_0}{\omega_0}(-1)^{n_c+1}\Theta(t)\Theta(T_p - t)\sin^2\left(\frac{\pi t}{T_p}\right)\sin(\omega_0 t + \varphi_0). \tag{2.29}$$

The peak field amplitude is $F(T_p/2) = F_0\cos\varphi_0$. Its absolute value is smaller than F_0 if $\varphi_0 \notin \{0, \pi\}$. The rather complicated form of the pulse has the important property

$$A(\infty) = -\int_{-\infty}^{\infty} F(t')\mathrm{d}t' = 0, \tag{2.30}$$

meaning that the pulse area vanishes for every carrier-envelope phase φ_0. This guarantees a momentum distribution centered around the origin (Rottke *et al.*, 2006). In the single-cycle case ($n_c = 1$), equation (2.28) can be simplified to

$$F(t) = -F_0\Theta(t)\Theta\left(\frac{2\pi}{\omega_0} - t\right)\sin\left(\frac{\omega_0 t}{2}\right)\sin\left(\frac{3\omega_0 t}{2} + \varphi_0\right), \tag{2.31}$$

i.e. the single-cycle pulse has a sine envelope. For $n_c > 1$, we see from (2.28) that the envelope cannot be factorized from the carrier. However, due to the $1/n_c$-scaling of the second term, the envelope can be well approximated by a squared sine for large values of n_c (Fig. 2.6). In any case, the envelope has a strong influence on the frequency spectrum of the pulse, i.e. the Fourier transform $\widehat{F}(\omega)$. The spectral bandwidth of the pulse is approximately given by

$$\Delta\omega = \frac{\pi}{T_p} = \frac{\omega_0}{2n_c}. \tag{2.32}$$

[6] An introduction to the creation and characterization of short laser pulses, see the tutorial of Monmayrant *et al.* (2010).

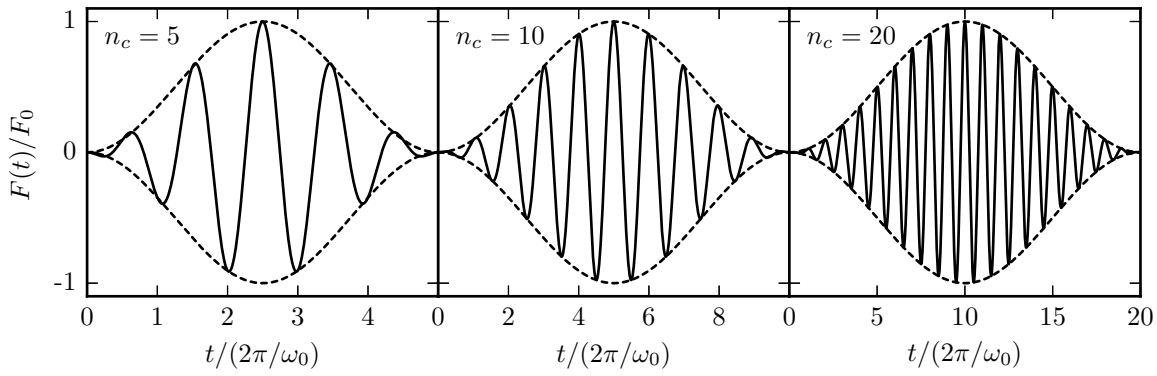

Figure 2.6. Electric field (2.28) of the laser pulse for different numbers of field cycles n_c (solid curves). The envelope approaches $\sin^2(\omega_0 t/2n_c)$ (dotted curves) as n_c is increased.

For the simulations, we need to specify the parameters F_0, ω_0, n_c and φ_0. On the frequency side, we study $\omega_0 = 0.06$ a.u. (near-infrared) and $\omega_0 = 0.1$ a.u. (blue). The first value corresponds to the central frequency of the popular Ti:sapphire laser which has a wavelength of around 800 nm. The second frequency is a computer-friendly one – since the pulse duration (along with the computation time) and the necessary size of the numerical grid scale as ω_0^{-1} and ω_0^{-2}, respectively, the numerical effort for $\omega_0 = 0.1$ a.u. is smaller compared to the Ti:sapphire frequency. Despite this numerical motivation, frequencies close to $\omega_0 = 0.1$ a.u. can be realized experimentally, e.g. by frequency doubling (Sheehy *et al.*, 1998; Ekanayake *et al.*, 2012; Henrichs *et al.*, 2013) or nonlinear mixing (Alnaser *et al.*, 2008) of a Ti:sapphire pulse.

The choice of field amplitudes F_0 is based on the ionization energies of the noble gas atoms. For sub-picosecond pulses with visible or near-infrared frequencies, multiple ionization of argon and neon is observed for intensities roughly between 10^{14} W/cm^2 ($F_0 = 0.05$ a.u.) and 10^{16} W/cm^2 ($F_0 = 0.53$ a.u.), as found in numerous experiments (Dietrich *et al.*, 1994; Larochelle *et al.*, 1998; Palaniyappan *et al.*, 2005; Ekanayake *et al.*, 2012). Since the ionization energies of our model were adjusted so as to mimic neon, the same interval of field amplitudes is appropriate. However, below $F_0 = 0.1$ a.u., the atomic potential is deformed only slightly by the field and the small amplitudes of the ionizing wave packets require a very accurate solution of the Schrödinger equation in order to obtain reliable yields and momentum distributions. Therefore, we only consider values of F_0 between 0.1 a.u. and 0.55 a.u., corresponding to intensities between $3.5 \cdot 10^{14}$ W/cm^2 and $1.1 \cdot 10^{16}$ W/cm^2 which correspond to the tunneling regime of single ionization (see Section 1.3.2). Note that the upper limit in F_0 is still well below the critical field amplitude $F_{crit} = 2^{3/2}/(3\varepsilon^2) = 0.9$ a.u. where the maximum (2.12) vanishes and the system is completely open.

Technically, a good measure of the pulse duration is the full width at half maximum (FWHM) of an envelope function which is fitted to the temporal intensity profile of the pulse (Monmayrant *et al.*, 2010). A Gaussian (Ekanayake *et al.*, 2012) or a squared hyperbolic secant (Fittinghoff *et al.*, 1992) are usually good choices for the

pulse envelope. However, if one wants to use these functions to construct an idealized pulse for a theoretical calculation, one faces the problem that they go to zero only at infinity and have to be cut off at some point in time which is difficult to choose uniformly for all field amplitudes. To avoid this problem, most theoretical pulses are constructed with trigonometric or trapezoidal (linear ramp on, flat top and linear ramp off) envelopes that have finite zeros and therefore a finite *total* pulse duration. The total pulse duration of (2.28) is $T_p = 2\pi n_c/\omega_0$. The FWHM pulse duration $T_{1/2}$ of (2.28), on the other hand, is bounded by $T_{1/2} = T_p/2$ (squared sine, n_c large) and $T_{1/2} = 2T_p/3$ (sine, $n_c = 1$). As illustrated by Fig. 2.6, $T_{1/2}$ will in general be closer to $T_p/2$. The corresponding FWHM pulse duration of the intensity $\propto |F(t)|^2$ is $T_{1/2,I} = 2T_p \arccos(1/2^{1/4})/\pi = 0.36T_p$. If we want our pulse to a have a prescribed FWHM intensity pulse duration $T^{exp}_{1/2,I}$, e.g. taken from an experimental publication, the number of field cycles has to be

$$n_c = 18.27 \cdot T^{exp}_{1/2,I}[\text{fs}] \cdot \omega_0[\text{a.u.}]. \tag{2.33}$$

Since $18.27 \cdot 0.057 \approx 1$, we have $n_c \approx T^{exp}_{1/2,I}[\text{fs}]$ for the Ti:sapphire laser.

To keep the computation times short, we will use $n_c \in \{2, 5, 7\}$ in this work. For $\omega_0 = 0.06$ a.u., $n_c = 5$ corresponds to $T^{exp}_{1/2,I} = 5$ fs which can be realized with modern laser systems (see e.g. Bergues *et al.* (2012); Camus *et al.* (2012); Kübel *et al.* (2014, 2016)). In all cases, the spectral bandwidth (2.32) is small compared to the energy level spacings of the lowest bound states in our model, so resonant transfer processes between these should be negligible (Chen *et al.*, 2010).

Unless a single-cycle pulse is used (Eckhardt *et al.*, 2010), the influence of φ_0 is expected to be small and therefore, we will always set $\varphi_0 = 0$ in the following. The terms peak field amplitude and field amplitude are equivalent in this case and will be used synonymously.

3. Ion yields

In this chapter, we calculate the ion yields of our model, i.e. the relative number of singly-, doubly- and triply-charged ions produced for fixed pulse parameters. First, we discuss the yields at the end of the pulse which are accessible in experiments. Afterwards, we study the rescattering properties of the laser pulse and the time-dependent yields to quantify the nonsequential ionization pathways.

3.1. Rate equations approach

Experimenters measure ion yields by focusing the laser into an ultrahigh vacuum chamber containing the target gas at a very low pressure, typically on the order of 10^{-10} - 10^{-9} Torr (10^{-8} - 10^{-7} Pa). The vacuum chamber is located inside a time-of-flight mass spectrometer which separates the ions according to their mass-to-charge ratios[1]. An ion yield obtained in this way represents an integral observable, in the sense that the ion signal of each charge state is summed over all times, positions and momenta. To a certain extent, this eliminates the influence of the orbital structure which is why the ion yield curves have a fairly uniform shape as a function of the field amplitude, regardless of whether the target is a noble gas (Walker *et al.*, 1994; Talebpour *et al.*, 1997a; Larochelle *et al.*, 1998) or consists of small molecules (Talebpour *et al.*, 1997b; Cornaggia and Hering, 1998). In particular, knee structures in the double and higher ionization yields are observed in almost each case.

Leaving aside the orbital structure and neglecting excited states, ionization of an atom A by a given laser pulse only depends on the ionization energies, i.e. the differences between the ground state energies of A^{i+} and $\mathrm{A}^{(i+1)+}$. Transitions between these energy levels can be described simply in terms of field- and energy-dependent rates (L'Huillier *et al.*, 1983b), leading to a system of coupled rate equations for the ion yields. For a three-electron atom and with the total particle number conserved, this system reads

$$\dot{P}_0 = -W_{01}P_0 - W_{02}P_0 - W_{03}P_0, \tag{3.1a}$$

$$\dot{P}_1 = \quad W_{01}P_0 - W_{12}P_1 - W_{13}P_1, \tag{3.1b}$$

$$\dot{P}_2 = \quad W_{02}P_0 + W_{12}P_1 - W_{23}P_2, \tag{3.1c}$$

$$\dot{P}_3 = \quad W_{03}P_0 + W_{13}P_1 + W_{23}P_2. \tag{3.1d}$$

[1] A good description of a typical experimental setup is given by Larochelle *et al.* (1998).

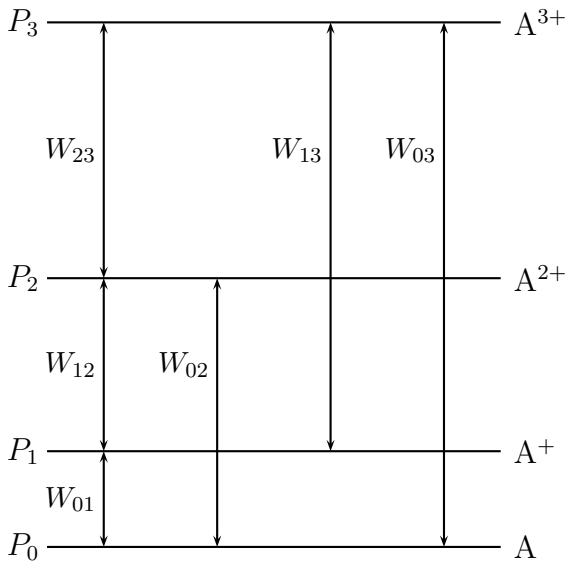

Figure 3.1. Illustration of population transfer between the different charge states i of a three-electron atom A. The relative population P_i of the A^{i+} ground state level (equal to the A^{i+} ion yield) changes during the pulse since population can be transferred to other levels at a time-dependent ionization rate W_{ij}.

Here, $P_0(t) \in [0,1]$ is the relative population of neutral atoms and $P_i(t) \in [0,1]$ for $i > 0$ is the A^{i+} ion yield (or the i-fold ionization yield), i.e. the relative population of the charge state i (see Fig. 3.1). $W_{ij}(t)$ is the instantaneous ionization rate from A^{i+} to A^{j+} ($i = 0,1,2; j = 1,2,3$ and $i < j$) which depends on the laser field $F(t)$ and the ionization energies. As first-order ordinary differential equations, the solutions of (3.1) can be expressed exactly in terms of integrals over the ionization rates. If we assume that there are only neutral atoms in the interaction volume before the laser pulse arrives, the initial conditions are $P_0(0) = 1$ and $P_1(0) = P_2(0) = P_3(0) = 0$. Defining the total ionization rate of each charge state,

$$W_0(t) := W_{01}(t) + W_{02}(t) + W_{03}(t), \tag{3.2a}$$
$$W_1(t) := W_{12}(t) + W_{13}(t), \tag{3.2b}$$
$$W_2(t) := W_{23}(t), \tag{3.2c}$$

and using variation of constants, we obtain

$$P_0(t) = \mathrm{e}^{-\int_0^t W_0(t')\mathrm{d}t'}, \tag{3.3a}$$
$$P_1(t) = \mathrm{e}^{-\int_0^t W_1(t')\mathrm{d}t'} \int_0^t W_{01}(t')P_0(t')\mathrm{e}^{\int_0^{t'} W_1(t'')\mathrm{d}t''}\mathrm{d}t', \tag{3.3b}$$
$$P_2(t) = \mathrm{e}^{-\int_0^t W_2(t')\mathrm{d}t'} \int_0^t [W_{02}(t')P_0(t') + W_{12}(t')P_1(t')]\,\mathrm{e}^{\int_0^{t'} W_2(t'')\mathrm{d}t''}\mathrm{d}t', \tag{3.3c}$$
$$P_3(t) = 1 - P_0(t) - P_1(t) - P_2(t). \tag{3.3d}$$

The total ion yield reads

$$P_{tot}(t) = P_1(t) + P_2(t) + P_3(t) = 1 - P_0(t) = 1 - \mathrm{e}^{-\int_0^t W_0(t')\mathrm{d}t'}. \tag{3.3e}$$

For a pulse with duration T_p, the final ion yields are given by $P_i(t = T_p)$ since all ionization rates vanish for $t \geq T_p$. Excluding recombination by assuming that all W_{ij} are either positive or zero[2], particle number conservation forces all population into the highest charge state if the pulse is long enough, i.e.

$$\lim_{T_p\to\infty} P_0(T_p) = \lim_{T_p\to\infty} P_1(T_p) = \lim_{T_p\to\infty} P_2(T_p) = 0, \tag{3.4a}$$

$$\lim_{T_p\to\infty} P_3(T_p) = 1. \tag{3.4b}$$

To quantify the depletion, one can ask for the pulse duration after which the initial population of neutral atoms ($P_0(0) = 1$) has decreased by a factor of 1/e. From (3.3a), we find that this pulse duration is implicitly given by

$$\int_0^{T_p} W_0(t)\mathrm{d}t = 1. \tag{3.5}$$

The corresponding total ion yield $P_{tot}(T_p) = 1 - 1/\mathrm{e}$ is said to be saturated in this case. In the tunneling regime, we expect the ionization rates to follow the time dependence of the field, i.e. $W_{ij}(t) = W_{ij}(F(t))$. Writing our laser pulse as $F(t) = F_0 f(t)$ with the field amplitude F_0 and a function $f(t) \in [-1, 1]$, equation (3.5) takes the form

$$\int_0^{T_p} W_0(F_0 f(t))\mathrm{d}t = 1. \tag{3.6}$$

For fixed F_0, this equation implies that saturation is solely determined by the pulse duration T_p and the function $f(t)$ containing the temporal pulse characteristics (frequency, envelope function, etc.). However, since $f(t)$ and T_p are fixed in most applications, the magnitude of the integral can only be influenced by F_0. Therefore, it is useful to define a saturation field amplitude as (Walsh *et al.*, 1993)

$$\int_0^{T_p} W_0(F_{sat}^{SI} f(t))\mathrm{d}t = 1. \tag{3.7a}$$

Since the total ion yield consists almost entirely of singly-charged ions at this point, we refer to F_{sat}^{SI} as the saturation field amplitude of single ionization. As F_0 is increased, the multiple ionization yields increase and the system will eventually undergo depletion of singly- and doubly-charged ions. Analogous to (3.7a), we define the saturation field amplitudes of double and triple ionization as

$$\int_0^{T_p} W_1(F_{sat}^{DI} f(t))\mathrm{d}t = 1 \tag{3.7b}$$

[2]In this case, the arrows in Fig. 3.1 only point upwards and the rate equations have a "one-way" structure.

and

$$\int_0^{T_p} W_2(F_{sat}^{TI} f(t))\mathrm{d}t = 1, \tag{3.7c}$$

respectively. By definition, the saturation field amplitudes depend on the pulse shape, the frequency and the pulse duration. For $F_0 > F_{sat}^{TI}$, virtually all atoms are triply-ionized at the end of the pulse, i.e. $P_0(T_p) = P_1(T_p) = P_2(T_p) \approx 0$ and $P_3(T_p) \approx 1$.

3.2. Ionization rates

To calculate the ion yields of our model from the general expressions (3.3), we need to specify the time-dependent ionization rates W_{ij}. We discuss the rates of single ionization ($i = j - 1$) and simultaneous multiple ionization ($i < j - 1$) separately and restrict ourselves to the tunneling regime.

The single ionization rates can be approximated by the formula of Ammosov, Delone and Krainov[3] (ADK). For an atom or ion in its ground state with charge $i = j - 1$ and ionization energy $E_{ij} = E_0^{j+} - E_0^{i+}$, the ADK tunnel ionization rate is given by (Ilkov *et al.*, 1992)

$$W_{ij}^{ADK}(F) = \left(\frac{3\mathrm{e}}{\pi}\right)^{\frac{3}{2}} \frac{j^2}{3n_{ij}^{*3}} \frac{1}{2n_{ij}^* - 1} \left(\frac{4\mathrm{e}j^3}{(2n_{ij}^* - 1)n_{ij}^{*3}|F|}\right)^{2n_{ij}^* - \frac{3}{2}} \exp\left(-\frac{2j^3}{3n_{ij}^{*3}|F|}\right) \tag{3.8}$$

where $F = F(t)$ is the laser field, $n_{ij}^* = j/\sqrt{2E_{ij}}$ an effective principal quantum number and $\mathrm{e} = \exp(1) = 2.71828\ldots$ Euler's number. It is easy to show that W_{ij}^{ADK} goes to zero for $F \to 0$, independent of n_{ij}^*. This is physically plausible since the width of the barrier in the atomic potential increases without bound as the field vanishes, making tunnel ionization eventually impossible. However, for very small values of F, the ADK formula underestimates the actual ionization rate since it does not incorporate multiphoton ionization. For large values of F, on the other hand, the Coulomb barrier is suppressed so strongly that an electron can escape over it (OBI) and the ADK rate overestimates the ionization rate (Scrinzi *et al.*, 1999; Tong and Lin, 2005). Overall, the best agreement of W_{ij}^{ADK} with the true single ionization rate is expected for $\omega_0 \ll E_{ij}$, $n_{ij}^* \gg 1$ and $\gamma_K \ll 1$ (Ammosov *et al.*, 1986).

By plugging the ADK single ionization rates into (3.3) and setting the simultaneous multiple ionization rates equal to zero, one obtains the time-dependent yields of single, sequential double and sequential triple ionization. If one plots the yields at the end of the pulse as a function of the field amplitude, one observes good agreement with experimentally measured ion yields in the sequential regime, even if $n_{ij}^* \gg 1$ and $\gamma_K \ll 1$ are not fulfilled (see e.g. Fittinghoff *et al.* (1992); Walker *et al.* (1994); Larochelle *et al.* (1998)). Therefore, an ADK fit has become a standard tool to identify the contributions of sequential multiple ionization in experimental ion yields.

[3]For an overview of other tunneling rate formulas, see the paper of Bauer and Mulser (1999).

Now we consider the simultaneous multiple ionization rates. Due to the prominent role of the electron repulsion, general analytical formulas for simultaneous n-fold ionization do not exist. Such formulas can only be derived by assuming a certain ionization mechanism. For example, if one assumes that the n electrons tunnel simultaneously from the ground state (collective n-electron tunnel ionization), one can derive an n-electron version of the ADK formula (Zon, 1999). For $n = 2$, the yields obtained with this rate strongly underestimate the experimental double ionization yields in the nonsequential regime (Eichmann *et al.*, 2000), indicating that collective tunneling is insignificant for simultaneous double ionization. Today, most experimental results support the conclusion that electron rescattering (see Section 1.4.1) is the main mechanism of simultaneous multiple ionization. However, a simple formula for the simultaneous rates based on the rescattering mechanism is, to the best of our knowledge, not available.

Several experiments (Walker *et al.*, 1994; Augst *et al.*, 1995; Talebpour *et al.*, 1997b; Guo *et al.*, 1998; Larochelle *et al.*, 1998; Sheehy *et al.*, 1998) observed a very weak F_0-dependence of the double to single ionization yield ratio close to saturation of single ionization. This property can be interpreted as resulting from a competition between single ionization and simultaneous double ionization which is caused by the depletion of neutral atoms that are required for both processes (Walker *et al.*, 1994). Most importantly, the competition effect implies that the simultaneous double ionization rate is approximately proportional to the single ionization rate near saturation, regardless of the ionization mechanisms. Generalizing this assumption to the other simultaneous rates and approximating the single ionization rates with the ADK formula, we obtain (Augst *et al.*, 1995)

$$W_{02} = \alpha_{02} W_{01}^{ADK}, \tag{3.9a}$$

$$W_{03} = \alpha_{03} W_{01}^{ADK}, \tag{3.9b}$$

$$W_{13} = \alpha_{13} W_{12}^{ADK}. \tag{3.9c}$$

The problem of this approximation is that the constants α_{ij} can only be determined a posteriori, either empirically or from the measured ion yield ratios. As a result, the dependence of the α_{ij} on the temporal laser parameters (frequency, pulse shape, pulse duration) is unknown.

In contrast to experimentally measured ion yields, numerically calculated ones are almost never fitted with ADK theory. One reason for this is that the derivation of the rate formula (3.8) starts from a singular three-dimensional Coulomb potential while most theoretical calculations use one-dimensional soft-core potentials. A modification of the ADK rate for soft-core potentials is presently not available, so we can only try to manually incorporate the effects of the regularization into the standard version (3.8) of the formula. As shown in Fig. 3.2, the soft-core potential has a wider barrier than the bare Coulomb potential, meaning that the ionization rate for a given energy E_{ij} is smaller. This issue can be accounted for by slightly increasing the effective quantum number n_{ij}^*, i.e. by decreasing the ionization energy E_{ij}. For the yields of the

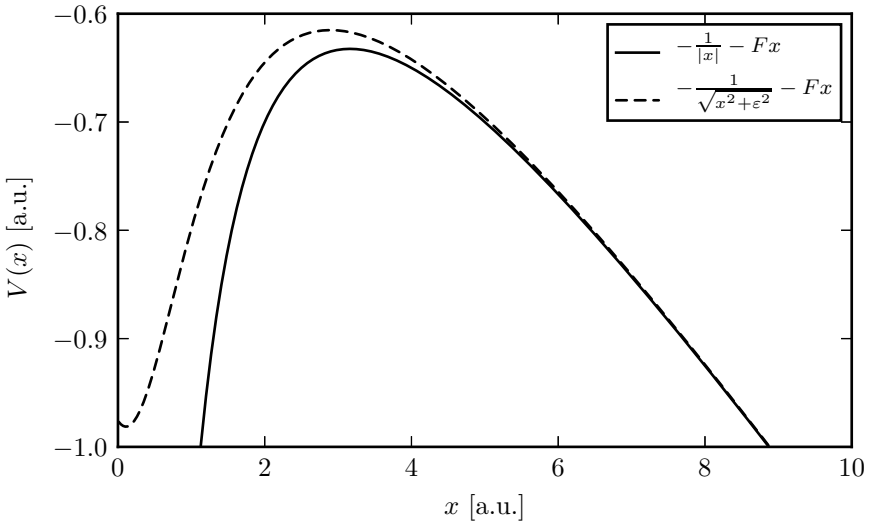

Figure 3.2. Comparison of the barriers for a bare Coulomb potential (solid curve) and a soft-core Coulomb potential (dashed curve) with $F = 0.1$ a.u. and $\varepsilon^2 = 1.05$ a.u.

two-electron Eckhardt-Sacha model (Thiede, 2011), we demonstrated that an ADK fit with modified effective quantum numbers is surprisingly accurate. Nevertheless, the adjustment of the ionization energies introduces even more empirical quantities into the rate equations.

In summary, calculating the ion yields of our model from an ADK-based solution of the rate equations (3.1) is not suitable since there are no expressions for the simultaneous multiple ionization rates and the influence of the cut-off parameter ε cannot be assessed. Therefore, we determine the yields by means of a quantum mechanical simulation.

3.3. Quantum approach

In this section, we describe how the ion yields can be calculated from the quantum mechanical wave function of the model. To simplify the expressions in the following, we define $\boldsymbol{r} := (r_1, r_2, r_3)$, $\nabla := (\partial/\partial r_1, \partial/\partial r_2, \partial/\partial r_3)$ and $\mathrm{d}^3 r := \mathrm{d}r_1 \mathrm{d}r_2 \mathrm{d}r_3$. Apart from compactness, this notation has the advantage that it applies to an arbitrary three-dimensional system and there is no need to specify the coordinates explicitly.

We start from the time-dependent Schrödinger equation

$$\mathrm{i}\frac{\partial}{\partial t}\psi(\boldsymbol{r}, t) = H\psi(\boldsymbol{r}, t) \tag{3.10}$$

for the wave function $\psi(\boldsymbol{r}, t)$. Multiplying (3.10) with ψ^* from the left and taking the imaginary part of both sides, we obtain the continuity equation (Schwabl, 2007)

$$\frac{\partial}{\partial t}\rho(\boldsymbol{r}, t) + \nabla \cdot \boldsymbol{j}(\boldsymbol{r}, t) = 0 \tag{3.11}$$

with the probability density

$$\rho(\boldsymbol{r},t) = |\psi(\boldsymbol{r},t)|^2 \tag{3.12}$$

and the probability current[4]

$$\boldsymbol{j}(\boldsymbol{r},t) = \mathrm{Im}(\psi^*(\boldsymbol{r},t)\nabla\psi(\boldsymbol{r},t)) = \frac{1}{2\mathrm{i}}\left[\psi^*(\boldsymbol{r},t)\nabla\psi(\boldsymbol{r},t) - \psi(\boldsymbol{r},t)\nabla\psi^*(\boldsymbol{r},t)\right]. \tag{3.13}$$

The continuity equation expresses the conservation of probability in the quantum system described by H. Integrating the equation over some volume $R \subset \mathbb{R}^3$ with a piecewise smooth boundary ∂R, e.g. a cube or a sphere, and using Gauss's theorem yields

$$\frac{\partial}{\partial t}\underbrace{\iiint_R |\psi(\boldsymbol{r},t)|^2 \mathrm{d}^3r}_{=:P_R(t)} = -\iiint_R \nabla\cdot\boldsymbol{j}(\boldsymbol{r},t)\mathrm{d}^3r = -\underbrace{\iint_{\partial R}\boldsymbol{j}(\boldsymbol{r},t)\cdot\mathrm{d}\boldsymbol{A}}_{=:f_R(t)} \tag{3.14}$$

where $P_R(t)$ is the probability contained in R and $f_R(t)$ is the probability flux through ∂R. Finally, time integration of (3.14) gives

$$P_R(t) = P_R(0) - \int_0^t f_R(t')\mathrm{d}t'. \tag{3.15}$$

If we divide the three-dimensional position space $\mathbb{R}^3$ into several volumes, the above equation holds for each of them. Furthermore, the probability flux separates into parts $f_{RS}(t)$ where $\partial(RS)$ is the boundary between R and the adjacent volume S. Note that even if some of these volumes are not compact, equation (3.15) remains valid since a normalizable wave function vanishes sufficiently rapidly for $|\boldsymbol{r}| \to \infty$ (Schwabl, 2007) and the integrals converge.

As usual in quantum mechanics (Becker *et al.*, 2012), we define ionization in terms of a spatial criterion, i.e. we consider an electron as ionized if its distance from the nucleus exceeds a prescribed positive value r_c. In the Eckhardt-Sacha model, each electron is described by a single coordinate, so ionization of electron i is equivalent to $|r_i| \geq r_c$. This inequality separates the coordinate space into cuboids. The probability P contained in a cuboid (equation (3.15)) can be identified with an ion yield where the charge state depends on the number of electron coordinates for which the inequality holds. Since the electrons are indistinguishable, some cuboids which are topologically disconnected describe the same charge state. To simplify the discussion, we combine these cuboids to sets that we shall call regions in the following.

$$\text{Region } 0 := \left\{(r_1,r_2,r_3)\in\mathbb{R}^3 \middle| |r_1|<r_c, |r_2|<r_c, |r_3|<r_c\right\} \tag{3.16a}$$

[4]This form of $\boldsymbol{j}$ only applies to the Hamiltonian (2.7) where the field interaction is expressed in length gauge. In velocity gauge, $F(t)r_i$ is replaced by $A(t)p_i$ and the probability current reads $\boldsymbol{j}(\boldsymbol{r},t) = \mathrm{Im}(\psi^*(\boldsymbol{r},t)\nabla\psi(\boldsymbol{r},t)) - \sqrt{2/3}|\psi(\boldsymbol{r},t)|^2 A(t)(1,1,1)$.

corresponds to the neutral atom (three electrons close to the nucleus),

$$\begin{aligned}\text{Region 1} := &\left\{(r_1,r_2,r_3)\in\mathbb{R}^3\middle||r_1|\geq r_c,|r_2|<r_c,|r_3|<r_c\right\}\\ &\cup\left\{(r_1,r_2,r_3)\in\mathbb{R}^3\middle||r_1|<r_c,|r_2|\geq r_c,|r_3|<r_c\right\}\\ &\cup\left\{(r_1,r_2,r_3)\in\mathbb{R}^3\middle||r_1|<r_c,|r_2|<r_c,|r_3|\geq r_c\right\}\end{aligned} \tag{3.16b}$$

to the singly-ionized atom (one electron ionized, two close to the nucleus),

$$\begin{aligned}\text{Region 2} := &\left\{(r_1,r_2,r_3)\in\mathbb{R}^3\middle||r_1|\geq r_c,|r_2|\geq r_c,|r_3|<r_c\right\}\\ &\cup\left\{(r_1,r_2,r_3)\in\mathbb{R}^3\middle||r_1|\geq r_c,|r_2|<r_c,|r_3|\geq r_c\right\}\\ &\cup\left\{(r_1,r_2,r_3)\in\mathbb{R}^3\middle||r_1|<r_c,|r_2|\geq r_c,|r_3|\geq r_c\right\}\end{aligned} \tag{3.16c}$$

to the doubly-ionized atom (two electrons ionized, one close to the nucleus) and

$$\text{Region 3} := \left\{(r_1,r_2,r_3)\in\mathbb{R}^3\middle||r_1|\geq r_c,|r_2|\geq r_c,|r_3|\geq r_c\right\}. \tag{3.16d}$$

to the triply-ionized atom (three electrons ionized). Since the regions have common boundaries, all physically possible ionization pathways can be realized. For the regions defined above, (3.14) gives four differential equations for the ion yields $P_i(t)$,

$$\dot{P}_0(t) = -f_{01}(t) - f_{02}(t) - f_{03}(t), \tag{3.17a}$$
$$\dot{P}_1(t) = f_{01}(t) - f_{12}(t) - f_{13}(t), \tag{3.17b}$$
$$\dot{P}_2(t) = f_{02}(t) + f_{12}(t) - f_{23}(t), \tag{3.17c}$$
$$\dot{P}_3(t) = f_{03}(t) + f_{13}(t) + f_{23}(t). \tag{3.17d}$$

To solve them with the initial conditions $P_0(0) = 1$ and $P_0(0) = P_1(0) = P_2(0) = 0$, the entire wave function has to be initially located inside region 0, i.e. r_c must be chosen large enough so that

$$P_0(0) = \int_{-r_c}^{r_c}\int_{-r_c}^{r_c}\int_{-r_c}^{r_c} |\psi(r_1,r_2,r_3,0)|^2 \mathrm{d}r_1\mathrm{d}r_2\mathrm{d}r_3 \approx 1. \tag{3.18}$$

Finally, we note that the above equations formally agree with the rate equations (3.1) if we define

$$f_{ij}(t) := W_{ij}(t)P_i(t). \tag{3.19}$$

In contrast to ADK theory, these rates $W_{ij}(t)$ can also be negative, so recombination of electrons is included. We will see in Section 3.6.4 that this allows us to observe the rescattering of an electron directly in the time-dependent yields.

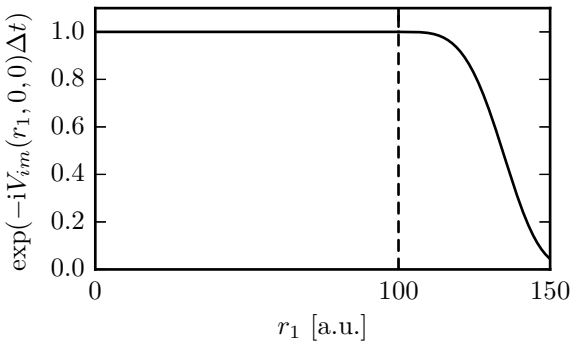

Figure 3.3. Exponential tail created by the imaginary potential (3.20) in one direction during one time step $\Delta t = 0.05$ a.u. with $r_{abs} = 100$ a.u. (dashed line) and $\eta = 10^{-5}$ a.u.

3.3.1. Numerical method

To calculate the probability fluxes, we must determine the three-electron wave function $\psi(r_1, r_2, r_3, t)$ by solving the three-dimensional time-dependent Schrödinger equation of the Hamiltonian (2.7). A grid-based approach is straightforward and sufficiently accurate for our purposes. In position space, the wave function $\psi(r_1, r_2, r_3, t)$ is represented on a cube-shaped grid of side length L with N grid points per dimension. Along the r_i-axis, the distance between two neighboring grid points j and $j+1$ (the position grid spacing) is $\Delta r = L/N$. The corresponding positions are $r_i^{(j)} = -L/2 + j\Delta r$ with $j = 0, \ldots, N-1$ (note that $r_i = L/2$ is not included). Starting from the normalized ground state for $F = 0$ which was found in Section 2.2.1 with imaginary time evolution, the wave function is evolved in discrete time steps Δt with the split-operator method. Since this technique is based on a Fourier representation of the wave function (see Appendix D.1 for details), the values of ψ at $r_i^{(0)} = -L/2$ and $r_i^{(N)} = L/2$ are equal so that leaving out the end point of the grid is justified. For a laser pulse with n_c field cycles, the time evolution is stopped after $n_c + 1$ field cycles, so ionizing wave packets still on their way towards region boundaries have a chance to cross them and contribute to the integrals of the probability fluxes.

From a physical perspective, using a finite grid length L is equal to embedding the system in a three-dimensional infinite square well potential. As a consequence, the parts of the electron wave function that reach the grid boundaries are reflected, hampering the free spreading of the wave function during ionization. This problem is reduced by adding a quartic imaginary potential

$$V_{im}(r_1, r_2, r_3) = -\mathrm{i}\eta \sum_{j=1}^{3} \Theta(|r_j| - r_{abs})(|r_j| - r_{abs})^4 \tag{3.20}$$

of strength η to the Hamiltonian (2.7). It acts as an absorbing boundary placed at a distance $0 \ll r_{abs} < L/2$ from the grid center. As part of the time evolution operator, (3.20) applies an exponential tail to the parts of the wave function which exceed r_{abs}

(see Fig. 3.3). We set $r_{abs} = L/2 - 50$ a.u. and $\eta = 10^{-5}$ a.u. as in the previous double ionization calculations of Prauzner-Bechcicki *et al.* (2008).

To obtain an ion yield $P_i(t)$ in our system, equation (3.15) suggests two possibilities[5]. The easiest way is to calculate $P_i(t)$ *directly*, i.e. to integrate the probability density over region i in every time step. However, the absorbing boundary will diminish the population in the outer regions and contributions coming from different regions cannot be separated so that one has access to the total yield of each ion only. Alternatively, we can solve the equations (3.17) by integrating the probability fluxes $f_{ij}(t)$ in time. This method was pioneered by the Taylor group (see e.g. Dundas *et al.* (1999); Parker *et al.* (2003)) and will be used in the following. Since regions 1 - 3 border the absorbing boundary, we have to add fluxes $-f_{i,\mathrm{abs}}(t)$ to the right-hand sides of (3.17b-d). The integrated flux from region i ($i = 1, 2, 3$) through the absorbing boundary is

$$P_{i,abs}(t) = \int_0^t f_{i,abs}(t')\mathrm{d}t'. \tag{3.21}$$

$\sum_{i=1}^{3} P_{i,abs}(t)$ equals the overall loss of probability on the grid, giving an alternative measure for the total ion yield. If r_{abs} is large enough and η is chosen so as to eliminate most of the reflected wave packets, the flux integration will not be perturbed by the absorbing boundary. Therefore, we leave the equations (3.17) unchanged and calculate $P_{i,abs}$ for monitoring purposes only. However, the assumption of an unperturbed flux integration loses its validity when a significant part of the wave function reaches beyond the absorbing boundary during the pulse (see Fig. 3.4). In this case, the integration of the fluxes across the outer region boundaries is cut off, so the corresponding yields saturate as a function of F_0 and do not continue to increase[6]. We will refer to this issue as physical convergence in the following. Its experimental counterpart is the size of the focal spot (determining the laser-gas interaction volume) relative to the detection plate of the time-of-flight spectrometer. If the laser has a Gaussian intensity profile in space and the focal spot is smaller than the detection plate, the yields increase as F_0^3 above saturation (Cervenan and Isenor, 1975). For a focal spot size which is greater than the detector, a reduction is observed (Walker *et al.*, 1994) which eventually leads to the yield becoming constant above saturation (Larochelle *et al.*, 1998).

In the flux integration method, each yield decomposes into three contributions which are calculated separately,

$$P_1(t) = \int f_{01}(t')\mathrm{d}t' - \int f_{12}(t')\mathrm{d}t' - \int f_{13}(t')\mathrm{d}t' =: P_{01}(t) - P_{12}(t) - P_{13}(t), \tag{3.22a}$$

$$P_2(t) = \int f_{02}(t')\mathrm{d}t' + \int f_{12}(t')\mathrm{d}t' - \int f_{23}(t')\mathrm{d}t' =: P_{02}(t) + P_{12}(t) - P_{23}(t), \tag{3.22b}$$

$$P_3(t) = \int f_{03}(t')\mathrm{d}t' + \int f_{13}(t')\mathrm{d}t' + \int f_{23}(t')\mathrm{d}t' =: P_{03}(t) + P_{13}(t) + P_{23}(t). \tag{3.22c}$$

[5]A comparison of the two approaches in two dimensions is given by Prauzner-Bechcicki *et al.* (2008).
[6]This numerical saturation effect is to be distinguished from the physical one discussed in Section 3.1.

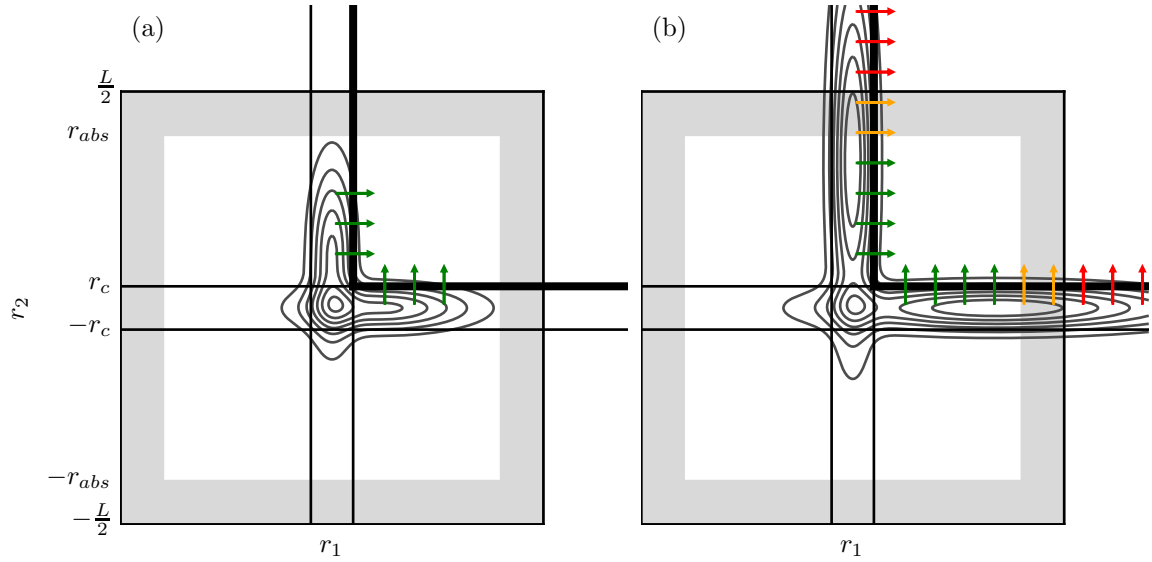

Figure 3.4. Illustration of physical convergence in two dimensions. Numerically, the wave function ψ is limited to a grid of side length L and is exponentially damped beyond the absorbing boundary (gray shaded area). (a) Most of $|\psi|^2$ is located near the grid center, so all significant contributions to the probability flux across the thick black boundary (green arrows) are captured and the corresponding yield is converged with respect to the grid length. (b) A non-negligible part of $|\psi|^2$ reaches beyond the absorbing boundary. Some significant contributions are either damped (yellow arrows) or completely lost (red arrows), i.e. the corresponding yield is not converged. Case (a) is typical for small field amplitudes and short pulses while case (b) is typical for large field amplitudes and long pulses.

The contributions P_{01}, P_{12} and P_{23} contain single ionization from the ground (or an excited) state of the neutral, singly-ionized and doubly-ionized atom, respectively. P_{02} (P_{03}), on the other hand, contains simultaneous double (triple) ionization from the neutral atom while P_{13} contains simultaneous double ionization from the singly-charged ion. At first glance, one could use the yield contributions P_{i3} to quantify the pathways of triple ionization as a function of the field amplitude (which is one of the goals of this work). However, the results would be ambiguous since the choice of the region boundaries determines which contribution is attributed to which pathway, as has been demonstrated for double ionization in two dimensions (Thiede, 2011). In the context of the two-active-electron approximation, this issue will be explained in detail in Section 3.4.3. Furthermore, we will show in Section 3.3.3 that P_2 and P_3 are not very sensitive to the choice of the region boundaries. For the sake of brevity, we will refer to P_{02}, P_{03} and P_{13} as the simultaneous ionization yields.

For the implementation of the flux integration method, we have to refine the division of the position space. If the division (3.16) is used, the boundaries between some regions are lines (0↔2, 1↔3) or single points (0↔3) instead of planes (0↔1, 1↔2, 2↔3). As a result, only a few grid points will contribute to the flux integrals of the simultaneous ionization yields and they can be expected to be small and insignificant. Therefore, we

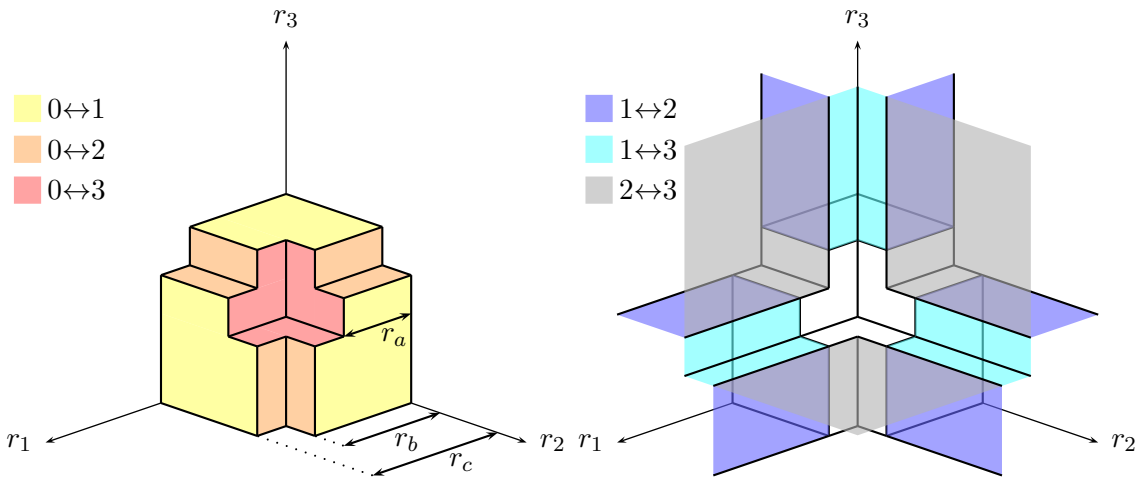

Figure 3.5. Division of the position space for the calculation of the ion yields (only first octant shown). Region 0 (neutral atom) is the volume bounded by the yellow, orange and red planes. Region 1 (singly-ionized atom) is the union of the six volumes bounded by the yellow, cyan and blue planes. Region 2 (doubly-ionized atom) is the union of the twelve volumes bounded by the orange, blue and gray planes. Region 3 (triply-ionized atom) is the union of the eight volumes bounded by the red, cyan and gray planes. The missing boundary planes of regions 1-3 are given by the absorbing boundary (not shown).

cut out the edges of the cuboids defined by r_c to get planes at every boundary, thus enhancing the simultaneous ionization yields. Introducing two additional distances r_a and r_b that fulfill $0 < r_a < r_b < r_c$, the new regions are defined according to Fig. 3.5. For r_b and r_c, we choose the values previously used in the two-electron calculations of Prauzner-Bechcicki *et al.* (2008),

$$r_b = 7 \text{ a.u.}, \tag{3.23a}$$
$$r_c = 12.5 \text{ a.u.}, \tag{3.23b}$$

based on the observation that the two-electron Eckhardt-Sacha potential and the restriction of the three-electron potential $V(r_1, r_2, r_3)$ to a coordinate plane are equivalent in form, apart from a constant and the geometrical factor of the field (see Section 2.2). The third distance r_a has to be somewhat smaller than r_b. Its choice is based on the position of the triple ionization saddle (2.12). $r_s^{TI}(F(t))$ is smallest when the field is close to its peak ($F(t) \approx F_0$). Most triple ionization events happen around these times since the strongly suppressed Coulomb barrier makes tunnel ionization or OBI likely. The saddle can be considered as the transition state of simultaneous triple ionization (see the discussion in Section 2.2), so we want the minimum of r_s^{TI} during the pulse to be smaller than r_a. For $\varepsilon^2 = 1.05$ a.u. and $0.1 \text{ a.u.} \leq F_0 \leq 0.55$ a.u., we have $1.65 \text{ a.u.} \leq r_s^{TI}(F_0) \leq 4.79$ a.u. Therefore, we set

$$r_a = 5 \text{ a.u.} \tag{3.23c}$$

With $\varepsilon^2 = 1.05$ a.u. and the chosen values for r_a, r_b and r_c, we have, to an excellent approximation, $P_0(0) = 1$ and $P_1(0) = P_2(0) = P_3(0) = 0$. To physically justify the division of the position space shown in Fig. 3.5, we have to show that (a) the overall size of region 0 (determined by r_c) is arbitrary provided $P_0(0) = 1$ and (b) cutting off the edges of the cuboids only alters the yields in a predictable way. Both will be done in Section 3.3.3.

3.3.2. Numerical parameters

When choosing the numerical parameters L, N, Δr and Δt for our simulations, we can build on the well-documented double ionization case. As usual, one has to make a compromise between speed and accuracy. On the one hand, we want to keep N as small as possible to minimize memory requirements and the number of floating point operations. On the other hand, for mathematically converged results, we want Δt and Δr to be as small as possible and, for physical convergence, L to be as large as possible. Based on what was found for double ionization (Prauzner-Bechcicki *et al.*, 2007, 2008), we expect that the ion yields will extend over several orders of magnitude as a function of F_0. Therefore, the accuracy of the yields for fixed F_0 does not have to be excessively high, provided the qualitative behavior of the curves is captured.

First, we discuss the position grid spacing Δr. As noted by Lappas and van Leeuwen (1998), it is a big advantage of the split-operator method that Δr can be comparatively large since the calculation of second spatial derivatives is circumvented by the Fourier transform to momentum space. In the AEM simulations performed with this method, $\Delta r = 0.4$ a.u. was found to give reliable results (Bauer, 1997; Panfili and Liu, 2003; Véniard *et al.*, 2003). Even in the full-dimensional helium calculations of the Taylor group, a radial grid spacing between 0.3 a.u. and 0.4 a.u. was found to be sufficient (Dundas *et al.*, 1999; Parker *et al.*, 2003). Finally, for the Crank-Nicolson scheme employed in simulations of the Ruiz model, a value of Δr between 0.3 a.u. (Ruiz *et al.*, 2006) and 0.5 a.u. (Baier *et al.*, 2006) was used. In both the Eckhardt-Sacha model and the AEM, each dimension corresponds to one electron, so the grid spacing can be straightforwardly generalized to three dimensions. In the previous two-electron calculations with the Eckhardt-Sacha model (Prauzner-Bechcicki *et al.*, 2007, 2008), $\Delta r = 0.2$ a.u. was used. Here, we trade the smaller grid spacing for a larger grid size L and use $\Delta r = 0.39$ a.u.

The time step Δt has to be small enough to allow for the application of the split-operator method, i.e. the approximation of the time-evolution operator by a product of short-time propagators. In particular, the time-dependent part of potential (2.8), i.e. the laser field $F(t)$, must be approximately constant in the interval $[t_i, t_i + \Delta t]$. Since $F(t_i + \Delta t) = F(t_i) + \dot{F}(t_i)\Delta t + \ldots$, this is equivalent to $F(t_i) \gg \dot{F}(t_i)\Delta t$ which certainly holds if Δt is small compared to the oscillation period $T = 2\pi/\omega_0$ of the pulse carrier. We have $T = 63$ a.u. for $\omega_0 = 0.1$ a.u. and $T = 105$ a.u. for $\omega_0 = 0.06$ a.u., so the choice $\Delta t = 0.05$ a.u., tried and tested in many simulations (see e.g. Ruiz *et al.* (2006); Prauzner-Bechcicki *et al.* (2008)), fulfills the requirement $\Delta t \ll T$.

Parameter	Symbol	Value
Position grid length	L	600 a.u.
Position grid spacing	Δr	100/256 a.u.
Time step	Δt	0.05 a.u.
Number of time steps	N_t	$\left\lceil \frac{2\pi(n_c+1)}{\omega_0 \Delta t} \right\rceil$
Space partitioning parameters	r_a	5 a.u.
	r_b	7 a.u.
	r_c	12.5 a.u.
Position of absorbing boundary	r_{abs}	$L/2 - 50$ a.u.
Strength of absorbing potential	η	10^{-5} a.u.

Table 3.1. Numerical parameters used for the calculation of the ion yields in this work. $\lceil x \rceil = \min\{n \in \mathbb{Z} \mid n \geq x\}$ is the ceiling function.

Due to the use of an absorbing boundary, the grid length L has a big impact on the physical accuracy of the results. The quiver radius $r_q = \sqrt{2/3} F_0/\omega_0^2$, i.e. the maximum excursion of a classical free electron in a periodic laser field which is obtained by solving Newton's equation $\ddot{r} = -\sqrt{2/3} F_0 \sin(\omega_0 t)$ with $r(0) = \dot{r}(0) = 0$, can give a first idea of the necessary grid length. Requiring that the position of the absorbing boundary ($r_{abs} = L/2 - 50$ a.u.) exceeds the maximum quiver radius, i.e.

$$r_{abs} > r_{q,max} = \sqrt{\frac{2}{3}} \frac{F_{0,max}}{\omega_{0,min}^2} \Leftrightarrow L/2 > \sqrt{\frac{2}{3}} \frac{0.55}{0.06^2} \text{ a.u.} + 50 \text{ a.u.}, \tag{3.24}$$

we find that L must be larger than 350 a.u. If this is the case and the pulse is not too long, most of the wave function will remain inside the grid in all three directions. However, we learn from double ionization that long pulses generally require larger grids, so the above estimate fails and an appropriate grid length must be found empirically. In this work, we use $L = 600$ a.u. with $N = 1536$ grid points per dimension, yielding the chosen position grid spacing of $\Delta r = L/N = 0.39$ a.u. To investigate physical convergence in the regime of large F_0, we will frequently increase L to 800 a.u. and N to 2048.

In Table 3.1, we summarize the numerical parameters of the yield calculations. Note that the *total* number of grid points N^3 is on the order of 10^9. To allow for an efficient computation, the yield program was parallelized using the Message Passing Interface (MPI) standard (see Appendix D.2) with which the workload was distributed onto 64 processors for $N = 1536$ and 256 processors for $N = 2048$.

3.3.3. Suitability of numerical parameters

In this section, we establish the reliability of the ion yields obtained with the parameters of Table 3.1 without further comment on their physical properties. We start by investigating the influence of the position grid spacing Δr on the yields. In Fig. 3.6,

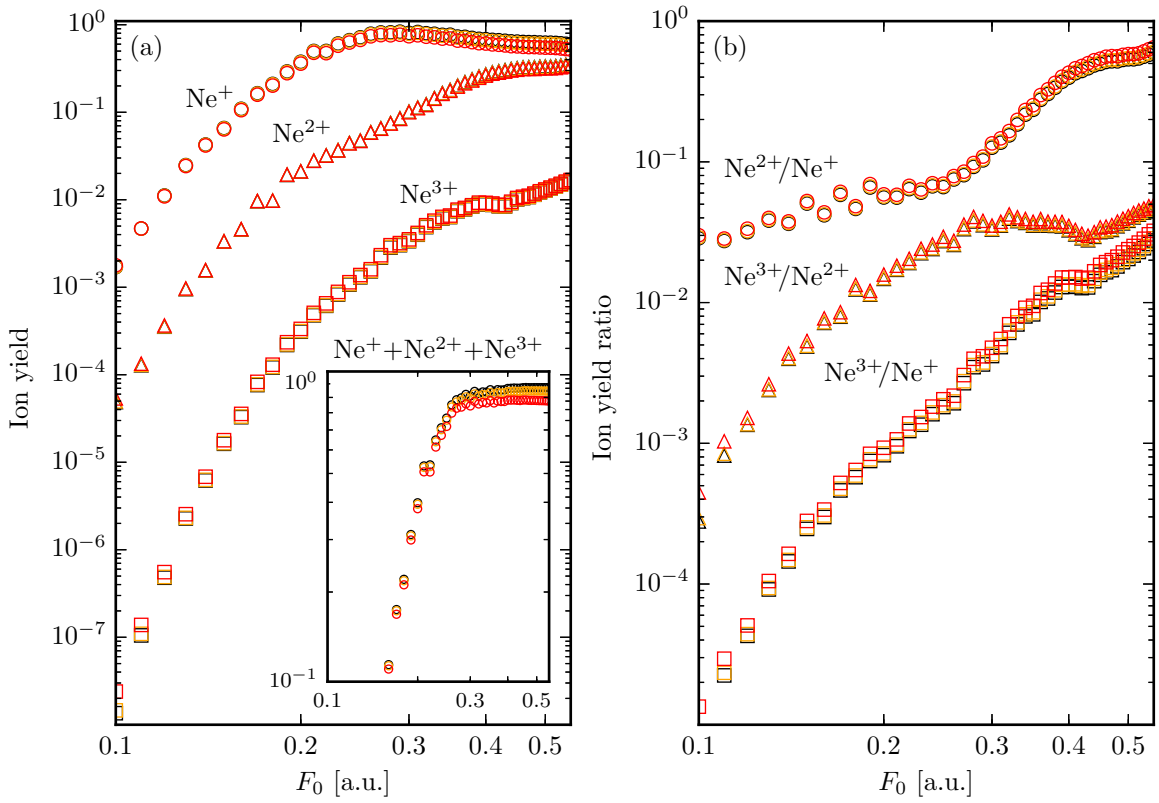

Figure 3.6. (a) Ion yields and (b) yield ratios for $n_c = 5$ and $\omega_0 = 0.1$ a.u. The grid length is $L = 200$ a.u., the grid spacing is varied from $\Delta r = 0.2$ a.u. (black markers) over $\Delta r = 0.26$ a.u. (orange markers) to $\Delta r = 0.39$ a.u. (red markers). All other numerical parameters are those from Table 3.1.

the ion yields and ratios obtained with the parameters of Table 3.1, but various values of Δr, are shown as a function of the field amplitude. A log-log plot is used since both the intensity (see Section 2.3) and the ion yields span several orders of magnitude. We observe that the yields are sufficiently converged except for two regimes. At the left end of the figure, for small F_0, the Ne^{3+} yields are very small in magnitude and the numerical error due to the large grid spacing becomes apparent. For even smaller field amplitudes and with the same resolution in space and time, the yields eventually become smaller than the numerical error and, since the latter is fairly independent of F_0, become constant. This is not visible in the figure, but familiar from two-electron calculations. Towards the opposite end of the figure, the total ion yield (shown in the inset), i.e. the sum of the single, double and triple ionization yields, approaches a constant value which decreases significantly as Δr is increased (Fig. 3.7). In all cases, the constant is smaller than one which is the value expected for field amplitudes above saturation (see Section 3.1). The reason for the reduction of the total ion yield is the finite resolution of the position grid: The larger Δr, the larger the numerical error of the two-point formula and the trapezoidal rule which are used to calculate the probability

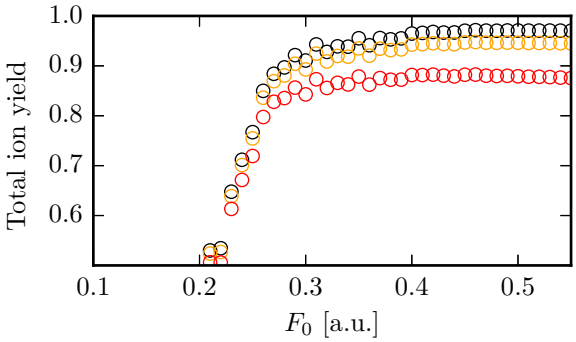

Figure 3.7. Close-up of the total ion yields shown in the inset of Fig. 3.6. The grid spacing is $\Delta r = 0.2$ a.u. (black markers), $\Delta r = 0.26$ a.u. (orange markers), $\Delta r = 0.39$ a.u. (red markers).

current and the probability flux, respectively. Nevertheless, the convergence problems for small and large field amplitudes are not severe, so the above results justify our choice $\Delta r = 0.39$ a.u.

Another feature apparent from Fig. 3.7 is the oscillatory behavior of the total ion yield between $F_0 = 0.25$ a.u. and $F_0 = 0.4$ a.u. To investigate this effect in a qualitative way, we considered the Hamiltonian that is obtained by setting $r_1 = r_2 = r_3$ and $p_2 = p_3 = 0$ in (2.7). In this one-dimensional system, both the oscillatory behavior and the effect of the yield becoming constant above a certain field amplitude persist, but the numerical effort of reducing Δr or changing the pulse parameters is much smaller compared to three dimensions. We found that the yields of the one-dimensional system converge to one above $F_0 = 0.14$ a.u. as Δr is decreased, but the oscillations survive. It was carefully checked that the oscillations depend on none of the other numerical parameters once convergence in Δr is reached. However, the amplitude of the oscillations increases with increasing pulse duration, so it can be concluded that the effect is due to resonances or wave packet interference on the grid.

The variation of the results with Δt is similar in magnitude to the variation with Δr and is therefore not shown. Since the split-operator method is formally independent of the number of spatial dimensions (see Appendix D.1), using the same time step as in two dimensions yields results which are equally reliable.

Now we investigate physical convergence. Fig. 3.8 shows the yields and ratios obtained with three different grid lengths L. For small field amplitudes where the spreading of the wave function and the probability loss due to the absorbing boundary are negligible, all grids essentially produce the same yields. Above $F_0 \approx 0.3$ a.u., however, the Ne^{2+} and Ne^{3+} yields for $L = 200$ a.u. (red markers) fall below the yields for $L = 400$ a.u. (orange markers). At the upper end of the field interval, the difference of the Ne^{3+} yields for the two grids is approximately one order of magnitude. Increasing the grid length from 400 a.u. to 600 a.u. (black markers) has a small effect on the yields. The effect on the ratios is stronger since the yields in both the numerator and the denominator change. According to the rate equations (3.17), the total ion yield

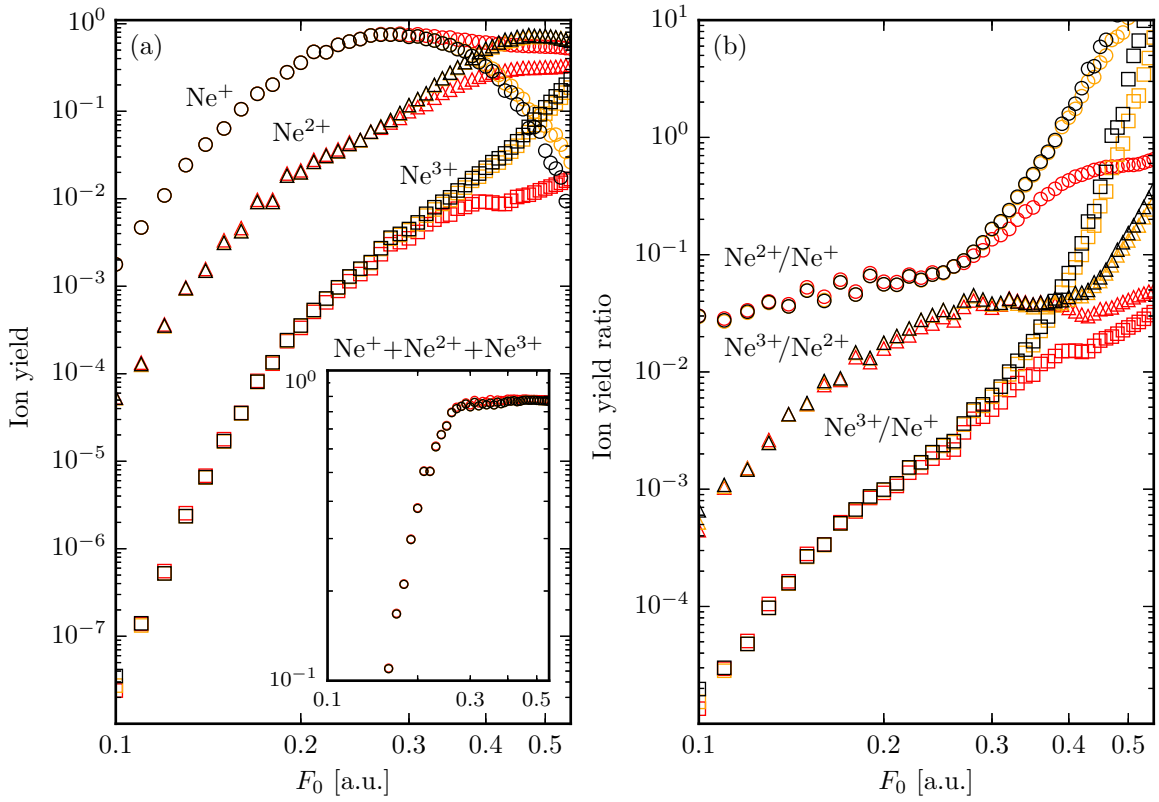

Figure 3.8. (a) Ion yields and (b) yield ratios for $n_c = 5$ and $\omega_0 = 0.1$ a.u. The grid spacing is $\Delta r = 0.39$ a.u., the grid length is varied from $L = 200$ a.u. (red markers) over $L = 400$ a.u. (orange markers) to $L = 600$ a.u. (black markers). All other numerical parameters are those from Table 3.1.

$P_{tot} = 1 - P_0$ (shown in the inset) is solely determined by the probability fluxes across the boundaries of region 0. All of these are calculated at positions $r_i \ll L$ which is why the total ion yield is fairly independent of L.

Next, we show that calculating the yields at a finite distance from the nucleus is reasonable. Clearly, a wave packet corresponding to one, two or three ionizing electron(s) will cover any distance[7] if it is given enough time to do so. Therefore, the overall size of the regions (determined by r_c) should have no significant influence on the yields, provided the evolution time is long enough (Parker *et al.*, 2003). In principle, this could be verified by calculating the ion yields P_i $(i = 1, 2, 3)$ for two different values of r_c (with r_a and r_b adjusted accordingly) and comparing them. However, since an ionizing, i.e. outgoing, electron wave packet will eventually leave the integration domain through the absorbing boundary, we can also compare P_i to the integrated probability

[7]Mathematically, ionization of the ith electron in (2.8) corresponds to letting $r_i \to \infty$ and neglecting its interaction with the field ($F(t)r_i = 0$). The need for the second assumption is due to the electric dipole approximation – a real laser field is position-dependent and will vanish far away from the nucleus.

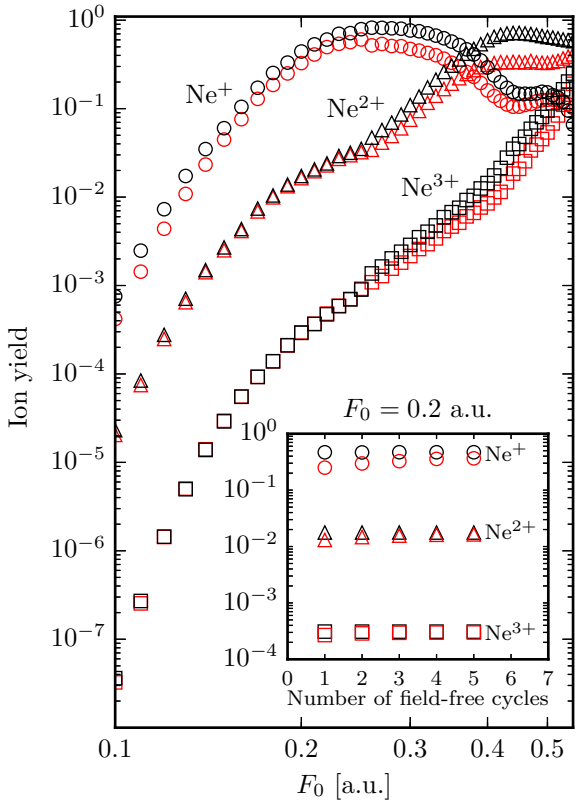

Figure 3.9. Ion yields for $n_c = 5$ and $\omega_0 = 0.06$ a.u. (black markers), compared to the integrated probability fluxes (3.21) from regions 1, 2 and 3 through the absorbing boundary (red markers). The numerical parameters are those from Table 3.1. Inset: Ion yields and integrated probability fluxes through the absorbing boundary for $F_0 = 0.2$ a.u. and different numbers of field-free cycles after the pulse.

flux $P_{i,abs}$ from region i through the absorbing boundary (equation (3.21)). Since the $P_{i,abs}$ are calculated together with the yields (3.17) anyway, additional calculations are not necessary in this case. As shown in Fig. 3.9, the yields closely follow each other, with $P_{i,abs} < P_i$ for all i and all F_0. This is expected since the outgoing wave packets have to travel a greater distance to reach the absorbing boundary and integration is stopped before the wave packets that are ionized late in the pulse have reached the boundary. By increasing the number of field-free cycles in the time integration, the wave packets have more time to reach the absorbing boundary and we therefore observe $P_{i,abs} \to P_i$. For $F_0 = 0.2$ a.u., this is illustrated in the inset of Fig. 3.9. Obviously, the P_i have already converged after one field-free cycle, justifying our integration time of $2\pi(n_c + 1)/\omega_0$.

In Fig. 3.10, the yields and ratios obtained with the regions defined by equations (3.16) ("cuboid version", black markers) and defined by Fig. 3.5 ("cut-out version", red markers) are compared. We observe that the overall qualitative shape of the curves, with all of their substructures, is preserved in the cut-out version. Since the boundary

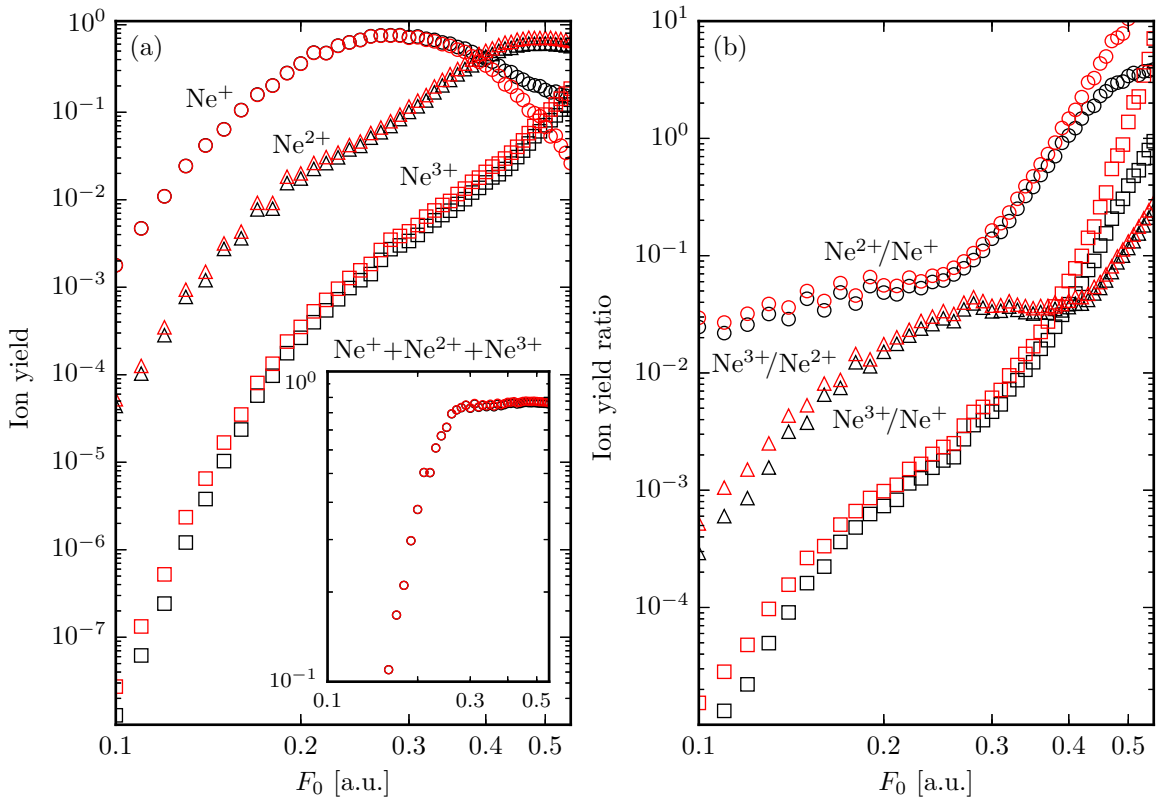

Figure 3.10. (a) Ion yields and (b) yield ratios for $n_c = 5$ and $\omega_0 = 0.1$ a.u., with the regions defined by equations (3.16) with $r_c = 12.5$ a.u. (black markers) and defined by Fig. 3.5 with $r_a = 5$ a.u., $r_b = 7$ a.u. and $r_c = 12.5$ a.u. (red markers). The grid length is $L = 400$ a.u., all other numerical parameters are those from Table 3.1.

$0 \leftrightarrow 1$ is nearly unaffected by the cutting, the Ne^+ yields agree very well for small field amplitudes. However, the boundaries $0 \leftrightarrow 2$, $0 \leftrightarrow 3$ and $1 \leftrightarrow 3$ are considerably larger in the cut-out version, so the Ne^{2+} and Ne^{3+} yields are generally enhanced. For large field amplitudes, this leads to the Ne^+ yield decreasing more strongly with F_0 than in the cuboid version. For the same reason, the ratios involving the Ne^+ yield increase more strongly with F_0 in this regime.

In summary, we have justified the numerical parameters and have elucidated some typical effects of the discretization. From now on, we will use the parameters of Table 3.1, except where indicated otherwise. In some cases, the yields near the lower end of the field interval are not sufficiently converged and we recalculate them with smaller Δr and smaller L. If this does not improve the situation, we omit the corresponding data points. Tables with all calculated yields from which the convergence may be judged can be found in Appendix A.1.

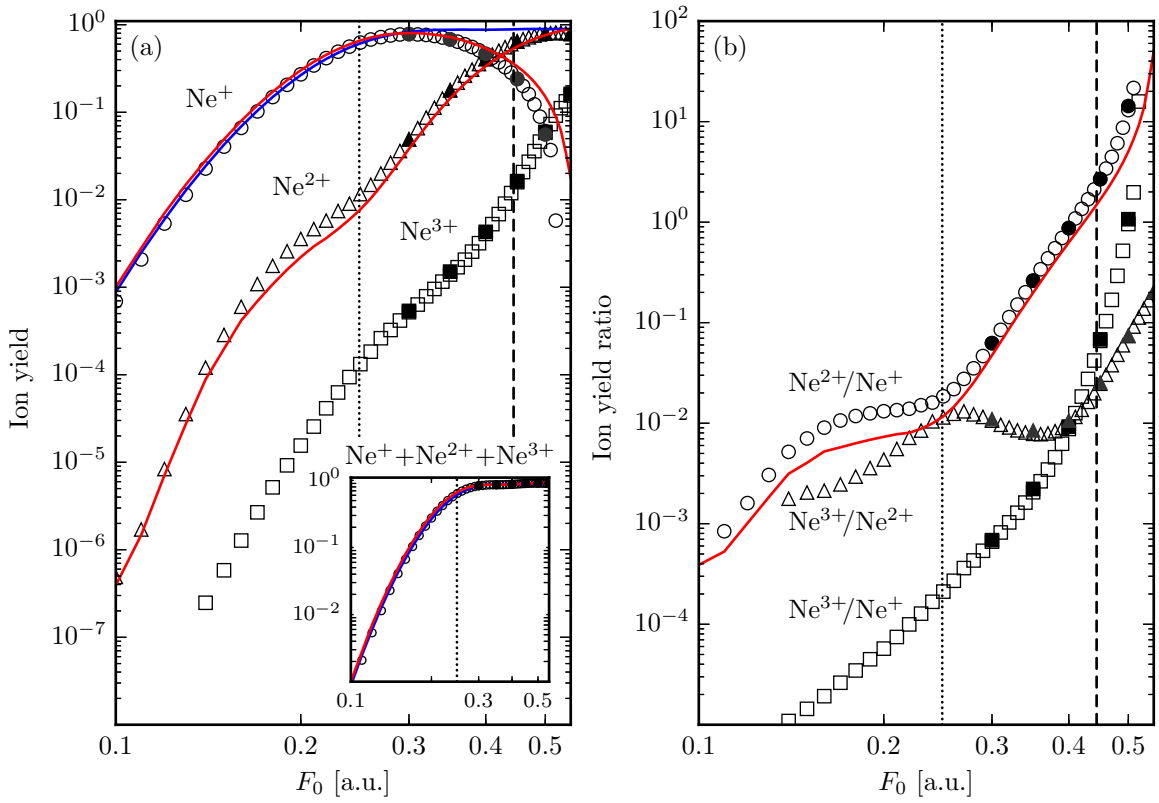

Figure 3.11. (a) Ion yields and (b) yield ratios for $n_c = 2$ and $\omega_0 = 0.06$ a.u. The saturation field amplitudes of single ionization ($F_{sat}^{SI} = 0.25$ a.u.) and double ionization ($F_{sat}^{DI} = 0.44$ a.u.) are indicated by dotted and dashed lines, respectively. The grid length is $L = 600$ a.u., but some results for $L = 800$ a.u. (solid markers) are overplotted to demonstrate physical convergence. The blue and red curves were obtained within a single- and two-active-electron approximation of the Hamiltonian (2.7), respectively (see Section 3.4.2 and 3.4.3).

3.4. Results: Two-cycle pulse

In this section, we discuss the ion yields obtained for a two-cycle pulse with fixed frequency. After a qualitative discussion of the structures and trends, we introduce approximate one- and two-electron Hamiltonians to identify the prevalent ionization pathways as a function of the field amplitude.

3.4.1. Qualitative discussion

Fig. 3.11a shows the ion yields at the end of a two-cycle ($n_c = 2$) pulse with frequency $\omega_0 = 0.06$ a.u. as a function of the field amplitude F_0. We first discuss the regime to the left of the dotted vertical line ($F_0 < 0.25$ a.u.). Here, all yields increase with F_0 and the magnitude of the yield for fixed F_0 decreases with increasing charge state of the ion. Both observations are readily understood by invoking ionization mechanisms based on tunnel ionization (which are at work for the field amplitudes under study):

ω_0 [a.u.]	$T^{exp}_{1/2,I}$ [fs]	n_c	Measured by	Ne^{i+}
0.114	40	83	Ekanayake *et al.* (2012)	1 - 5
0.073	100	133	Dietrich *et al.* (1994)	1, 2
0.058	40	42	Palaniyappan *et al.* (2005)	1 - 8
0.057	200	208	Larochelle *et al.* (1998)	1, 2
0.057	50	52	Chowdhury and Walker (2003)	1 - 8

Table 3.2. Experimental references for intensity-dependent ion yields of neon. The approximate number of field cycles n_c was calculated from the frequency ω_0 and the FWHM intensity pulse duration $T^{exp}_{1/2,I}$ according to equation (2.33). The last column lists the charge states which were observed in the respective experiment.

As F_0 is increased, the deformation of the atomic potential increases so that more and more electron wave packets can tunnel through the barriers near the saddle points in the potential. Due to the different saddle energies (see equation (2.14)), the tunneling rates differ by orders of magnitude and consequently, single ionization is more likely than double ionization, which is in turn more likely than triple ionization.

For $F_0 = F^{SI}_{sat} = 0.25$ a.u. (dotted vertical line), the Ne^+ yield is saturated, i.e. equal to $1 - 1/e$. The saturation is accompanied by a pronounced knee structure in the Ne^{2+} yield. Above saturation, the Ne^+ yield reaches a maximum and, due to the conservation of probability enforced by the rate equations (3.17), decreases once the Ne^{2+} yield is of comparable order of magnitude. Likewise, the Ne^{2+} yield saturates at $F_0 = F^{DI}_{sat} = 0.44$ a.u. (dashed line), preceded by a faint knee structure in the Ne^{3+} yield. The Ne^{2+} yield starts to decrease above $F_0 \approx 0.5$ a.u. when the Ne^{3+} yield becomes large, but this is barely visible in the figure. Finally, we note that although virtually all atoms are ionized above F^{SI}_{sat} by definition, the total ion yield (shown in the inset) does not approach one for large field amplitudes, but a slightly smaller number (about 0.89). As shown in Section 3.3.3, this is due to the finite resolution Δr of the position space grid.

Table 3.2 collects some references for intensity-dependent yield measurements of neon (for a similar overview including other noble gases, see Larochelle *et al.* (1998)). Overall, the qualitative agreement of our simulation results with the experimental ones is remarkable. At first glance, this is surprising, given the fact that our pulse with $n_c = 2$ is orders of magnitude shorter than the ones used in the experiments where n_c varied roughly between 40 and 200. Nevertheless, it is plausible since our model reduces the electron dynamics in such a way that multiple ionization is much more likely than it would be in full space, thereby mimicking the effect of a longer pulse duration.

Next, we consider the yield ratios Ne^{2+}/Ne^+, Ne^{3+}/Ne^+ and Ne^{3+}/Ne^{2+}. In contrast to the individual yields, the knee structures are more pronounced in the ratios since the dependence of the numerator yield on the production of the previous charge state (the denominator yield) is removed (Chowdhury and Walker, 2003). As shown in Fig. 3.11b, the slopes of the yield ratios change dramatically near saturation. Below F^{SI}_{sat}, the

dependence of the Ne^{2+}/Ne^{+} yield ratio on F_0 is rather weak, with an inflection point occurring near $F_0 = 0.2$ a.u. A similar behavior was found in a recent experiment by Kübel *et al.* (2016) on argon with 4 fs pulses at the same frequency. Between F_{sat}^{SI} and F_{sat}^{DI}, the Ne^{2+}/Ne^{+} ratio shows a near-power-law increase $\propto F_0^{9.3}$ before diverging above F_{sat}^{DI} due to the vanishing Ne^{+} yield. The Ne^{3+}/Ne^{2+} yield ratio, on the other hand, does not increase monotonically but exhibits a pronounced dip right before saturation of double ionization, indicating a regime where double ionization increases more quickly with F_0 than triple ionization. Around F_{sat}^{DI}, we also observe a power law-like increase $\propto F_0^{10.8}$ of the ratio and, for even larger values of F_0, a divergence due to the vanishing Ne^{2+} yield. Finally, the Ne^{3+}/Ne^{+} yield ratio increases monotonically without any sudden change of slope.

Since the yields as well as the ratios show no flattening for large field amplitudes, we can assume that the chosen grid size of $L = 600$ a.u. is large enough for the current pulse duration, i.e. the yields are physically converged. To demonstrate this, we also included a few data points in Fig. 3.11 which were obtained with $L = 800$ a.u. (solid markers).

Most of the above discussion was qualitative. Now we try to understand the above results quantitatively, starting with single ionization.

3.4.2. Single-active-electron approximation

In the potential landscape, single ionization corresponds to an electron wave packet crossing the index-1 saddle near the coordinate axis (see Fig. 2.2), e.g. via tunneling or OBI. The crossing is essentially a one-dimensional process since only one electron coordinate (say r_1) becomes large while the other two remain small. This suggests a single-active-electron (SAE) ansatz

$$\psi(r_1, r_2, r_3, t) = \psi_{SAE}(r_1, t)\phi_0^+(r_2, r_3), \tag{3.25}$$

i.e. to factorize the total three-electron wave function ψ into a time-dependent one-electron part ψ_{SAE} and a stationary two-electron part ϕ_0^+ equal to the ground state wave function of the singly-charged ion. Since the electrons 2 and 3 do not participate in the single ionization event, we can average the Hamiltonian (2.7) over ϕ_0^+. Assuming $\langle\phi_0^+|\phi_0^+\rangle = 1$, this yields

$$\begin{aligned} H_{SAE} &= \langle\phi_0^+|H|\phi_0^+\rangle \\ &= \frac{p_1^2}{2} - \frac{3}{\sqrt{r_1^2+\varepsilon^2}} - \sqrt{\frac{2}{3}}F(t)r_1 + \underbrace{\langle\phi_0^+|\frac{p_2^2}{2} + \frac{p_3^2}{2} + V_2 + V_3 + V_{23}|\phi_0^+\rangle}_{=E_0^+=\text{const.}} \\ &\quad - \sqrt{\frac{2}{3}}F(t)\langle\phi_0^+|r_2 + r_3|\phi_0^+\rangle + \langle\phi_0^+|V_{12}|\phi_0^+\rangle + \langle\phi_0^+|V_{13}|\phi_0^+\rangle. \end{aligned} \tag{3.26}$$

where E_0^+ is the ground state energy of the singly-charged ion (see Section 2.2.1). We have $\langle\phi_0^+|r_2 + r_3|\phi_0^+\rangle = 0$ due to the symmetry of ϕ_0^+ and $\langle\phi_0^+|V_{12}|\phi_0^+\rangle = \langle\phi_0^+|V_{13}|\phi_0^+\rangle$

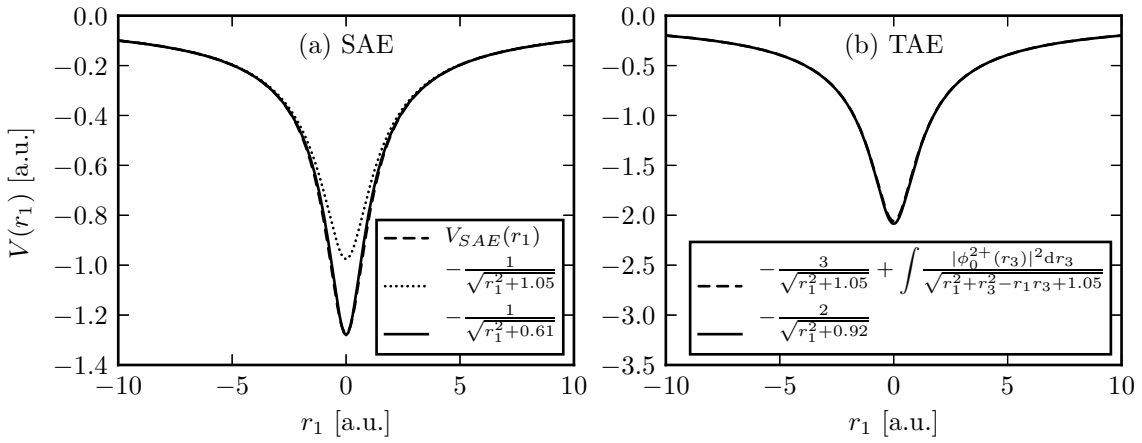

Figure 3.12. (a) Effective one-electron potential obtained by making a SAE ansatz and averaging the Hamiltonian (2.7) over the bound electrons (dashed curve), compared to the restriction of the potential to the subspace of the single ionization saddle (dotted curve) and a soft-core Coulomb potential with a different cut-off parameter (solid curve). (b) Attractive potential for one electron obtained by making a TAE ansatz and averaging the Hamiltonian (2.7) over the bound electron (dashed curve), compared to a soft-core Coulomb potential with a different cut-off parameter (solid curve).

due to the indistinguishability of the electrons. Therefore, H_{SAE} can be written as

$$H_{SAE} = \frac{p_1^2}{2} + V_{SAE}(r_1) - \sqrt{\frac{2}{3}} F(t) r_1 + E_0^+ \tag{3.27}$$

where we defined the effective core potential

$$V_{SAE}(r_1) = -\frac{3}{\sqrt{r_1^2+\varepsilon^2}} + 2\iint \frac{|\phi_0^+(r_2,r_3)|^2 dr_2 dr_3}{\sqrt{r_1^2+r_3^2-r_1r_3+\varepsilon^2}}. \tag{3.28}$$

A mere restriction of the potential in (2.7) to the subspace of the single ionization saddle (approximately given by $r_2 = r_3 = 0$) yields

$$\widetilde{V}_{SAE}(r_1) = -\frac{1}{\sqrt{r_1^2+\varepsilon^2}} - \frac{5}{\varepsilon}. \tag{3.29}$$

The constant $-5/\varepsilon$ results from the smoothed Coulomb interactions and corresponds to a time-independent shift of the energy axis. Therefore, the constant is irrelevant for both the electron dynamics and the yields and can be neglected.

The averaged potential (3.28) and the restricted potential (3.29) are compared in Fig. 3.12a. We observe that the averaging produces a deeper minimum at $r_1 = 0$ than the restriction. Moreover, we find that the averaged potential V_{SAE} can be accurately fitted with a soft-core Coulomb potential with a smaller cut-off parameter ε_{SAE}, i.e.

$$V_{SAE}(r_1) = -\frac{1}{\sqrt{r_1^2+\varepsilon_{SAE}^2}} \tag{3.30}$$

with $\varepsilon_{SAE}^2 = 0.61$ a.u. for $\varepsilon^2 = 1.05$ a.u. For the sake of simplicity, we will use this potential in the following instead of the exact result (3.28). Neglecting the constant E_0^+, we thus arrive at the one-dimensional SAE Hamiltonian of our model,

$$H_{SAE} = \frac{p_1^2}{2} - \frac{1}{\sqrt{r_1^2 + 0.61}} - \sqrt{\frac{2}{3}} F(t) r_1 \tag{3.31}$$

which, for $F(t) = 0$, has the ground state energy $E_0^{SAE} = -0.82$ a.u. Calculating the single ionization yield P_1^{SAE} of this system amounts to a time integration of the probability current at two points $r_1 = \pm r_c$. We choose $r_c = 12.5$ a.u. for consistency with the division of the three-dimensional position space. Since the characteristic length scales of the potentials in (2.7) and (3.31), i.e. the cut-off parameters, are different, we adjust the position grid spacing according to

$$\Delta r_{SAE} = \frac{\varepsilon_{SAE}}{\varepsilon} \Delta r = \sqrt{\frac{0.61}{1.05}} \frac{100}{256} \text{ a.u.} \approx 0.3 \text{ a.u.} \tag{3.32}$$

to make sure that the accuracy of the results is comparable. All other numerical parameters remain unchanged. As shown in Fig. 3.11a, the SAE single ionization yield (blue curve) is in very good agreement with the three-dimensional Ne^+ yield up to its maximum. Furthermore, the SAE approximation reproduces the saturation field amplitude of single ionization $F_{sat}^{SI} = 0.25$ a.u. (dotted line in the figure). This value is close to the static OBI field amplitude of the SAE Hamiltonian

$$F_{OBI}^{SI} = 0.22 \text{ a.u.} \tag{3.33}$$

The connection between saturation and the onset of OBI was established early on (Augst *et al.*, 1989, 1991) and will be further elucidated in Section 3.5.5. Note that (3.33) is smaller than the estimate (2.24) for the three-electron model since the ionization energy of the SAE Hamiltonian (0.82 a.u.) is smaller than the first ionization energy of the three-electron Hamiltonian (0.86 a.u.).

Above F_{sat}^{SI}, the population of Ne^+ ions is strongly depleted by ionization to higher charge states. Since Ne^+ represents the highest possible charge state within the SAE approximation, the SAE single ionization yield is virtually constant in this regime and in very good agreement with the total ion yield of the three-electron model (inset of Fig. 3.11a). Therefore, using the SAE approximation, the convergence problems of the total ion yield discussed in Section 3.3.3 can be circumvented since the computational cost of using a smaller grid spacing Δr is much lower in one dimension than in three dimensions.

3.4.3. Two-active-electron approximation

Next, we investigate double ionization. Analogous to the SAE approximation, we can introduce a two-active-electron (TAE) approximation by assuming that only two

electrons interact with the field and one remains in its ground state. The TAE ansatz reads[8]

$$\psi(r_1, r_2, r_3, t) = \psi_{TAE}(r_1, r_2, t)\phi_0^{2+}(r_3) \tag{3.34}$$

where ϕ_0^{2+} is the ground state wave function of the doubly-charged ion. Averaging (2.7) over ϕ_0^{2+} yields the Hamiltonian

$$H_{TAE} = \frac{p_1^2}{2} + \frac{p_1^2}{2} + V_{TAE}(r_1, r_2) - \sqrt{\frac{2}{3}}F(t)(r_1 + r_2) + E_0^{2+} \tag{3.35}$$

with the effective potential

$$\begin{aligned} V_{TAE}(r_1, r_2) = &-\frac{3}{\sqrt{r_1^2 + \varepsilon^2}} - \frac{3}{\sqrt{r_2^2 + \varepsilon^2}} + \frac{1}{\sqrt{r_1^2 + r_2^2 - r_1 r_2 + \varepsilon^2}} \\ &+ 2\int \frac{|\phi_0^{2+}(r_3)|^2 \mathrm{d}r_3}{\sqrt{r_1^2 + r_3^2 - r_1 r_3 + \varepsilon^2}}. \end{aligned} \tag{3.36}$$

As shown in Fig. 3.12b, we have

$$-\frac{3}{\sqrt{r_1^2 + 1.05}} + \int \frac{|\phi_0^{2+}(r_3)|^2 \mathrm{d}r_3}{\sqrt{r_1^2 + r_3^2 - r_1 r_3 + 1.05}} \approx -\frac{2}{\sqrt{r_1^2 + 0.92}}. \tag{3.37}$$

Therefore, the potential

$$V_{TAE}(r_1, r_2) = -\frac{2}{\sqrt{r_1^2 + 0.92}} - \frac{2}{\sqrt{r_2^2 + 0.92}} + \frac{1}{\sqrt{r_1^2 + r_2^2 - r_1 r_2 + 1.05}} \tag{3.38}$$

is a good approximation to the true TAE potential (3.36) and will be used in the following. The TAE Hamiltonian thus reads (the constant E_0^{2+} is again neglected)

$$H_{TAE} = \sum_{i=1}^{2} \left(\frac{p_i^2}{2} - \frac{2}{\sqrt{r_i^2 + 0.92}} - \sqrt{\frac{2}{3}}F(t)r_i \right) + \frac{1}{\sqrt{r_1^2 + r_2^2 - r_1 r_2 + 1.05}}. \tag{3.39}$$

Its ground state energy is $E_0^{TAE} = -2.37$ a.u. for vanishing field. The single and double ionization yields P_1^{TAE} and P_2^{TAE} of (3.39) can be calculated with the two-dimensional version of the flux integration method described by Prauzner-Bechcicki *et al.* (2008). We use $r_b = 7$ a.u., $r_c = 12.5$ a.u. and adjust the grid spacing according to (3.32) which yields $\Delta r_{TAE} = 0.37$ a.u. Only at the lower end of the field interval, we choose a smaller grid spacing of $\Delta r_{TAE} = 0.1$ a.u. to improve accuracy.

In Fig. 3.11a, the TAE yields and ratios are shown as red curves. We find that the TAE approximation correctly captures the dependence of the Ne^{2+} yield and the Ne^{2+}/Ne^{+} ratio on the field amplitude (apart from the slight decrease of the Ne^{2+} yield

[8] A more sophisticated ansatz is described by Kamta and Starace (2002).

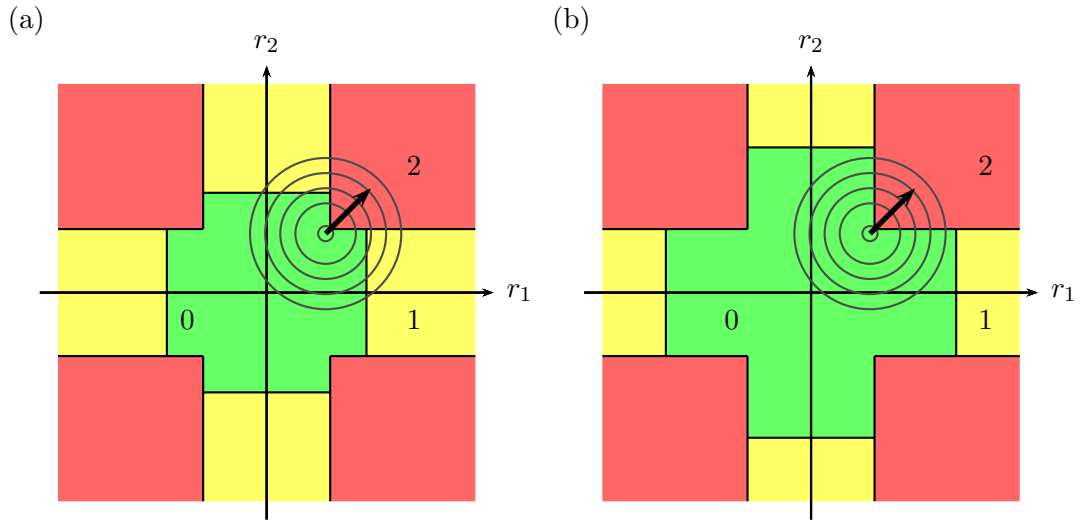

Figure 3.13. Illustration of ionization pathway attribution in two dimensions. During simultaneous double ionization, an ionizing two-electron wave packet (gray circles) moves along the diagonal of position space and crosses the boundary between region 0 (neutral atom, green) and region 2 (doubly-ionized atom, red). (a) The transversal width of the wave packet is larger than the extension of the boundary and the integrated probability flux from region 1 (singly-ionized atom, yellow) to region 2 exceeds the flux from region 0 to 2. The event is classified as sequential double ionization. (b) The boundary between region 0 and 1 is placed at larger values of $|r_i|$. Now the integrated probability flux from region 0 to 2 exceeds the flux from region 1 to 2 and the event is classified as simultaneous double ionization.

for large field amplitudes), but somewhat underestimates the three-electron results for $F_0 < F_{sat}^{SI}$ where simultaneous double ionization dominates. This is surprising since the argument that lead to (3.25) suggests that the TAE ansatz (3.34) works best for simultaneous double ionization, i.e. a situation where two electrons collectively ionize across the double ionization saddle near $r_1 = r_2$, $r_3 \approx 0$. The root of this discrepancy is our choice of the region boundaries over which the probability flux is integrated or, roughly speaking, which part of the probability flux is attributed to which ionization pathway. For two spatial dimensions, this problem is illustrated in Fig. 3.13: If the transversal width of the ionizing two-electron wave packet is considerably larger than the width of the boundary between region 0 and 2 (a), the integrated probability flux from region 1 to 2 (the sequential double ionization yield) exceeds the integrated probability from region 0 to 2 (the simultaneous double ionization yield) and the event is classified as sequential rather than simultaneous double ionization. By moving the boundary between region 0 and 1, this problem can be remedied (b). Without moving the boundary, the attribution problem can be circumvented by comparing the TAE double ionization yield to the simultaneous Ne^{2+} yield P_{02} (see equation (3.22b)) instead of comparing it to the *total* Ne^{2+} yield P_2. As shown in Fig. 3.14, the agreement of P_{02} and P_2^{TAE} is very good below F_{sat}^{SI}, confirming our initial expectation.

One may wonder if it is possible to simplify the TAE approximation in the simul-

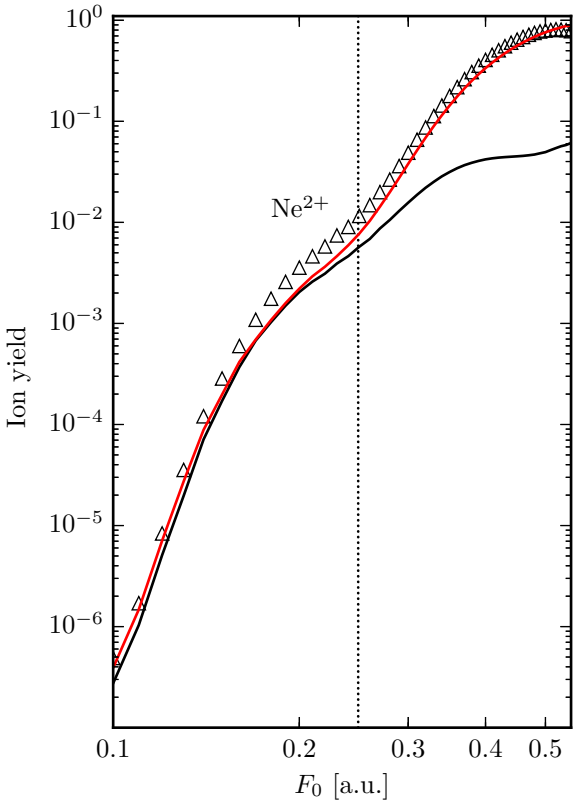

Figure 3.14. Total Ne^{2+} yield (triangles) and simultaneous Ne^{2+} yield (black curve) for $n_c = 2$ and $\omega_0 = 0.06$ a.u., compared to the TAE double ionization yield (red curve). The saturation field amplitude of single ionization ($F_{sat}^{SI} = 0.25$ a.u.) is indicated by the dotted line.

taneous regime even more by setting $r_1 = r_2$ in (3.36). However, the resulting single-electron potential is not useful to describe simultaneous double ionization since, as is well known, a second electron is needed to bring energy into the system via a rescattering event. Based on the idea that the rescattering electron recombines with the residual one to form an excited two-electron state, one could assume that the system is initially in an excited state and calculate the corresponding yields. Due to our lack of knowledge concerning the relevant excitation cross sections, such an approach amounts to a trial-and-error of excited states. We calculated yields for both the ground state and several excited states of the potential (3.36) for $r_1 = r_2$, but the results did not agree with the yields from the three-electron model.

3.4.4. Product yields

The ability of the SAE approximation to reproduce the Ne^+ yields below saturation (Fig. 3.11a) implies that the product ansatz (3.25) is justified for single ionization, i.e. two electrons are left in the ground state of the singly-charged ion after one electron

has left the atom. Since the singly-charged ion also interacts with the laser field, one or both of the remaining electrons can ionize subsequently. However, these ionization steps are decoupled and hence independent from the previous single ionization step. Therefore, for an ionization pathway of i-fold ionization ($i = 1, 2, 3$) starting with single ionization, the Ne^{i+} yield at the end of the pulse can be written as a product of the SAE single ionization yield P_1^{SAE} and the $(i-1)$-fold ionization yield P_{i-1}^{+} of the singly-charged ion in the laser field. The yields P_{i-1}^{+} are calculated from the two-dimensional Hamiltonian of the singly-charged ion in the laser field,

$$H_+ = \sum_{i=1}^{2} \left(\frac{p_i^2}{2} - \frac{3}{\sqrt{r_i^2 + \varepsilon^2}} - \sqrt{\frac{2}{3}} F(t) r_i \right) + \frac{1}{\sqrt{(r_1 - r_2)^2 + r_1 r_2 + \varepsilon^2}}, \tag{3.40}$$

using the same method as in the previous section, but with the region boundaries $r_b = 5$ a.u. and $r_c = 7$ a.u. and the grid spacing $\Delta r = 0.1$ a.u.

The product of the single ionization yield and the population of singly-charged ions (which decreases as F_0 is increased), i.e.

$$P_S(F_0) := P_1^{SAE}(F_0) P_0^{+}(F_0), \tag{3.41a}$$

describes single ionization of the neutral atom (0-1) with subsequent depletion of singly-charged ions due to further ionization. Analogously,

$$P_{SS}(F_0) := P_1^{SAE}(F_0) P_1^{+}(F_0) \tag{3.41b}$$

describes sequential double ionization (0-1-2), i.e. single ionization followed by single ionization. Finally,

$$P_{SD}(F_0) := P_1^{SAE}(F_0) P_2^{+}(F_0) \tag{3.41c}$$

describes single ionization followed by double ionization. This product yield comprises the pathways 0-1-3 and 0-1-2-3 of triple ionization.

In Fig. 3.15a, the above product yields are compared to the yields of the three-electron model. P_S (green curve) agrees very well with the Ne^+ yield up to $F_0 \approx F_{sat}^{DI}$ (dashed vertical line), but overestimates it for larger field amplitudes. As a consequence, the corresponding yield ratios (green and orange curve in Fig. 3.15b) increase not as strongly as the three-electron results. To explain this, we write P_S as

$$P_S(F_0) = P_1^{SAE}(F_0) P_0^{+}(F_0) = P_1^{SAE}(F_0) \Bigg(1 - \underbrace{\sum_{i=2}^{3} P_{i-1}^{+}(F_0)}_{=: P_{tot}^{+}(F_0)} \Bigg) \tag{3.42}$$

where we defined the total ion yield of the singly-charged ion P_{tot}^{+} and used the conservation of probability enforced by the rate equations from which the P_{i-1}^{+} are calculated. Analogous to the total ion yield P_{tot} which, due to the finite grid spacing Δr, approaches

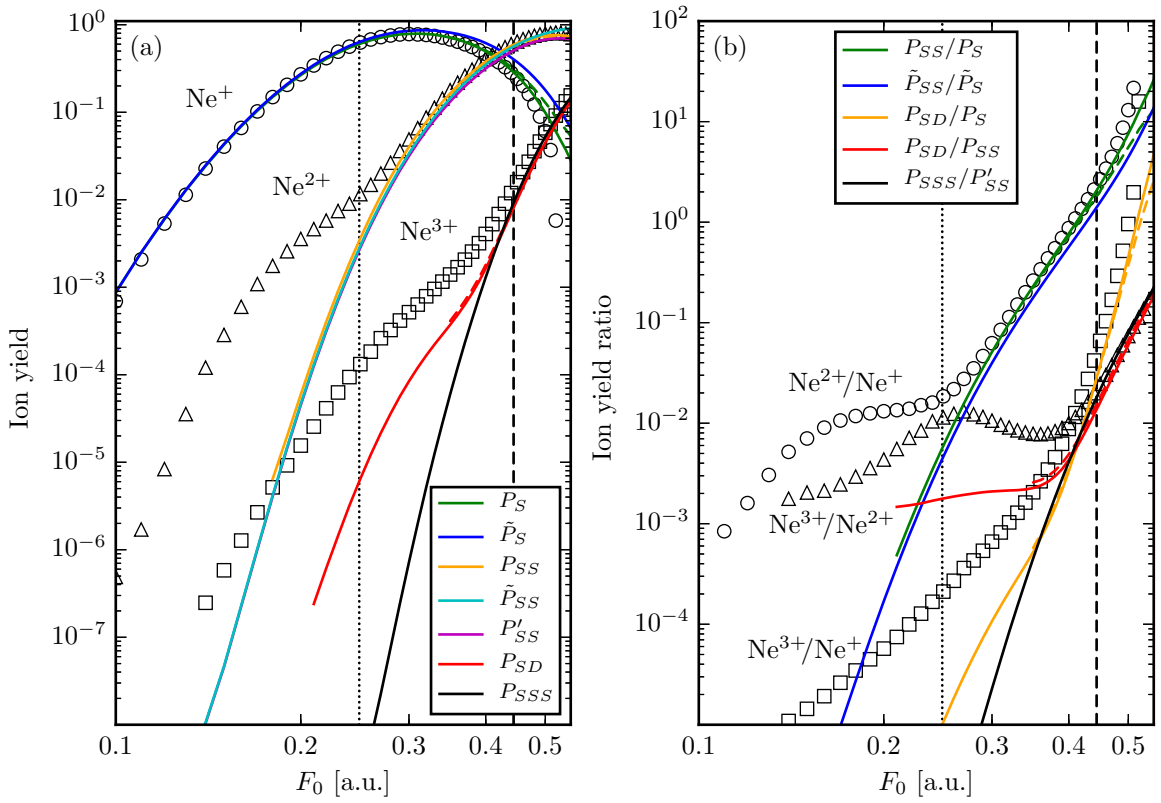

Figure 3.15. (a) Ion yields and (b) yield ratios for $n_c = 2$ and $\omega_0 = 0.06$ a.u., compared to various product yields (colored curves). The grid spacing is $\Delta r = 0.1$ a.u. (solid curves) and $\Delta r = 0.39$ a.u. (dashed curves). The saturation field amplitudes of single and double ionization are indicated by the dotted and dashed lines, respectively.

a number smaller than one above F_{sat}^{SI} (the saturation field amplitude of single ionization from the neutral atom), P_{tot}^{+} approaches a number smaller than one above $F_{sat}^{SI,+}$ (the saturation field amplitude of single ionization from the singly-charged ion) which is found to agree with F_{sat}^{DI}. Therefore, the product yield P_S cannot decrease to zero for $F_0 > F_{sat}^{DI}$. To illustrate the influence of the grid spacing in this regime, the product yield P_S obtained with $\Delta r = 0.39$ a.u. is also shown in Fig. 3.15a (dashed green curve). Below F_{sat}^{DI}, the agreement with the yield for $\Delta r = 0.1$ a.u. is very good but above, the large-Δr yield is slightly larger.

The product yield P_{SS} (orange curve) agrees with the Ne^{2+} yield for $F_0 > F_{sat}^{SI}$ (i.e. above the knee) but dramatically underestimates it for smaller field amplitudes. This shows once more that the knee structure in the double ionization yield is due to a change of the prevalent double ionization pathway from nonsequential, i.e. simultaneous, double ionization (0-2) to sequential double ionization (0-1-2). The change itself can be understood from the electron dynamics in the potential: Since F_{sat}^{SI} is very close to F_{OBI}^{SI}, the prevalent mechanism of single ionization changes from tunneling to classical OBI near F_{sat}^{SI}. In contrast to tunnel ionization, the initial velocity of the released

electron is nonzero for OBI. Consequently, in a given time interval, an OBI electron can reach a greater distance from the nucleus than a tunneled electron, thereby reducing the probability of rescattering (leading to simultaneous double ionization) and making sequential escape more likely than simultaneous escape.

The third product yield $P_{SD} = P_1^{SAE} P_2^+$ (red curve) exhibits a clear knee structure near F_{sat}^{DI}. Since P_1^{SAE} is virtually constant in this regime of field amplitudes (Fig. 3.11), the knee is due to a transition in the double ionization yield P_2^+. Applying the arguments of the previous paragraph to the singly-charged ion, we conclude that the knee structure in P_2^+ is due to the change of the prevalent double ionization pathway from 1-3 to 1-2-3 near $F_{sat}^{DI} \approx F_{sat}^{SI,+}$. Therefore, the prevalent triple ionization pathway in the product yield P_{SD} is 0-1-3 below and 0-1-2-3 above F_{sat}^{DI}. The agreement of P_{SD} and the Ne^{3+} yield for $F_0 > F_{sat}^{DI}$ implies that 0-1-2-3, i.e. sequential triple ionization, is the prevalent triple ionization pathway of the three-electron model in this regime. Conversely, the disagreement of the yields for $F_0 < F_{sat}^{DI}$ implies that the prevalent triple ionization pathway in this regime is *not* 0-1-3, in striking contrast to the expectation of Feuerstein *et al.* (2000) described in Section 1.5. We will discuss this in more detail in the next section.

For single ionization from the singly-charged ion, we can again make a SAE ansatz. Applying the procedure of Section 3.4.2 to (3.40) yields the SAE Hamiltonian of the singly-charged ion

$$H_{SAE}^+ = \frac{p_1^2}{2} - \frac{2}{\sqrt{r_1^2 + 0.92}} - \sqrt{\frac{2}{3}} F(t) r_1 \tag{3.43}$$

with ground state energy $E_0^{SAE,+} = -1.54$ a.u. for $F(t) = 0$. The corresponding OBI field amplitude $F_{OBI}^{SI,+} = 0.39$ a.u. is close to the saturation field amplitude of double ionization $F_{sat}^{DI} = 0.44$ a.u., as expected above. Note that the potential of (3.43) is equal to the singly-ionized TAE potential (which is obtained by letting $r_2 \to \infty$ in (3.38) and setting $F(t) r_2 = 0$), demonstrating the consistency of our approximations. With the ionization yields $P_i^{SAE,+}$ of (3.43) which are calculated with $r_c = \pm 7$ a.u. and $\Delta r = 0.05$ a.u., we can define the product yields

$$\tilde{P}_S(F_0) := P_1^{SAE}(F_0) P_0^{SAE,+}(F_0), \tag{3.44a}$$

$$\tilde{P}_{SS}(F_0) := P_1^{SAE}(F_0) P_1^{SAE,+}(F_0). \tag{3.44b}$$

Analogous to the SAE approximation of the neutral atom, we expect

$$P_0^{SAE,+}(F_0) \approx P_0^+(F_0), \tag{3.45a}$$

$$P_1^{SAE,+}(F_0) \approx P_1^+(F_0) \tag{3.45b}$$

and therefore

$$\tilde{P}_S(F_0) \approx P_S(F_0), \tag{3.46a}$$

$$\tilde{P}_{SS}(F_0) \approx P_{SS}(F_0) \tag{3.46b}$$

for $F_0 < F_{sat}^{DI}$. This expectation is confirmed in Fig. 3.15a where $\tilde{P}_S$ and $\tilde{P}_{SS}$ are shown as blue and cyan curves, respectively.

After two electrons have ionized independently, the third electron is left in the ground state of the doubly-charged ion. With the ionization yields P_i^{2+} of the Hamiltonian

$$H_{2+} = \frac{p_1^2}{2} - \frac{3}{\sqrt{r_1^2 + \varepsilon^2}} - \sqrt{\frac{2}{3}} F(t) r_1 \tag{3.47}$$

describing the interaction of the doubly-charged ion with the laser field, we can again define product yields.

$$P'_{SS}(F_0) := \tilde{P}_{SS}(F_0) P_0^{2+}(F_0) = P_1^{SAE}(F_0) P_1^{SAE,+}(F_0) P_0^{2+}(F_0) \tag{3.48}$$

describes sequential double ionization (0-1-2) with subsequent depletion of doubly-charged ions while

$$P_{SSS}(F_0) := \tilde{P}_{SS}(F_0) P_1^{2+}(F_0) = P_1^{SAE}(F_0) P_1^{SAE,+}(F_0) P_1^{2+}(F_0) \tag{3.49}$$

describes sequential triple ionization (0-1-2-3). P'_{SS} and P_{SSS} are shown in Fig. 3.15 as magenta and black curves, respectively. Above F_{sat}^{DI}, P_{SSS} is in good agreement with both the Ne^{3+} yield and P_{SD}, confirming our previous conclusion that sequential triple ionization dominates the production of Ne^{3+} above the knee. P'_{SS}, on the other hand, is in good agreement with $\tilde{P}_{SS}$ (by construction) and P_{SS}. Above F_{sat}^{DI}, the depletion of doubly-charged ions becomes evident, but the difference between P'_{SS} and the other two product yields is still negligible. Therefore, sequential double ionization will only be described by the product yield P_{SS} in the following.

3.4.5. The pathway 0-2-3

The product yields P_{SS} and P_{SSS} introduced in the previous section allow for an unambiguous identification of the sequential ionization regimes in the Ne^{2+} and Ne^{3+} yield curves ($F_0 > F_{sat}^{SI}$ and $F_0 > F_{sat}^{DI}$, respectively). Consequently, the parts not captured by these product yields must result from nonsequential ionization pathways. For double ionization, we immediately concluded that the excess Ne^{2+} yield below F_{sat}^{SI} is due to simultaneous double ionization (0-2) since it is the only nonsequential pathway of double ionization. For triple ionization, however, there are three nonsequential pathways, namely 0-3, 0-1-3 and 0-2-3. Single ionization followed by simultaneous double ionization (0-1-3) – contained in the product yield P_{SD} – was ruled out as the prevalent pathway below F_{sat}^{DI} in the previous section. Simultaneous triple ionization (0-3) is also not important for the present pulse parameters since we observed neither a knee structure in the Ne^{3+} yield near F_{sat}^{SI} nor a regime of weak F_0-dependence in the Ne^{3+}/Ne^{+} yield ratio in Fig. 3.15. Therefore, we focus on simultaneous double ionization followed by single ionization (0-2-3). For the sake of clarity, the Ne^{3+} yield, the Ne^{3+}/Ne^{2+} yield ratio, the product yield P_{SD} and the ratio P_{SD}/P_{SS} are shown again in Fig. 3.16.

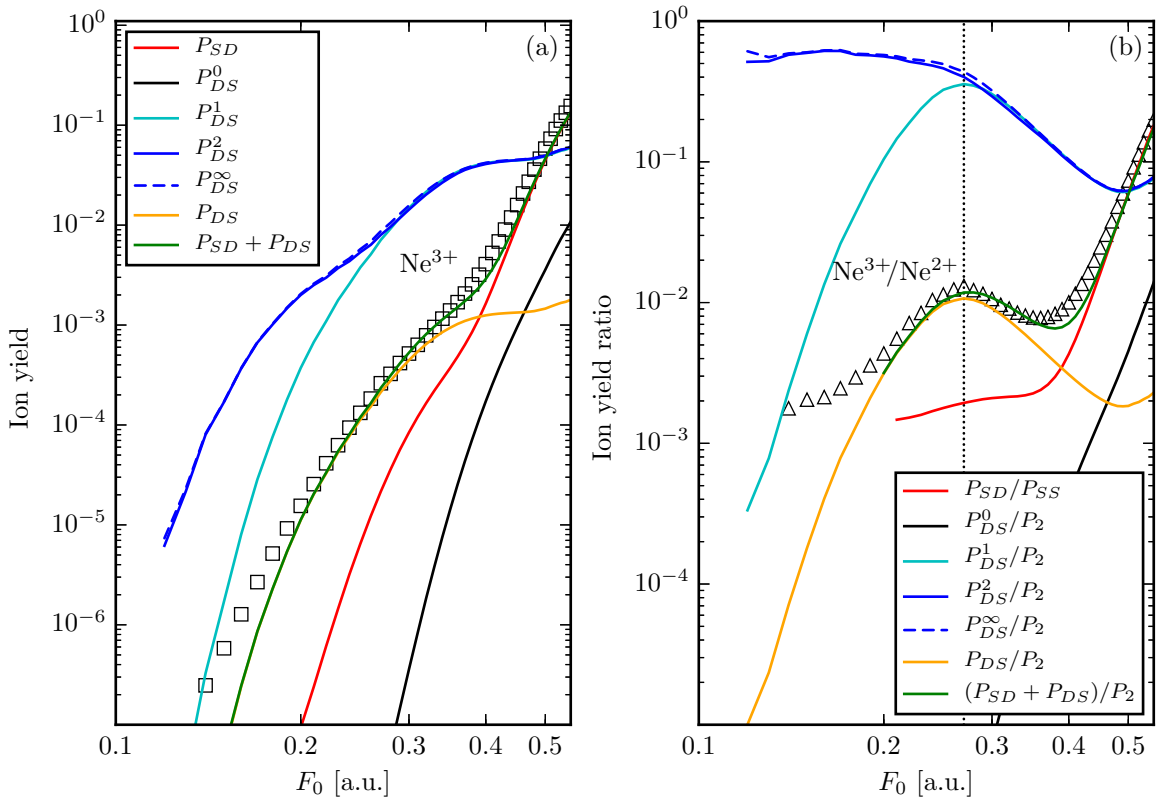

Figure 3.16. (a) Ne^{3+} yields for $n_c = 2$ and $\omega_0 = 0.06$ a.u., compared to the product yields P_{SD} (red curve) and the product yields P^n_{DS} for $n = 0$ (black curve), $n = 1$ (cyan curve), $n = 2$ (solid blue curve) and $n \to \infty$ (dashed blue curve). P_{DS} (orange curve) is equal to $0.03P^1_{DS}$. (b) Corresponding ion yield ratios. The field amplitude corresponding to the local maximum of the Ne^{3+}/Ne^{2+} ratio ($F_0 = 0.27$ a.u.) is indicated by the dotted line.

Several authors (Feuerstein *et al.*, 2000; Rudenko *et al.*, 2008a) expect that 0-2-3 is insignificant compared to 0-1-3 since the tunneling probability of the single ionization step (0-1 and 2-3, respectively) strongly decreases with the ionization energy which is higher for the doubly-charged ion ($E_I^{2+} = 2.29$ a.u.) than for the neutral atom ($E_I = 0.86$ a.u.). This expectation is based on the assumption that the third electron in 0-2-3 ionizes from the ground state of the doubly-charged ion, i.e. that the pathway can be described by the product yield

$$P^0_{DS}(F_0) := P_{02}(F_0)P_1^{2+,0}(F_0) \tag{3.50}$$

where $P_{02}(F_0)$ is the simultaneous double ionization yield of the neutral atom (see equation (3.22b)) and $P_1^{2+,0}(F_0) = P_1^{2+}(F_0)$ is the single ionization yield of the doubly-charged ion in the ground state (indicated by the additional superscript 0). Plotting P^0_{DS} in Fig. 3.16a (black curve) confirms that simultaneous double ionization followed by tunnel ionization of a ground state electron does not contribute significantly to the Ne^{3+} yield.

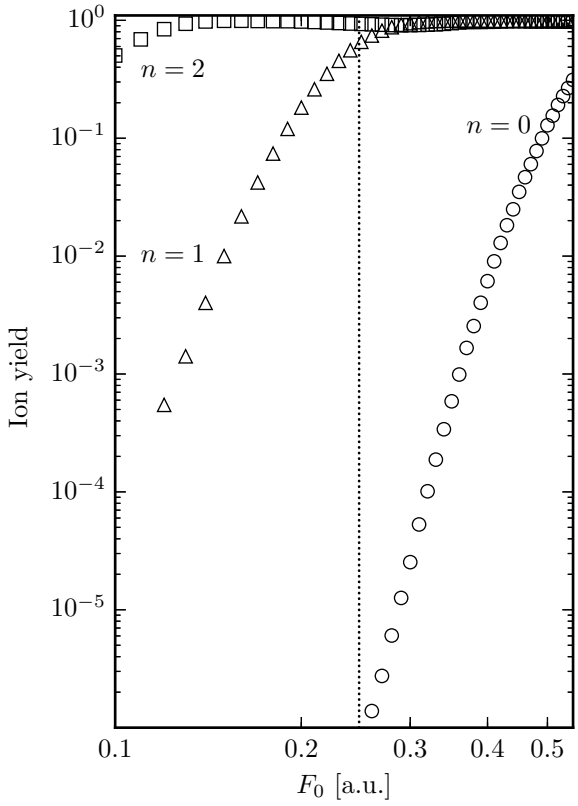

Figure 3.17. Single ionization yields of the Ne^{2+} ion (3.47) for $n_c = 2$ and $\omega_0 = 0.06$ a.u., with the electron initially in the ground state ($n = 0$), the first excited state ($n = 1$) and the second excited state ($n = 2$). The saturation field amplitude of single ionization from the first excited state of Ne^{2+} is equal to the saturation field amplitude of single ionization from the ground state of Ne ($F_{sat}^{SI} = 0.25$ a.u.) and is indicated by the dotted line.

The above scenario of 0-2-3 is not entirely plausible. Since the creation of the doubly-charged ion is preceded by a rescattering step, it is not very likely that the third electron remains in its ground state after the two others have ionized. Rather, due to the electron repulsion, the kinetic energy brought into the system via rescattering is distributed among *all* electrons, i.e. there is a nonzero probability that the third electron is left in an excited state of the doubly-charged ion. This conclusion is supported by classical trajectory calculations (Tang *et al.*, 2013) where excitation of the third electron was observed for the pathway 0-2-3.

To verify the importance of excitation for 0-2-3, we generalize the product yield (3.50) to an arbitrary bound state of the doubly-charged ion with quantum number n,

$$P_{DS}^{n}(F_0) := P_{02}(F_0) P_1^{2+,n}(F_0). \tag{3.51}$$

In Fig. 3.17, the ionization yields $P_1^{2+,n}(F_0)$ for the ground state ($n = 0$), the first excited state ($n = 1$) and the second excited state ($n = 2$) are shown. We find that the saturation field amplitude strongly decreases with increasing n, i.e. increasing initial

energy. As can be seen from the one-dimensional potential of the doubly-charged ion, the OBI field amplitude shows the same qualitative dependence on the initial energy, so the observation once again illustrates the close connection between saturation and OBI. The saturation field amplitude of $P_1^{2+,1}(F_0)$ is 0.25 a.u., equal to F_{sat}^{SI} for the neutral atom in the ground state (dotted vertical line). $P_1^{2+,2}(F_0)$, on the other hand, already saturates at the lower end of our field interval. Extrapolating this trend to higher excited states, we conclude that the yields for $n > 2$ saturate well below $F_0 = 0.1$ a.u. Therefore, we have $P_1^{2+,n}(F_0) \approx 1$ for $n > 2$ and

$$P_{DS}^{n}(F_0) \approx P_{02}(F_0) \cdot 1 =: P_{DS}^{\infty} \tag{3.52}$$

for $n > 2$ and our interval of field amplitudes. The rapid convergence with increasing n is confirmed by Fig. 3.16a where we show the product yields P_{DS}^1, P_{DS}^2 and P_{DS}^{∞}.

Plotting the yield ratios $P_{DS}^{n}(F_0)/P_2(F_0)$ in Fig. 3.16b, we find that the one involving the first excited state ($n = 1$, cyan curve) exactly reproduces the position of the local maximum in the Ne^{3+}/Ne^{2+} ratio ($F_0 = 0.27$ a.u., vertical dashed line). Leaving aside the different magnitude of the ratios for a start, the maximum can be explained by the fact that the first excited state of the doubly-charged ion and the ground state of the neutral atom have the same saturation field amplitude $F_{sat}^{SI} = 0.25$ a.u. Below F_{sat}^{SI}, the ratio P_{02}/P_2 is only weakly F_0-dependent since simultaneous double ionization dominates in this regime ($P_2 \approx P_{02}$[9]). However, tunnel ionization from the first excited state of Ne^{2+} becomes more probable with increasing F_0 due to the increasingly suppressed barrier, so $P_1^{2+,1}$ increases with F_0. Above F_{sat}^{SI}, OBI sets in and $P_1^{2+,1}$ is saturated, i.e. virtually constant (Fig. 3.17). On the other hand, F_{sat}^{SI} marks the transition to the regime where double ionization is dominated by sequentially escaping electrons, so the ratio P_{02}/P_2 decreases with F_0. As a result of the above trends, $P_1^{2+,1} \cdot P_{02}/P_2 = P_{DS}^1/P_2$ has a local maximum slightly above F_{sat}^{SI}.

The definition of the product yield P_{DS}^1 implies that *all* doubly-charged ions created after double ionization are in the first excited state. However, since excitation is a quantum mechanical process, it can be assumed that the doubly-charged ion is promoted to the first excited state only with a probability $P_{exc} < 1$ determined by an excitation cross section (which is a function of the impact energy E_{rec} of the recolliding electron). Therefore, a better definition of the product yield describing the pathway 0-2-3 is

$$P_{DS}(F_0) := P_{exc} P_{DS}^1(F_0) = P_{exc} P_{02}(F_0) P_1^{2+,1}(F_0). \tag{3.53}$$

As a first approximation, we assume $P_{exc} = \text{const.}$ and determine the constant empirically. For $P_{exc} = 0.03$, P_{DS} (orange curve in Fig. 3.16a) fits the Ne^{3+} yield very well for intermediate field amplitudes, leaving little room for the pathway 0-3. The transition to the regime of sequential triple ionization is captured by the sum $P_{DS} + P_{SD}$ (green curve). Moreover, the ratio $(P_{DS} + P_{SD})/P_2$ (green curve in Fig. 3.16b) reproduces the local maximum and the subsequent dip in the Ne^{3+}/Ne^{2+} ratio although the latter is

[9] Due to our yield calculation method (see Section 3.4.3), P_{02} is smaller than P_2.

(a)	Product yield	Symbol	Line style, color
Single	P_S	S	
Sequential double	$\tilde{P}_{SS}$	SS	
Sequential triple	P_{SSS}	SSS	
Double	P_2^{TAE}	D	
Single, Double	P_{SD}	SD	
Simultaneous double, Single	P_{DS}	DS	
SD + DS	$P_{SD} + P_{DS}$	SDS	

(b)	Ratio	Line style, color
Sequential double / Single	P_{SS}/P_S	
Sequential triple / Double	P_{SSS}/P'_{SS}	
Double / Single	P_2^{TAE}/P_1^{TAE}	
SD / Double	P_{SD}/P_{SS}	
DS / Double	P_{DS}/P_2	
(SD + DS) / Double	$(P_{SD} + P_{DS})/P_2$	
(SD + DS) / Single	$(P_{SD} + P_{DS})/P_S$	

Table 3.3. Plotting convention for (a) the product yields and (b) the corresponding ratios.

shifted to a slightly larger field amplitude. This effect might be due to our assumption of an energy-independent excitation probability. For impact energies larger than the ionization energy, excitation cross sections decrease with E_{rec}, typically rather slowly on a logarithmic scale[10]. We expect $E_{rec} \propto U_p \propto F_0^2$ from the rescattering mechanism, so P_{exc} will slightly decrease with F_0, pushing the dip to a smaller field amplitude. The dependence of E_{rec} on the pulse parameters will be analyzed in Section 3.6.

In summary, we have provided convincing evidence that the pathway 0-2-3 plays an important role for the triple ionization yields of our model if excitation of the doubly-charged ion is taken into account. However, the weak part in our line of argument is the need to estimate the excitation probability P_{exc} from the yields of the three-electron model. The calculation of excitation cross sections is beyond the scope of this work, so we will restrict ourselves to looking for traces of the pathway 0-2-3 in the momentum distributions calculated in Chapter 4.

From now on, we will simplify the notation and denote the product yields only by their symbols (e.g. S, SD, SSS), both in the plots and in the text. Furthermore, in those plots where multiple, overlapping product yields are compared, each of them is assigned a specific linestyle and color. These are shown in Table 3.3a. For the sake of completeness, the TAE double ionization yield is also included in the table. For the corresponding ratios (Table 3.3b), we always choose the line style and color based on the numerator yield.

[10] For (approximate) ionization and excitation cross sections of the noble gas atoms, see e.g. de Jesus *et al.* (2004), Micheau *et al.* (2009) or DiChiara *et al.* (2012).

3.4.6. Changing the frequency

Now we change the frequency of our two-cycle laser pulse to $\omega_0 = 0.1$ a.u. The corresponding yields and ratios are shown in the right column of Fig. 3.18. They were not tested for physical convergence since our experience from double ionization tells us that if the yields are converged on a grid for some frequency, they will also be converged on this grid for a larger frequency due to the smaller quiver radius. In the figure, the background color indicates if the prevalent species at the end of the pulse is Ne (green), Ne^+ (yellow) or Ne^{2+} (red). The boundary between the green and yellow (yellow and red) regime is equal to the saturation field amplitude of single (double) ionization.

Comparing the results for both frequencies, some differences strike the eye. First of all, the knee structures in the Ne^{2+} and Ne^{3+} yield curves are less pronounced for $\omega_0 = 0.1$ a.u. although the deviation from the sequential product yields (dashed and dotted black curves) and the strong change of slope in the Ne^{3+}/Ne^{2+} ratio near F_{sat}^{DI} indicate that nonsequential ionization pathways are still present. Secondly, the dip in the Ne^{3+}/Ne^{2+} ratio is gone. Thirdly, we observe pronounced structures in the Ne^{2+} yield below F_{sat}^{SI}. It was shown in Fig. 3.6 that the mathematical convergence of the yields is sufficient, so the numerical resolution cannot be responsible for this. Moreover, there is no obvious reason why the structures should be confined to a small interval of field amplitudes if their origin was merely numerical.

We expect that ionization with $\omega_0 = 0.1$ a.u. has a certain multiphoton component since already a single-figure number of photons is sufficient to allow for a promotion of an electron from the ground state of the neutral atom to an excited state (see Fig. 2.4). A pure multiphoton mechanism of single ionization where an electron absorbs nine photons from the field can be ruled out since the Ne^+ yield would scale as F_0^{18} in this case (Mainfray and Manus, 1991). Such a power law would result in a steep linear growth of the yield in the log-log plot which is not observed. Moreover, the Ne^+ yield still agrees very well with the product yield S (solid black curve) which is based on the SAE approximation of tunneling (see the introduction of Section 3.4.2). Therefore, we can conclude that tunneling is still the prevalent mechanism of single ionization. A more qualitative explanation for this is given by the Keldysh parameter of single ionization $\gamma_K = \sqrt{3/2}\omega_0\sqrt{2E_I}/F_0 = 0.16/F_0$. For the field amplitudes considered here, γ_K is never large compared to one, in contrast to what is expected for the multiphoton regime (see Section 1.3.2).

From the prevalence of tunneling in single ionization, it can be inferred that rescattering remains the driving force behind simultaneous double and triple ionization for $\omega_0 = 0.1$ a.u. However, since the recollision energy $\propto \omega_0^{-2}$ is dramatically reduced compared to $\omega_0 = 0.06$ a.u., we expect that direct impact ionization of a second electron (ROBI) is suppressed compared to excitation (RESI). The maximum excursion of the tunneled electron in the laser field $\propto \omega_0^{-1}$ is also smaller for the larger frequency, so the small recollision energy may be overcompensated by an increased recollision efficiency, resulting in a significant nonsequential signal. Even if the energy of the recolliding electron is not large enough to excite a second electron, it can still be recaptured into an

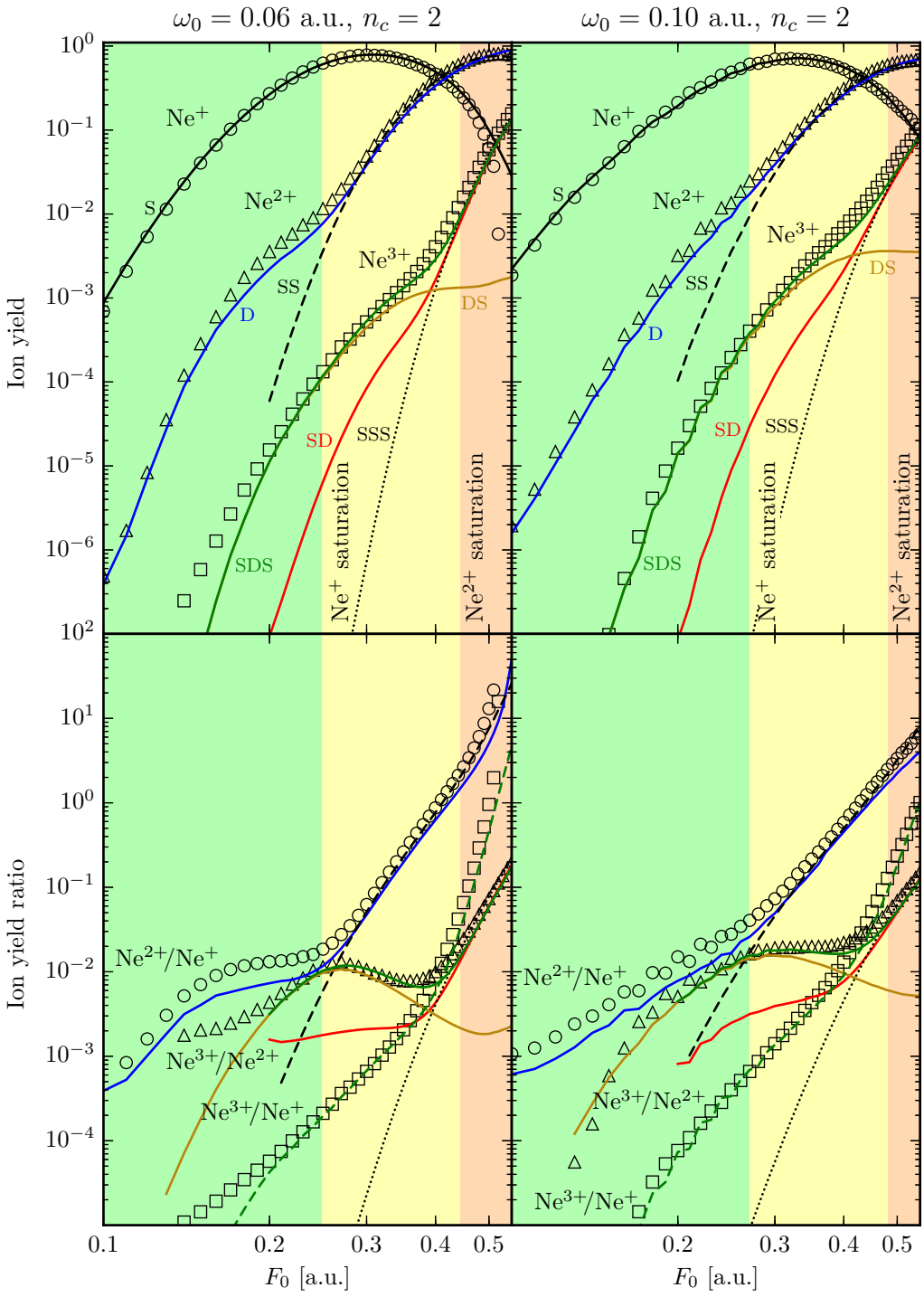

Figure 3.18. Ion yields (first row) and yield ratios (second row) for the two-cycle pulse with $\omega_0 = 0.06$ a.u. (left column) and $\omega_0 = 0.1$ a.u. (right column), compared to the product yields of Table 3.3 (colored curves). The background color indicates if the prevalent species at the end of the pulse is Ne (green), Ne^+ (yellow) or Ne^{2+} (red).

excited state of the neutral atom. This is called frustrated tunnel ionization (Nubbemeyer *et al.*, 2008). All excited states are above the single ionization barrier already for very small field amplitudes[11], so electrons in these states can ionize rapidly during the pulse.

Now we turn our attention to the structures in the Ne^{2+} yield below F_{sat}^{SI}. Based on previous two-electron calculations where similar structures were observed (Corso *et al.*, 2000; Panfili and Liu, 2003; Bannow, 2013), we can assume that they correspond to enhancements of the Ne^{2+} yield which are very well localized in F_0. By investigating the dependence of the double ionization yield curves on the temporal pulse parameters (duration, frequency, envelope function), Panfili and Liu (2003) concluded that the enhancements result from a resonant n-photon transition between the Stark-shifted ground state and a ponderomotively shifted excited state of the atom. Here, such a conclusion would be premature for at least two reasons. On the one hand, Panfili and Liu used a pulse with a much larger frequency ($\omega_0 = 0.18$ a.u.), a longer duration (four to ten cycles) and a trapezoidal shape. On the other hand, they observed enhancements in *both* the single and the double ionization yield, in contrast to our results.

To explain both the nonsequential Ne^{2+} yield and the local enhancements below F_{sat}^{SI}, we can also consider an extension of the RESI scenario (see Section 1.4.1) where one electron tunnels out, is rescattered and promotes a second electron to an excited state of the singly-charged ion before escaping. In most cases, the excited electron will tunnel ionize near the next field extremum, creating the smooth baseline of the nonsequential Ne^{2+} yield. However, if the field amplitude is suitable, the electron may undergo a resonant transition to an even higher excited state of the singly-charged ion from which it can ionize subsequently (e.g. over the barrier or via multiphoton ionization). As a result, the Ne^{2+} yield for this field amplitude is increased. The described mechanism is plausible for a number of reasons. First, as argued above, rescattering still occurs and the recollision energy is reduced so that the importance of RESI relative to two-electron ROBI is increased. Secondly, a transition between excited states of the singly-charged ion requires a maximum of eight 0.1 a.u. photons (see Fig. 2.4). This number is reduced to four if one starts from the fifth excited state. In view of the used field amplitudes, such a transition might be sufficiently probable. Thirdly, the Ne^{3+} yield curve is smooth since promotion of an electron to an excited state of the doubly-charged ion requires much more energy than can be gained by rescattering with the current frequency. Finally, the fact that the enhancements only occur below F_{sat}^{SI} is a strong indicator for a rescattering-related effect since, above F_{sat}^{SI}, rescattering is suppressed due to OBI (see Section 3.4.4).

The disappearance of the dip in the Ne^{3+}/Ne^{2+} ratio below F_{sat}^{DI} can be traced back to the increased importance of the pathway 0-1-3 relative to 0-2-3 in this regime. As visible in the bottom row of Fig. 3.18, the ratio P_{SD}/P_{SS} (red curve) is larger for $\omega_0 = 0.1$ a.u. than for $\omega_0 = 0.06$ a.u. and also increases more quickly with F_0. At the same time, the ratio P_{DS}/P_2 (dark yellow line) decreases more slowly above F_{sat}^{SI}

[11] For example, the first excited state (located -0.31 a.u. in energy below the one-electron continuum) is above barrier for $F \geq 0.03$ a.u.

due to the slower decrease of the ratio P_{02}/P_2. As a result of both effects, the sum ratio (green curve) is nearly constant below F_{sat}^{DI}. Note that the empirical excitation probability P_{exc} of the doubly-charged ion was slightly increased from 0.03 to 0.035 for $\omega_0 = 0.1$ a.u. In view of the increased recollision efficiency discussed above, a higher excitation probability is plausible. A table with all empirical values of P_{exc} used in this work can be found in Appendix A.1.

The frequency dependence of multiple ionization is difficult to estimate from integral ion yields alone. This is especially true for experimentally measured yields (compare the neon yields of Palaniyappan *et al.* (2005) obtained for $\omega_0 = 0.057$ a.u. with those of Ekanayake *et al.* (2012) obtained for $\omega_0 = 0.114$ a.u.). In particular, the observation of resonant structures is rendered impossible by the inevitable intensity averaging of the ion signals produced in the focal volume of the laser (Strohaber *et al.*, 2010). However, for fixed intensity, pronounced resonant structures are visible in the measured momentum distributions of single ionization (Rudenko *et al.*, 2004; Alnaser *et al.*, 2006; Liu *et al.*, 2007). The origin of these structures will be discussed in Section 4.2.

3.5. Results: Longer pulses

In this section, we increase the laser pulse duration for both frequencies to five and seven cycles. The corresponding FWHM intensity pulse durations are between 3 fs and 6 fs according to equation (2.33) which is close to the shortest pulse duration for which triple ionization was observed experimentally (4 fs, Kübel *et al.* (2016)).

3.5.1. Numerical issues

For the two-cycle pulse studied in Section 3.4, the yields were physically converged with respect to the chosen grid length $L = 600$ a.u. since the spatial spread of the wave function ψ was small. For a longer pulse, in contrast, a non-negligible part of ψ will enter the absorbing region of the grid when the field amplitude is large enough. The contribution of this part to the ion yields is lost (see Fig. 3.4), so the calculated yields are too small (Ne^{2+}, Ne^{3+}) or, due to probability conservation, too large (Ne^{+}). For $n_c = 5$ and $\omega_0 = 0.06$ a.u., this is illustrated in Fig. 3.19 where some data points from a calculation with $L = 800$ a.u. (solid markers) are plotted on top of the results for $L = 600$ a.u. We observe that the differences are significant only above saturation of double ionization, i.e. in the red area, and only for the Ne^{+} yield and its corresponding ratios.

In Section 3.4, we found that the three-dimensional yields for large field amplitudes can be well approximated by products of yields of one- and two-dimensional systems, demonstrating the prevalence of sequential ionization pathways in this regime. Comparing the more converged yields for $L = 800$ a.u. to the product yields, we see that this approximation still works for a longer pulse. In one and two dimensions, the grid size can be increased with much less effort. Therefore, we can use the product yields

to predict the three-electron yields where the limited grid size prevents their correct calculation.

3.5.2. Five-cycle pulse

The five-cycle yields and ratios for both frequencies are shown in Fig. 3.19. We start by discussing the results for $\omega_0 = 0.06$ a.u., i.e. the left column of the figure. First, we note that the saturation field amplitude of single ionization F_{sat}^{SI} has decreased from 0.25 a.u. to 0.22 a.u., i.e. the Ne^+ yield for fixed F_0 in the green regime is larger compared to $n_c = 2$. This is also true for the Ne^{2+} and the Ne^{3+} yields, confirming the intuitive expectation that the more energy is pumped into the system, the more ions are created. Secondly, we observe that the knee structure in the Ne^{2+} yield curve has become more pronounced, in the sense that the deviation of the yield from the prediction based on a purely sequential ionization mechanism (dashed black curve) is larger compared to $n_c = 2$. This increased importance of simultaneous double ionization below F_{sat}^{SI} also manifests itself in the Ne^{2+}/Ne^+ ratio where the narrow regime of weak F_0-dependence has changed into a broad plateau, a feature which has been observed in a number of experiments (see e.g. Walker *et al.* (1994); Larochelle *et al.* (1998); Bhardwaj *et al.* (2001)). Again, the strong increase of the ratio beyond F_{sat}^{SI} signifies the change of the prevalent ionization pathway from simultaneous double ionization (0-2) to sequential double ionization (0-1-2), as illustrated by the good agreement of the Ne^{2+}/Ne^+ ratio with the product yield ratio P_{SS}/P_S in this regime.

In the Ne^{3+} yield curve, a knee structure near F_{sat}^{SI} is still not visible. However, in the Ne^{3+}/Ne^+ ratio, we find a pronounced plateau which roughly begins at $F_0 = 0.15$ a.u. and ends near $F_0 = F_{sat}^{SI}$. Analogous to double ionization, we consider this a signature of simultaneous triple ionization (0-3). This conclusion is strongly supported by two facts. First, the plateau is located below F_{sat}^{SI} where neutral atoms are the prevalent precursor species. Secondly, the sum yield SDS of the other triple ionization pathways (green curve) agrees reasonably well with the Ne^{3+} yield above F_{sat}^{SI}, but considerably underestimates it below. The pathway which starts to dominate the Ne^{3+} yield right above F_{sat}^{SI} is 0-2-3 (dark yellow curve). This is plausible since 0-2 (which is contained in 0-2-3) still exists above F_{sat}^{SI} and its contribution to the Ne^{2+} yield – which can be found by mentally extrapolating the yield at the knee to higher field amplitudes (Prauzner-Bechcicki *et al.*, 2007, 2008; Thiede, 2011) – is about two orders of magnitude larger than the Ne^{3+} yield in this regime. Therefore, even if only a small fraction of the rescattered electrons creates an excited state of the doubly-charged ion (here, we assumed $P_{exc} = 0.07$), the resulting product yield of 0-2-3 still exceeds that of 0-3.

The behavior of the yields for large field amplitudes is qualitatively equal to the two-cycle case. However, the dip in the Ne^{3+}/Ne^{2+} yield ratio is much less pronounced. This is due to the larger relative contribution of the pathway 0-1-3: Compared to $n_c = 2$, the ratio P_{SD}/P_{SS} (red curve) has increased by a factor between three and four while the three-dimensional Ne^{3+}/Ne^{2+} ratio has only increased by a factor between two and three.

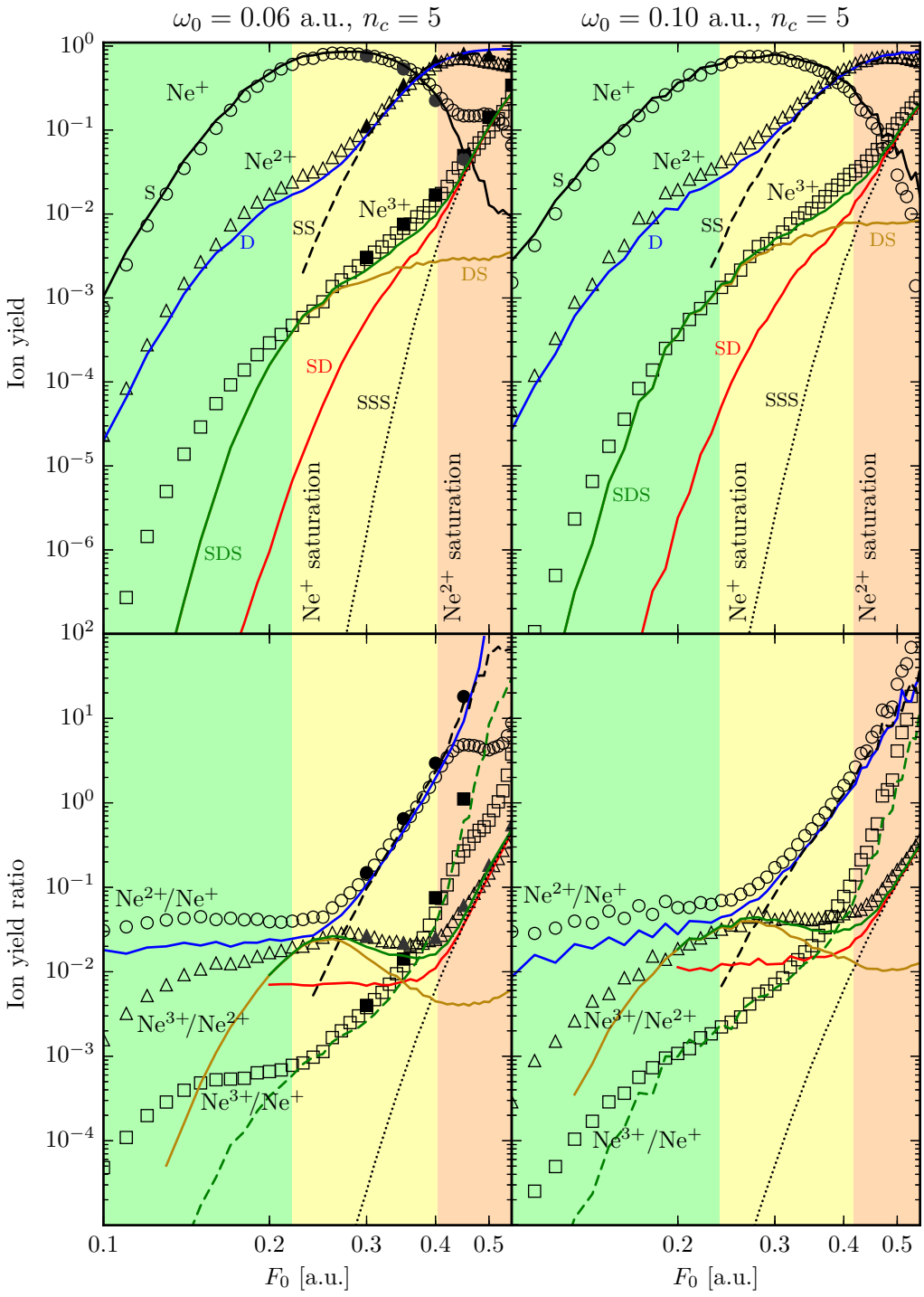

Figure 3.19. Same as Fig. 3.18, but for $n_c = 5$. For the smaller frequency, some data points obtained with the larger grid length $L = 800$ a.u. are superimposed (solid markers). The differences are significant only above saturation of double ionization (red area) and only for the Ne$^+$ yield and the ratios Ne^{2+}/Ne$^+$, Ne^{3+}/Ne$^+$.

Next, we consider the yields for $\omega_0 = 0.1$ a.u. The previously discussed effects of the longer pulse duration are also visible here, but there are some important differences. First of all, the Ne^{2+}/Ne^{+} ratio slowly rises with F_0 below saturation, in contrast to $\omega_0 = 0.06$ a.u. where it is more or less constant (on a logarithmic scale). In the Ne^{3+}/Ne^{+} ratio, a regime of weak F_0-dependence is not visible at all. The only evidence for the pathway 0-3 is the part of the ratio at small field amplitudes which is not captured by the other triple ionization pathways (dashed green curve). The second point to be noted is that the resonant enhancements in the Ne^{2+}/Ne^{+} ratio already visible for $n_c = 2$ are even more pronounced for $n_c = 5$. The positions of the enhancements are nearly unchanged compared to $n_c = 2$, as expected for a resonant process that is mainly determined by the field amplitude (Panfili and Liu, 2003). Most importantly, the Ne^{+} yield curve now also shows considerable structure. Assuming that the structure results from enhancements of the Ne^{+} yield located near the same field amplitudes as the enhancements in the Ne^{2+} yield would not only explain the stronger enhancements in the ratio, but also support the conclusion of Panfili and Liu that a resonant process involving an excited state of the neutral atom is responsible for them. However, it is very hard to spot localized enhancements in the Ne^{+} yield on top of the tunneling baseline. Therefore, we consider the TAE approximation instead. On the one hand, the TAE ratio (blue curve in the figure) accurately reproduces the positions of the enhancements in the three-dimensional Ne^{2+}/Ne^{+} ratio. On the other hand, increasing the resolution in F_0 by a factor of ten is possible with little computational effort.

The TAE yields for $\omega_0 = 0.1$ a.u. and $n_c = 5$ are shown in Fig. 3.20a (blue curves) together with the corresponding ratio (black curve). First, due to the higher resolution in F_0, we observe enhancements both in the single and the double ionization yield which are localized at similar, but not always identical field amplitudes. Secondly, the local maxima (minima) of the ratio occur close to the enhancements in the Ne^{2+} (Ne^{+}) yield. Thirdly, the separation in F_0 between two enhancements in the ratio is virtually constant below saturation ($\Delta F_0 \approx 0.02$ a.u.).

To explain the yield enhancements in terms of multiphoton resonances, we follow the elementary arguments of Panfili and Liu (2003). For a resonant n-photon transition from the ground state of the neutral atom with energy E_0 to a ponderomotively shifted excited state with energy E_j, the equation[12]

$$E_0 + n\omega_0 = E_j + \frac{2}{3}U_p = E_j + \frac{2}{3}\left(\frac{F_0}{2\omega_0}\right)^2 \tag{3.54}$$

must hold. For a fixed value of j and n larger than

$$n_{min}(\omega_0, E_j) := \min\{n \in \mathbb{N} | E_0 - E_j + n\omega_0 \geq 0\}, \tag{3.55}$$

[12] In a laser field, the ground state energy experiences a negative AC Stark shift ΔE_0. Panfili and Liu approximated ΔE_0 using second-order perturbation theory which usually overestimates the Stark shift for strong fields (Delone and Krainov, 1999). Calculation of the Stark shift with a more general formula (cf. Appendix A.2) reveals that ΔE_0 is small compared to ω_0 for the TAE system, so we neglect it here.

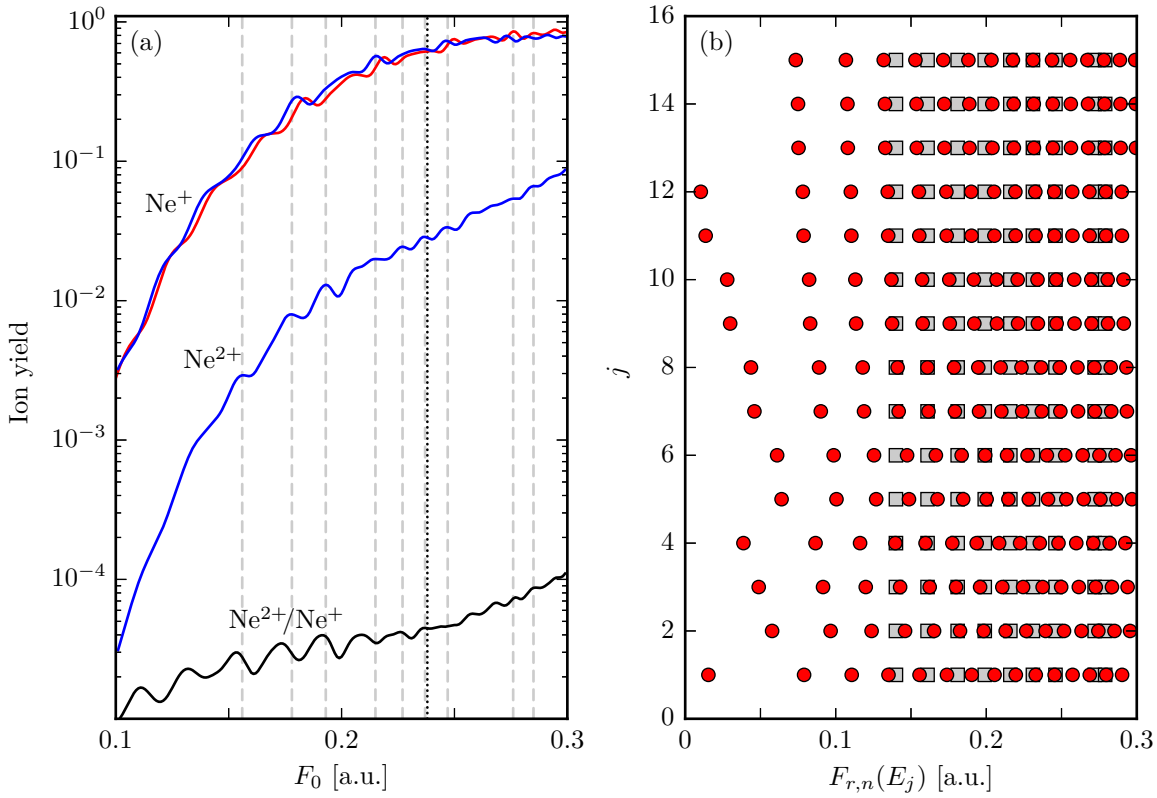

Figure 3.20. (a) TAE single and double ionization yields (blue curves), TAE ratio of double to single ionization (black curve) and SAE single ionization yield (red curve) for $n_c = 5$ and $\omega_0 = 0.1$ a.u. For the sake of clarity, the ratio was multiplied by 10^{-3}. The gray lines mark the most pronounced maxima in the double ionization yield while the dotted black line indicates the saturation field amplitude of single ionization. (b) Comparison of the n-photon resonance field amplitudes (3.56) of the jth excited state (red circles) to the field amplitudes of the local maxima in the double ionization yield (gray squares). In each row, the number of photons increases from left to right.

we therefore expect an enhancement of the single and double ionization yield at the field amplitude

$$F_{r,n}(E_j) = 2\omega_0\sqrt{\frac{3}{2}}\sqrt{E_0 - E_j + n\omega_0}. \tag{3.56}$$

Fig. 3.20b shows $F_{r,n}(E_j)$ for the fifteen lowest excited states of the TAE Hamiltonian (red circles). In each row, the number of photons n increases from left to right. We observe that the influence of E_j is strong only for the first few values of n. However, if n is large, $F_{r,n}(E_j)$ is similar for all j. This can be understood by plugging (3.55) into (3.56) which yields

$$F_{r,n} \approx 2\omega_0^{3/2}\sqrt{\frac{3}{2}}\sqrt{n - n_{min}}. \tag{3.57}$$

According to this approximation, the field amplitude of a resonant enhancement is only determined by ω_0 and the number of excess photons $n - n_{min}$. Due to the definition of n_{min}, the approximation error under the square root is smaller than ω_0, i.e. the smaller ω_0, the better the approximation (3.57) and the weaker the influence of the energy levels E_j. This explains why the TAE yields show enhancements at virtually the same field amplitudes as the three-dimensional yields and the SAE yield (red curve in Fig. 3.20a) although the spectra of the underlying Hamiltonians below the one-electron continuum are somewhat different (Fig. 3.21).

As illustrated by Fig. 3.20b, equation (3.56) might be able explain the local enhancements of the single and double ionization yields. However, the similarity of the $F_{r,n}(E_j)$ makes it virtually impossible to identify a particular transition in the yields, so we must look for alternative approaches. For example, we could decrease the field amplitude towards $F_0 = 0$ where the $F_{r,n}(E_j)$ for different j are sufficiently far apart. However, the small magnitude of the yields in this regime requires a numerical accuracy which is not easily achieved, regardless of the number of spatial dimensions. Alternatively, we could calculate the populations of the excited states as a function of F_0 and link enhancements in them to enhancements in the yields. An example of this approach is given by Panfili and Liu (2003). By considering the irreducible representations of the states involved in the resonant transition (see Appendix C.3), one may derive multiphoton selection rules, thereby reducing the number of excited states to consider. However, all of this is beyond the scope of the present study, so our understanding of the resonant processes which are at work in our model must remain fragmentary for now.

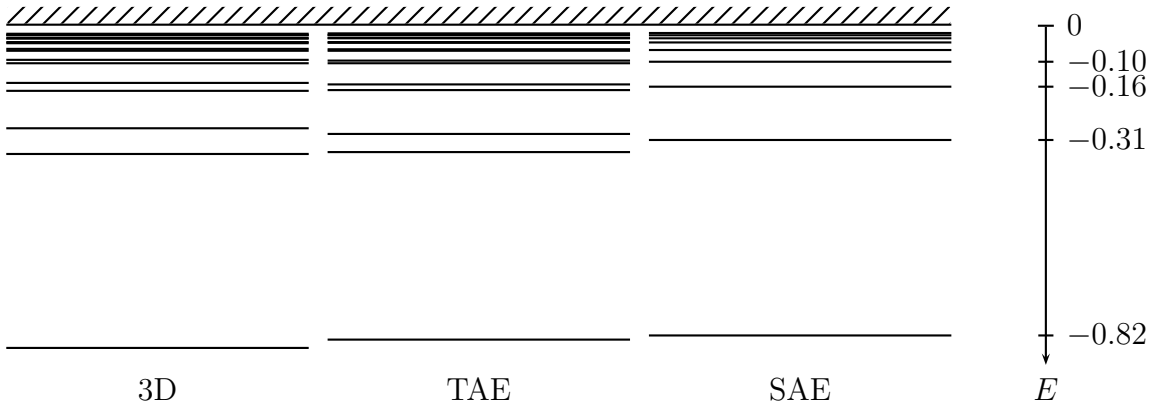

Figure 3.21. Bound-state energy spectra of the three-dimensional Hamiltonian (2.7) with $\varepsilon^2 = 1.05$ a.u., the TAE Hamiltonian (3.39) and the SAE Hamiltonian (3.31). The hatched area indicates the one-electron continuum.

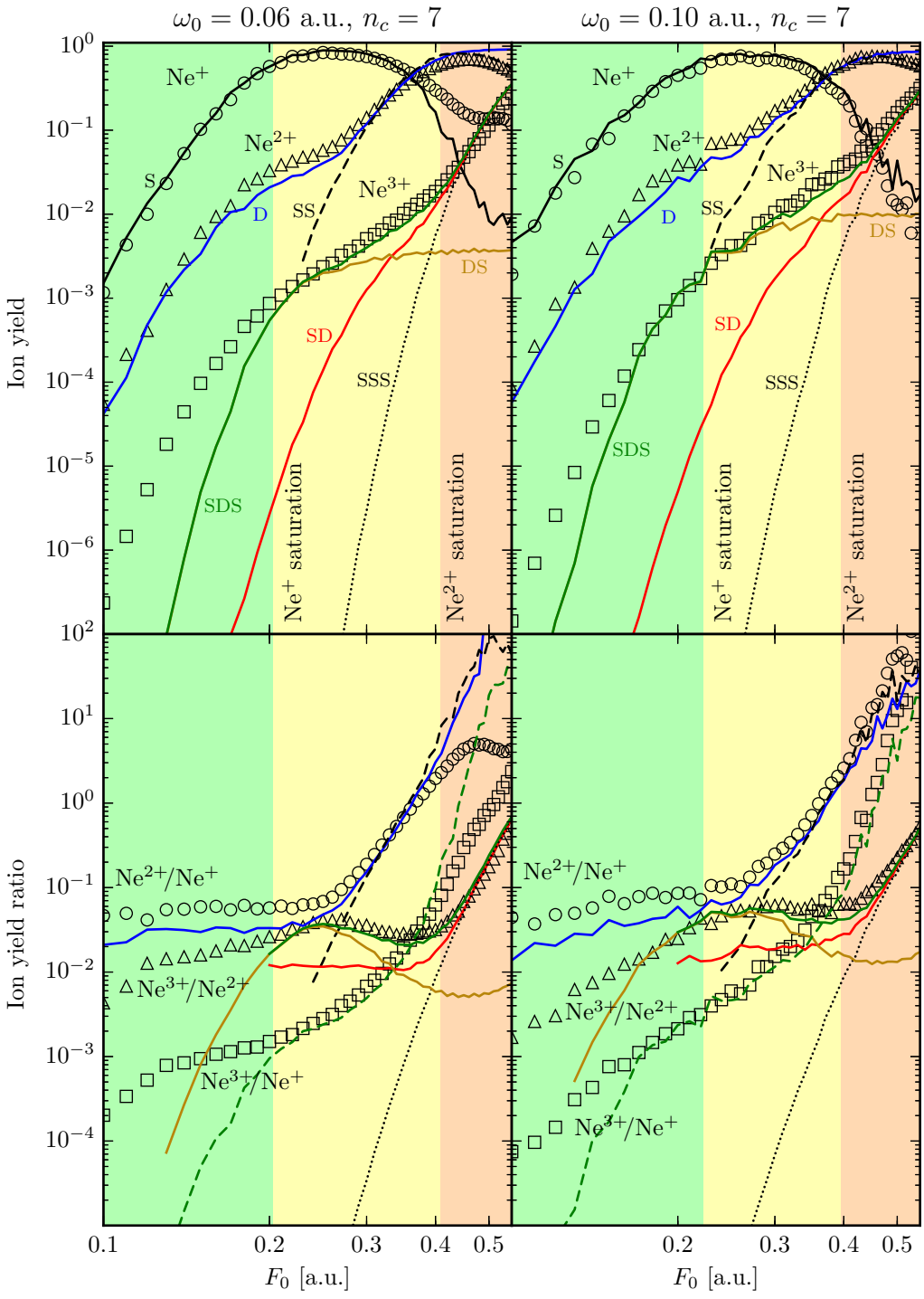

Figure 3.22. Same as Fig. 3.18, but for $n_c = 7$. The convergence issues for large field amplitudes are the same as in Fig. 3.19.

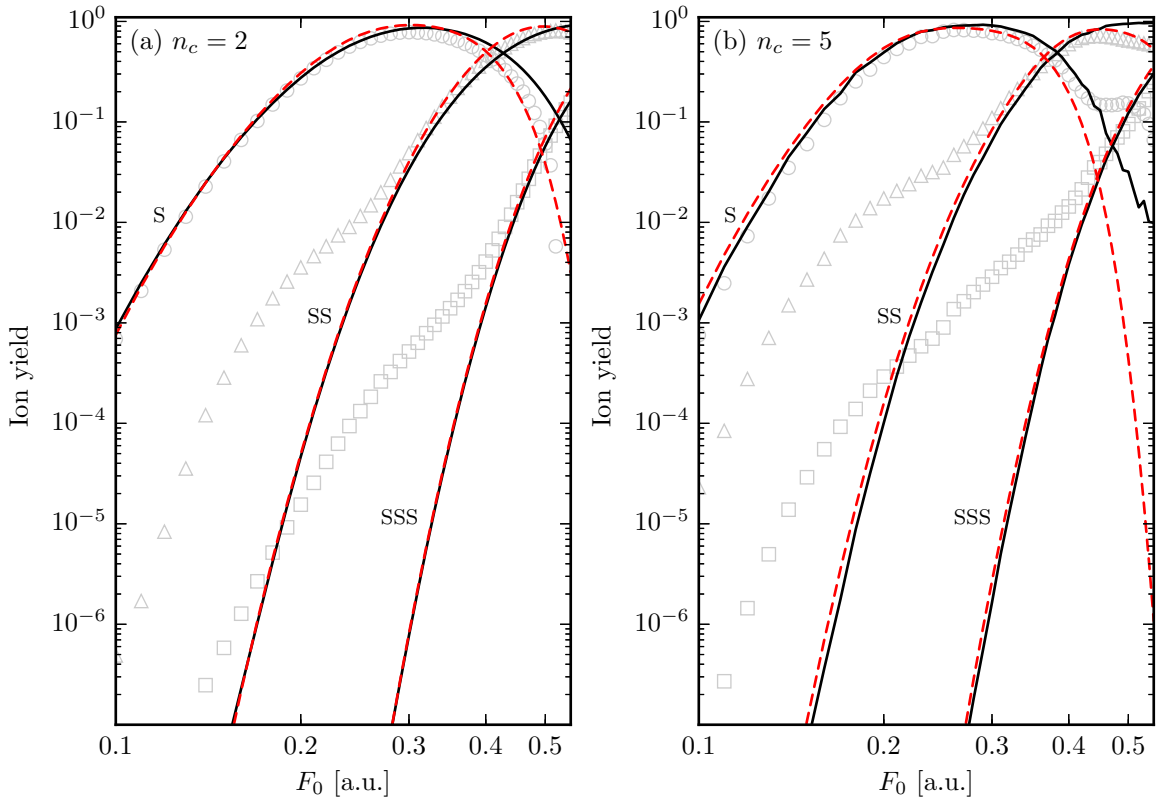

Figure 3.23. Product yields of sequential ionization (black curves) for the two- and five-cycle pulse with $\omega_0 = 0.06$ a.u., compared to the ADK yields (dashed red curves) calculated by solving the rate equations (3.1) with the single ionization rates equal to the ADK formula (3.8) and the simultaneous multiple ionization rates equal to zero. The effective quantum numbers are $n^*_{01} = 1.162 \cdot (2E_I)^{-1/2} = 1.135 \cdot (-2E_0^{SAE})^{-1/2}$, $n^*_{12} = 1.109 \cdot 2(2E_I^+)^{-1/2}$ and $n^*_{23} = 1.091 \cdot 3(2E_I^{2+})^{-1/2}$. The ion yields of the three-electron model are shown in the background.

3.5.3. Seven-cycle pulse

We have also calculated the ion yields for a pulse with seven cycles ($n_c = 7$). They are shown in Fig. 3.22. Although the trends discussed in the previous section continue in the yield curves, the differences to the five-cycle yields are generally small and no new effects appear. The irregularities of the yields visible at the right end of the field interval probably result from wave packet interference on the grid. On the one hand, the absorbing boundaries minimize the wave function reflections on the grid boundaries, but do not suppress them completely. This means that if the pulse is long enough and the grid is too small, a significant amount of wave packets will be reflected back into the region close to the nucleus, thus disturbing the probability flux integration. On the other hand, even if the grid is large enough, long pulses will cause interference effects due to the large number of ejected electron wave packets (Prauzner-Bechcicki *et al.*, 2008).

3.5.4. Comparison with ADK theory

As mentioned in Section 3.2, the ADK formula (3.8) is a powerful tool for quantitatively understanding the F_0-dependence of experimentally measured ion yields in those regimes where sequential ionization dominates. For our model, the single ionization yield and the sequential parts of the multiple ionization yields can be predicted very well with the SAE-based product yields S, SS and SSS. Nevertheless, a representation of these yields in terms of an analytical formula is desirable for the sake of simplicity. Therefore, we give two examples for an ADK fit of the product yields.

For the two- and the five-cycle pulse with $\omega_0 = 0.06$ a.u., Fig. 3.23 compares the product yields S, SS and SSS (black curves) to the ADK yields (dashed red curves) calculated by solving the rate equations (3.1) with the single ionization rates equal to the ADK formula (3.8) and the simultaneous multiple ionization rates equal to zero. By slightly increasing the effective quantum numbers[13] n^*_{01}, n^*_{12} and n^*_{23} and substituting $F(t) \to \sqrt{2/3}F(t)$ (due to our model geometry), the two-cycle product yields can be fitted remarkably well below saturation of each charge state. For the five-cycle pulse, the ADK yields obtained with the same n^*_{ij} still closely follow the product yields but fail to give an accurate fit. However, this can be accomplished with a different choice of the n^*_{ij}. Herein lies another important advantage of the ADK formula: At small field amplitudes where an accurate solution of the Schrödinger equation is difficult to obtain even for a one-dimensional system, a correct sequential yield may be found by extrapolation of an ADK fit calculated for larger field amplitudes.

3.5.5. Saturation versus over-the-barrier ionization

Having investigated the ion yields for various frequencies and pulse durations, we now discuss the relationship between saturation of a yield and the onset of single-electron over-the-barrier ionization (OBI).

We start with OBI. The static OBI field amplitude of single ionization from the neutral atom F^{SI}_{OBI} describes the situation when the energy of the single ionization saddle is equal to the ground state energy. Analogously, one can define the OBI field amplitudes of single ionization from the singly- and doubly-charged ion $F^{SI,+}_{OBI}$ and $F^{SI,2+}_{OBI}$. For a Hamiltonian with two or more spatial dimensions, the OBI field amplitude can only be estimated (see Section 2.2.2). Therefore, instead of the full Hamiltonians (2.7) and (3.40) of the neutral atom and the singly-charged ion, we consider the corresponding SAE approximations (3.31) and (3.43). The SAE potentials of the charge states Ne, Ne^+ and Ne^{2+} are

$$V(r_1) = -\frac{Z}{\sqrt{r_1^2 + \varepsilon^2}} - \sqrt{\frac{2}{3}} F r_1. \tag{3.58}$$

The corresponding nuclear charges Z, cut-off parameters ε and ground state energies

[13] As discussed in Section 3.2, this manual adjustment is a way to partially account for the soft-core Coulomb potentials used in our simulations.

	Z	ε^2 [a.u.]	E_0 [a.u.]	F_{OBI} [a.u.]	$F_{OBI}/(E_0^2/Z)$
SAE (Ne)	1	0.61	−0.82	0.22	0.33
SAE (Ne^+)	2	0.92	−1.54	0.39	0.33
Ne^{2+}	3	1.05	−2.29	0.58	0.33

Table 3.4. Properties of the SAE potentials (3.58) for Ne, Ne^+ and Ne^{2+}: Nuclear charge Z, cut-off parameter ε, ground state energy E_0 and OBI field amplitude F_{OBI}.

	$\omega_0 = 0.06$ a.u.			$\omega_0 = 0.10$ a.u.		
n_c	F_{sat}^{SI} [a.u.]	F_{sat}^{DI} [a.u.]	$F_{sat}^{DI}/F_{sat}^{SI}$	F_{sat}^{SI} [a.u.]	F_{sat}^{DI} [a.u.]	$F_{sat}^{DI}/F_{sat}^{SI}$
2	0.25 (0.25)	0.44 (0.46)	1.76 (1.84)	0.27 (0.28)	0.48 (0.51)	1.78 (1.82)
5	0.22 (0.22)	0.40 (0.40)	1.82 (1.82)	0.24 (0.24)	0.42 (0.43)	1.75 (1.79)
7	0.20 (0.21)	0.40 (0.39)	2.00 (1.86)	0.22 (0.22)	0.40 (0.41)	1.82 (1.86)
OBI	0.22	0.39	1.77	0.22	0.39	1.77

Table 3.5. Saturation field amplitudes of single (SI) and double ionization (DI) for the frequencies and numbers of field cycles used in this work, found by equating the Ne^++Ne^{2+}+Ne^{3+} sum yield (for SI) and the Ne^{2+}+Ne^{3+} sum yield (for DI) with $1 - 1/e$. The predictions of the SAE-based yields P_1^{SAE} (for SI) and P_{SS} (for DI) are shown in parentheses. The static OBI field amplitudes of the SAE Hamiltonians (3.31) and (3.43) are given in the last line.

E_0 are collected in Table 3.4. The OBI field amplitudes were found by equating E_0 with the energy of the local maximum of $V(r_1)$. For $\varepsilon = 0$, this energy is

$$V_s(F) = -2\left(\frac{2}{3}\right)^{1/4}\sqrt{Z|F|}, \tag{3.59}$$

yielding the OBI field amplitude

$$F_{OBI} = \sqrt{\frac{3}{2}}\frac{E_0^2}{4Z} = 0.31\frac{E_0^2}{Z}. \tag{3.60}$$

As evident from Table 3.4, F_{OBI} approximately scales with E_0^2/Z even for $\varepsilon \neq 0$, only with a slightly larger prefactor.

Next, we consider saturation. According to the definitions (3.7), the saturation field amplitude of single ionization F_{sat}^{SI} is the value of F_0 for which the total ion yield (Ne^++Ne^{2+}+Ne^{3+}) at the end of the pulse equals $1 - 1/e = 0.632$. Similarly, at the saturation field amplitudes of double ionization (F_{sat}^{DI}) and triple ionization (F_{sat}^{TI}), the Ne^{2+}+Ne^{3+} sum yield and the Ne^{3+} yield are equal to $1 - 1/e$, respectively. With linear interpolation, F_{sat}^{SI} and F_{sat}^{DI} can be easily calculated from our yields. However, F_{sat}^{TI} cannot be determined since the Ne^{3+} yield is still well below $1 - 1/e$ at the upper end of our field interval.

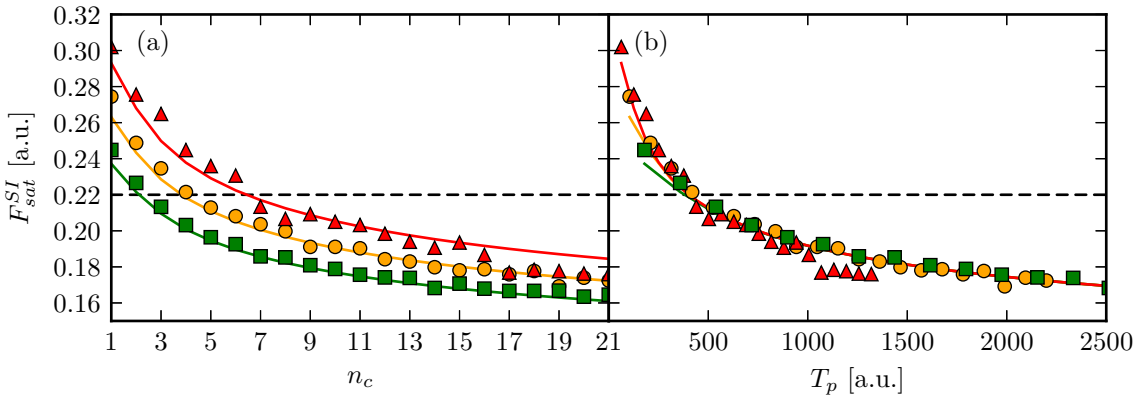

Figure 3.24. Saturation field amplitude of the SAE approximation (3.31) for $\omega_0 = 0.06$ a.u. (circles), $\omega_0 = 0.1$ a.u. (triangles) and $\omega_0 = 0.035$ a.u. (squares) as a function of (a) the number of field cycles and (b) the pulse duration. The static OBI field amplitude of single ionization is indicated by the horizontal dashed line. The colored curves are the predictions of the ADK formula with $n_{01}^* = 1.147 \cdot (2E_I)^{-1/2} = 1.12 \cdot (-2E_0^{SAE})^{-1/2}$.

The saturation field amplitudes of single and double ionization for the pulse parameters of this work are collected in Table 3.5. For the five- and seven-cycle pulse with $\omega_0 = 0.06$ a.u., F_{sat}^{DI} might be a little smaller since the Ne^{2+} yields for long pulses and large field amplitudes are not physically converged on the chosen grid, i.e. too small (see Section 3.5.1 and Fig. 3.19). Nevertheless, F_{sat}^{SI} and F_{sat}^{DI} are in good agreement with the values determined from the SAE-based yields P_1^{SAE} and P_{SS} for which physical convergence was ensured. Most importantly, the saturation field amplitudes decrease with decreasing frequency and increasing pulse duration. These trends are in agreement with various experiments (see e.g. L'Huillier *et al.* (1983a); Mainfray and Manus (1991)) and follow directly from the definitions (3.7). Finally, we note that the ratio of $F_{sat}^{DI}/F_{sat}^{SI}$ is always close to 1.8, indicative of a scaling relation. Therefore, it is sufficient to consider single ionization in the following.

To study how F_{sat}^{SI} varies with n_c and ω_0, we calculate the F_0-dependent single ionization yields of the SAE Hamiltonian (3.31) for $1 \leq n_c \leq 21$ and three frequencies. The corresponding saturation field amplitudes are shown in Fig. 3.24a as a function of n_c. For all frequencies, F_{sat}^{SI} decreases with increasing n_c. The non-monotonicity of this decrease, especially for large n_c and large ω_0, is a result of wave packet interference and resonances which disturb the monotonicity of the SAE yield curve near saturation. A scaling of F_{sat}^{SI} with ω_0 or n_c is not apparent, not even in a (semi)logarithmic plot. However, if F_{sat}^{SI} is plotted as a function of the pulse duration $T_p = 2\pi n_c/\omega_0$ (Fig. 3.24b), the curves for the three frequencies essentially collapse onto a single curve, revealing that F_{sat}^{SI} is mainly determined by the ratio n_c/ω_0. The reason for this can be inferred from the definition (3.7a): If the pulse envelope was equal to one, both ω_0 and n_c could be scaled out of the integral and F_{sat}^{SI} would be constant for constant n_c/ω_0. For our trigonometric envelope, this scaling is approximately preserved since the ionization rate is largest near the center of the pulse where the envelope does not vary much.

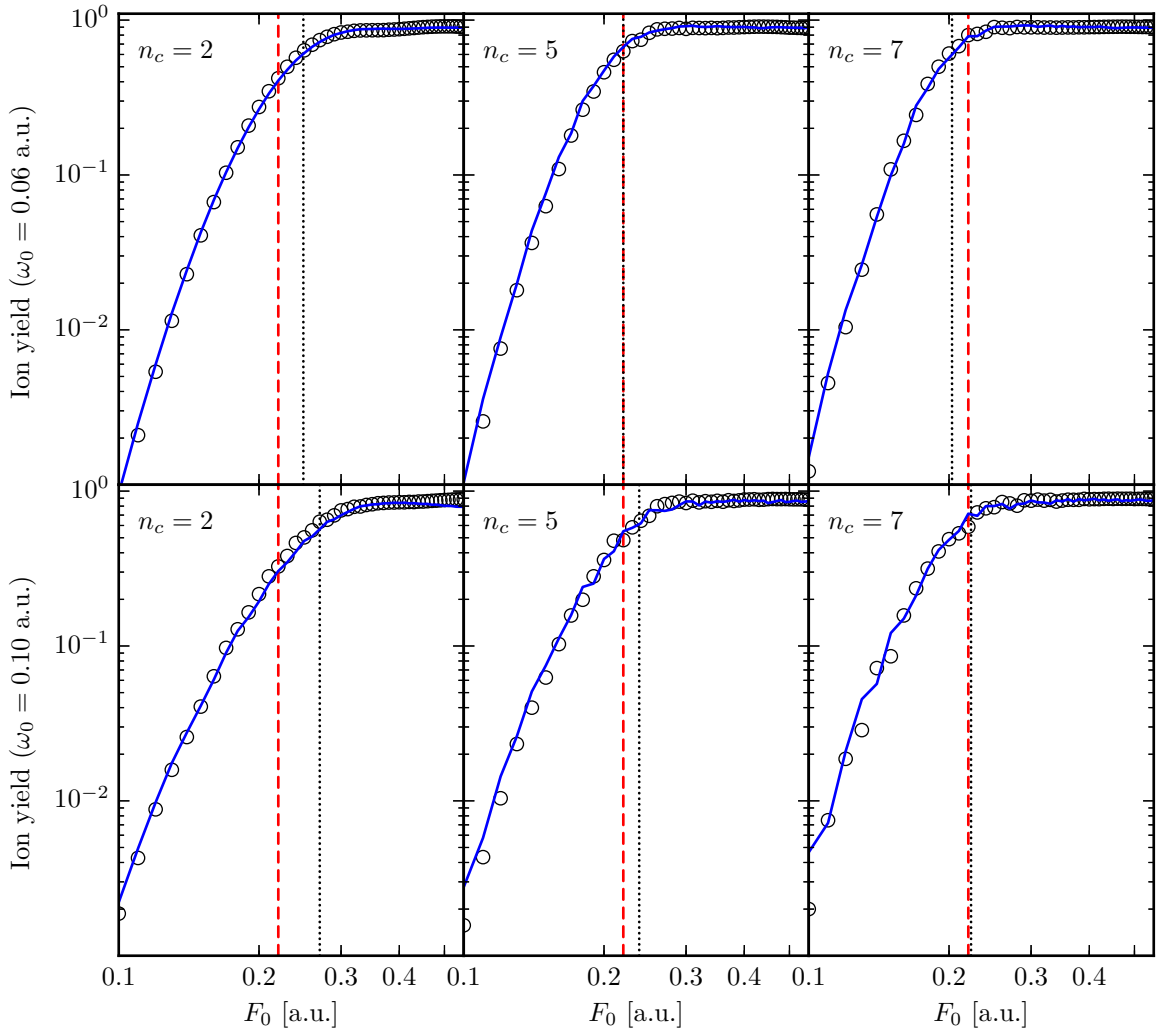

Figure 3.25. Total ion yields for the frequencies and numbers of field cycles used in this work (circles), compared to the SAE single ionization yields (blue curves). The static OBI field amplitude of single ionization from the neutral atom ($F_{OBI}^{SI} = 0.22$ a.u.) is indicated by the dashed red line while the dotted black lines indicate the respective saturation field amplitudes of single ionization.

Now we connect OBI and saturation. Intuitively, one expects that once classical single ionization, i.e. OBI, becomes possible, the ground state population is rapidly depleted and the single ionization yield saturates. Therefore, F_{OBI}^{SI} and F_{sat}^{SI} should be similar and scale with E_0 and Z in a similar way. These expectations are confirmed by Table 3.5 and Fig. 3.25, but not by Fig. 3.24 where the pulse duration extends to much larger values. To explain this, we consider the definition of F_{sat}^{SI} from Section 3.1,

$$\int_0^{T_p} W_0(F_{sat}^{SI} f(t))\mathrm{d}t = 1 \tag{3.61}$$

where $F_{sat}^{SI} f(t) = F(t)$ is the time-dependent laser pulse with duration T_p and W_0 is the single ionization rate, containing contributions from both OBI and tunnel ionization. We discuss two extreme cases. If T_p is very small, the ionization rate (and therefore F_{sat}^{SI}) must be large in order to make the integral equal to one. This means that the single ionization saddle energy will be below the ground state energy for a large fraction of the pulse duration. As a consequence, OBI can contribute significantly to the single ionization yield and we have $F_{sat}^{SI} > F_{OBI}^{SI}$. If T_p is very large, OBI is not needed to achieve saturation – the field amplitude must only be large enough so that the tunneling contributions of the n_c field cycles add up to one in (3.61). The larger T_p, the smaller the contribution of each field cycle can be, implying that F_{sat}^{SI} decreases to zero as $T_p \to \infty$. Therefore, $F_{sat}^{SI} < F_{OBI}^{SI}$ for very long pulses. Clearly, it depends on F_{OBI}^{SI} (i.e. the ground state energy) and the ionization rate what a "very short" or a "very long" pulse is. For our ground state energies (Table 3.4) and frequencies, seven cycles are not enough to push the saturation field amplitude well below the OBI field amplitude. This requires a considerably longer pulse (Fig. 3.24).

By replacing the unknown ionization rate W_0 in (3.61) with the ADK formula, we can quantitatively confirm the above line of argument and fit the data points in Fig. 3.24. This is done as follows. First, we select a frequency and a number of field cycles for which saturation is solely due to tunneling ($F_{sat}^{SI} < F_{OBI}^{SI}$), e.g. $\omega_0 = 0.06$ a.u. and $n_c = 10$. Next, we determine the correction of the effective quantum number n_{01}^* in the ADK formula such that F_{sat}^{SI} is reproduced. We obtain $n_{01}^* = 1.147 \cdot (2E_I)^{-1/2}$ which is slightly smaller than the value used for the fit in the previous section. Finally, we calculate F_{sat}^{SI} for all other ω_0 and n_c by finding the zero of the function

$$\begin{aligned} g(F_0) &= 1 - \int_0^{T_p} W_{01}^{ADK}(F_0 f(t))\mathrm{d}t \\ &= 1 - \mathcal{A}(n_{01}^*) \int_0^{T_p} (F_0|f(t)|)^{\frac{3}{2}-2n_{01}^*} \mathrm{e}^{-\frac{\mathcal{B}(n_{01}^*)}{F_0|f(t)|}} \mathrm{d}t \end{aligned} \tag{3.62}$$

where the constants $\mathcal{A}(n_{01}^*)$ and $\mathcal{B}(n_{01}^*)$ can be found in equation (3.8). The resulting saturation field amplitudes, shown in Fig. 3.24 as colored curves, agree remarkably well with the quantum results. The deviations can be explained by the restrictions of the ADK formula: For the largest frequency, resonant enhancements and multiphoton effects cannot be neglected in the ion yield, especially for long pulses. Therefore, the

agreement of the saturation field amplitudes with a prediction based on pure tunneling is less good. Moreover, the ADK formula is known to overestimate the ionization rate in the OBI regime which is why the ADK saturation field amplitudes for small n_c are notably smaller than the quantum results. This can be seen as an indirect proof of the importance of OBI for saturation in this regime. The above restrictions notwithstanding, the quality of the ADK prediction is entirely sufficient, given the finite F_0-resolution of our numerical ion yields (0.01 a.u.).

Finally, we can use the ADK prediction to estimate the asymptotic behavior of F_{sat}^{SI}. For large T_p, the modulation of the pulse envelope becomes negligible near the center of the pulse and we have

$$\begin{aligned} 1 &= \mathcal{A}(n_{01}^*) \int_0^{T_p} (F_{sat}^{SI}|f(t)|)^{\frac{3}{2}-2n_{01}^*} \mathrm{e}^{-\frac{\mathcal{B}(n_{01}^*)}{F_{sat}^{SI}|f(t)|}} \mathrm{d}t \\ &\approx \mathcal{A}(n_{01}^*) \frac{T_p}{2\pi} \int_0^{2\pi} (F_{sat}^{SI}|\cos(t')|)^{\frac{3}{2}-2n_{01}^*} \mathrm{e}^{-\frac{\mathcal{B}(n_{01}^*)}{F_{sat}^{SI}|\cos(t')|}} \mathrm{d}t' \end{aligned} \tag{3.63}$$

for saturation. The right-hand side of this equation can only be one if the integral decreases as $1/T_p$. Since the integration limits are constant, this implies that F_{sat}^{SI} decreases with increasing T_p. However, if F_{sat}^{SI} decreases, the behavior of the integrand is dominated by the exponential and the peaks at the extrema of $\cos(t')$ become sharper. Therefore, in the limit $T_p \to \infty$, we have

$$\frac{1}{T_p} \propto \int_0^{2\pi} (F_{sat}^{SI}|\cos(t')|)^{\frac{3}{2}-2n_{01}^*} \mathrm{e}^{-\frac{\mathcal{B}(n_{01}^*)}{F_{sat}^{SI}|\cos(t')|}} \mathrm{d}t' \propto \mathrm{e}^{-\frac{B(n_{01}^*)}{F_{sat}^{SI}}} \tag{3.64}$$

or

$$F_{sat}^{SI} \propto \frac{1}{\ln(\text{const.} \cdot T_p)}. \tag{3.65}$$

This logarithmically slow decrease of the saturation field amplitude with T_p is already apparent from Fig. 3.24. For example, we have $F_{sat}^{SI} = 0.20$ a.u. for $\omega_0 = 0.06$ a.u. and $n_c = 7$. To decrease F_{sat}^{SI} by a factor of two, a pulse with $n_c = 2723$ cycles is needed!

3.6. Results: Rescattering analysis

In Section 3.4 and 3.5, we frequently observed regimes of weak F_0-dependence ("plateaus") in the yield ratios Ne^{2+}/Ne^+, Ne^{3+}/Ne^+ and Ne^{3+}/Ne^{2+} which originate from the nonsequential ionization pathways 0-2, 0-3 and 0-1-3, respectively. The plateaus disappear near saturation of the denominator yield, indicating a change of the prevalent ionization pathway to a more stepwise one (0-1-2, 0-2-3 and 0-1-2-3, respectively). However, it is still unclear what the onset of a plateau signifies, how the occurrence and magnitude of the plateau is influenced by the frequency and pulse duration of the laser and, most importantly, why the nonsequential ionization yield and the yield of the precursor ion are nearly proportional in the plateau regime.

To answer these questions, one has to find approximate expressions for the nonsequential ionization yields. The ultimate goal (with respect to computational cost and interpretational simplicity) would be to express them in terms of one-electron yields, analogous to the product yields of the previous sections. This seems hopeless since the simultaneous ionization step contained in each nonsequential pathway hinges on the energy transfer between a recolliding electron and the residual one(s) for which the electron repulsion is vital. Nevertheless, the first step of the rescattering mechanism is single ionization of an independent electron. If one could determine the fraction of the singly-ionizing electrons that is rescattered and the time and energy constraints of the recollision, it might be possible to estimate the nonsequential yields entirely from single ionization.

In this section, some steps in this direction will be taken. First, we study classical rescattering of a one-dimensional electron in the laser field (2.28) and investigate the distribution of recollision times and energies for different pulse durations. Afterwards, we use this information to calculate the classical recollision thresholds of our model, i.e. the field amplitudes below which classical ionization of one or two electrons by the recolliding electron (ROBI) is energetically forbidden. Finally, we propose a splitting of the probability flux from the neutral to the singly-ionized region to determine the rescattering yield (and therefore the yields of 0-2 and 0-3).

3.6.1. Simple man's model

Consider an atom exposed to a linearly polarized laser field $F(t)$. According to the rescattering mechanism, an electron wave packet tunnels through the potential barrier at a time t_0 with a probability $p_{tun}(t_0)$. The wave packet is then accelerated in the laser field and finally driven back towards the nucleus where it can recollide inelastically, thus transferring some of its energy gained in the laser field to the other electrons. This recollision energy and the recollision time can be estimated from the so-called "simple man's model" which treats the tunneled electron as a one-dimensional classical point charge and neglects all Coulomb interactions (Corkum *et al.*, 1989; Krause *et al.*, 1992; Corkum, 1993; Kulander *et al.*, 1995).

The simple man's model is fully specified by Newton's equation

$$\ddot{x}(t) = -F(t) \tag{3.66a}$$

with appropriate initial conditions for the position x and the velocity $\dot{x}$ of the tunneled electron. For non-negligible tunneling probabilities $p_{tun}(t_0)$, the exit position $x(t_0)$ outside the barrier is small compared to the quiver radius F_0/ω_0^2 of the electron in the laser field (Delone and Krainov, 1998), so we can set $x(t_0) = 0$. A similar argument justifies the choice $\dot{x}(t_0) = 0$ (Kulander *et al.*, 1995). With these initial conditions, the velocity and position of the electron at time t are given by

$$\dot{x}(t) = A(t) - A(t_0) \tag{3.66b}$$

and

$$x(t) = \int_{t_0}^{t} A(t')\mathrm{d}t' - A(t_0)(t - t_0), \tag{3.66c}$$

respectively, where $A(t) = -\int_{-\infty}^{t} F(t')\mathrm{d}t'$ is the vector potential of the field. According to (3.66c), the tunneled electron oscillates in the laser field. As a result, the electron may recollide with the nucleus ($x = 0$) once or multiple times, depending on the tunneling time t_0 and the pulse duration. The recollision time t_{rec} is defined as the time of the first recollision, i.e.

$$t_{rec}(t_0) = \min\{t > t_0 | x(t) = 0\}. \tag{3.67}$$

The recollision energy is

$$E_{rec}(t_0) = \frac{1}{2}\dot{x}^2(t_{rec}(t_0)) = \frac{1}{2}\left[A(t_{rec}(t_0)) - A(t_0)\right]^2. \tag{3.68}$$

The probability for a recollision of the electron at $t_{rec}(t_0)$ is determined by the tunneling probability $p_{tun}(t_0)$. Therefore, by integrating Newton's equation (3.66a) for a uniform distribution of tunneling times t_0, singling out the recolliding trajectories and weighting (t_{rec}, E_{rec}) with $p_{tun}(t_0)$, one can obtain a probability distribution $P(t_{rec}, E_{rec})$. We calculate this distribution for two fields $F(t)$, namely the pulse (2.28) with pulse duration $T_p = 2\pi n_c/\omega_0$ and vector potential (2.29) and the periodic field

$$F(t) = F_0 \cos(\omega_0 t) \tag{3.69}$$

with period $T = 2\pi/\omega_0$ and vector potential

$$A(t) = -F_0 \sin(\omega_0 t)/\omega_0. \tag{3.70}$$

The tunneling probability is approximated by the ADK formula (3.8) using the ionization energy of the SAE approximation, i.e.

$$p_{tun}(t_0) = W_{01}^{ADK}(F(t_0))\Delta t_0 = C \cdot |F(t_0)|^{3/2-2n_{01}^*} \exp\left(-\frac{2}{3n_{01}^{*3}|F(t_0)|}\right) \tag{3.71}$$

with $n_{01}^* = 1/\sqrt{-2E_0^{SAE}} = 0.78$. Since we are only interested in relative probabilities, the constant C is set to one.

Since both the pulse and the periodic field are of the form $F(t) = F_0 f(\omega_0 t)$, ω_0 and F_0 can be eliminated from (3.66) - (3.68) by choosing new scales for time, position and velocity. With the substitution rule, ω_0 can also be scaled out of $p_{tun}(t_0)$ and $P(t_{rec}, E_{rec})$. Therefore, we set $\omega_0 = 1$ a.u. for the calculations. F_0, on the other hand, cannot be eliminated from $p_{tun}(t_0)$. For the time being, we set $F_0 = 0.15$ a.u. Although ω_0 and F_0 are fixed for the calculations, we will include them in all following equations in order to keep the discussion as general as possible.

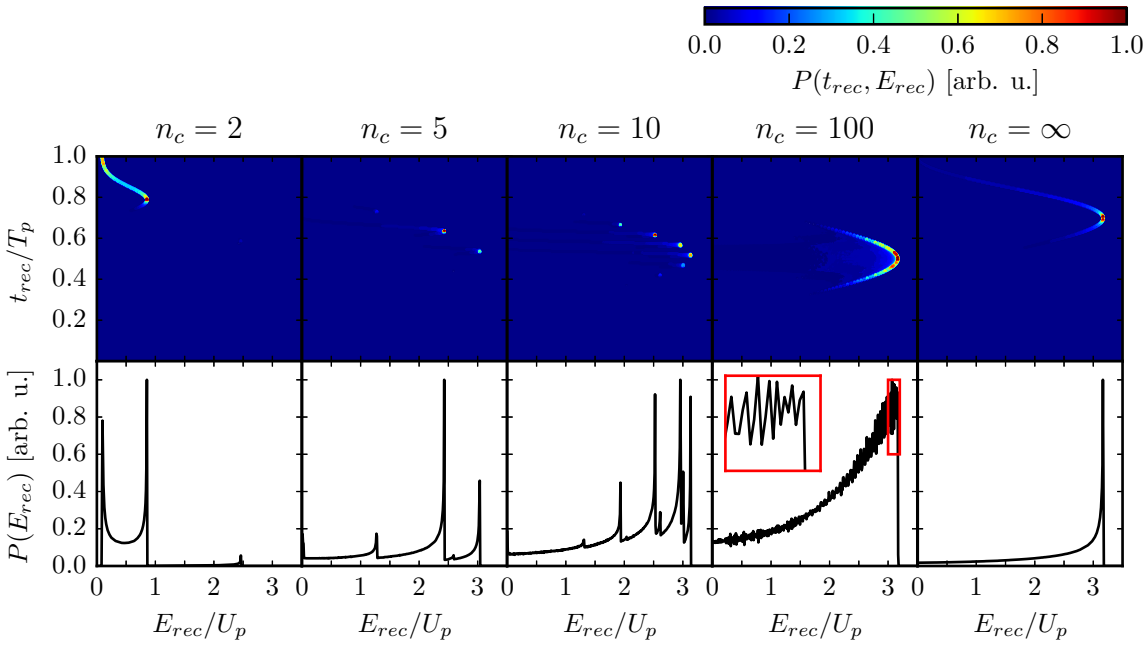

Figure 3.26. First row: Distribution of recollision times and energies $P(t_{rec}, E_{rec})$ for the pulse (2.28) with different numbers of field cycles n_c and for a periodic field ("$n_c = \infty$"). For the periodic field, the recollision time is plotted in units of $T = 2\pi/\omega_0$. The distributions were obtained by integrating Newton's equation (3.66a) for equally spaced tunneling times t_0 with initial conditions $x(t_0) = \dot{x}(t_0) = 0$ and weighting each recolliding trajectory with the ADK tunneling probability. The number of calculated trajectories was 10^6 (with $t_0 \in [0, T_p]$) for the pulses and 10^5 (with $t_0 \in [0, T/2]$) for the periodic field. Second row: Distribution of recollision energies $P(E_{rec}) = \int P(t_{rec}, E_{rec}) \mathrm{d}t_{rec}$.

For the pulse, the only parameter left to specify is the number of field cycles n_c which determines the pulse duration $T_p = 2\pi n_c/\omega_0$. We consider $1 \leq n_c \leq 10$ and, as an example of a very long pulse, $n_c = 100$. For each pulse duration, we integrate (3.66a) for $N = 10^6$ equally spaced tunneling times from the interval $[0, T_p]$[14]. If $x(t_{rec}) = 0$ for some time $t_0 < t_{rec} \leq T_p$, the integration is stopped and (t_{rec}, E_{rec}) and $p_{tun}(t_0)$ are recorded. Otherwise, the trajectory is discarded. After all trajectories have been calculated, the (t_{rec}, E_{rec}) space is binned ($\omega_0 \Delta t_{rec} = 0.005, \Delta E_{rec}/U_p = 0.008$) and the tunneling weights are collected in a two-dimensional histogram. For the periodic field, we calculate the distribution in the same way. However, due to the periodicity, it is sufficient to consider tunneling times from the first half cycle, i.e. $t_0 \in [0, T/2]$. The number of tunneling times is $N = 10^5$, i.e. the tunneling time step is equal to that of the five-cycle pulse ($\omega_0 \Delta t_0 = 3 \cdot 10^{-5}$).

In Fig. 3.26, we show the distribution of recollision times and energies $P(t_{rec}, E_{rec})$ and the distribution of recollision energies $P(E_{rec}) = \int P(t_{rec}, E_{rec}) \mathrm{d}t_{rec}$ for the pulses with $n_c = 2, 5, 10, 100$ and for the periodic field ("$n_c = \infty$"). We first discuss the results

[14]The tunneling time step $\Delta t_0 = T_p/N$ is a function of n_c, but even for the pulse with 100 cycles, it is small enough to ensure good statistics.

for the periodic case. The distribution $P(t_{rec}, E_{rec})$ has a maximum at $t_{rec} = 0.7T$, $E_{rec} = 3.17U_p$. This energy also represents the maximum recollision energy for the periodic field, i.e. $P(E_{rec})$ has a cut-off at $3.17U_p$. At the same energy, $P(E_{rec})$ exhibits a sharp asymmetric peak (a so-called caustic). This result was first obtained by Corkum (1993) and can be explained as follows. The probability of finding an electron with a recollision energy in the interval $[E_{rec}, E_{rec} + \mathrm{d}E_{rec}]$ is proportional to the tunneling probability in the time interval $[t_0, t_0 + \mathrm{d}t_0]$ (Gallagher, 1988), i.e.

$$P(E_{rec})\mathrm{d}E_{rec} \propto W_{01}^{ADK}(t_0)\mathrm{d}t_0, \tag{3.72}$$

or

$$P(E_{rec}) \propto W_{01}^{ADK}(t_0(E_{rec})) \left| \frac{\mathrm{d}E_{rec}}{\mathrm{d}t_0} \right|^{-1}. \tag{3.73}$$

Therefore, if $E_{rec}(t_0)$ has a local maximum ($\mathrm{d}E_{rec}/\mathrm{d}t_0 = 0$), $P(E_{rec})$ exhibits a caustic at the corresponding energy. As illustrated in Fig. 3.27a, the caustic at $E_{rec} = 3.17U_p$ results from electrons tunneling near $t_0 = (0.05 + n/2)T$ ($n \in \mathbb{Z}$), i.e. shortly after an extremum of the field (Corkum, 1993; Delone and Krainov, 1998). These electrons recollide near $t_{rec} = (0.7 + n/2)T$, i.e. shortly before the second next zero-crossing of the field. This explains the location of the maximum in $P(t_{rec}, E_{rec})$.

Now we discuss the distributions of the pulses. Until now, the recollision properties of pulses with a single-figure number of field cycles have received little attention in the literature since such short pulses were not available experimentally. However, this has changed in the last few years (Bergues *et al.*, 2012; Camus *et al.*, 2012; Kübel *et al.*, 2014, 2016). We will show that the features of the pulse distributions $P(t_{rec}, E_{rec})$ (first four columns of Fig. 3.26) can be understood in terms of the periodic result modulated with the pulse envelope. As an example, consider the five-cycle pulse whose recollision energy $E_{rec}(t_0)$ is shown in Fig. 3.27b. Close to every local maximum, $E_{rec}(t_0)$ resembles the periodic result. The energies of the local maxima of the recollision energy approximately follow the pulse envelope shifted by a half cycle. According to (3.73), every maximum of $E_{rec}(t_0)$ produces a caustic in $P(E_{rec})$. However, some of them are suppressed due to the negligible ADK tunneling probability of the respective tunneling time. Since the maxima in $E_{rec}(t_0)$ are separated by about a half cycle, the recollision times in Fig. 3.26 are separated by this interval as well. Note that this result is somewhat obscured since t_{rec} is plotted in units of the pulse duration (equal to $2n_c$ half cycles).

For the case of the periodic field, the most probable recollision energy E_{rec}^{mp} (the energy of the global maximum of $P(E_{rec})$), equals the maximum recollision energy $E_{rec}^{max} = 3.17U_p$ (the cut-off energy of $P(E_{rec})$). For the pulses, in contrast, we find from Fig. 3.26 that $E_{rec}^{mp} < E_{rec}^{max} < 3.17U_p$. This can be explained as follows. An electron which produces a local maximum in $E_{rec}(t_0)$ recollides roughly a half cycle after tunneling out,

$$t_{rec}(t_0) \approx t_0 + \frac{T}{2}. \tag{3.74}$$

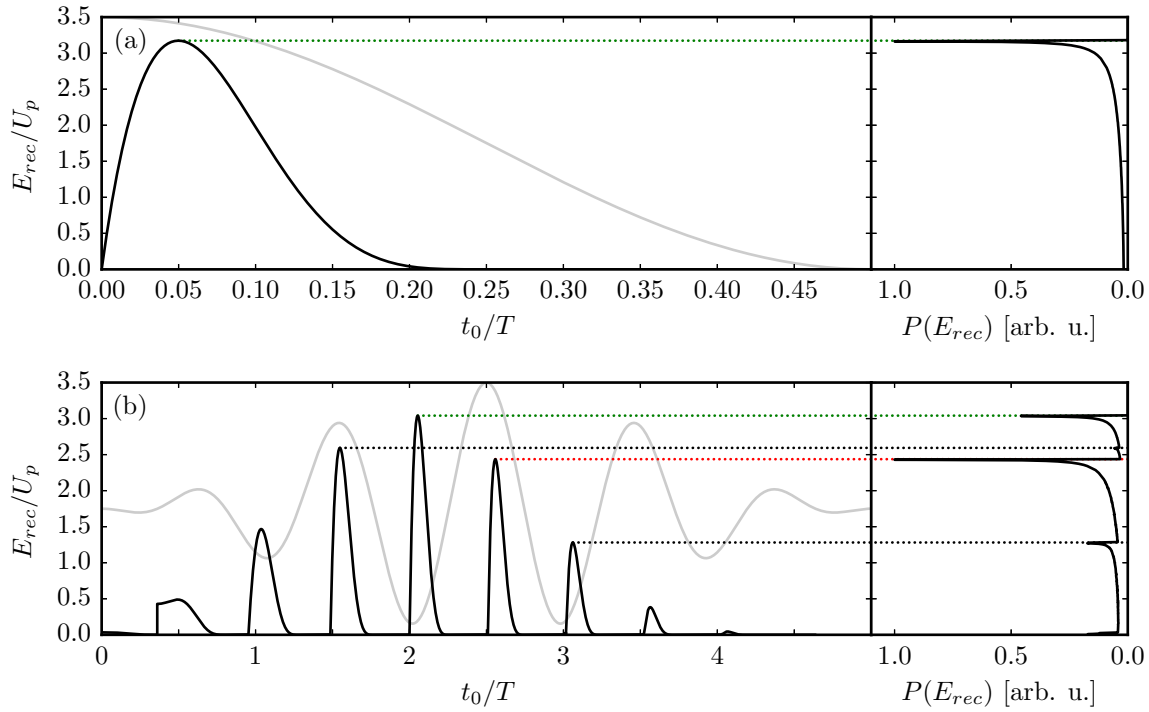

Figure 3.27. (a) Recollision energy as a function of the tunneling time (left, black curve) for the periodic field $F(t) = F_0 \cos(\omega_0 t)$ with $T = 2\pi/\omega_0$ (left, gray curve). Electrons tunneling at $t_0 = 0.05T + nT/2$ ($n \in \mathbb{Z}$), i.e. shortly after an extremum of the field, recollide with the maximum energy of $E_{rec} = 3.17U_p$ (dotted green line). The local maximum of $E_{rec}(t_0)$ produces a caustic in the distribution of recollision energies $P(E_{rec})$ (right). (b) Same as (a), but for the five-cycle pulse. Every local maximum of $E_{rec}(t_0)$ produces a caustic in $P(E_{rec})$ at the corresponding energy (dotted black lines), but some of them are suppressed by the negligible ADK tunneling probability. The maximum recollision energy (dotted green line) is reached if the electron tunnels near the minimum preceding the global maximum of the field. For tunneling shortly after the global maximum, the most probable recollision energy (dotted red line) is reached.

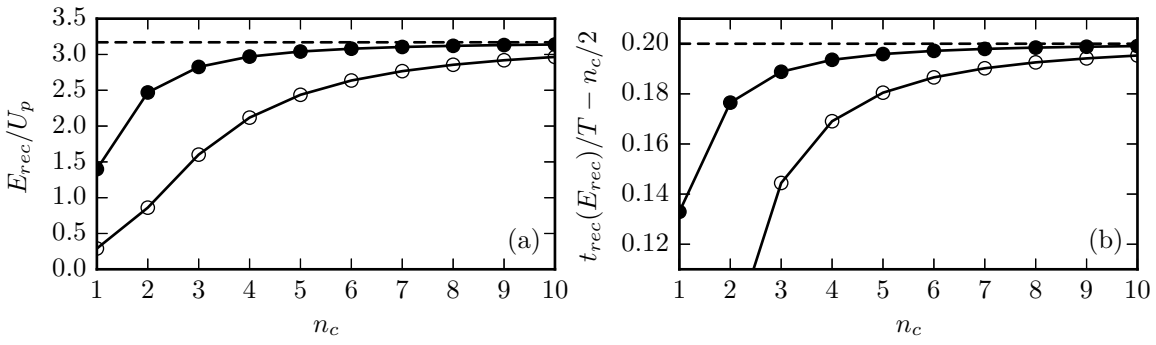

Figure 3.28. (a) Maximum recollision energy E_{rec}^{max} (solid markers) and most probable recollision energy E_{rec}^{mp} (empty markers) for the laser pulse (2.28). (b) Corresponding recollision times $t_{rec}(E_{rec}^{max})$ and $t_{rec}(E_{rec}^{mp})$ as a function of the number of field cycles. To ease comparison, $t_{rec}(E_{rec}^{mp})$ was shifted down by $T/2$. The results for the periodic field ($E_{rec}^{max} = E_{rec}^{mp} = 3.17U_p$ and $t_{rec}(E_{rec}^{max}) = 0.2T$) are indicated by the dashed lines.

If the electron recollides while the pulse envelope is still rising, i.e.

$$t_{rec}(t_0) \leq \frac{T_p}{2} \Leftrightarrow t_0 \leq \frac{T_p}{2} - \frac{T}{2}, \tag{3.75}$$

the energies $E_{rec}(t_0)$ of the local maxima increase (see Fig. 3.27b). Therefore, the maximum recollision energy E_{rec}^{max} is reached if the electron tunnels near the minimum preceding the global field maximum ($t_0 \approx T_p/2 - T/2$). The tunneling probability has its global maximum at the global maximum of the field, so the recollision energy corresponding to an electron tunneling near $t_0 = T_p/2$ receives the highest weight in $P(E_{rec})$ and is therefore the most probable one. However, the pulse envelope has decreased when the electron recollides, so the recollision energy is smaller than E_{rec}^{max}. Analogously, the energies of the later maxima in $E_{rec}(t_0)$ decrease.

When n_c is increased, the pulse envelope approaches one in the vicinity of the global maximum, i.e. the amplitude of the maximum and the surrounding extrema become comparable and the pulse locally resembles the periodic field. As a consequence, E_{rec}^{mp} converges to E_{rec}^{max} and E_{rec}^{max} converges to $3.17U_p$. This is shown in Fig. 3.28a and Table 3.6. In experiments, one typically has $n_c \gg 10$ (see Table 3.2), so the assumption $E_{rec}^{max} = 3.17U_p$ is well justified there. For the recollision time associated with E_{rec}^{max}, we expect $t_{rec}(E_{rec}^{max}) = (0.5 + 0.2/n_c)T_p = (0.5n_c + 0.2)T$ in the limit of large n_c, based on the periodic case where $t_{rec}(E_{rec}^{max}) = (0.5 + 0.2)T$. This expectation is confirmed in Fig. 3.28b where we show $t_{rec}(E_{rec}^{max})/T - n_c/2$ as a function of n_c (solid markers). In Fig. 3.26, the convergence cannot be observed since t_{rec} is plotted in units of T_p for the pulses and in units of T for the periodic field. The recollision time associated with E_{rec}^{mp}, i.e. $t_{rec}(E_{rec}^{mp})$ (empty markers in Fig. 3.28b), converges to $t_{rec}(E_{rec}^{max}) + T/2$ for large n_c. The additional half cycle is subtracted in the figure to ease comparison. In view of the Fig. 3.28, the notion of the periodic field as a pulse with an infinite number of field cycles is justified, both with respect to the recollision energy and the recollision time.

n_c	E_{rec}^{max}/U_p	E_{rec}^{mp}/U_p	$t_{rec}(E_{rec}^{max})/T$ $-n_c/2$	$t_{rec}(E_{rec}^{mp})/T$ $-n_c/2$
1	1.399	0.290	0.133	0.419
2	2.469	0.861	0.176	0.581
3	2.826	1.601	0.189	0.644
4	2.970	2.118	0.194	0.669
5	3.041	2.437	0.196	0.680
6	3.080	2.636	0.197	0.687
7	3.105	2.767	0.198	0.690
8	3.120	2.856	0.198	0.693
9	3.131	2.919	0.199	0.694
10	3.139	2.965	0.199	0.695
⋮	⋮	⋮	⋮	⋮
100	3.173	3.171	0.200	0.700
⋮	⋮	⋮	⋮	⋮
∞	3.173	3.173	0.200	0.700

Table 3.6. Maximum recollision energy E_{rec}^{max}, most probable recollision energy E_{rec}^{mp} and corresponding recollision times for the laser pulse (2.28) as a function of the number of field cycles. $n_c = \infty$ corresponds to the periodic field.

In the above trajectory calculations, we discarded all electrons which do not return to the nucleus before the end of the pulse. However, it can be seen from Fig. 3.26 that, for $n_c = 2$, a certain fraction of the electrons recollides at a later time, albeit with negligible kinetic energy. This can be understood as follows. If the position of an electron at the end of the pulse $x(T_p)$ is positive and its velocity $\dot{x}(T_p)$ negative (or vice versa), the electron will recollide at

$$t_{rec} = T_p + \left| \frac{x(T_p)}{\dot{x}(T_p)} \right| \tag{3.76}$$

with kinetic energy

$$E_{rec} = \frac{1}{2}\dot{x}^2(t_{rec}) = \frac{1}{2}\dot{x}^2(T_p) = \frac{1}{2}A^2(t_0). \tag{3.77}$$

The only trajectories with significant tunneling probability start near an extremum of the field, i.e. a turning point of the vector potential. For $n_c = 2$, there are three turning points with corresponding recollision energies $0.03U_p$, $0.27U_p$ and 0. As n_c is increased, the turning points approach the zeros of the vector potential so that $E_{rec} \to 0$ and $t_{rec} \to \infty$. At the same time, the weight of the trajectories increases due to the increasing tunneling probability. Therefore, inclusion of the "late electrons" would only lead to a higher peak near $E_{rec} = 0$ in $P(E_{rec})$. However, for the discussion of high-energy recollision events, these trajectories are irrelevant which is why we left them out in the first place.

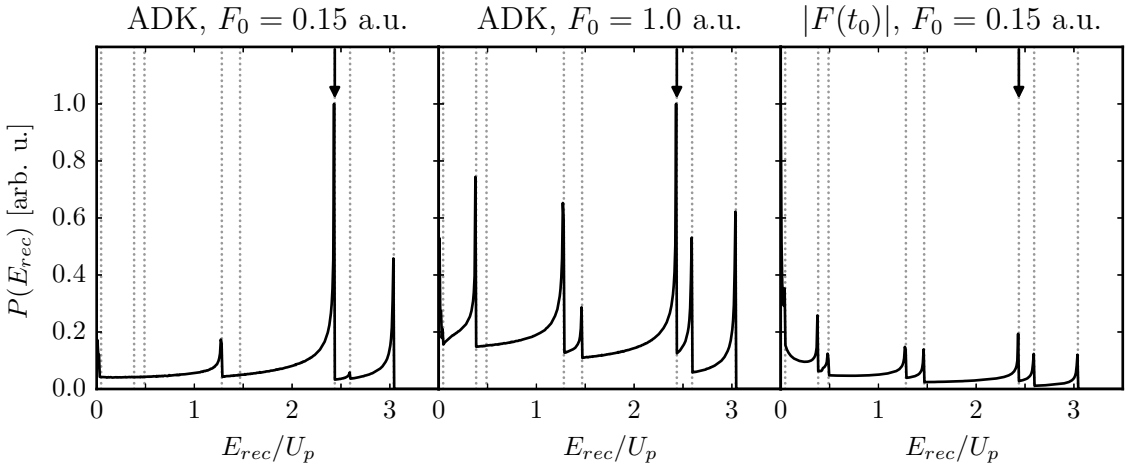

Figure 3.29. Distribution of recollision energies for the five-cycle pulse, obtained with different tunneling probabilities and field amplitudes. The energies corresponding to the maxima of $E_{rec}(t_0)$ are indicated by the dotted lines. The arrow indicates the energy of the maximum in the interval $[T_p/2, T_p/2 + T/2]$.

To conclude this section, we note that the above results are rather insensitive to the choice of the tunneling probability $p_{tun}(t_0)$, provided that it increases monotonically with $|F(t_0)|$ and decays to zero rapidly enough as $|F(t_0)| \to 0$. This is illustrated in Fig. 3.29 where we show $P(E_{rec})$ for the five-cycle pulse, weighted with the ADK probability for two different field amplitudes (left and middle) and weighted with $|F(t_0)|$ (right). The positions of the caustics are unchanged since the maxima of $E_{rec}(t_0)$ (Fig. 3.27b) are independent of $p_{tun}(t_0)$. In particular, the cut-off energy E_{rec}^{max} of the distribution is well-defined. However, we see that $p_{tun}(t_0)$ strongly influences the relative heights of the caustics, i.e. the relative probabilities of the recollision energies. This raises the question whether defining the most probable recollision energy E_{rec}^{mp} as the energy of the highest peak in $P(E_{rec})$ is justified. In the above discussion, the occurrence of a most probable recollision energy was traced back to the shape of the pulse, especially to the fact that the global maximum of any tunneling probability must coincide with the global field maximum ($t_0 = T_p/2$). If $p_{tun}(t_0)$ vanishes sufficiently rapidly for $|F(t_0)| \to 0$, the effect of the decreasing pulse envelope is amplified in $P(E_{rec})$ and the highest peak will be located at the energy of the local maximum of $E_{rec}(t_0)$ in the interval $[T_p/2, T_p/2 + T/2]$ (indicated by the arrow in the figure). This is true for the ADK tunneling probability, but not for the tunneling probability $\propto |F(t_0)|$ where the highest peak is located near $E_{rec} = 0$. However, the last tunneling probability is rather unphysical, so we can conclude that E_{rec}^{mp} is well-defined. Since we know the interval of tunneling times for which E_{rec}^{mp} is reached, we can determine it from $E_{rec}(t_0)$ and resolution issues of the histogram $P(E_{rec})$ do not distort the result.

3.6.2. Influence of the Coulomb potential

To bring the simple man's model closer to a true quantum system, we can introduce a soft-core potential $-1/\sqrt{x^2+\varepsilon^2}$ in (3.66) and set the initial energy of the electron to the quantum mechanical ground state energy E_0. The new equation of motion reads

$$\ddot{x}(t) = -\frac{x(t)}{(x^2(t)+\varepsilon^2)^{3/2}} - F(t). \tag{3.78}$$

For the integration, we use the SAE parameters $\varepsilon^2 = 0.61$ a.u. and $E_0 = -0.82$ a.u. and retain the initial condition $\dot{x}(t_0) = 0$. $x(t_0)$ is set to the exit position of the tunneled electron outside the Coulomb barrier which is a solution of the equation

$$-\frac{1}{\sqrt{x^2(t_0)+\varepsilon^2}} - F(t_0)x(t_0) = E_0. \tag{3.79}$$

The recollision energy now takes the form

$$E_{rec} = \frac{\dot{x}^2(t_{rec})}{2} - \frac{1}{\sqrt{x^2(t_{rec})+\varepsilon^2}} - F(t_{rec})x(t_{rec}) = \frac{\dot{x}^2(t_{rec})}{2} - \frac{1}{\varepsilon}. \tag{3.80}$$

The distribution of recollision times and energies is calculated in the same way as in the previous section. Since the electron starts at a certain distance from the nucleus, the return to $x = 0$ can take a long time, especially for $F(t_0) \to 0$ where $x(t_0) \to \infty$. For simplicity, we only monitor the trajectories for recollision on the interval $[t_0, t_0 + T]$. Furthermore, we note that neither F_0 nor ω_0 can be scaled out of the equation of motion (3.78). Therefore, the recollision energy does not scale with U_p anymore and each combination of field parameters actually requires a new calculation. Here, we only show the results for $F_0 = 0.15$ and $\omega_0 = 0.06$ a.u., but test calculations with $F_0 = 0.1$ a.u., $F_0 = 0.2$ a.u. and $\omega_0 = 0.1$ a.u. indicate that our conclusions are also valid for other field parameters.

The recollision energy $E_{rec}(t_0)$ for the periodic field (3.69) with $F_0 = 0.15$ a.u. and $\omega_0 = 0.06$ a.u. is shown in Fig. 3.30a. In comparison to Fig. 3.27a, the local maximum of $E_{rec}(t_0)$ associated with the caustic in $P(E_{rec})$ is shifted to smaller t_0 and has a slightly higher energy ($3.3U_p$), in agreement with the result obtained by Kulander *et al.* (1995) for a smaller value of ε^2. Moreover, a second, rather sharp maximum occurs in $E_{rec}(t_0)$ near the zero-crossing of the field. This maximum is solely due to the nonzero initial position of the electron, as illustrated by the dashed red curve which was found by integrating Newton's equation (3.66) without the Coulomb potential, but with the initial position determined by (3.79). An inspection of the trajectories reveals that the maximum is the result of two processes working in opposite directions. On the one hand, if the electron tunnels out just before the field switches its sign ($t_0 \lessapprox T/4$), the initial distance to the nucleus is large, making a recollision within a field cycle very unlikely. On the other hand, such an electron is accelerated towards the nucleus for nearly an entire half cycle and can thus gain a large kinetic energy. At a certain

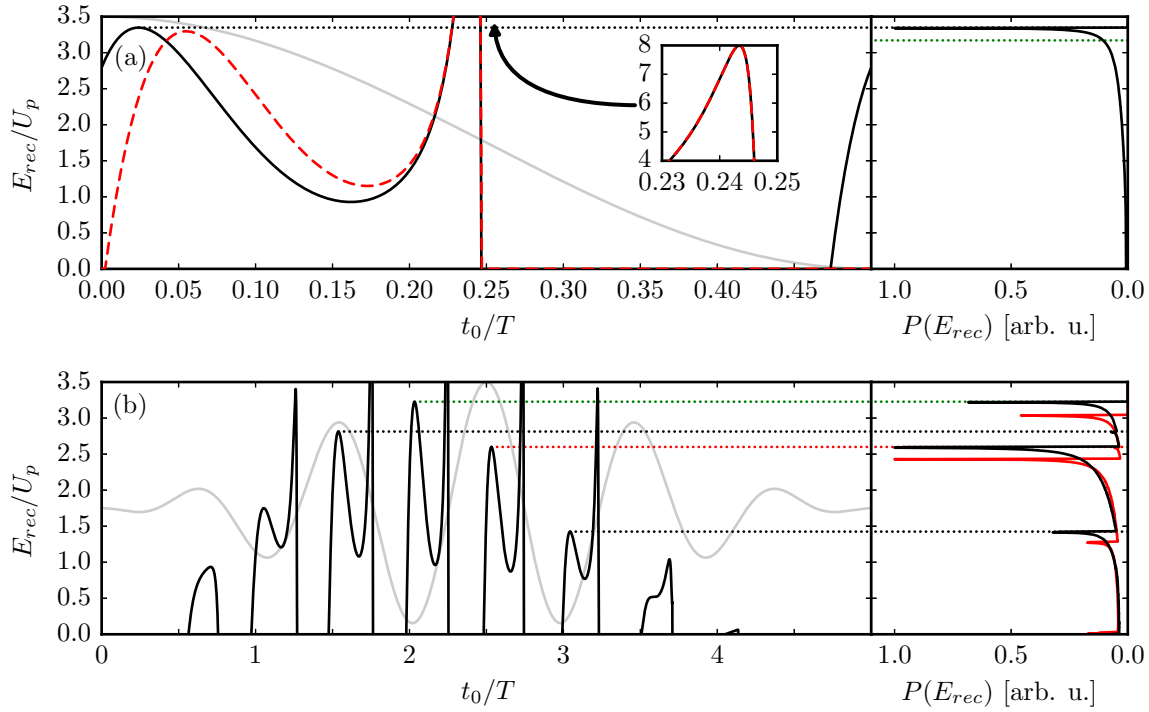

Figure 3.30. (a) Recollision energy as a function of the tunneling time (left, black curve) for the periodic field with $F_0 = 0.15$ a.u., $\omega_0 = 0.06$ a.u. $T = 2\pi/\omega_0$ (left, gray curve) and an additional soft-core Coulomb potential $-1/\sqrt{x^2 + 0.61}$. The electron starts with zero velocity at the exit position outside the Coulomb barrier determined by equation (3.79). If the electron tunnels at $t_0 = 0.02T + nT/2$ ($n \in \mathbb{Z}$), i.e. shortly after an extremum of the field, it recollides with $E_{rec} = 3.3U_p$ (dotted black line) which is slightly larger than the simple man's result $3.17U_p$ (dotted green line). For tunneling right before the zero-crossing of the field, the electron can gain a recollision energy of up to $7.99U_p$ (inset). Due to the time dependence of the tunneling probability, only the first maximum of $E_{rec}(t_0)$ produces a caustic in the distribution of recollision energies $P(E_{rec})$ (right). The dashed red curve is the result of a calculation with the simple man's model using the same initial conditions as above. (b) Same as (a), but for the five-cycle pulse. Every local maximum of $E_{rec}(t_0)$ produces a caustic in $P(E_{rec})$ at the corresponding energy (dotted black lines), but some of them are suppressed by the negligible ADK tunneling probability. The maximum recollision energy (dotted green line) is reached if the electron tunnels near the minimum preceding the global maximum of the field. For tunneling shortly after the global maximum, the most probable recollision energy (dotted red line) is reached. $P(E_{rec})$ is compared to the result of the simple man's model (red curve).

tunneling time t_0^*, the electron reaches the nucleus *exactly* a half cycle after tunneling out,

$$t_{rec} = t_0^* + \frac{T}{2}, \tag{3.81}$$

i.e. entirely without being decelerated by the field. In the simple man's model, the recollision energy (3.68) of this electron is

$$E_{rec}(t_0^*) = \frac{F_0^2}{2\omega_0^2}\left[\sin(\omega_0 t_{rec}) - \sin(\omega_0 t_0^*)\right]^2 = 8U_p \sin^2(\omega_0 t_0^*). \tag{3.82}$$

From the recollision condition $x(t_{rec}) = 0$, we obtain an implicit equation for t_0^*,

$$\begin{aligned} x(t_0^*) &= -\frac{F_0}{\omega_0^2}\left[\cos(\omega_0 t_{rec}) - \cos(\omega_0 t_0^*) + \omega_0(t_{rec} - t_0^*)\sin(\omega_0 t_0^*)\right] \\ &= \frac{F_0}{\omega_0^2}\left[2\cos(\omega_0 t_0^*) - \pi \sin(\omega_0 t_0^*)\right]. \end{aligned} \tag{3.83}$$

A numerical solution of equation (3.83) for $F_0 = 0.15$ a.u. and $\omega_0 = 0.06$ a.u. yields $t_0^* = 0.243T < T/4$ and $E_{rec}(t_0^*) = 7.99U_p$, equal to the tunneling time and energy of the second maximum shown in the inset of Fig. 3.30a. For $T/4 > t_0 > t_0^*$, the electron is first accelerated for $T/2$ and then decelerated once the electric field changes its sign, thus reaching the nucleus with a kinetic energy smaller than $E_{rec}(t_0^*)$, the less the nearer t_0 is to $T/4$. Since the tunneling probability close to the zero-crossing of the field is negligible, none of these trajectories contributes significantly to $P(E_{rec})$. In particular, this means that the energy $E_{rec}(t_0^*)$ does not produce a caustic. Therefore, the energy of the first maximum of $E_{rec}(t_0)$ still represents the cut-off of $P(E_{rec})$.

In Fig. 3.30b, $E_{rec}(t_0)$ and $P(E_{rec})$ for the five-cycle pulse with $F_0 = 0.15$ a.u. and $\omega_0 = 0.06$ a.u. are shown. Apart from the new sub-cycle structure, $E_{rec}(t_0)$ undergoes the same modulations by the pulse envelope discussed in the previous section. Most importantly, $P(E_{rec})$ does not differ much from the simple man's result (red curve), i.e. the energies E_{rec}^{max} and E_{rec}^{mp} are similar to the values obtained without the soft-core Coulomb potential.

In summary, we find that the presence of a Coulomb potential influences the recollision properties of the electron only slightly (mainly through the finite initial distance to the nucleus), so we can continue to use the simple man's model in the following.

3.6.3. Classical recollision thresholds

Now we return to our three-electron model. For each simultaneous multiple ionization step contained in the nonsequential pathways (0-2, 0-3, 1-3), the rescattering mechanism implies the existence of a recollision threshold field amplitude $F_{i\text{-}j}$ below which ROBI is energetically forbidden, i.e. the energy E_{rec} of the recolliding electron is not sufficient to lift the residual electron(s) over the energy barrier so that they can

escape classically (Fig. 1.3). In Section 3.5.5, we found that the onset of single-electron OBI from the ground state is accompanied by a plateau in the total ion yield (Fig. 3.25) which results from complete ionization of the ground state population. By analogy, we conjecture that the plateaus in the yield ratios signify the onset of ROBI: For field amplitudes below $F_{i\text{-}j}$, the remaining electrons can at best be promoted to an excited state from which they can tunnel ionize near the next field extremum (RESI). Due to the higher ionization energy, the tunneling probability of this excited state increases more slowly with F_0 than the single-electron tunneling probability of the neutral atom ground state, so the ratio increases with F_0 in this regime. Above $F_{i\text{-}j}$, in contrast, the ROBI probability is equal to one, so all of the rescattered single-electron probability flux is converted into two- or three-electron ionization probability, thus giving rise to the plateau in the respective ratio.

To verify the above conjecture, we first calculate the recollision threshold field amplitudes of our model. A straightforward way to do this is to equate the maximum recollision energy $2E_{rec}^{max}/3 = g(n_c)(2U_p/3)$ (where $g(n_c)$ is shown in the second column of Table 3.6) to the ionization energy of the respective simultaneous ionization step. This yields[15]

$$F_{0\text{-}2} = 2\omega_0\sqrt{\frac{3}{2}}\sqrt{\frac{E_I^+}{g(n_c)}}, \tag{3.84a}$$

$$F_{0\text{-}3} = 2\omega_0\sqrt{\frac{3}{2}}\sqrt{\frac{E_I^+ + E_I^{2+}}{g(n_c)}}, \tag{3.84b}$$

$$F_{1\text{-}3} = 2\omega_0\sqrt{\frac{3}{2}}\sqrt{\frac{E_I^{2+}}{g(n_c)}}. \tag{3.84c}$$

These field amplitudes fulfill $F_{0\text{-}2} < F_{1\text{-}3} < F_{0\text{-}3}$ since $E_I^+ < E_I^{2+} < E_I^+ + E_I^{2+}$. For a more accurate determination of the $F_{i\text{-}j}$, we have to take the results of Section 3.6.1 into account. First of all, the rescattered electron will generally arrive at the nucleus with a recollision energy $E_{rec} < E_{rec}^{max}$. Secondly, the field is nonzero at the time t_{rec} of the recollision. As a result, the ionization energies E_I are "field-modified", i.e. lowered by the negative energy V_s of the corresponding ionization saddle. For 0-2 and 0-3, the electron recollides with the singly-charged ion, so we need the time-dependent energies $V_s^{SI,+}$ and $V_s^{DI,+}$ of the single and double ionization saddle, respectively. $V_s^{SI,+}$ is obtained from the potential of the SAE approximation (3.43) while $V_s^{DI,+}$ is obtained from the potential (3.40) of the singly-charged ion in the subspace $r_1 = r_2$. For 1-3, the electron tunnels from the singly-charged ion and recollides with the doubly-charged ion whose single ionization saddle energy $V_s^{SI,2+}$ is obtained from the potential in (3.47). With these saddle energies, the implicit equations for the threshold field amplitudes

[15]Note that the field amplitude is reduced by a factor of $\sqrt{2/3}$ due to the geometry of our model (see Section 2.2), so the ponderomotive energy acquires a factor of 2/3.

read

$$\frac{2}{3}E_{rec}(F_{0\text{-}2}f(t_{rec})) = E_I^+ + V_s^{SI,+}(F_{0\text{-}2}f(t_{rec})), \tag{3.85a}$$

$$\frac{2}{3}E_{rec}(F_{0\text{-}3}f(t_{rec})) = E_I^+ + E_I^{2+} + V_s^{DI,+}(F_{0\text{-}3}f(t_{rec})), \tag{3.85b}$$

$$\frac{2}{3}E_{rec}(F_{1\text{-}3}f(t_{rec})) = E_I^{2+} + V_s^{SI,2+}(F_{1\text{-}3}f(t_{rec})) \tag{3.85c}$$

where we write the electric field of the laser as $F(t) = F_0 f(t)$. For a recollision close to a zero-crossing of $F(t)$, the field modification terms only represent a small correction to the ionization energies and we can still expect $F_{0\text{-}2} < F_{1\text{-}3} < F_{0\text{-}3}$.

To solve the equations (3.85), we need to choose E_{rec} and t_{rec}. The analysis in the previous sections has shown that there is no such thing as "the" recollision energy and time, only combinations which are more probable than others. We consider two combinations, namely the maximum recollision energy E_{rec}^{max} and the most probable recollision energy E_{rec}^{mp} (Fig. 3.28a), each with its corresponding recollision time (Fig. 3.28b). A recollision with maximum energy and a nonzero field modification represents the best-case scenario for ROBI, so these parameters yield lower bounds for the threshold field amplitudes. The most probable combination, on the other hand, takes the tunneling probability into account and can therefore be expected to yield results which are close to the true thresholds.

The threshold field amplitudes for the two frequencies and various numbers of field cycles are listed in Table 3.7. Our expectation $F_{0\text{-}2} < F_{1\text{-}3} < F_{0\text{-}3}$ is confirmed in all cases. Since the recollision energy is proportional to ω_0^{-2}, the $F_{i\text{-}j}$ increase with ω_0 for constant n_c. Furthermore, due to $E_{rec}^{max} > E_{rec}^{mp}$, the $F_{i\text{-}j}$ calculated from E_{rec}^{max} are generally smaller than the ones calculated from E_{rec}^{mp}. As n_c is increased, both E_{rec}^{mp} and E_{rec}^{max} approach $3.17U_p$, so the threshold field amplitudes calculated from these energies converge to the same value. If we leave out the field modification of the ionization energy ($V_s^{SI,+} = V_s^{DI,+} = V_s^{SI,2+} = 0$ in equations (3.85)), the resulting threshold field amplitudes are higher, with the differences to the field-modified results on the order of 10^{-1} a.u. for small and 10^{-2} a.u. for large values of n_c. This illustrates that the actual recollision time of the electron is of minor relevance for long pulses.

An alternative method to define the threshold field amplitudes can be based on a combination of (3.85) and tunneling-weighted classical trajectories. Consider the function

$$R_{i\text{-}j}(F_0) = \frac{\int_0^{T_p} W^{ADK}(t_0)\chi_1(t_0)\chi_2^{i\text{-}j}(t_0)\mathrm{d}t_0}{\int_0^{T_p} W^{ADK}(t_0)\chi_1(t_0)\mathrm{d}t_0} \tag{3.86}$$

where W^{ADK} is the ADK single ionization rate of the neutral atom (for 0-2 and 0-3) or the singly-charged ion (for 1-3). The characteristic function χ_1 measures if the electron tunneling at t_0 returns to the nucleus at some time $t_0 < t_{rec}(t_0) \leq T_p$. χ_2, on the other hand, measures if the energy of this electron exceeds the threshold of the i-j pathway. In this sense, (3.86) gives the fraction of recolliding trajectories with favorable energy

	$\omega_0 = 0.06$ a.u.			$\omega_0 = 0.10$ a.u.		
n_c	$F_{0\text{-}2}$ [a.u.]	$F_{0\text{-}3}$ [a.u.]	$F_{1\text{-}3}$ [a.u.]	$F_{0\text{-}2}$ [a.u.]	$F_{0\text{-}3}$ [a.u.]	$F_{1\text{-}3}$ [a.u.]
1	0.27 (0.13)	0.41 (0.20)	0.34 (0.16)	0.42 (0.20)	0.63 (0.30)	0.53 (0.25)
2	0.16 (0.10)	0.25 (0.15)	0.20 (0.12)	0.26 (0.15)	0.39 (0.24)	0.32 (0.19)
3	0.12 (0.09)	0.19 (0.14)	0.15 (0.11)	0.19 (0.15)	0.29 (0.22)	0.24 (0.18)
4	0.11 (0.09)	0.16 (0.14)	0.13 (0.11)	0.17 (0.14)	0.26 (0.22)	0.21 (0.18)
5	0.10 (0.09)	0.15 (0.14)	0.12 (0.11)	0.16 (0.14)	0.24 (0.22)	0.20 (0.18)
6	0.10 (0.09)	0.15 (0.14)	0.12 (0.11)	0.15 (0.14)	0.23 (0.21)	0.19 (0.17)
7	0.09 (0.09)	0.14 (0.14)	0.12 (0.11)	0.15 (0.14)	0.23 (0.21)	0.18 (0.17)
8	0.09 (0.09)	0.14 (0.14)	0.11 (0.11)	0.15 (0.14)	0.22 (0.21)	0.18 (0.17)
9	0.09 (0.09)	0.14 (0.14)	0.11 (0.11)	0.14 (0.14)	0.22 (0.21)	0.18 (0.17)
10	0.09 (0.09)	0.14 (0.14)	0.11 (0.11)	0.14 (0.14)	0.22 (0.21)	0.18 (0.17)
⋮	⋮	⋮	⋮	⋮	⋮	⋮
100	0.09 (0.09)	0.13 (0.13)	0.11 (0.11)	0.14 (0.14)	0.21 (0.21)	0.17 (0.17)
⋮	⋮	⋮	⋮	⋮	⋮	⋮
∞	0.09 (0.09)	0.13 (0.13)	0.11 (0.11)	0.14 (0.14)	0.21 (0.21)	0.17 (0.17)

Table 3.7. Recollision threshold field amplitudes as a function of n_c, calculated by solving the equations (3.85) with the most probable recollision energy and the corresponding recollision time (see Table 3.6). The results obtained with the maximum recollision energy and time are shown in parentheses. $n_c = \infty$ corresponds to the periodic field.

	$\omega_0 = 0.06$ a.u.			$\omega_0 = 0.10$ a.u.		
n_c	$F_{0\text{-}2}$ [a.u.]	$F_{0\text{-}3}$ [a.u.]	$F_{1\text{-}3}$ [a.u.]	$F_{0\text{-}2}$ [a.u.]	$F_{0\text{-}3}$ [a.u.]	$F_{1\text{-}3}$ [a.u.]
1	0.29	0.39	0.47	0.38	0.43	0.61
2	0.17	0.24	0.25	0.24	0.28	0.37
3	0.12	0.16	0.17	0.17	0.23	0.24
4	0.10	0.15	0.14	0.15	0.22	0.20
5	0.09	0.14	0.13	0.14	0.21	0.19
6	0.09	0.14	0.12	0.14	0.21	0.18
7	0.09	0.14	0.12	0.14	0.21	0.18
8	0.09	0.14	0.12	0.14	0.21	0.18
9	0.09	0.14	0.12	0.14	0.21	0.18
10	0.09	0.14	0.12	0.14	0.21	0.18
⋮	⋮	⋮	⋮	⋮	⋮	⋮
100	0.09	0.13	0.11	0.14	0.20	0.17
⋮	⋮	⋮	⋮	⋮	⋮	⋮
∞	0.08	0.13	0.11	0.13	0.20	0.17

Table 3.8. Recollision threshold field amplitudes as a function of n_c, calculated from $R_{i\text{-}j}(F_0)$ as $F_{i\text{-}j} = \min\{F_0 | R_{i\text{-}j}(F_0) = 0.1\}$. $n_c = \infty$ corresponds to the periodic field.

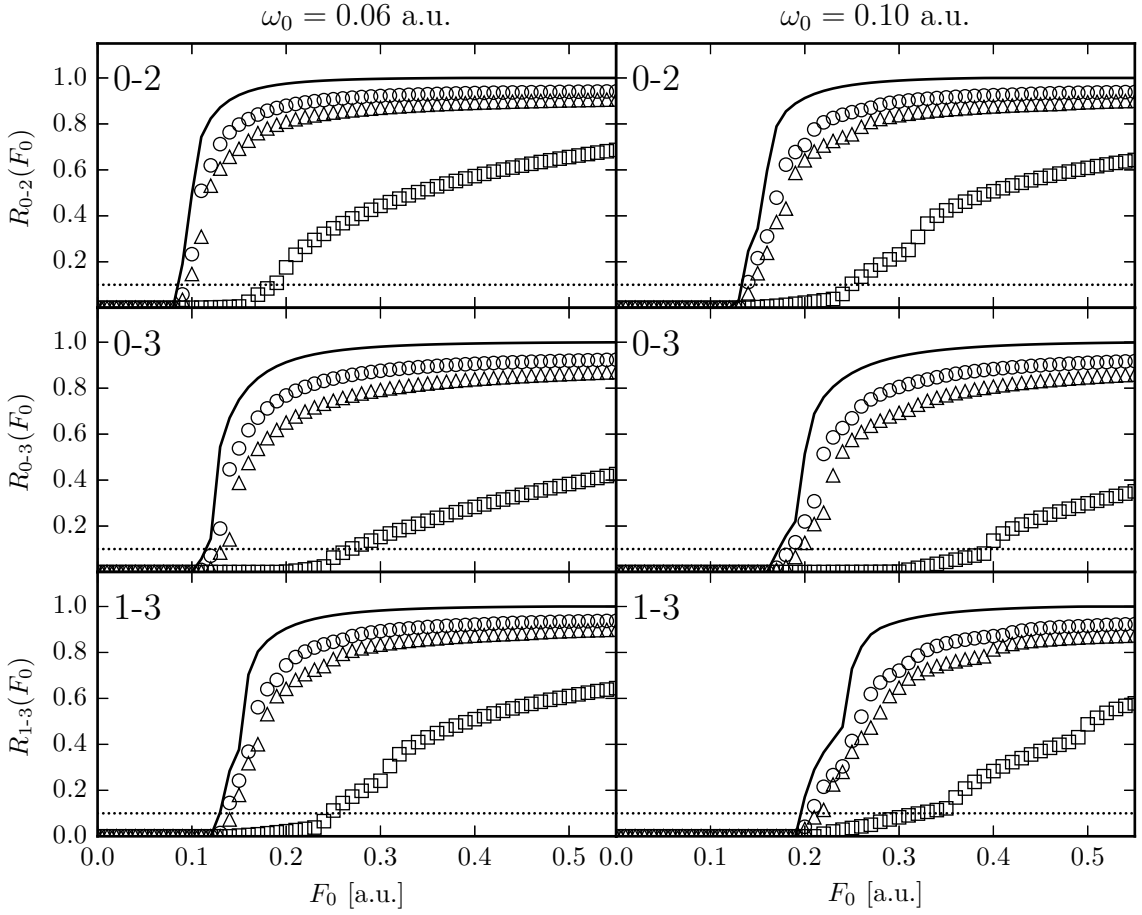

Figure 3.31. Fraction of recolliding electrons $R_{i\text{-}j}(F_0)$ exceeding the energy threshold of i-j, determined from the simple man's model for $n_c = 2$ (squares), $n_c = 5$ (triangles) and $n_c = 7$ (circles). The limiting case of a periodic field ("$n_c = \infty$") is shown as a solid black curve. The recollision threshold field amplitude $F_{i\text{-}j}$ is defined as the value of F_0 for which $R_{i\text{-}j}(F_0) = 0.1$ (dotted line).

properties for simultaneous multiple ionization as a function of F_0. It can be shown that ω_0 can be scaled out of W^{ADK} and χ_1, but not out of χ_2. Therefore, the $F_{i\text{-}j}$ determined from the above equation depend on ω_0.

$R_{i\text{-}j}(F_0)$ is shown in Fig. 3.31 for the three simultaneous multiple ionization steps and the values of ω_0 and n_c considered in this work. In most cases, $R_{i\text{-}j}(F_0)$ rises rather steeply. Since the field amplitude at which the function changes from zero to nonzero values depends on the resolution in F_0 and the time resolution of the trajectory calculation, defining the threshold field amplitudes as $F_{i\text{-}j} = \min\{F_0 | R_{i\text{-}j}(F_0) > 0\}$ is not reasonable. A definition which yields similar but more robust values is

$$F_{i\text{-}j} = \min\{F_0 | R_{i\text{-}j}(F_0) = 0.1\}. \tag{3.87}$$

The resulting threshold field amplitudes are shown in Table 3.8. In most cases, they are close to the threshold field amplitudes obtained with the most probable recollision

energy and time (Table 3.7). This is not surprising since both definitions rely on the time dependence of the tunneling probability.

Next, we check how well the classical recollision threshold field amplitudes of Table 3.7 and Table 3.8 – obtained in one dimension and without a Coulomb potential – can explain the onset of the plateaus in our quantum mechanical yield ratios. In Fig. 3.32, we plot the Ne^{2+}/Ne^{+} and the Ne^{3+}/Ne^{+} ratios together with the three predictions of the threshold field amplitudes $F_{0\text{-}2}$ and $F_{0\text{-}3}$ which are indicated by colored arrows: The green (red) ones were obtained from (3.85) with the most probable (maximum) recollision energy and time (method A and B), the black ones from (3.86) with $F_{i\text{-}j} = \min\{F_0 | R_{i\text{-}j}(F_0) = 0.1\}$ (method C). We observe that the difference between A, B and C is large only for the two-cycle pulse, so our choice of the appropriate method to predict the $F_{i\text{-}j}$ can be based on this case. For $\omega_0 = 0.06$ a.u. and $n_c = 2$, A and C predict the onset of the plateau in the Ne^{2+}/Ne^{+} ratio very well while B underestimates it. Since A and C yield similar field amplitudes in almost all cases, we will only use method A in the following, i.e. we focus on the green arrows.

First, we note a general qualitative property in Fig. 3.32: Whenever the recollision threshold field amplitude $F_{0\text{-}i}$ is considerably smaller than the saturation field amplitude F_{sat}^{SI} (indicated by the dotted line), a plateau – or at least a regime of weak F_0-dependence – is visible in the Ne^{i+}/Ne^{+} ratio. For $F_{0\text{-}i} \approx F_{sat}^{SI}$ or $F_{0\text{-}i} > F_{sat}^{SI}$, this is not the case, confirming the expectation that ROBI gives the dominant contribution to the Ne^{i+} yield only if the rescattering yield is much larger than the single ionization yield from Ne^{+} (for $i = 2$) or the simultaneous double ionization yield from Ne (for $i = 3$). Both assumptions only hold for field amplitudes smaller than F_{sat}^{SI} (cf. Fig. 3.19).

For the yield ratios where a plateau exists *and* its onset is sufficiently pronounced (Ne^{2+}/Ne^{+} for $n_c = 2$ and Ne^{3+}/Ne^{+} for $n_c = 5, 7$, all with $\omega_0 = 0.06$ a.u.), we find quantitative agreement of the threshold field amplitude with the onset. In all other cases (Ne^{2+}/Ne^{+} for $n_c = 5, 7$ and both frequencies), the agreement is hard to judge. For the smaller frequency, this is because the threshold field amplitudes $F_{0\text{-}2}$ lie at the lower end of the field interval. In order to visualize the onset of the plateau in the Ne^{2+}/Ne^{+} ratio, we would have to calculate the yields for even smaller field amplitudes which is not possible due to the enormous numerical accuracy needed in this regime. For the larger frequency, on the other hand, the threshold field amplitudes are larger, but the onset of ROBI is obscured by the resonant enhancements of the Ne^{2+} yield and probably other competing ionization processes, e.g. RESI.

In Fig. 3.33, we compare the threshold field amplitudes $F_{1\text{-}3}$ to the Ne^{3+}/Ne^{2+} yield ratios obtained from the singly-charged ion[16], i.e. P_{SD}/P_{SS} (red triangles). Again, we only consider the green arrows. For all combinations of ω_0 and n_c shown in the figure, $F_{1\text{-}3}$ is much smaller than the saturation field amplitude of double ionization F_{sat}^{DI} (indicated by the dashed line). As a result, the ratios always exhibit a regime of weak F_0-dependence. For the longer pulses, the regime is very wide but its onset cannot

[16]The ratios obtained from the atom are also shown, but they are not suitable for comparison since they also contain contributions of other triple ionization pathways (0-3, 0-2-3).

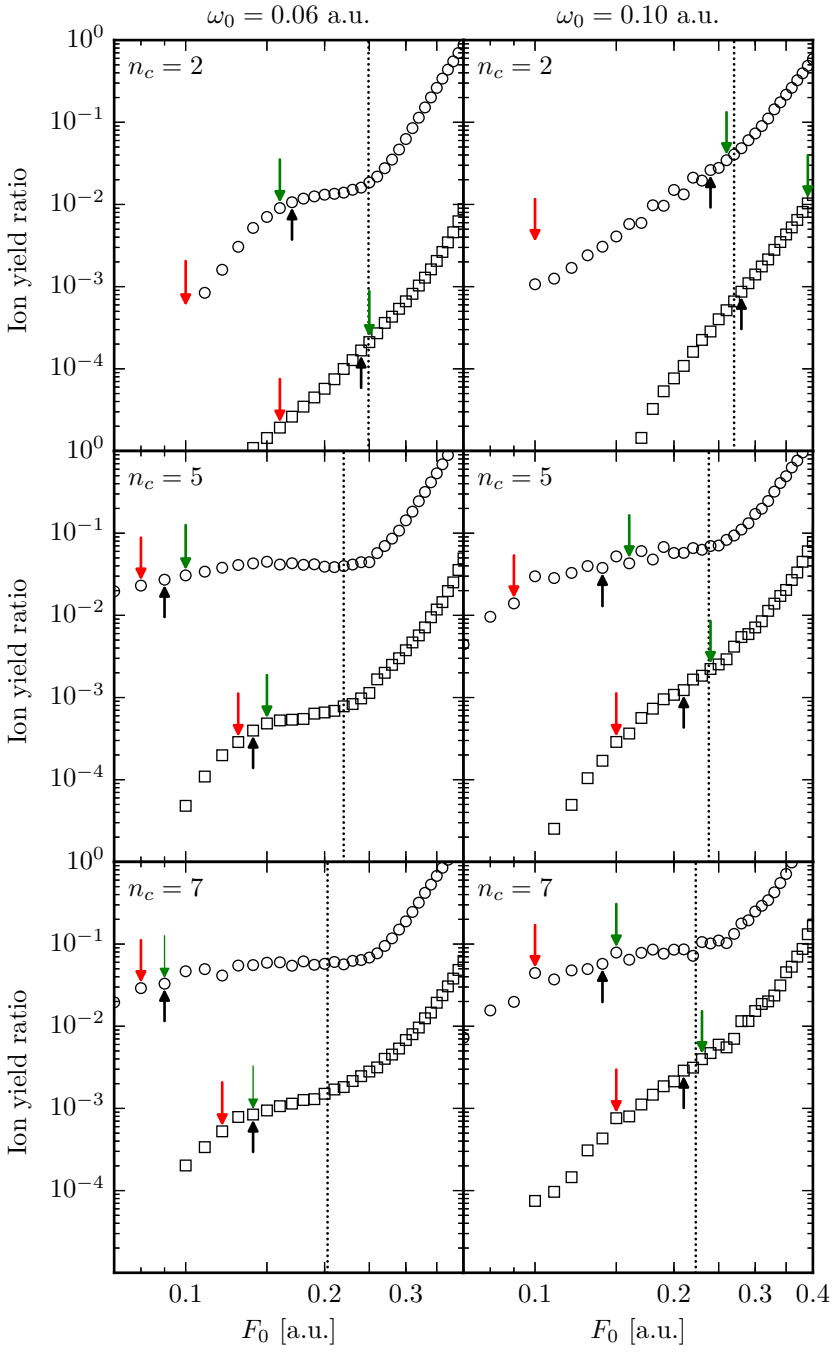

Figure 3.32. Ne^{2+}/Ne^{+} (circles) and Ne^{3+}/Ne^{+} (squares) yield ratios as a function of F_0. The arrows indicate the classical recollision thresholds $F_{0\text{-}2}$ (for Ne^{2+}/Ne^{+}) and $F_{0\text{-}3}$ (for Ne^{3+}/Ne^{+}) which were calculated with three different methods: From (3.85) with the maximum recollision energy and time (red), with the most probable recollision energy and time (green) and from (3.86) with $F_{i\text{-}j} = \min\{F_0 | R_{i\text{-}j}(F_0) = 0.1\}$ (black). For each pair (n_c, ω_0), the saturation field amplitude of single ionization is indicated by the dotted line.

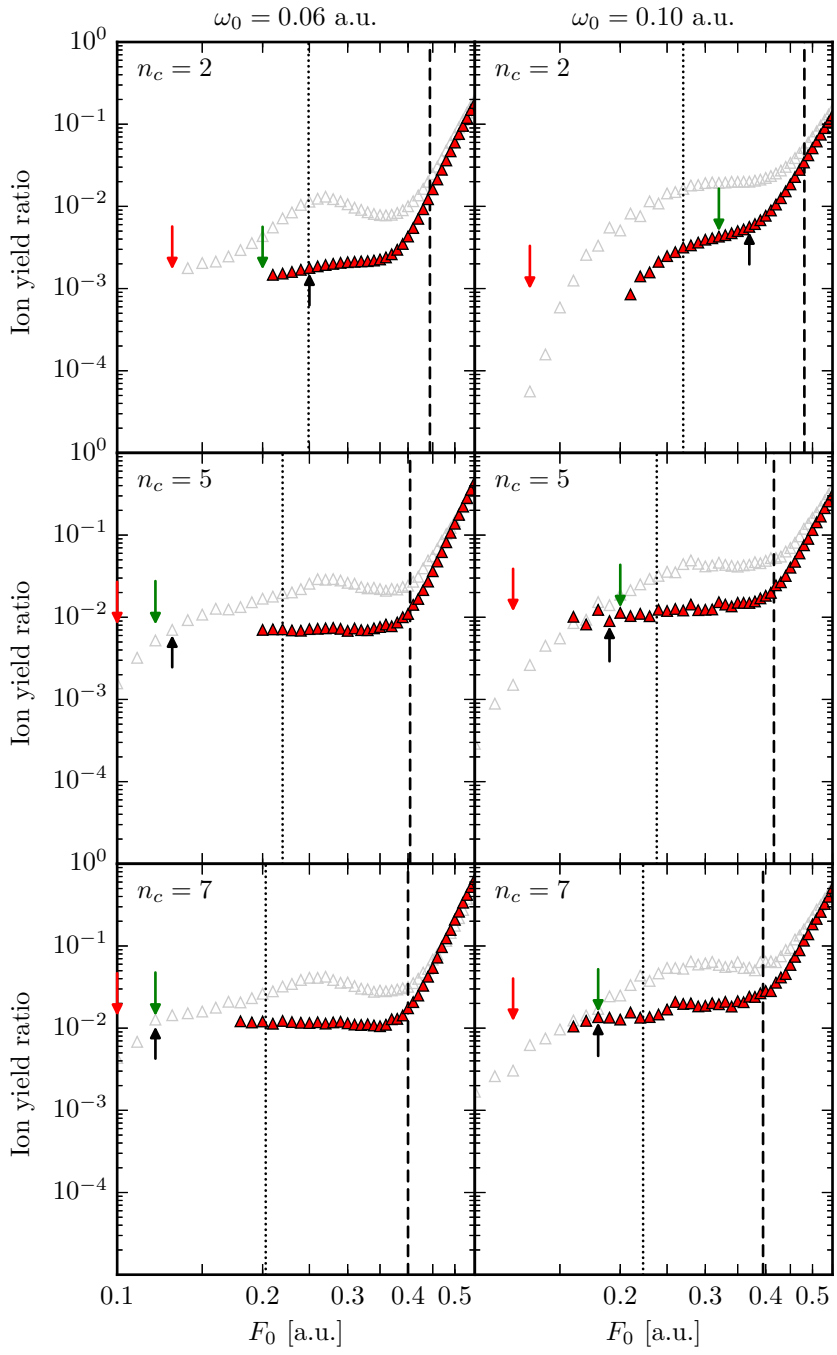

Figure 3.33. Ne^{3+}/Ne^{+} yield ratio obtained from the singly-charged ion (red triangles) and the neutral atom (empty triangles) as a function of F_0. The arrows indicate the classical recollision thresholds $F_{1\text{-}3}$ which were calculated with three different methods: From (3.85) with the maximum recollision energy and time (red), with the most probable recollision energy and time (green) and from (3.86) with $F_{i\text{-}j} = \min\{F_0 | R_{i\text{-}j}(F_0) = 0.1\}$ (black). For each pair (n_c, ω_0), the saturation field amplitudes of single and double ionization are indicated by the dotted and dashed lines, respectively.

be found due to the insufficient convergence of the yields for small field amplitudes. Therefore, a quantitative comparison of the threshold field amplitudes $F_{1\text{-}3}$ with the yield ratios is not possible in these cases.

3.6.4. Rescattering yield

The recollision thresholds offer a *qualitative* explanation for the occurrence of the plateaus in the Ne^{2+}/Ne^{+} and Ne^{3+}/Ne^{+} yield ratios. To understand the magnitude of the ratios in the plateau regimes, we estimate the ionization yields of the pathways 0-2 and 0-3 from the rescattered probability flux, taking full advantage of the fact the we have access to the ion yields at every point in time during the pulse.

In Fig. 3.34, we show the time-dependent ion yields for the five-cycle pulse with $\omega_0 = 0.06$ a.u. and the field amplitude $F_0 = 0.20$ a.u. which is in the plateau regime of both the Ne^{2+}/Ne^{+} and the Ne^{3+}/Ne^{+} ratio (see Fig. 3.32). Near the fourth extremum of the field ($\omega_0 t/2\pi \approx 1.5$), the tunneling probability is high enough so that a significant part of the wave function can escape through the single ionization barrier, leading to a steep increase of the Ne^{+} yield. At the next zero-crossing of the field ($\omega_0 t/2\pi \approx 1.75$), the tunneling probability is negligible and the Ne^{+} yield remains apparently constant. At $\omega_0 t/2\pi \approx 2$, i.e. roughly a half cycle after the onset of single ionization, the Ne^{2+} and Ne^{3+} yields start to increase.

The sequence of the yield-increases described above is in qualitative agreement with the prediction of the rescattering mechanism. Therefore, one may wonder how rescattering manifests itself in the yields. Taking a closer look at the Ne^{+} yield near a zero-crossing of the field (inset in the figure), we notice a small dip, i.e. the Ne^{+} yield decreases before increasing again. In view of equation (3.17b), the decrease either originates from probability flowing from region 1 to region 2 or 3 (f_{12} or f_{13} positive – single ionization or simultaneous double ionization from the singly-charged ion) or from region 1 back into region 0 (f_{01} negative – rescattering). Since the Ne^{2+} and Ne^{3+} yields do not increase significantly in the dip region and the SAE single ionization yield (dashed green curve) shows the same dip although there is no higher charge state to which probability can flow, we conclude that the dips are due to rescattering. In order to calculate the magnitude of the dips, i.e. the rescattering yield, we decompose the integral over the probability flux f_{01} as

$$P_{01}(t) = \int_0^t f_{01}(t')\mathrm{d}t' =: \int_0^t f_{out}(t')\mathrm{d}t' - \int_0^t f_{rsc}(t')\mathrm{d}t' =: P_{out}(t) - P_{rsc}(t) \qquad (3.88)$$

where $f_{out}, f_{rsc} \geq 0$ are the outgoing flux and the rescattering flux, respectively. A similar decomposition of the probability flux was proposed by Yu *et al.* (2013), albeit in a different context. In practice, the decomposition is accomplished by checking in every time step if f_{01} is smaller or larger than zero. Plotting the rescattering yield $P_{rsc}(t)$ next to the Ne^{2+} yield in Fig. 3.34 (red curve), we observe a clear correlation, i.e. the difference between two slowdowns of the yield increase (indicated by the gray lines) is approximately equal. The same correlation is observed for the Ne^{3+} yield if

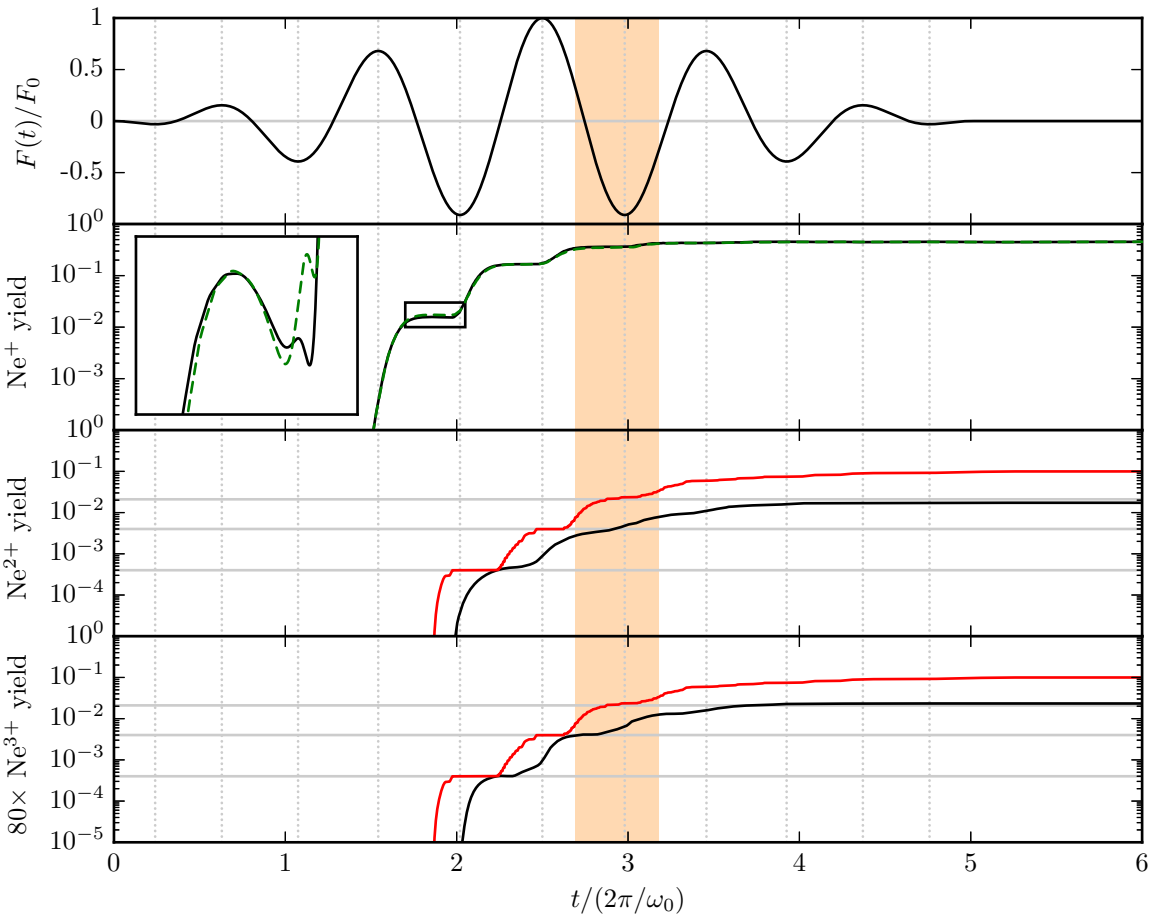

Figure 3.34. Time-dependent ion yields for $n_c = 5$, $\omega_0 = 0.06$ a.u. and $F_0 = 0.20$ a.u. (black curves), compared to the SAE single ionization yield (dashed green curve) and the rescattering yield calculated from the Ne^+ yield (red curve). The horizontal gray lines are drawn to guide the eye. The orange region corresponds to the time interval between a recollision with the maximum and the most probable energy.

the latter is multiplied by 80 (or, equivalently, the rescattering yield is multiplied by 1/80). The need to scale the Ne^{3+} yield arises from the fact that a recollision leading to triple ionization is much less probable than one leading to double ionization. In other words, if all rescattered probability P_{rsc} leads to multiple ionization, there exists a certain branching ratio $r \ll 1$ so that $(1-r)P_{rsc}$ is converted to double and rP_{rsc} to triple ionization. r is some unknown function of the pulse parameters, so the value $r = 1/80$ appropriate for our case had to be determined empirically.

The observed correlations support our idea that, in the plateau regimes, all rescattered probability is converted into simultaneous multiple ionization probability. However, this is true only up to the field extremum following the global field maximum ($\omega_0 t/2\pi \approx 3$). At this point, the rescattering yield is approximately equal to the (scaled) multiple ionization yields at the end of the pulse. The subsequent increase

of the rescattering yield for later times indicates at least one additional rescattering event which, according to our interpretation, does not lead to simultaneous multiple ionization. This observation of a recollision cut-off is in qualitative agreement with classical two-electron calculations (see e.g. Ho and Eberly (2005); Beran (2014); Li *et al.* (2016); Dong *et al.* (2016)) where it was found that the number of recollision events becomes negligible once the pulse envelope starts to decay, i.e. shortly after the pulse maximum. Inspection of the trajectories calculated with the simple man's model reveals that the recollision cut-off time t_c is located between the times of electron recollision with maximum and most probable energy (orange region in Fig. 3.34).

Since we do not know how the recollision cut-off and the branching ratio depend on the pulse parameters, an accurate determination of the 0-2 and 0-3 ionization yields from the rescattering yield is hopeless. However, as a first approximation, we can assume that the cut-off time coincides with the first field minimum after the field maximum ($t_c = \min\{t > T_p/2 | \dot{F}(t) = 0\}$) and use our empirical value of $r = 1/80$ for the branching ratio, independent of the frequency and field amplitude. This will be referred to as the "rescattering approximation" in the remainder of this section. In Fig. 3.35, the ratios $(1-r)P_{rsc}(t_c)/P_1(T_p)$ (approximating the yield of 0-2, red circles) and $rP_{rsc}(t_c)/P_1(T_p)$ (approximating the yield of 0-3, red squares) are compared to the Ne^{2+}/Ne^{+} and Ne^{3+}/Ne^{+} ratios obtained from the full calculation (empty markers). The 0-3 ratio of the rescattering approximation is only shown for $\omega_0 = 0.06$ a.u. and $n_c = 5$ since there is no plateau in the Ne^{3+}/Ne^{+} ratio for the other cases. Strictly speaking, one could set $r = 0$ for these cases, but since r is small anyway, we continue to use $r = 1/80$ for the sake of consistency. For both frequencies and pulse durations, we find that the ratios obtained from the rescattering approximation agree quite well with the results of the full calculation although t_c was chosen based on the time-dependent ion yields for *fixed* pulse parameters. This demonstrates the universality of the recollision cut-off. For the larger frequency, the rescattering approximation even captures the gentle rise of the Ne^{2+}/Ne^{+} ratio with F_0 and some of the local enhancements. This indicates that the enhancements result from a rescattering-related effect, as suspected in Section 3.4.6.

Although the Ne^{2+}/Ne^{+} and Ne^{3+}/Ne^{+} ratios in the plateau regime are not *exactly* reproduced by the above approximation, their order of magnitude is predicted correctly. Therefore, we have partially accomplished our goal of estimating the nonsequential yields in the plateau regime solely from single ionization. The numerical effort can be reduced even more by applying the rescattering approximation to the SAE single ionization yield. This gives very similar results (blue curves in the figure).

3.6.5. Comparison with experiments

The procedure outlined in the previous section cannot be applied to experimentally measured ion yields since their time dependence is inaccessible. Nevertheless, we can check whether the intensity-dependent ion yield ratios available in the literature are compatible with the notion of a recollision threshold by making a comparison analogous

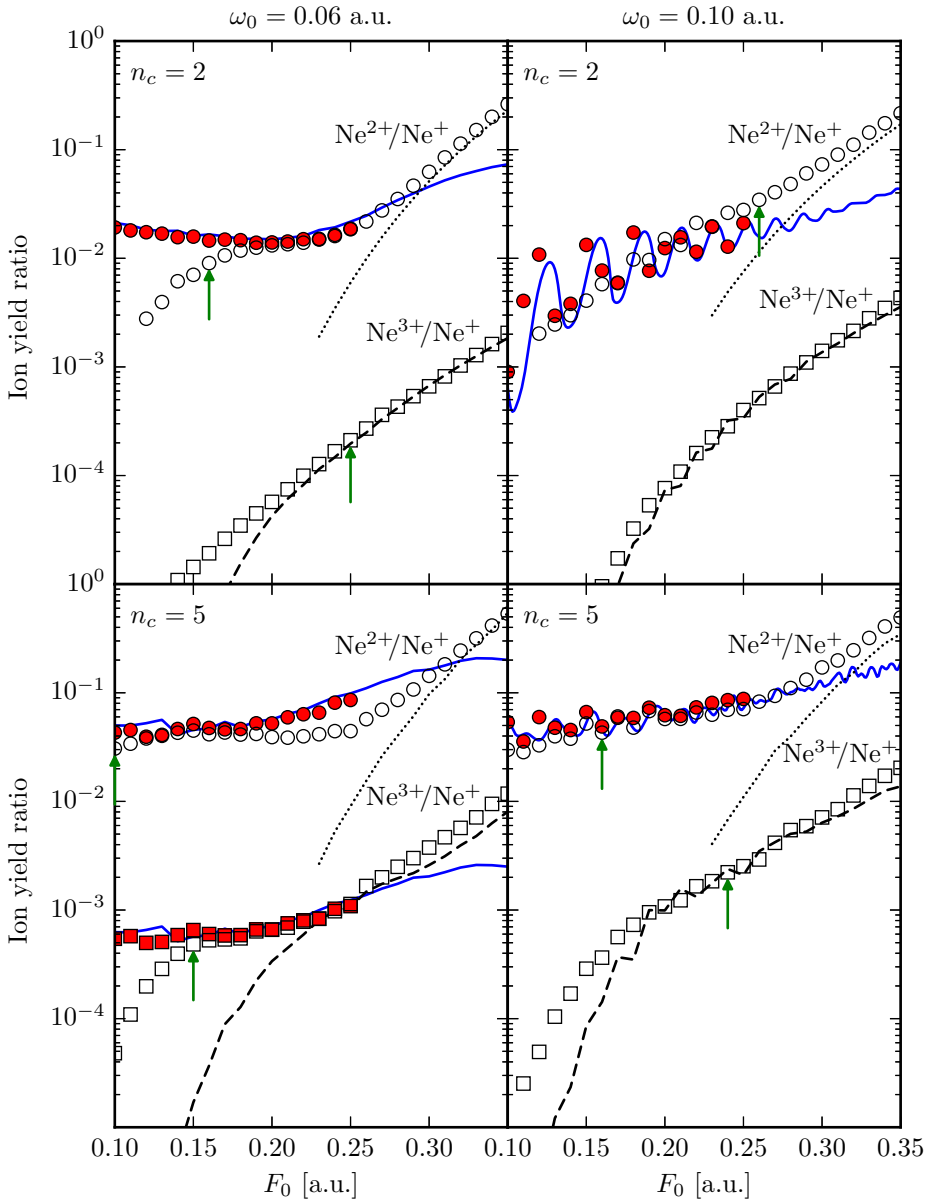

Figure 3.35. Ne^{2+}/Ne^+ and Ne^{3+}/Ne^+ yield ratios (empty markers), compared to the ratios obtained from the Ne^+ yield within the rescattering approximation (red markers, see text for details). The green arrows indicate the classical recollision thresholds $F_{0\text{-}2}$ (for Ne^{2+}/Ne^+) and $F_{0\text{-}3}$ (for Ne^{3+}/Ne^+). The dotted and dashed curves correspond to the product yields SS and DS, respectively. The blue curve is the result obtained by combining the SAE and the rescattering approximation.

to Fig. 3.32. Unfortunately, we must restrict ourselves to the ratio of double to single ionization since it is the only yield ratio usually shown in publications[17], despite the fact that intensity-dependent triple ionization yields have been measured for neon, argon, krypton and xenon. To enable the reader to verify our conclusions, the laser pulses in this section will be described in terms of peak intensity, wavelength and FWHM duration.

Considering that experimental laser pulses usually have a large number of field cycles (see e.g. Table 3.2), the calculation of the recollision threshold intensity $I_{0\text{-}2}$ is easy: As shown in Section 3.6.1, the electrons typically recollide with the maximum energy of $3.17U_p$ and very close to a zero-crossing of the field where the field modification of the ionization energy is negligible. Therefore, the recollision threshold of the pathway 0-2 is defined by $3.17U_p = E_I^+$. Using the conversion formulas (U.1) for the intensity and wavelength, we obtain the recollision threshold intensity

$$I_{0\text{-}2}[\mathrm{W/cm^2}] = 3.38 \cdot 10^{18} \cdot \frac{E_I^+[\mathrm{eV}]}{(\lambda[\mathrm{nm}])^2}. \tag{3.89}$$

Identifying $I_{0\text{-}2}$ with the onset of a plateau in an experimentally measured double to single ionization yield ratio is difficult for several reasons. First of all, intensity averaging in the focal volume of the laser shifts possible structures in the yield ratio (including the plateau onset) to different intensities, makes the structures less pronounced or even washes them out completely. Secondly, several calculations for long pulses indicate that there are processes which contribute to the plateau in the yield ratio of real atoms but are not captured by a one-dimension-per-electron model like ours, e.g. Coulomb focusing (Brabec *et al.*, 1996; Bhardwaj *et al.*, 2001). Finally, as in the numerical calculations, there is always some ambiguity as how to define the plateau onset intensity. This problem is aggravated by the ion count uncertainty which distorts the ratios, especially for the noble gases with the largest ionization energies (helium and neon).

In Table 3.9, we present an overview of the experiments where the double to single ionization yield ratio was measured and a regime of weak intensity dependence was observed. A Ti:sapphire laser (with wavelength $\lambda \approx 800$ nm) or its frequency-doubled version ($\lambda \approx 400$ nm) was used in all cases. Mostly, the regime of weak intensity dependence had the form of a plateau. Since the raw yield data are not available, the plateau onset intensities I_{on} (fifth column) were estimated by eye from the figures in the respective papers, with an uncertainty interval taking the ambiguity of the onset into account. Due to the arbitrariness of this approach, the agreement of I_{on} and the calculated threshold intensity $I_{0\text{-}2}$ (sixth column) is hard to judge. Nevertheless, $I_{0\text{-}2}$ is contained in the interval in most cases, especially for argon and xenon. For these two atoms, multiple yield data sets obtained with different pulse durations are available. These show that the plateau onset does not significantly change if $n_c \gg 10$,

[17] To the best of our knowledge, the only intensity-dependent *triple* to single ionization yield ratio has been published by Kübel *et al.* (2016) for argon. However, since it does not exhibit a regime of weak intensity dependence, we do not consider it here.

	λ [nm]	$T^{exp}_{1/2,I}$ [fs]	n_c	I_{on} [TW/cm^2]	$I_{0\text{-}2}$ [TW/cm^2]	Measured by
He	780	160	171	900 ± 400	303	Walker *et al.* (1994)
He	390	160	341	900 ± 400	1209	Sheehy *et al.* (1998)
Ne	800	50	52	-	216	Bhardwaj *et al.* (2001)
Ne	800	12	12	-	216	Bhardwaj *et al.* (2001)
Ar	800	200	208	150 ± 50	146	Larochelle *et al.* (1998)
Ar	780	100	107	150 ± 50	154	Chaloupka *et al.* (2003)
Ar	800	30	31	150 ± 50	146	Guo *et al.* (1998)
Ar	750	4	4	250 ± 100	166	Kübel *et al.* (2016)
Ar	394	45	95	-	602	Henrichs *et al.* (2013)
Kr	800	200	208	-	129	Talebpour *et al.* (1997a)
Xe	800	200	208	80 ± 20	112	Talebpour *et al.* (1997a)
Xe	790	100	105	80 ± 40	115	Rudati *et al.* (2004)
Xe	780	100	107	80 ± 40	118	Chaloupka *et al.* (2003)
Xe	770	100	108	80 ± 40	121	Rudati *et al.* (2004)
Xe	800	30	31	90 ± 60	112	Guo *et al.* (1998)

Table 3.9. Experiments on laser-induced ionization of noble gases where the double to single ionization yield ratio was measured as a function of intensity. In each case, a regime of weak intensity dependence was observed. The onset of this regime I_{on} (estimated by eye from the publications where possible) is compared to the threshold intensity $I_{0\text{-}2}$ calculated from equation (3.89). The approximate number of field cycles n_c was calculated from the wavelength λ and the FWHM intensity pulse duration $T^{exp}_{1/2,I}$ according to equation (2.33).

corroborating our result that the recollision threshold intensity is virtually independent of the pulse duration for long pulses, as predicted by equation (3.89). However, if the pulse duration is decreased to a single-figure number of field cycles (Kübel *et al.*, 2016), a calculation of the threshold intensity must take both the decreased recollision energy and the time-dependent field modification into account (equation (3.85a)). Depending on the pulse shape, both effects result in a value of $I_{0\text{-}2}$ which is somewhat higher than the prediction of equation (3.89) and closer to the onset of sequential double ionization. Therefore, it comes as no surprise that the intensity-dependent Ar^{2+}/Ar^{+} ratio of Kübel *et al.* hardly shows a plateau.

The above conclusions notwithstanding, an unequivocal observation of the 0-2 recollision threshold in the experimental ion yield ratios is not possible due to the many effects which distort the measured data. However, the threshold manifests itself in the electron momentum distributions of double ionization, as shown by Liu *et al.* (2008b, 2010, 2011) for argon. Above $I_{0\text{-}2}$, the authors found a distribution similar to the right-hand side of Fig. 1.2 with maxima in the first and third quadrant (indicating electrons escaping in the same direction). Below $I_{0\text{-}2}$, in contrast, they observed maxima in the second and fourth quadrant (indicating electrons escaping back-to-back). For neon, this structural change in the momentum distributions is absent.

4. Momentum distributions

In this chapter, we calculate the momentum distributions of multiple ionization, i.e. the ion yields as a function of the electron and ion momenta. In these differential observables, the contributing ionization pathways can be disentangled to some extent by using the predictions of tunnel ionization and the classical rescattering mechanism. The momentum distributions are studied as a function of the field amplitude and the frequency and are interpreted based on the results of the previous chapter.

4.1. Quantum approach

In this section, we derive the momentum-resolved ionization yields from the wave function $\psi(r_1, r_2, r_3)$ and discuss their numerical calculation.

4.1.1. Electron momentum distributions

Before the laser pulse is switched on, the three-electron wave function ψ equals the normalized ground state of the neutral atom. At the end of the pulse ($t = t_f$), in contrast, the wave function is a superposition of neutral, singly-, doubly- and triply-ionized states. If we again assume that the ionized electrons are located in different regions R_i of the position space $\mathbb{R}^3$ (with $\bigcup_{i=0}^{3} R_i = \mathbb{R}^3$ and $R_i \cap R_j = \emptyset$ for $i \neq j$), we can isolate the yields P_i of the charge states by performing a partition of unity,

$$\begin{aligned}\langle\psi(t_f)|\psi(t_f)\rangle &= \iiint_{\mathbb{R}^3} \langle\psi(t_f)|r_1, r_2, r_3\rangle\langle r_1, r_2, r_3|\psi(t_f)\rangle \mathrm{d}r_1\mathrm{d}r_2\mathrm{d}r_3 \\ &= \langle\psi(t_f)|\underbrace{\sum_{i=0}^{3}\mathcal{P}_i}_{=1}|\psi(t_f)\rangle = \sum_{i=0}^{3}\langle\psi(t_f)|\mathcal{P}_i|\psi(t_f)\rangle = \sum_{i=0}^{3} P_i. \end{aligned} \tag{4.1}$$

In the above equation, we defined the operator

$$\mathcal{P}_i := \iiint_{R_i} |r_1, r_2, r_3\rangle\langle r_1, r_2, r_3| \mathrm{d}r_1\mathrm{d}r_2\mathrm{d}r_3 \tag{4.2}$$

which projects the wave function onto positions associated with the i-fold ionized atom. As a projection operator, $\mathcal{P}_i$ is idempotent, i.e. $\mathcal{P}_i^2 = \mathcal{P}_i^\dagger\mathcal{P}_i = \mathcal{P}_i$. It is convenient to rewrite (4.2) as

$$\mathcal{P}_i = \iiint_{\mathbb{R}^3} \chi_i(r_1, r_2, r_3)|r_1, r_2, r_3\rangle\langle r_1, r_2, r_3| \mathrm{d}r_1\mathrm{d}r_2\mathrm{d}r_3 \tag{4.3}$$

with the characteristic function $\chi_i(r_1, r_2, r_3)$ of R_i which equals one if $(r_1, r_2, r_3) \in R_i$ and zero otherwise. Using (4.1) and the idempotence of $\mathcal{P}_i$, it follows that

$$\sum_{i=0}^{3} \chi_i(r_1, r_2, r_3) = 1, \tag{4.4a}$$

$$\sum_{i=0}^{3} \chi_i^2(r_1, r_2, r_3) = 1 \tag{4.4b}$$

for all $(r_1, r_2, r_3) \in \mathbb{R}^3$. With the help of the characteristic function χ_i, the i-fold ionization yield

$$P_i := \langle \psi(t_f) | \mathcal{P}_i | \psi(t_f) \rangle = \iiint_{R_i} |\psi(r_1, r_2, r_3, t_f)|^2 \mathrm{d}r_1 \mathrm{d}r_2 \mathrm{d}r_3 \tag{4.5}$$

can be written as

$$P_i = \iiint_{\mathbb{R}^3} |\underbrace{\psi(r_1, r_2, r_3, t_f)\chi_i(r_1, r_2, r_3)}_{=:\psi_i(r_1, r_2, r_3)}|^2 \mathrm{d}r_1 \mathrm{d}r_2 \mathrm{d}r_3 \tag{4.6}$$

where we defined the wave function ψ_i of the i-fold ionized atom. Since $\chi_i \chi_j = 0$ for $i \neq j$, the wave function parts corresponding to different charge states are orthogonal to each other. As a consequence, the squared modulus of the total wave function is the sum of the squared moduli of the wave functions of the different charge states, i.e.

$$|\psi(r_1, r_2, r_3, t_f)|^2 = \sum_{i=0}^{3} |\psi_i(r_1, r_2, r_3)|^2 = \left(\sum_{i=0}^{3} \chi_i^2 \right) |\psi(r_1, r_2, r_3, t_f)|^2. \tag{4.7}$$

For single and double ionization, we can define characteristic subfunctions that specify which electrons are ionized,

$$\psi_1 = \chi_1 \psi = \chi_{1,1}\psi + \chi_{1,2}\psi + \chi_{1,3}\psi =: \psi_{1,1} + \psi_{1,2} + \psi_{1,3}, \tag{4.8a}$$

$$\psi_2 = \chi_2 \psi = \chi_{2,12}\psi + \chi_{2,13}\psi + \chi_{2,23}\psi =: \psi_{2,12} + \psi_{2,13} + \psi_{2,23}. \tag{4.8b}$$

Again, the wave function parts are orthogonal to each other. Using the linearity of the integral and the indistinguishability of the electrons, the single and double ionization yield can be written as

$$\begin{aligned} P_1 &= \iiint_{\mathbb{R}^3} |\psi_1(r_1, r_2, r_3)|^2 \mathrm{d}r_1 \mathrm{d}r_2 \mathrm{d}r_3 = \iiint_{\mathbb{R}^3} \sum_{j=1}^{3} |\psi_{1,j}(r_1, r_2, r_3)|^2 \mathrm{d}r_1 \mathrm{d}r_2 \mathrm{d}r_3 \\ &= 3 \iiint_{\mathbb{R}^3} |\psi_{1,1}(r_1, r_2, r_3)|^2 \mathrm{d}r_1 \mathrm{d}r_2 \mathrm{d}r_3 \end{aligned} \tag{4.9a}$$

and

$$P_2 = \iiint_{\mathbb{R}^3} |\psi_2(r_1, r_2, r_3)|^2 \mathrm{d}r_1 \mathrm{d}r_2 \mathrm{d}r_3 = \iiint_{\mathbb{R}^3} \sum_{\substack{j,k=1 \\ j<k}}^{3} |\psi_{2,jk}(r_1, r_2, r_3)|^2 \mathrm{d}r_1 \mathrm{d}r_2 \mathrm{d}r_3$$
$$= 3 \iiint_{\mathbb{R}^3} |\psi_{2,12}(r_1, r_2, r_3)|^2 \mathrm{d}r_1 \mathrm{d}r_2 \mathrm{d}r_3, \tag{4.9b}$$

respectively. From now on, we omit the limits of integration if it is clear from the context that we integrate over the full space of positions (or momenta).

Now that the wave function at the end of the pulse has been suitably projected, we can extract the momentum information by Fourier transforming the wave function parts with respect to the coordinates of the ionized electron(s), taking the squared modulus and integrating over the bound electron(s). This way, we obtain the electron momentum distributions (i.e. the momentum-resolved ionization yields) of single, double and triple ionization,

$$g^{+}(p_1) = 3 \iint \left| \int \psi_{1,1}(r_1, r_2, r_3) \mathrm{e}^{\mathrm{i}p_1 r_1} \mathrm{d}r_1 \right|^2 \mathrm{d}r_2 \mathrm{d}r_3, \tag{4.10a}$$
$$g^{2+}(p_1, p_2) = 3 \int \left| \iint \psi_{2,12}(r_1, r_2, r_3) \mathrm{e}^{\mathrm{i}(p_1 r_1 + p_2 r_2)} \mathrm{d}r_1 \mathrm{d}r_2 \right|^2 \mathrm{d}r_3, \tag{4.10b}$$
$$g^{3+}(p_1, p_2, p_3) = \left| \iiint \psi_3(r_1, r_2, r_3) \mathrm{e}^{\mathrm{i}(p_1 r_1 + p_2 r_2 + p_3 r_3)} \mathrm{d}r_1 \mathrm{d}r_2 \mathrm{d}r_3 \right|^2$$
$$= |\widehat{\psi}_3(p_1, p_2, p_3)|^2. \tag{4.10c}$$

We suppress prefactors $\propto 1/\sqrt{2\pi}$ since they only ensure the normalization of the Fourier transform, but are of no significance for the shape of the distributions. To prove that the above expressions are indeed the sought-after momentum distributions, we have to show that integration over the momenta gives the respective ionization yield. For single ionization, we obtain

$$\int g^{+}(p_1) \mathrm{d}p_1 = 3 \iiint \left| \int \psi_{1,1}(r_1, r_2, r_3) \mathrm{e}^{\mathrm{i}p_1 r_1} \mathrm{d}r_1 \right|^2 \mathrm{d}r_2 \mathrm{d}r_3 \mathrm{d}p_1$$
$$= 3 \iiiint \psi^*_{1,1}(r_1', r_2, r_3) \psi_{1,1}(r_1, r_2, r_3) \mathrm{d}r_1 \mathrm{d}r_1' \mathrm{d}r_2 \mathrm{d}r_3 \int \mathrm{e}^{\mathrm{i}p_1 (r_1 - r_1')} \mathrm{d}p_1$$
$$= 3 \iiiint \psi^*_{1,1}(r_1', r_2, r_3) \psi_{1,1}(r_1, r_2, r_3) \delta(r_1 - r_1') \mathrm{d}r_1 \mathrm{d}r_1' \mathrm{d}r_2 \mathrm{d}r_3$$
$$= 3 \iiint |\psi_{1,1}(r_1, r_2, r_3)|^2 \mathrm{d}r_1 \mathrm{d}r_2 \mathrm{d}r_3 = P_1. \tag{4.11}$$

In the same way, one can verify that

$$\iint g^{2+}(p_1, p_2)\mathrm{d}p_1\mathrm{d}p_2 = P_2, \tag{4.12a}$$

$$\iiint g^{3+}(p_1, p_2, p_3)\mathrm{d}p_1\mathrm{d}p_2\mathrm{d}p_3 = P_3. \tag{4.12b}$$

As in Chapter 3, we define the charge state regions R_i according to equations (3.16). Since we do not integrate probability fluxes across the boundaries, there is no need to cut off the edges of the volumes and the division of the position space is hence specified by a single critical distance $r_c > 0$ (the "ionization radius") beyond which an electron is considered ionized. The characteristic functions χ_i are suitable combinations of Heaviside step functions $\Theta(r)$. Defining the rectangular function

$$\square(r) := \Theta(r_c - |r|) = \begin{cases} 1, & |r| \leq r_c, \\ 0, & |r| > r_c, \end{cases} \tag{4.13}$$

they can be written as

$$\chi_0 = \square(r_1)\square(r_2)\square(r_3), \tag{4.14a}$$

$$\chi_1 = \underbrace{[1-\square(r_1)]\square(r_2)\square(r_3)}_{=\chi_{1,1}} + \underbrace{\square(r_1)[1-\square(r_2)]\square(r_3)}_{=\chi_{1,2}} + \underbrace{\square(r_1)\square(r_2)[1-\square(r_3)]}_{=\chi_{1,3}}, \tag{4.14b}$$

$$\chi_2 = \underbrace{[1-\square(r_1)][1-\square(r_2)]\square(r_3)}_{=\chi_{2,12}} + \underbrace{[1-\square(r_1)]\square(r_2)[1-\square(r_3)]}_{=\chi_{2,13}} + \underbrace{\square(r_1)[1-\square(r_2)][1-\square(r_3)]}_{=\chi_{2,23}}, \tag{4.14c}$$

$$\chi_3 = [1-\square(r_1)][1-\square(r_2)][1-\square(r_3)]. \tag{4.14d}$$

These definitions fulfill (4.4a) and (4.4b) since $\Theta(r)(1-\Theta(r)) = 0$ for all r. However, due to the steplike envelope in position space, the Fourier-transformed wave function – and hence the momentum distributions – will show nonphysical local maxima (so-called side lobes) in momentum space, an effect known as spectral leakage. To minimize it, we replace the rectangular function in the above equations by a Hann window function

$$\mathcal{W}(r) = \begin{cases} \frac{1}{2}\left[1 + \cos\left(\pi\frac{r}{r_c}\right)\right], & |r| \leq r_c, \\ 0, & |r| > r_c \end{cases} \tag{4.15}$$

that smoothly falls from one to zero. The new characteristic functions still represent a partition of unity, i.e. (4.4a) still holds. However, the orthogonal decomposition of

the total probability density $|\psi|^2$ is destroyed since

$$\mathcal{W}(r)(1-\mathcal{W}(r)) = \begin{cases} \frac{1}{4}\sin^2\left(\pi\frac{r}{r_c}\right), & |r| \leq r_c, \\ 0, & |r| > r_c \end{cases} \tag{4.16}$$

is not zero everywhere. As a consequence,

$$\sum_{i=0}^{3} \chi_i^2(r_1, r_2, r_3) = \prod_{i=1}^{3} [1 + 2\mathcal{W}(r_i)(\mathcal{W}(r_i) - 1)] \tag{4.17}$$

only equals one if $|r_i| > r_c$ for all i. For the decomposition of the singly- and doubly-ionized probability density $|\psi_1|^2$ and $|\psi_2|^2$, the same problem arises. Therefore, the decomposition of the wave function with (4.15) instead of (4.13) is only an approximate projection. Conceptually, replacing the Heaviside step function by a smooth window function is not a problem since there exists no sharp boundary between "bound" and "ionized" anyway, at least not for the long-range Coulomb potentials considered here. Nevertheless, we expect that the momentum distribution of each charge state also contains small contributions from other charge states. In particular, for single and double ionization, there will be contributions from the other electrons which were projected out.

The momentum distribution of triple ionization (4.10) is a function of three variables. In principle, we could use isosurfaces to visualize it, but it is not a priori clear how to choose the points of constant value. Furthermore, handling the very large data files on a standard computer is almost impossible. Therefore, we express the distributions as a function of other coordinates and integrate, thus ending up with one- and two-dimensional distributions. These transformations are described in the next two sections.

4.1.2. Ion momentum distributions

In order to obtain distributions which have an experimental counterpart, we express the functions (4.10) in terms of the momentum components of the ion with charge $i \in \{1, 2, 3\}$. Since the photon momenta are negligible for the frequencies considered in the present work ($p_\gamma = \mathcal{O}(10^{-4})$ a.u.), the relation between the electron momenta (p_1, p_2, p_3) and the ion momentum $\boldsymbol{p}^{i+}$ follows from momentum conservation

$$\boldsymbol{p}^{i+} = (p_{\perp,x}^{i+}, p_{\perp,y}^{i+}, p_{\parallel}^{i+}) = -\sum_{j=1}^{i} \boldsymbol{p}_j. \tag{4.18}$$

Here, $p_{\parallel}^{i+}$ is the longitudinal (parallel to the field polarization axis) ion momentum while $p_{\perp,x}^{i+}$ and $p_{\perp,y}^{i+}$ are the transversal (perpendicular to the field polarization axis) ion

momenta. The momentum vectors of the electrons follow from (2.6) and are given by

$$\boldsymbol{p}_1 = (p_{1,x}, p_{1,y}, p_{1,z}) = \left(-\frac{1}{2\sqrt{3}} p_1, \quad \frac{1}{2} p_1, \sqrt{\frac{2}{3}} p_1 \right), \tag{4.19a}$$

$$\boldsymbol{p}_2 = (p_{2,x}, p_{2,y}, p_{2,z}) = \left(-\frac{1}{2\sqrt{3}} p_2, -\frac{1}{2} p_2, \sqrt{\frac{2}{3}} p_2 \right), \tag{4.19b}$$

$$\boldsymbol{p}_3 = (p_{3,x}, p_{3,y}, p_{3,z}) = \left(\frac{1}{\sqrt{3}} p_3, 0, \sqrt{\frac{2}{3}} p_3 \right). \tag{4.19c}$$

From equation (4.18), we find

$$p_{\parallel}^{+} = -\sqrt{\frac{2}{3}} p_1, \tag{4.20a}$$

$$p_{\perp,x}^{+} = \frac{1}{2\sqrt{3}} p_1, \tag{4.20b}$$

$$p_{\perp,y}^{+} = -\frac{1}{2} p_1 \tag{4.20c}$$

for the singly-charged ion created by single ionization of electron 1,

$$p_{\parallel}^{2+} = -\sqrt{\frac{2}{3}} \left(p_1 + p_2 \right), \tag{4.21a}$$

$$p_{\perp,x}^{2+} = \frac{1}{2\sqrt{3}} \left(p_1 + p_2 \right), \tag{4.21b}$$

$$p_{\perp,y}^{2+} = -\frac{1}{2} \left(p_1 - p_2 \right) =: p_{\perp}^{2+} \tag{4.21c}$$

for the doubly-charged ion created by double ionization of the electrons 1 and 2 and

$$p_{\parallel}^{3+} = -\sqrt{\frac{2}{3}} \left(p_1 + p_2 + p_3 \right), \tag{4.22a}$$

$$p_{\perp,x}^{3+} = -\frac{1}{2\sqrt{3}} \left(-p_1 - p_2 + 2p_3 \right), \tag{4.22b}$$

$$p_{\perp,y}^{3+} = -\frac{1}{2} \left(p_1 - p_2 \right) \tag{4.22c}$$

for the triply-charged ion created by triple ionization of all three electrons. Note that the transformation $(p_1, p_2, p_3) \rightarrow (p_{\perp,x}^{i+}, p_{\perp,y}^{i+}, p_{\parallel}^{i+})$ produces only one linearly independent ion momentum component for single ionization ($p_{\parallel}^{+}$) and two linearly independent ion momentum components for double ionization ($p_{\parallel}^{2+}$, $p_{\perp}^{2+}$). In other words, there is no new physical information in the other components. For triple ionization, all three ion momentum components are linearly independent but the transversal ones are neither even nor odd under particle exchange, in contrast to the components of single and

double ionization. To circumvent this problem, we introduce polar coordinates in the planes perpendicular to the field polarization axis,

$$p_{\perp,x}^{3+} = p_{\perp}^{3+} \cos\varphi_{\perp}^{3+}, \tag{4.23a}$$

$$p_{\perp,y}^{3+} = p_{\perp}^{3+} \sin\varphi_{\perp}^{3+}. \tag{4.23b}$$

The radial transversal ion momentum

$$p_{\perp}^{3+} = \sqrt{\left(p_{\perp,x}^{3+}\right)^2 + \left(p_{\perp,y}^{3+}\right)^2} = \frac{1}{\sqrt{3}}\sqrt{p_1^2 + p_2^2 + p_3^2 - (p_1p_2 + p_1p_3 + p_2p_3)} \tag{4.24}$$

is obviously invariant under particle exchange. Combining (4.24) and (4.22a), we find the important relation

$$p_1^2 + p_2^2 + p_3^2 = 2(p_{\perp}^{3+})^2 + \frac{1}{2}(p_{\parallel}^{3+})^2. \tag{4.25}$$

Now we can deduce the ion momentum distributions $\widetilde{g}^{i+}$ from the electron momentum distributions g^{i+}. For the singly-charged ion, we find

$$\widetilde{g}^{+}(p_{\parallel}^{+}) = \sqrt{\frac{3}{2}}g^{+}\left(p_1(p_{\parallel}^{+})\right) = \sqrt{\frac{3}{2}}g^{+}\left(-\sqrt{\frac{3}{2}}p_{\parallel}^{+}\right). \tag{4.26}$$

The constant prefactor in the above equation (and in the following equations) results from the substitution rule, i.e.

$$\int g^{+}(p_1)\mathrm{d}p_1 = \int \widetilde{g}^{+}(p_{\parallel}^{+})\mathrm{d}p_{\parallel}^{+}. \tag{4.27}$$

For the doubly-charged ion, the ion momentum distribution is two-dimensional and is given by

$$\widetilde{g}^{2+}(p_{\perp}^{2+}, p_{\parallel}^{2+}) = \sqrt{\frac{3}{2}}g^{2+}\left(p_1(p_{\perp}^{2+}, p_{\parallel}^{2+}), p_2(p_{\perp}^{2+}, p_{\parallel}^{2+})\right). \tag{4.28}$$

By integration, we obtain the longitudinal ion momentum distribution

$$\widetilde{g}^{2+}(p_{\parallel}^{2+}) = \int \widetilde{g}^{2+}(p_{\perp}^{2+}, p_{\parallel}^{2+})\mathrm{d}p_{\perp}^{2+} \tag{4.29}$$

and the transversal ion momentum distribution

$$\widetilde{g}^{2+}(p_{\perp}^{2+}) = \int \widetilde{g}^{2+}(p_{\perp}^{2+}, p_{\parallel}^{2+})\mathrm{d}p_{\parallel}^{2+}. \tag{4.30}$$

Finally, for the triply-charged ion, we obtain a three-dimensional distribution which can be expressed either as a function of the longitudinal ion momentum and the Cartesian transversal ion momenta,

$$\widetilde{g}^{3+}(p_{\perp,x}^{3+}, p_{\perp,y}^{3+}, p_{\parallel}^{3+}) = \sqrt{2}g^{3+}\left(p_j(p_{\perp,x}^{3+}, p_{\perp,y}^{3+}, p_{\parallel}^{3+})\right), \tag{4.31}$$

or as a function of the longitudinal ion momentum, the radial transversal ion momentum and the angle $\varphi_\perp^{3+}$,

$$\widetilde{g}^{3+}(p_\perp^{3+}, \varphi_\perp^{3+}, p_\parallel^{3+}) = \sqrt{2} g^{3+}\left(p_j(p_\perp^{3+}, \varphi_\perp^{3+}, p_\parallel^{3+})\right) \tag{4.32}$$

(where $p_j(\dots) = p_1(\dots), p_2(\dots), p_3(\dots)$). In any case, the longitudinal ion momentum distribution is well-defined and reads

$$\widetilde{g}^{3+}(p_\parallel^{3+}) = \iint \widetilde{g}^{3+}(p_{\perp,x}^{3+}, p_{\perp,y}^{3+}, p_\parallel^{3+}) \mathrm{d}p_{\perp,x}^{3+} \mathrm{d}p_{\perp,y}^{3+} \tag{4.33a}$$

$$= \iint \widetilde{g}^{3+}(p_\perp^{3+}, \varphi_\perp^{3+}, p_\parallel^{3+}) p_\perp^{3+} \mathrm{d}p_\perp^{3+} \mathrm{d}\varphi_\perp^{3+}. \tag{4.33b}$$

In COLTRIMS experiments, the full momentum vector of the triply-charged ion can be measured. Nevertheless, the three-dimensional distribution of the ion momentum components is usually reduced to a two-dimensional version by integrating over one transversal ion momentum component (see e.g. Moshammer *et al.* (2000)). Since the full-dimensional atom-laser system has a cylindrical symmetry with respect to the field axis, the three-dimensional information is retained even in the integrated version (Zrost *et al.*, 2006). Here, we only have a discrete rotational symmetry of 120° around the field axis which can be somewhat eliminated if we integrate over the angle $\varphi_\perp^{3+}$. This gives the two-dimensional distribution

$$\widetilde{g}^{3+}(p_\perp^{3+}, p_\parallel^{3+}) = \int \widetilde{g}^{3+}(p_\perp^{3+}, \varphi_\perp^{3+}, p_\parallel^{3+}) \mathrm{d}\varphi_\perp^{3+} \tag{4.34}$$

and the corresponding transversal ion momentum distribution

$$\widetilde{g}^{3+}(p_\perp^{3+}) = \int \widetilde{g}^{3+}(p_\perp^{3+}, p_\parallel^{3+}) \mathrm{d}p_\parallel^{3+}. \tag{4.35}$$

Furthermore, (4.33b) can be rewritten as

$$\widetilde{g}^{3+}(p_\parallel^{3+}) = \int \widetilde{g}^{3+}(p_\perp^{3+}, p_\parallel^{3+}) p_\perp^{3+} \mathrm{d}p_\perp^{3+}. \tag{4.36}$$

The discrete rotational symmetry can be illustrated by considering the distribution of the Cartesian transversal ion momenta,

$$\widetilde{g}^{3+}(p_{\perp,x}^{3+}, p_{\perp,y}^{3+}) = \int \widetilde{g}^{3+}(p_{\perp,x}^{3+}, p_{\perp,y}^{3+}, p_\parallel^{3+}) \mathrm{d}p_\parallel^{3+}. \tag{4.37}$$

4.1.3. Angular and energy distributions

Instead of transforming to Cartesian or cylindrical ion momentum coordinates, we can also write the electron momentum distribution of i-fold ionization as a function of $i-1$ angles and the total kinetic energy of the electrons

$$E = \sum_{j=1}^{i} \frac{p_j^2}{2}. \tag{4.38}$$

For single ionization, there are only two possible directions, i.e. left and right along the coordinate axis of the electron. From

$$P_1 = \int_{-\infty}^{\infty} g^+(p_1)\mathrm{d}p_1 = \int_0^{\infty} \frac{g^+\left(-\sqrt{2E}\right) + g^+\left(\sqrt{2E}\right)}{\sqrt{2E}}\mathrm{d}E, \tag{4.39}$$

we obtain the energy distribution of single ionization

$$h^+(E) = g^+\left(-\sqrt{2E}\right) + g^+\left(\sqrt{2E}\right). \tag{4.40}$$

For double ionization, we express the electron momentum distribution in polar coordinates

$$p_1 = k\cos\varphi, \tag{4.41a}$$
$$p_2 = k\sin\varphi \tag{4.41b}$$

with $k = \sqrt{2E}$. This transforms the double ionization yield integral to

$$\begin{aligned} P_2 &= \iint g^{2+}(p_1, p_2)\mathrm{d}p_1\mathrm{d}p_2 = \iint g^{2+}(k\cos\varphi, k\sin\varphi)k\mathrm{d}k\mathrm{d}\varphi \\ &= \iint g^{2+}\left(\sqrt{2E}\cos\varphi, \sqrt{2E}\sin\varphi\right)\mathrm{d}E\mathrm{d}\varphi. \end{aligned} \tag{4.42}$$

The angular distribution of double ionization is

$$h^{2+}(\varphi) = \int g^{2+}\left(\sqrt{2E}\cos\varphi, \sqrt{2E}\sin\varphi\right)\mathrm{d}E \tag{4.43}$$

and the energy distribution

$$h^{2+}(E) = \int g^{2+}\left(\sqrt{2E}\cos\varphi, \sqrt{2E}\sin\varphi\right)\mathrm{d}\varphi. \tag{4.44}$$

Finally, for triple ionization, we use spherical coordinates

$$p_1 = k\sin\vartheta\cos\varphi, \tag{4.45a}$$
$$p_2 = k\sin\vartheta\sin\varphi, \tag{4.45b}$$
$$p_3 = k\cos\vartheta \tag{4.45c}$$

to transform the yield integral. Integration gives the angular distribution of triple ionization

$$h^{3+}(\vartheta, \varphi) = \int g^{3+}\left(\sqrt{2E}\sin\vartheta\cos\varphi, \sqrt{2E}\sin\vartheta\sin\varphi, \sqrt{2E}\cos\vartheta\right)\sqrt{2E}\mathrm{d}E \tag{4.46}$$

and the energy distribution

$$h^{3+}(E) = \iint g^{3+}\left(\sqrt{2E}\sin\vartheta\cos\varphi, \sqrt{2E}\sin\vartheta\sin\varphi, \sqrt{2E}\cos\vartheta\right)\sin\vartheta\mathrm{d}\vartheta\mathrm{d}\varphi. \tag{4.47}$$

We will discuss the above distributions only in those cases where they provide additional information on the ionization processes.

4.1.4. Numerical method

To calculate the distributions derived above, we have to represent the wave function $\psi(r_1, r_2, r_3, t_f)$ as accurately as possible while keeping the computational effort small. ψ spatially spreads while the laser field is nonzero, so a non-negligible part of it will reach the grid boundaries during the evolution, unless a very large grid or a very short pulse is used. Without an absorbing potential in the Hamiltonian, the norm is conserved, but the wave function is reflected on the grid boundaries, thus disturbing the spreading and resulting in an incorrect final momentum distribution. With absorbing boundaries, however, the norm decreases with time and the Fourier transform $\widehat{\psi}$ lacks the momentum information contained in the absorbed parts. To overcome this problem, we keep the absorbed parts, but evolve them with Hamiltonians that drop the Coulomb interactions of those electrons which are sufficiently far away from the nucleus. Using the velocity gauge version of the laser-atom interaction where the vector potential is coupled to the electron momenta, the absorbed parts can then be evolved in momentum representation where the reflection problem does not occur.

The procedure we just described is equivalent to the splitting algorithm of Heather and Metiu (1987) (not to be confused with the split-operator method used to calculate the wave function). To understand how it works and to introduce the notation, we study a one-dimensional example with one electron. Consider the velocity-gauge Hamiltonian

$$H_R = \frac{p^2}{2} + V(r) - A(t)p \tag{4.48}$$

with a Coulomb potential $V(r)$. The position space $\mathbb{R}$ is divided into an "inner" region R and an "outer" (or "asymptotic") region R' which are defined by $|r| \leq r_{abs}$ and $|r| > r_{abs}$, respectively. Each region is provided with a wave function. $\psi_R(r)$ is evolved with the Hamiltonian (4.48) and is kept in position representation. $\psi_{R'}$, on the other hand, is evolved with the Hamiltonian

$$H_{R'} = \frac{p^2}{2} - A(t)p \tag{4.49}$$

that neglects $V(r)$. Therefore, $\psi_{R'}$ can be kept in momentum representation, $\widehat{\psi}_{R'}(p)$. In each time step of the evolution, $\psi_R(r)$ is split into two terms,

$$\psi_R(r) = \underbrace{\mathcal{T}(r)\psi_R(r)}_{=:\widetilde{\psi}_R(r)} + \underbrace{(1-\mathcal{T}(r))\psi_R(r)}_{=:\Delta\psi_R^{R'}(r)}, \tag{4.50}$$

using the divider function[1]

$$\mathcal{T}(r) := \begin{cases} 1, & |r| \leq r_{abs}, \\ \mathrm{e}^{-\eta(|r|-r_{abs})^4}, & |r| > r_{abs}. \end{cases} \tag{4.51}$$

[1] In Chapter 3, this exponential tail was created by adding the imaginary potential (3.20) to the Hamiltonian, resulting in a non-unitary time evolution operator. Here, the exponential tail is applied *after* the evolution to the next time step. Other examples for divider functions are given by Grobe *et al.* (1999).

The first term in (4.50),

$$\widetilde{\psi}_R(r) = \begin{cases} \psi_R(r), & |r| \le r_{abs}, \\ \mathrm{e}^{-\eta(|r|-r_{abs})^4}\psi_R(r), & |r| > r_{abs}, \end{cases} \tag{4.52}$$

is the wave function that remains after cutting out the part which has crossed the boundary $|r| = r_{abs}$. This part is equal to the second term in (4.50), i.e.

$$\Delta\psi_R^{R'}(r) = \begin{cases} 0, & |r| \le r_{abs}, \\ \left(1 - \mathrm{e}^{-\eta(|r|-r_{abs})^4}\right)\psi_R(r), & |r| > r_{abs}. \end{cases} \tag{4.53}$$

Here, the subscript specifies the source region (R) and the superscript the target region (R') of the cut out wave function part. In the following, we will refer to $\Delta\psi_R^{R'}$ as the "outgoing part" of the wave function ψ_R. After the wave function has been split according to (4.50), the transfer is completed by coherently adding[2] the Fourier transform of $\Delta\psi_R^{R'}$ to $\widehat{\psi}_{R'}$.

Instead of splitting ψ_R in *each* time step, one could also monitor the norm of ψ_R near $|r| = r_{abs}$ during the pulse and only perform the splitting when the norm exceeds some threshold value, as done by Grobe *et al.* (1999). This would speed up the calculations but the dependence of the results on the threshold value would require careful testing. With a splitting performed in every time step, we are on the safe side, at the price of an increased computation time.

As emphasized by Heather and Metiu (1987), the splitting (4.50) is not a projection, i.e. $\widetilde{\psi}_R(r)$ and $\Delta\psi_R^{R'}(r)$ are not orthogonal to each other. Consequently, the splitting does not conserve the norm of the total wave function. This is seen as follows. Let $\langle\psi_R|\psi_R\rangle = 1$ and $\psi_{R'} = 0$ at $t = 0$. Then the norm of the total wave function $\psi = \psi_R + \psi_{R'}$ is one, too. After the wave functions have been evolved to the next time step, ψ_R has changed, but still fulfills $\langle\psi_R|\psi_R\rangle = 1$ since the time evolution operator is unitary. $\psi_{R'}$ is still equal to zero. Now the first splitting is performed, i.e. ψ_R is replaced by $\widetilde{\psi}_R$ and $\Delta\psi_R^{R'}$ is added to $\psi_{R'}$. Afterwards, the wave functions are evolved with their Hamiltonians H_R and $H_{R'}$ to the next time step, thus acquiring different phase factors $\exp(\mathrm{i}\varphi)$ and $\exp(\mathrm{i}\varphi')$. The norm of the total wave function, evaluated in position representation, now equals

$$\begin{aligned} \langle\psi|\psi\rangle &= \int_{-\infty}^{\infty} |\psi(r)|^2 \mathrm{d}r = \int_{-\infty}^{\infty} |\mathrm{e}^{\mathrm{i}\varphi(r)}\mathcal{T}(r)\psi_R(r) + \mathrm{e}^{\mathrm{i}\varphi'(r)}(1-\mathcal{T}(r))\psi_R(r)|^2 \mathrm{d}r \\ &= 1 - \int_{-\infty}^{-r_{abs}} |\psi_R(r)|^2 2\mathrm{e}^{-\eta(|r|-r_{abs})^4}(1-\mathrm{e}^{-\eta(|r|-r_{abs})^4})[1-\cos(\varphi(r)-\varphi'(r))]\mathrm{d}r \\ &\quad - \int_{r_{abs}}^{\infty} |\psi_R(r)|^2 2\mathrm{e}^{-\eta(|r|-r_{abs})^4}(1-\mathrm{e}^{-\eta(|r|-r_{abs})^4})[1-\cos(\varphi(r)-\varphi'(r))]\mathrm{d}r. \end{aligned} \tag{4.54}$$

Since the integrands are positive, the norm is smaller than one.

[2]In this context, the word coherent shall emphasize that the complex wave functions $\widehat{\psi}_{R'}$ and $\Delta\widehat{\psi}_R^{R'}$ are summed rather than their absolute values, thus allowing for interferences.

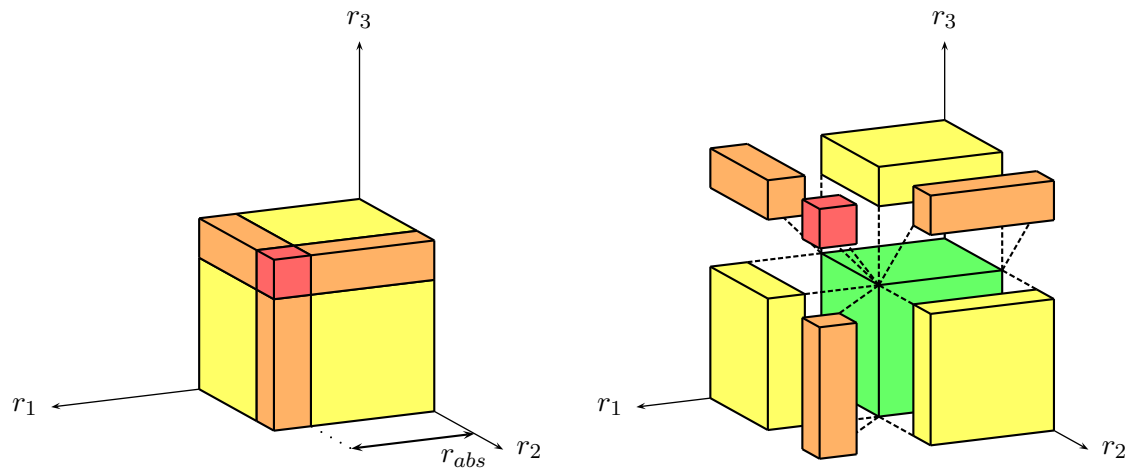

Figure 4.1. Division of the position space (only first octant shown) according to the three-dimensional Heather-Metiu method. In region N (green), the wave function is evolved with the full Eckhardt-Sacha Hamiltonian while the evolution in regions S_i (yellow), regions D_{ij} (orange) and region T (red) omits the Coulomb interaction of one, two and three electrons, respectively.

The Heather-Metiu method was extended to two dimensions by Grobe *et al.* (1999) and Lein *et al.* (2000). We now develop the three-dimensional version. First, the position space is divided into regions X_{ij} as shown in Fig. 4.1. The symbol X indicates how much electrons have crossed the threshold distance r_{abs}, i.e. if the atom is *formally* in a neutral (N), singly- (S), doubly- (D) or triply-ionized (T) state. Additional indices ij specify which electron coordinates exceed r_{abs}. We emphasize that the symbols S, D and T are only chosen for a compact notation – they are not equivalent to the regions R_i of Section 4.1.1 which specify the parts of the wave function in position space that are considered as ionized.

Now we discuss the regions X_{ij} in more detail.

- Region N ($|r_i| \leq r_{abs}\ \forall i$). The electrons interact with each other, the nucleus and the laser field. For the evolution, we use the full three-electron Eckhardt-Sacha Hamiltonian in velocity gauge,

$$H_N = \sum_{i=1}^{3} \left(\frac{p_i^2}{2} - \frac{3}{\sqrt{r_i^2 + \varepsilon^2}} - \sqrt{\frac{2}{3}} A(t) p_i \right) + \sum_{\substack{i,j=1 \\ i<j}}^{3} \frac{1}{\sqrt{(r_i - r_j)^2 + r_i r_j + \varepsilon^2}}. \tag{4.55}$$

  The wave function $\psi_N(r_1, r_2, r_3, t)$ is kept in position representation, apart from the necessary Fourier transforms in the split-operator time evolution.

- Regions S_1, S_2, S_3 (one $|r_i|$ exceeds r_{abs} and two do not). For the evolution, we neglect the Coulomb interactions of the ith electron. As an example, consider

the Hamiltonian of S_1 ($|r_1| > r_{abs}$, $|r_2| \leq r_{abs}$, $|r_3| \leq r_{abs}$),

$$H_{S_1} = \sum_{i=1}^{3} \left(\frac{p_i^2}{2} - \sqrt{\frac{2}{3}} A(t) p_i \right) - \frac{3}{\sqrt{r_2^2 + \varepsilon^2}} - \frac{3}{\sqrt{r_3^2 + \varepsilon^2}} + \frac{1}{\sqrt{(r_2 - r_3)^2 + r_2 r_3 + \varepsilon^2}}. \tag{4.56}$$

The wave function $\psi_{S_1}(p_1, r_2, r_3, t)$ is kept in a mixed position-momentum representation.

- Regions D_{12}, D_{13}, D_{23} (two $|r_i|$ exceed r_{abs} and one does not). For the evolution, we neglect the Coulomb interactions of the electrons i and j. As an example, consider the Hamiltonian of D_{12} ($|r_1| > r_{abs}$, $|r_2| > r_{abs}$, $|r_3| \leq r_{abs}$),

$$H_{D_{12}} = \sum_{i=1}^{3} \left(\frac{p_i^2}{2} - \sqrt{\frac{2}{3}} A(t) p_i \right) - \frac{3}{\sqrt{r_3^2 + \varepsilon^2}}. \tag{4.57}$$

Again, the wave function $\psi_{D_{12}}(p_1, p_2, r_3, t)$ is kept in a mixed position-momentum representation.

- Region T ($|r_i| > r_{abs}$ $\forall i$). For the evolution, we only keep the interaction of the electrons with the laser,

$$H_T = \sum_{i=1}^{3} \left(\frac{p_i^2}{2} - \sqrt{\frac{2}{3}} A(t) p_i \right). \tag{4.58}$$

The wave function $\psi_T(p_1, p_2, p_3, t)$ is kept in momentum representation throughout the whole calculation – since there is no potential, Fourier transforms are not necessary.

The union of the regions 0, 1, 2 and 3 introduced in Chapter 3 is equal to region N while the absorbing region is equal to the union of S, D and T. The total wave function of the three-electron system is the coherent sum

$$\psi = \psi_N + \psi_{S_1} + \psi_{S_2} + \psi_{S_3} + \psi_{D_{12}} + \psi_{D_{13}} + \psi_{D_{23}} + \psi_T. \tag{4.59}$$

Before the laser pulse hits the atom, we have $\psi = \psi_N$ and $\psi_{S_i} = \psi_{D_{ij}} = \psi_T = 0$. Due to the indistinguishability of the electrons, S_1, S_2 and S_3, as well as D_{12}, D_{13} and D_{23}, are physically equivalent, so it is sufficient to consider S_1 and D_{12} in the following.

If each of the above Hamiltonians was studied independently, i.e. if there was no transfer of probability between the regions, we would have the exact factorizations

$$\psi_{S_1}(p_1, r_2, r_3, t) = \phi(p_1, t) \psi_{\mathrm{Ne}^+}(r_2, r_3, t), \tag{4.60a}$$

$$\psi_{D_{12}}(p_1, p_2, r_3, t) = \phi(p_1, t) \phi(p_2, t) \psi_{\mathrm{Ne}^{2+}}(r_3, t), \tag{4.60b}$$

$$\psi_T(p_1, p_2, p_3, t) = \phi(p_1, t) \phi(p_2, t) \phi(p_3, t) \tag{4.60c}$$

where $\phi(p,t)$ is the wave function of a one-dimensional electron in the time-dependent laser field, i.e. a solution of the equation

$$\mathrm{i}\frac{\partial}{\partial t}\phi(p,t) = \left[\frac{p^2}{2} - \sqrt{\frac{2}{3}}A(t)p\right]\phi(p,t). \tag{4.61}$$

With the transfer, the factorizations only hold approximately. However, they are assumed to hold exactly in order for the transfer to make sense.

Having defined the regions, we can develop the splitting of the respective wave functions. In two or three spatial dimensions, the outgoing parts $\Delta\psi$ can cross multiple boundaries simultaneously or sequentially, so the splitting is a little more elaborate than (4.50). Writing $\mathcal{T}_i := \mathcal{T}(r_i)$ and $\Delta\psi_N := (1-\mathcal{T}_1\mathcal{T}_2\mathcal{T}_3)\psi_N$ for short, the splitting of the wave function in region N reads

$$\begin{aligned}
\psi_N = {} & \underbrace{\mathcal{T}_1\mathcal{T}_2\mathcal{T}_3\psi_N}_{=:\widetilde{\psi}_N} + \underbrace{\mathcal{T}_2\mathcal{T}_3\Delta\psi_N\Theta(|r_1|-r_{abs})}_{=:\Delta\psi_N^{S_1}} + \underbrace{\mathcal{T}_1\mathcal{T}_3\Delta\psi_N\Theta(|r_2|-r_{abs})}_{=:\Delta\psi_N^{S_2}} \\
& + \underbrace{\mathcal{T}_1\mathcal{T}_2\Delta\psi_N\Theta(|r_3|-r_{abs})}_{=:\Delta\psi_N^{S_3}} + \underbrace{\mathcal{T}_3(1-\mathcal{T}_1-\mathcal{T}_2)\Delta\psi_N\Theta(|r_1|-r_{abs})\Theta(|r_2|-r_{abs})}_{=:\Delta\psi_N^{D_{12}}} \\
& + \underbrace{\mathcal{T}_2(1-\mathcal{T}_1-\mathcal{T}_3)\Delta\psi_N\Theta(|r_1|-r_{abs})\Theta(|r_3|-r_{abs})}_{=:\Delta\psi_N^{D_{13}}} \\
& + \underbrace{\mathcal{T}_1(1-\mathcal{T}_2-\mathcal{T}_3)\Delta\psi_N\Theta(|r_2|-r_{abs})\Theta(|r_3|-r_{abs})}_{=:\Delta\psi_N^{D_{23}}} \\
& + \underbrace{(1+\mathcal{T}_1\mathcal{T}_2+\mathcal{T}_1\mathcal{T}_3+\mathcal{T}_2\mathcal{T}_3-\mathcal{T}_1-\mathcal{T}_2-\mathcal{T}_3)\Delta\psi_N\prod_{j=1}^{3}\Theta(|r_j|-r_{abs})}_{=:\Delta\psi_N^{T}}\,.
\end{aligned} \tag{4.62a}$$

The wave function of region S_1 does not depend on r_1 and is decomposed as

$$\begin{aligned}
\psi_{S_1} = {} & \underbrace{\mathcal{T}_2\mathcal{T}_3\psi_{S_1}}_{=:\widetilde{\psi}_{S_1}} + \underbrace{\mathcal{T}_3(1-\mathcal{T}_2\mathcal{T}_3)\Theta(|r_2|-r_{abs})\psi_{S_1}}_{=:\Delta\psi_{S_1}^{D_{12}}} + \underbrace{\mathcal{T}_2(1-\mathcal{T}_2\mathcal{T}_3)\Theta(|r_3|-r_{abs})\psi_{S_1}}_{=:\Delta\psi_{S_1}^{D_{13}}} \\
& + \underbrace{(1-\mathcal{T}_2-\mathcal{T}_3)(1-\mathcal{T}_2\mathcal{T}_3)\Theta(|r_2|-r_{abs})\Theta(|r_3|-r_{abs})\psi_{S_1}}_{=:\Delta\psi_{S_1}^{T}}\,.
\end{aligned} \tag{4.62b}$$

Note that there is no term $\Delta\psi_{S_1}^{D_{23}}$ since it would correspond to a part of the wave function ψ_{S_1} ($|r_1| > r_{abs}$) extending into the region where $|r_1| < r_{abs}$. On the one hand, ψ_{S_1} does not depend on r_1 and can therefore not be split with respect to this coordinate. On the other hand, the transfer is geometrically impossible since S_1 and D_{23} are not adjacent to each other. For the wave function of region D_{12} which depends

Transfer	FT dimension	Example
$N \to S_i$	1	$\Delta\psi_N^{S_1}(\underline{r_1}, r_2, r_3, t)$
$N \to D_{ij}$	2	$\Delta\psi_N^{D_{12}}(\underline{r_1}, \underline{r_2}, r_3, t)$
$N \to T$	3	$\Delta\psi_N^{T}(\underline{r_1}, \underline{r_2}, \underline{r_3}, t)$
$S_i \to D_{ij}$	1	$\Delta\psi_{S_1}^{D_{12}}(p_1, \underline{r_2}, r_3, t)$
$S_i \to T$	2	$\Delta\psi_{S_1}^{T}(p_1, \underline{r_2}, \underline{r_3}, t)$
$D_{ij} \to T$	1	$\Delta\psi_{D_{12}}^{T}(p_1, p_2, \underline{r_3}, t)$

Table 4.1. Fourier transforms used for the transfer of the wave function between the regions shown in Fig. 4.1. In the examples, the coordinates with respect to which the wave function is Fourier transformed are underlined.

neither on r_1 nor on r_2, the splitting reads

$$\psi_{D_{12}} = \underbrace{\mathcal{T}_3\psi_{D_{12}}}_{=:\widetilde{\psi}_{D_{12}}} + \underbrace{(1-\mathcal{T}_3)\psi_{D_{12}}}_{=:\Delta\psi_{D_{12}}^{T}}. \tag{4.62c}$$

Finally, we note that the wave function of region T is not split since it depends on none of the coordinates. The reader can convince himself that the above splittings are correct by verifying that all wave function prefactors on the right-hand sides of (4.62a-c) sum up to one, no matter how the coordinates r_1, r_2 and r_3 are chosen.

Overall, the wave functions are updated in each time step according to

$$\psi_N \longrightarrow \widetilde{\psi}_N, \tag{4.63a}$$
$$\psi_{S_i} \longrightarrow \widetilde{\psi}_{S_i} + \Delta\psi_N^{S_i}, \tag{4.63b}$$
$$\psi_{D_{ij}} \longrightarrow \widetilde{\psi}_{D_{ij}} + \Delta\psi_N^{D_{ij}} + \Delta\psi_{S_i}^{D_{ij}} + \Delta\psi_{S_j}^{D_{ij}}, \tag{4.63c}$$
$$\psi_T \longrightarrow \psi_T + \Delta\psi_N^T + \Delta\psi_{S_1}^T + \Delta\psi_{S_2}^T + \Delta\psi_{S_3}^T + \Delta\psi_{D_{12}}^T + \Delta\psi_{D_{13}}^T + \Delta\psi_{D_{23}}^T. \tag{4.63d}$$

The necessary Fourier transforms are listed in Table 4.1. Note the one-way character of the splitting algorithm – once a wave function part has crossed a boundary and is transferred to another region, there is no way back. While this is no problem for single ionization, rescattering (and nonsequential ionization) might be hampered if the excursion of the electron accelerated in the laser field is too large. Therefore, we want the boundary r_{abs} to be as far out as possible (cf. the discussion in Section 4.1.6).

At the end of the simulation ($t = t_f$), we formally have to Fourier transform all wave functions to position space, collect them in the final wave function (4.59), extract the different charge state wave functions from it with the projection (4.14) where the rectangular function is replaced by the Hann window function (4.15), and finally calculate the distributions (4.10) by performing one or more additional Fourier transforms back to momentum space. However, the projection (4.14) is linear and (4.59) is a linear superposition of wave functions, so we can also project each wave function separately

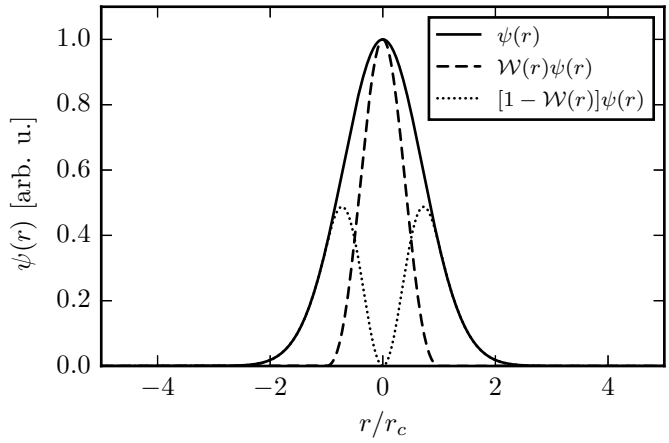

Figure 4.2. Splitting of a Gaussian wave function $\psi(r)$ (solid curve) into a bound part (dashed curve) and an ionized part (dotted curve) with the Hann window function $\mathcal{W}(r)$.

before adding them. Moreover, for the regions S_1 and D_{12}, we found that it makes virtually no difference whether the position-space wave functions ($\psi_{S_1}(r_1, r_2, r_3)$ and $\psi_{D_{12}}(r_1, r_2, r_3)$) are projected with respect to all three electrons or the mixed position-momentum wave functions ($\psi_{S_1}(p_1, r_2, r_3)$ and $\psi_{D_{12}}(p_1, p_2, r_3)$) are projected only with respect to the bound electrons ($2, 3$ and 3). In the second case, the wave function can be kept in momentum representation with respect to the ionized electrons (1 and $1, 2$). Therefore, the number of Fourier transforms is reduced and the calculation of the distributions (4.10) is less time-consuming. With the abbreviation $\mathcal{W}_i := \mathcal{W}(r_i)$ for the window function, the (quasi-)projections of the wave functions read

$$\begin{aligned}
\psi_N = {} & \underbrace{\mathcal{W}_1\mathcal{W}_2\mathcal{W}_3\psi_N}_{\text{no electron ionized}} + \underbrace{(1-\mathcal{W}_1)\mathcal{W}_2\mathcal{W}_3\psi_N}_{\text{electron 1 ionized}} + \underbrace{\mathcal{W}_1(1-\mathcal{W}_2)\mathcal{W}_3\psi_N}_{\text{electron 2 ionized}} + \underbrace{\mathcal{W}_1\mathcal{W}_2(1-\mathcal{W}_3)\psi_N}_{\text{electron 3 ionized}} \\
& + \underbrace{(1-\mathcal{W}_1)(1-\mathcal{W}_2)\mathcal{W}_3\psi_N}_{\text{electrons 1, 2 ionized}} + \underbrace{(1-\mathcal{W}_1)\mathcal{W}_2(1-\mathcal{W}_3)\psi_N}_{\text{electrons 1, 3 ionized}} + \underbrace{\mathcal{W}_1(1-\mathcal{W}_2)(1-\mathcal{W}_3)\psi_N}_{\text{electrons 2, 3 ionized}} \\
& + \underbrace{(1-\mathcal{W}_1)(1-\mathcal{W}_2)(1-\mathcal{W}_3)\psi_N}_{\text{all electrons ionized}}, \qquad (4.64a) \\
\psi_{S_1} = {} & \underbrace{\mathcal{W}_2\mathcal{W}_3\psi_{S_1}}_{\text{electron 1 ionized}} + \underbrace{(1-\mathcal{W}_2)\mathcal{W}_3\psi_{S_1}}_{\text{electrons 1, 2 ionized}} + \underbrace{\mathcal{W}_2(1-\mathcal{W}_3)\psi_{S_1}}_{\text{electrons 1, 3 ionized}} \\
& + \underbrace{(1-\mathcal{W}_2)(1-\mathcal{W}_3)\psi_{S_1}}_{\text{all electrons ionized}}, \qquad (4.64b) \\
\psi_{D_{12}} = {} & \underbrace{\mathcal{W}_3\psi_{D_{12}}}_{\text{electrons 1, 2 ionized}} + \underbrace{(1-\mathcal{W}_3)\psi_{D_{12}}}_{\text{all electrons ionized}}, \qquad (4.64c) \\
\psi_T = {} & \psi_T. \qquad (4.64d)
\end{aligned}$$

For a one-dimensional Gaussian wave function ψ, the splitting induced by the window function is illustrated in Fig. 4.2.

4.1.5. Pulse parameters

The laser pulse parameters were already discussed in Section 2.3. For the analysis of the momentum distributions, we pick five field amplitudes F_0 from our interval, namely 0.15 a.u., 0.2 a.u., 0.3 a.u., 0.4 a.u. and 0.5 a.u. The first value is favored over $F_0 = 0.1$ a.u. since a high-accuracy calculation of the momentum distribution is difficult for such a small field amplitude. The distributions are calculated for both frequencies ($\omega_0 = 0.06$ a.u. and $\omega_0 = 0.1$ a.u.), $\varphi_0 = 0$ and $n_c = 5$. The restriction to one value of n_c arises from the limited computational resources available for this work.

4.1.6. Numerical parameters

Most of the numerical parameters were already discussed in Section 3.3.2, so we focus on those which are important for the momentum distributions. If Δr is the position grid spacing and $L = N\Delta r$ is the position grid length, the momentum grid spacing is

$$\Delta p = \frac{2\pi}{L} \tag{4.65}$$

and the momentum grid length is $L_p = N\Delta p$ with

$$p_{min} = -\frac{\pi}{\Delta r}, \tag{4.66a}$$

$$p_{max} = \frac{\pi}{\Delta r} - \Delta p. \tag{4.66b}$$

The apparent asymmetry in the momenta is remedied by the Fourier method used to calculate the wave function (see Section 3.3.1 and Appendix D.1). To determine suitable values for Δr and L, several test calculations were performed which yielded two results. First, for all frequencies and field amplitudes considered, the significant part of the electron momentum distribution is confined to a cube of side length 16 a.u. around the origin in momentum space. Secondly, the shape of the momentum distribution in this cube strongly depends on L. Following the first observation, we can continue to use $\Delta r = 0.39$ a.u. since $|p_{min}| = 8$ a.u. and $L_p = 16$ a.u. in this case. The second observation suggests that L is the crucial parameter of the calculation. Due to the use of the splitting algorithm with its characteristic distance $r_{abs} = L/2 - 50$ a.u., this is not surprising. As seen from the one-dimensional example (4.54), the norm is approximately conserved if the wave function is either negligible beyond r_{abs} or the laser-electron interaction is much larger than the Coulomb interactions in this regime ($\varphi \approx \varphi'$). Therefore, we want r_{abs} and L to be as large as possible. With the chosen position grid spacing, we can achieve $r_{abs} = 200$ a.u. ($L = 500$ a.u.), a value which was used in several double ionization calculations (Grobe *et al.*, 1999; Lein *et al.*, 2000; Prauzner-Bechcicki *et al.*, 2008).

The influence of L on the momentum grid spacing (4.54) is rather unimportant since already $L = 200$ a.u. gives a momentum resolution which is better than in

Parameter	Symbol	Value
Position grid length	L	500 a.u.
Position grid spacing	Δr	100/256 a.u.
Time step	Δt	0.05 a.u.
Number of time steps	N_t	$\left\lceil \frac{2\pi(n_c+1)}{\omega_0 \Delta t} \right\rceil$
Splitting algorithm boundary	r_{abs}	$L/2 - 50$ a.u.
Strength of divider function	η	10^{-5} a.u.
Ionization radius	r_c	50 a.u.
Gaussian smoothing width	σ_p	0.07 a.u.

Table 4.2. Numerical parameters used for the calculation of the momentum distributions in this work. $\lceil x \rceil = \min\{n \in \mathbb{Z} \mid n \geq x\}$ is the ceiling function.

any COLTRIMS experiment reported until now[3]. For this reason, and to remove substructures resulting from the discretization of the wave function (Prauzner-Bechcicki *et al.*, 2007), the resolution of the momentum distributions is reduced by convolving them with a Gaussian function with respect to each momentum coordinate. This method is known as Gaussian smoothing. Following Prauzner-Bechcicki *et al.* (2008), the FWHM of the Gaussian is set to $\sigma_p = 0.07$ a.u. which equals the best COLTRIMS momentum resolution reported for double ionization until now (Weckenbrock *et al.*, 2004). Since σ_p is much smaller than the typical width of the momentum distribution in each direction (which approximately scales with the square root of the ponderomotive energy), the Gaussian smoothing does not seriously perturb the large-scale structures in the results.

Finally, we must choose a value for the "ionization radius" r_c beyond which an electron is considered ionized. In contrast to Chapter 3, we do not integrate probability fluxes, so there is no need to use a very small value of r_c. However, r_{abs} can be considered as an upper bound for r_c since the Coulomb interactions are neglected beyond this distance anyway. Again, we follow Prauzner-Bechcicki *et al.* (2008) and set $r_c = 50$ a.u.

The numerical parameters for the calculation of the momentum distributions are summarized in Table 4.2. In the next section, we justify our choices of Δr, L and r_c.

4.1.7. Suitability of numerical parameters

To investigate the dependence of the momentum distributions on Δr and L, it is sufficient to consider $\omega_0 = 0.06$ a.u. since, compared to $\omega_0 = 0.1$ a.u., the spreading of the wave function in position space is increased and the momentum distributions will therefore be influenced more strongly by the splitting algorithm. We only consider two extreme cases for the field amplitude, i.e. a small one which is in the nonsequential regime of double and triple ionization ($F_0 = 0.15$ a.u.) and a large one which is in the

[3]For a discussion of momentum resolutions achievable with COLTRIMS, see e.g. Ullrich *et al.* (2003).

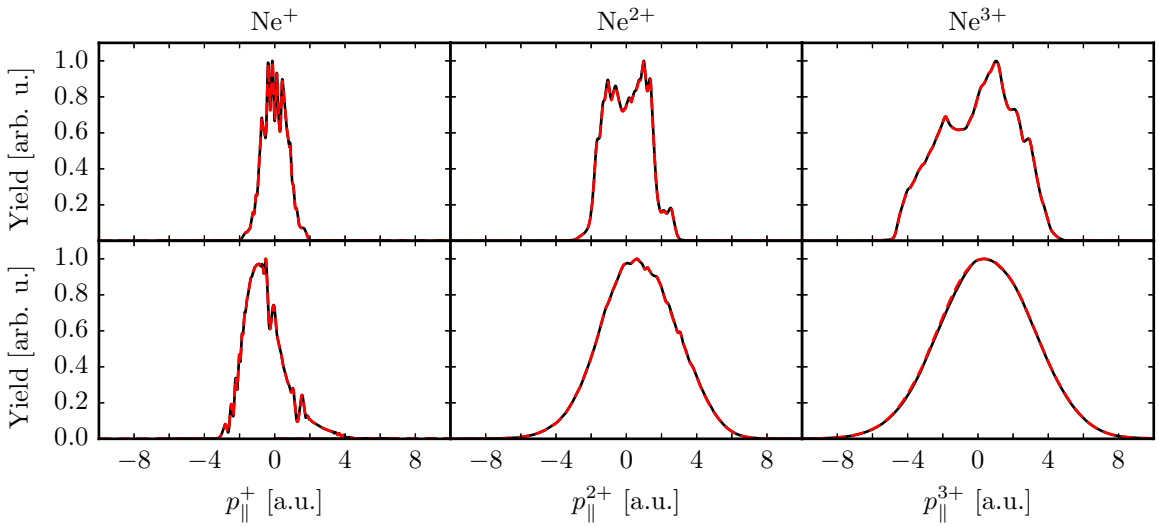

Figure 4.3. Longitudinal Ne^{i+} ion momentum distributions for $n_c = 5$, $\omega_0 = 0.06$ a.u. with $F_0 = 0.15$ a.u. (first row) and $F_0 = 0.5$ a.u. (second row). The position grid length is $L = 300$ a.u., the position grid spacing is $\Delta r = 0.39$ a.u. (black curves) and $\Delta r = 0.2$ a.u. (dashed red curves). All other numerical parameters are those from Table 4.2.

sequential regime ($F_0 = 0.5$ a.u.). Furthermore, we restrict ourselves to the longitudinal ion momentum distributions of each charge state. Since these one-dimensional functions are found by integration, the calculation errors add up and we expect a greater sensitivity to numerical parameter changes. To facilitate comparison, all momentum distributions are normalized to a maximum yield of 1 a.u.

In Fig. 4.3, we show the momentum distributions for $L = 300$ a.u. and the two position grid spacings $\Delta r = 0.2$ a.u. (dashed red curves) and $\Delta r = 0.39$ a.u. (black curves). We find that the differences are negligible, justifying the use of the larger grid spacing in the following. In contrast, the dependence of the distributions on L is much stronger, as apparent from Fig. 4.4. Nevertheless, we observe a rapid convergence of the results as L is increased, with no significant changes beyond $L = 500$ a.u. Therefore, we can safely settle for this grid length.

Next, we can ask how a change of the ionization radius r_c affects the momentum distributions. This is shown in Fig. 4.5. For the smaller field amplitude (first row), a larger value of r_c results in a deeper minimum near zero longitudinal momentum in all cases. For the larger field amplitude (second row), in contrast, changing r_c has almost no influence on the distributions[4]. This can be explained as follows. If F_0 is small, the probability of tunnel ionization and associated processes (such as rescattering) are small so that very few electron wave packets reach a large distance from the nucleus. As a result, the probability density in position space at the end of the pulse is still

[4]The maximum yield shrinks with increasing r_c, but this is not visible due to the normalization of the distributions to a maximum yield of 1 a.u.

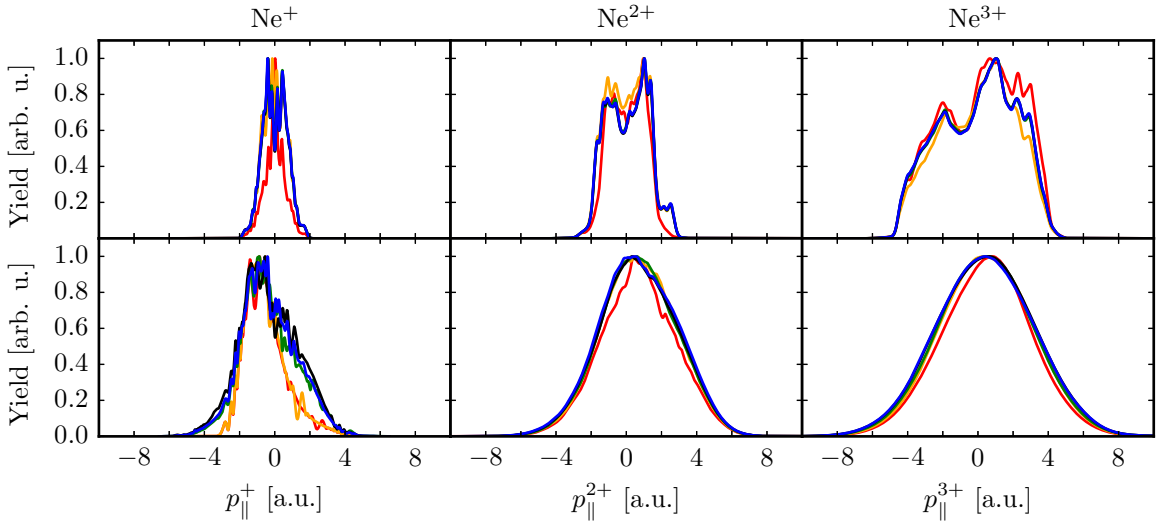

Figure 4.4. Longitudinal Ne^{i+} ion momentum distributions for $n_c = 5$, $\omega_0 = 0.06$ a.u. with $F_0 = 0.15$ a.u. (first row) and $F_0 = 0.5$ a.u. (second row). The position grid spacing is $\Delta r = 0.39$ a.u., the position grid length is $L = 200$ a.u. (red curves), $L = 300$ a.u. (orange curves), $L = 400$ a.u. (green curves), $L = 500$ a.u. (black curves) and $L = 600$ a.u. (blue curves). All other numerical parameters are those from Table 4.2.

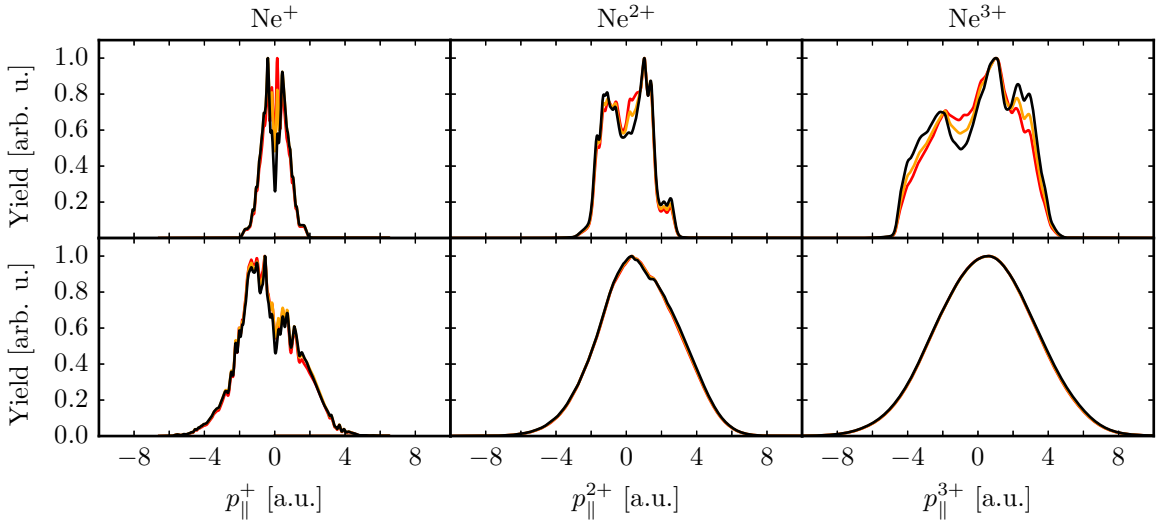

Figure 4.5. Longitudinal Ne^{i+} ion momentum distributions for $n_c = 5$, $\omega_0 = 0.06$ a.u. with $F_0 = 0.15$ a.u. (first row) and $F_0 = 0.5$ a.u. (second row). The ionization radius is $r_c = 25$ a.u. (red curves), $r_c = 50$ a.u. (orange curves) and $r_c = 100$ a.u. (black curves). All other numerical parameters are those from Table 4.2.

close to that of the ground state, i.e. most of the probability is concentrated around $r_1 = r_2 = r_3 = 0$. A small amount of probability, however, is located at larger distances. In this part of the wave function, small (large) distances $|r_i|$ from the nucleus roughly correspond to small (large) momenta p_i, i.e. "slow" ("fast") electrons. Therefore, the larger r_c, the more small distances are removed from the underlying wave function and the less small momenta are contained in the momentum distribution. For large values of F_0, on the other hand, the tunneling (or OBI) probability is so high that the electrons cans easily reach large distances. Consequently, most of the probability will be located further out and the large-distance part of the wave function is less sensitive to a change of r_c.

In summary, we have established the suitability of the chosen parameters Δr, L and r_c. From now on, we will use the numerical parameters of Table 4.2, except where indicated otherwise.

4.2. Results

In this section, we present and discuss the momentum distributions for the five-cycle pulse. Each ionization stage is considered separately.

4.2.1. Single ionization

We begin with a short reminder of the classical constraints of the ion momentum for single ionization (Feuerstein *et al.*, 2000). According to the simple man's model (see Section 3.6.1) described by Newton's equation

$$\ddot{x}(t) = -\sqrt{\frac{2}{3}}F(t), \tag{4.67}$$

the final drift momentum of an electron tunneling out at time t_0 with zero initial momentum is, for our pulse,

$$\dot{x}(T_p) = \sqrt{\frac{2}{3}}[\underbrace{A(T_p)}_{=0} - A(t_0)] = \sqrt{\frac{2}{3}}\frac{F_0}{\omega_0}(-1)^{n_c+1}\sin^2\left(\frac{\pi t_0}{T_p}\right)\sin(\omega_0 t_0). \tag{4.68}$$

The corresponding longitudinal Ne^+ ion drift momentum at the end of the pulse is

$$p_\parallel^+(T_p) = -\sqrt{\frac{2}{3}}\dot{x}(T_p) = \frac{2}{3}\frac{F_0}{\omega_0}(-1)^{n_c}\sin^2\left(\frac{\pi t_0}{T_p}\right)\sin(\omega_0 t_0). \tag{4.69}$$

The maximum drift momentum of the Ne^+ ion is $|p_\parallel^+| = 2F_0/(3\omega_0) = 2\cdot 2\sqrt{U_p}/3$ which can only be reached if the electron tunnels at a zero-crossing of the electric field $F(t)$, i.e. at an extremum of the vector potential $A(t)$. Since the tunneling probability is zero at a zero-crossing, we expect cut-offs in the ion momentum distribution at

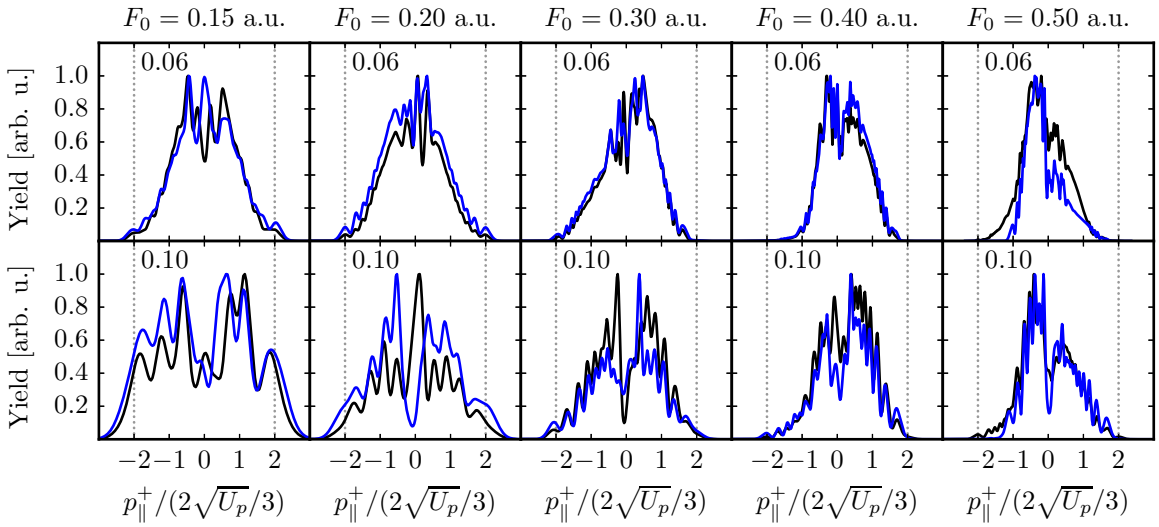

Figure 4.6. Longitudinal Ne^+ ion momentum distributions for $n_c = 5$, $\omega_0 = 0.06$ a.u. (first row) and $n_c = 5$, $\omega_0 = 0.1$ a.u. (second row), calculated from the three-dimensional model (black curves) and from the one-dimensional SAE approximation (blue curves). The dotted lines indicate the classical momentum limits of single ionization ($p_\parallel^+ = \pm 2 \cdot 2\sqrt{U_p}/3$).

$p_\parallel^+ = \pm 2 \cdot 2\sqrt{U_p}/3$. The maxima of the tunneling probability, on the other hand, coincide with the extrema of $F(t)$, i.e. the turning points of $A(t)$. For long pulses, one has $A(t) \approx 0$ at all turning points. For short pulses, the vector potential differs significantly from zero at some of the turning points. However, the global maximum of the tunneling probability remains at $t = T_p/2$ where $A(t) = 0$. Therefore, we expect the maximum of the longitudinal Ne^+ ion momentum distribution in the vicinity of $p_\parallel^+ = 0$, both for long and short pulses.

The longitudinal Ne^+ ion momentum distributions for $n_c = 5$ and both frequencies are shown in Fig. 4.6. Most of them are in qualitative agreement with the tunneling-weighted classical picture described above, i.e. near-zero momenta are favored over larger ones and the distributions are bounded by the maximum classical drift momentum of the Ne^+ ion (indicated by the vertical dotted lines). However, the *shape* of the distributions is in marked contrast to tunneling theory which predicts a smooth Gaussian function (Delone and Krainov, 1991)

$$\widetilde{g}^+(p_\parallel^+) = g_0 \exp\left(-\left(\frac{3}{2}\right)^{3/2} \frac{(2E_I)^{3/2}\omega_0^2}{3F_0^3}(p_\parallel^+)^2\right) \tag{4.70a}$$

$$= g_0 \exp\left(-\sqrt{\frac{2}{3}}\frac{(2E_I)^{3/2}}{12F_0}\left(\frac{p_\parallel^+}{2\sqrt{U_p}/3}\right)^2\right) \tag{4.70b}$$

peaking at $p_\parallel^+ = 0$. Instead, all distributions, especially those for the higher frequency, show a rich structure of peaks and a minimum near zero longitudinal ion momentum.

Both effects have also been observed in a number of experiments (Moshammer *et al.*, 2003; Rudenko *et al.*, 2004; Alnaser *et al.*, 2006; Liu *et al.*, 2007). Finally, for $p_\parallel^+$ in units of $2\sqrt{U_p}/3$, the distributions get notably narrower as F_0 is increased. This contradicts (4.70b) where the scaled FWHM increases with $\sqrt{F_0}$.

In Chapter 3, we were able to reproduce the *integral* Ne^+ yield with a one-dimensional SAE approximation, so one may wonder if this is also possible for the momentum-resolved yield. In one dimension, the formalism of Section 4.1 is dramatically simplified and the momentum distributions can be calculated rapidly. The results are shown in Fig. 4.6 as blue curves. Remarkably, the SAE momentum distributions follow the three-dimensional distributions quite well, even capturing the positions of most peaks. Perfect agreement cannot be expected for at least two reasons. First of all, the projection technique used to determine the wave function of the singly-ionized atom (see Section 4.1.1) cannot eliminate the second and third electron completely from the three-dimensional distributions. Secondly, Fig. 3.21 shows that the eigenvalue spectra of the three-electron Hamiltonian (2.7) and the SAE Hamiltonian (3.31) are different below the one-electron continuum (albeit similar), so the tunneling probabilities and resonance conditions are different as well.

Within the SAE approximation, we can investigate the dependence of the peaks and dips on the pulse parameters without effort. First, since equation (4.70) was derived in the quasistatic limit ($\omega_0 \to 0$), decreasing the frequency should yield distributions with a more Gaussian shape. This expectation is confirmed by Fig. 4.7 where we compare the five-cycle SAE momentum distributions of four frequencies ($\omega_0 = 0.1$ a.u., $\omega_0 = 0.06$ a.u., $\omega_0 = 0.035$ a.u. and $\omega_0 = 0.023$ a.u.[5]). The smaller the value of ω_0 for fixed F_0, the less structure is observed in the edges of the distributions and the better they can be fitted with Gaussians (red curves). Nevertheless, even for the smallest frequency, there is considerable structure in the distributions close to $p_\parallel^+ = 0$ which, according to the semiclassical picture outlined in the first paragraph, results from electrons tunneling near the extrema of the field. The structures persist and get more symmetric if the pulse duration is increased (Fig. 4.8). In contrast, the structures are reduced if a shorter pulse is used (Fig. 4.9).

The above observations suggest an interpretation of the momentum distributions in terms of interfering classical trajectories. On the one hand, such an approach is attractive as it would easily explain why the peaks in the momentum distributions of the SAE approximation and the three-dimensional model nearly coincide. On the other hand, interfering classical trajectories can explain the related one-electron phenomena of high harmonic generation and above-threshold ionization, as shown by van de Sand and Rost (2000) and de Bohan *et al.* (2002). Our approach to explain the structures in the ion momentum distributions of single ionization is inspired by these works, but much simpler in nature. In our qualitative model, the electron motion is described by the one-dimensional simple man's model (equation (4.67)) but the electrons are represented by Gaussian wave packets instead of point charges. The momentum distribution

[5]The choice of the additional frequencies is motivated by the experiment of Alnaser *et al.* (2008).

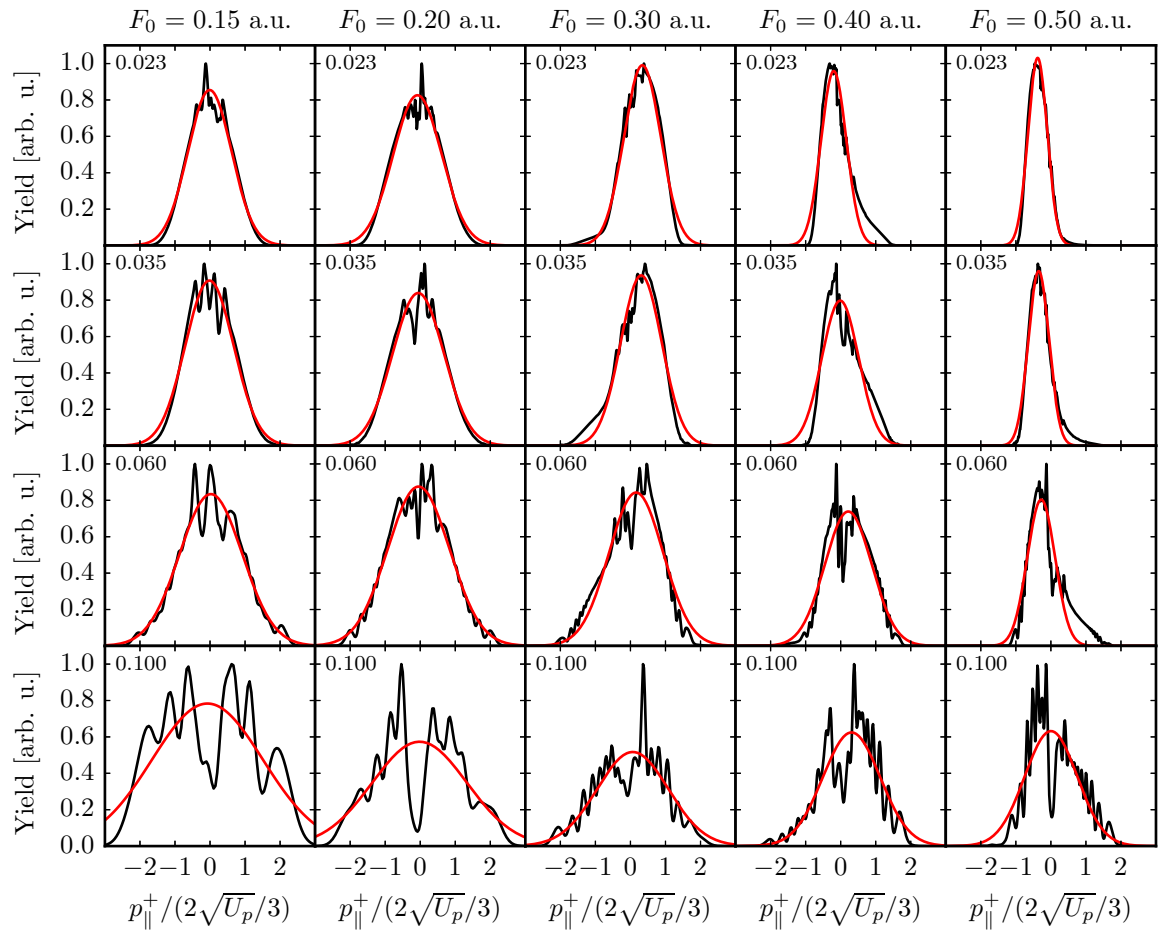

Figure 4.7. SAE Ne^+ ion momentum distributions (black curves) for $n_c = 5$ and (from top to bottom) $\omega_0 = 0.023$ a.u., $\omega_0 = 0.035$ a.u., $\omega_0 = 0.06$ a.u. and $\omega_0 = 0.1$ a.u., compared to the result of a Gaussian curve fit (red curves).

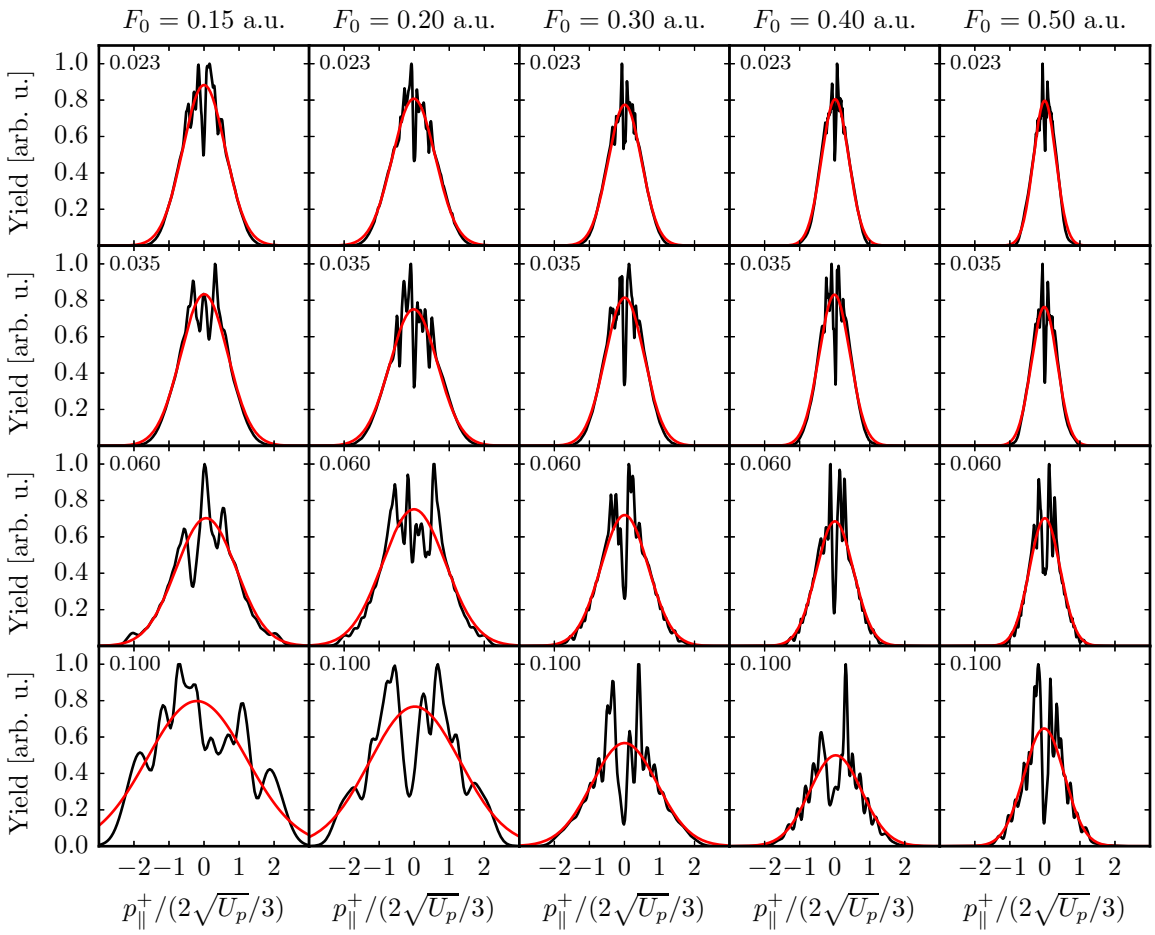

Figure 4.8. Same as Fig. 4.7, but for $n_c = 20$.

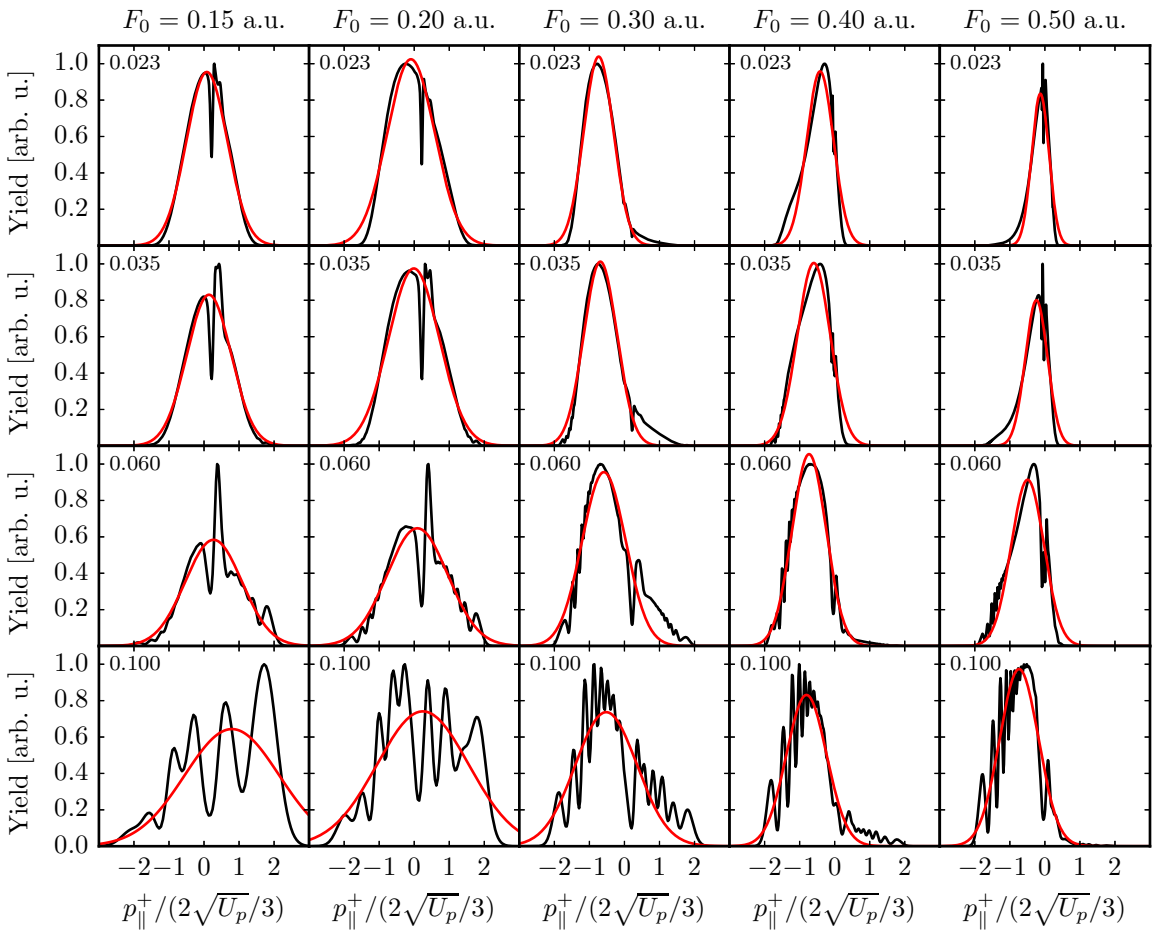

Figure 4.9. Same as Fig. 4.7, but for $n_c = 2$.

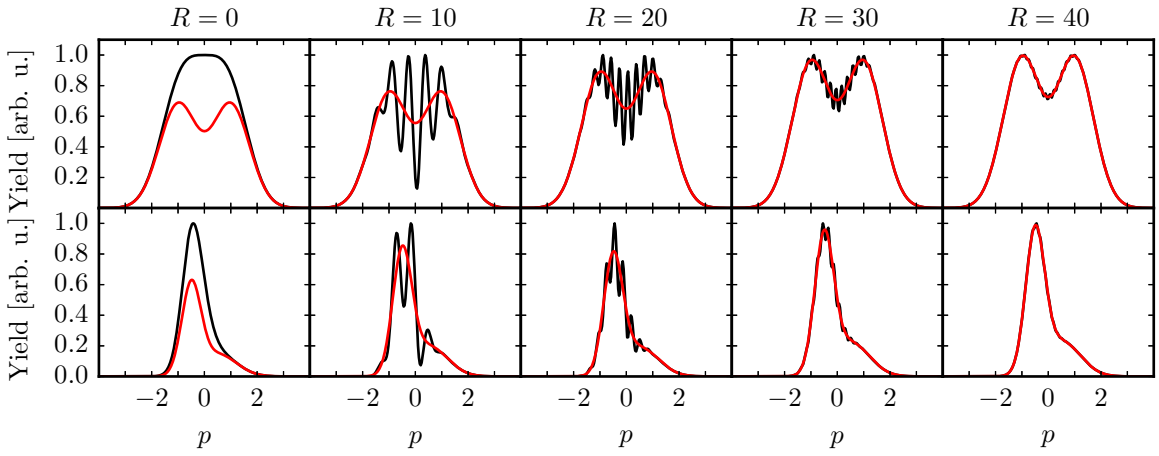

Figure 4.10. Momentum distributions (4.72) of two Gaussian wave packets spatially separated by a distance R (black curves) for $A_0 = A_1 = \sigma_0 = \sigma_1 = -p_0 = p_1 = 1$ (first row) and $A_0 = 2A_1 = 1$, $\sigma_0 = 2\sigma_1 = 2$, $-p_0 = p_1 = 0.5$ (second row). The red curves are the results without the interference term. All distributions were convolved with a Gaussian with a width of $\sigma_p = 0.07$.

at the end of the pulse is created as follows. When the laser field attains a local extremum ($t = t_e$), an ionizing electron wave packet with zero mean momentum is ejected from the potential well and starts to oscillate in the laser field. The initial amplitude of the wave packet is determined by the tunneling probability. At the end of the pulse, the mean momentum of the wave packet is $p_f = -\sqrt{2/3}A(t_e)$ according to (4.68) and Ehrenfest's theorem. If there were no other wave packets present, the longitudinal Ne^+ ion momentum distribution would peak at $p_\parallel^+ = -\sqrt{2/3}p_f = 2A(t_e)/3$. However, the wave packet will interfere with other wave packets created at other local extrema. Due to the oscillation in the field, the spatial separation of wave packets ejected at different times t_e increases with F_0 and $1/\omega_0$. Therefore, interference is suppressed for small ω_0 or large F_0 and the momentum distribution is essentially equal to the incoherent sum of the momentum distributions of the separate wave packets. Moreover, depending on the relative amplitude of the wave packets, the ion momentum distribution will exhibit multiple maxima at $p_\parallel^+ = 2A(t_e)/3$. For large frequencies, however, interference cannot be neglected and will shift the maxima to other values of $p_\parallel^+$.

To illustrate the influence of interference on the momentum distributions, we consider a superposition of two Gaussian wave packets which are spatially separated by a distance R,

$$\begin{aligned}\psi(x) &= \psi_0(x) + \psi_1(x) \\ &= \frac{A_0}{\sqrt{2\pi\sigma_0^2}} \mathrm{e}^{-\frac{x^2}{2\sigma_0^2}} \mathrm{e}^{\mathrm{i}p_0 x} + \frac{A_1}{\sqrt{2\pi\sigma_1^2}} \mathrm{e}^{-\frac{(x-R)^2}{2\sigma_1^2}} \mathrm{e}^{\mathrm{i}p_1 x}.\end{aligned} \tag{4.71}$$

Calculating the Fourier transform of $\psi(x)$ and taking the squared modulus, we obtain

the momentum distribution

$$g(p) = |\widehat{\psi}(p)|^2 = A_0^2 \mathrm{e}^{-\sigma_0^2(p-p_0)^2} + A_1^2 \mathrm{e}^{-\sigma_1^2(p-p_1)^2} + 2A_0A_1 \mathrm{e}^{-\frac{\sigma_0^2}{2}(p-p_0)^2 - \frac{\sigma_1^2}{2}(p-p_1)^2} \cos\left[R(p_1-p)\right]. \tag{4.72}$$

In Fig. 4.10, we show $|\widehat{\psi}(p)|^2$ for the case where the two wave packets move in opposite directions ($p_0 = -p_1$), using two sets of parameters A_i, σ_i and various values of R. For comparison, the incoherent momentum distributions, i.e.

$$g_{in}(p) = |\widehat{\psi_0}(p)|^2 + |\widehat{\psi_1}(p)|^2 = A_0^2 \mathrm{e}^{-\sigma_0^2(p-p_0)^2} + A_1^2 \mathrm{e}^{-\sigma_1^2(p-p_1)^2}, \tag{4.73}$$

are also shown (red curves). To mimic the resolution of our quantum mechanical momentum distributions, all distributions were smoothed with a Gaussian with a width of $\sigma_p = 0.07$. The first thing to note is that $g(p)$ approaches $g_{in}(p)$ with increasing spatial separation. However, this is mainly a result of the Gaussian smoothing: Since the interference term in (4.72) has a modulation frequency of R, the separation between two interference peaks is on the order of π/R. For $R = 40$, the peak separation is $\pi/R = 0.079 \approx \sigma_p$, i.e. close to the momentum resolution of the distributions. As a result, the interference peaks are strongly suppressed and the maxima of $g(p)$ agree with the maxima of $g_{in}(p)$. For smaller R, however, the interference modulation of the distributions is so strong that the maxima of $g_{in}(p)$ are not visible in $g(p)$. In some cases, e.g. for $R = 10$, the interference conditions are such that a deep minimum near $p = 0$ is observed.

Now we apply the interference model to our simulation results. In Fig. 4.11 - 4.13, we show the SAE Ne^+ ion momentum distributions for 2, 5 and 20 field cycles together with the classical ion momenta (4.69) expected for tunnel ionization at the extrema of the field, i.e. $p_\parallel^+ = 2A(t_e)/3$ with $t_e \in [0, T_p]$ and $F'(t_e) = 0$ (gray lines). In all figures, the typical separation of the local maxima decreases from left to right and bottom to top. This supports our conclusion that the local maxima correspond to interference peaks whose separation decreases with F_0 and $1/\omega_0$ (note that these trends are amplified by the chosen momentum scale). For the two- and five-cycle pulse, we observe that the momentum range containing the local maxima gets more and more enclosed by the classical ion momenta as the frequency is decreased. For the smallest frequency, the momenta of some local maxima even coincide with classical ion momenta. This is in line with our Gaussian example: As the frequency is decreased, the spatial separation of the ionized wave packets increases. At the same time, the strength of the interference peaks decreases due to the finite momentum resolution, bringing the momentum distribution closer to the incoherent sum of the wave packet momentum distributions which, according to the simple man's model, peak at $p_\parallel^+ = 2A(t_e)/3$.

For the pulses with $n_c = 20$ (Fig. 4.13), the classical ion momenta (gray lines) are concentrated around $p_\parallel^+ = 0$ since the extrema of the field approach the zeros of the vector potential for large n_c, i.e. $2A(t_e)/3 \to 0$. For $\omega_0 \leq 0.035$ a.u. (first two rows of the figure), these momenta enclose the two highest peaks of the SAE momentum

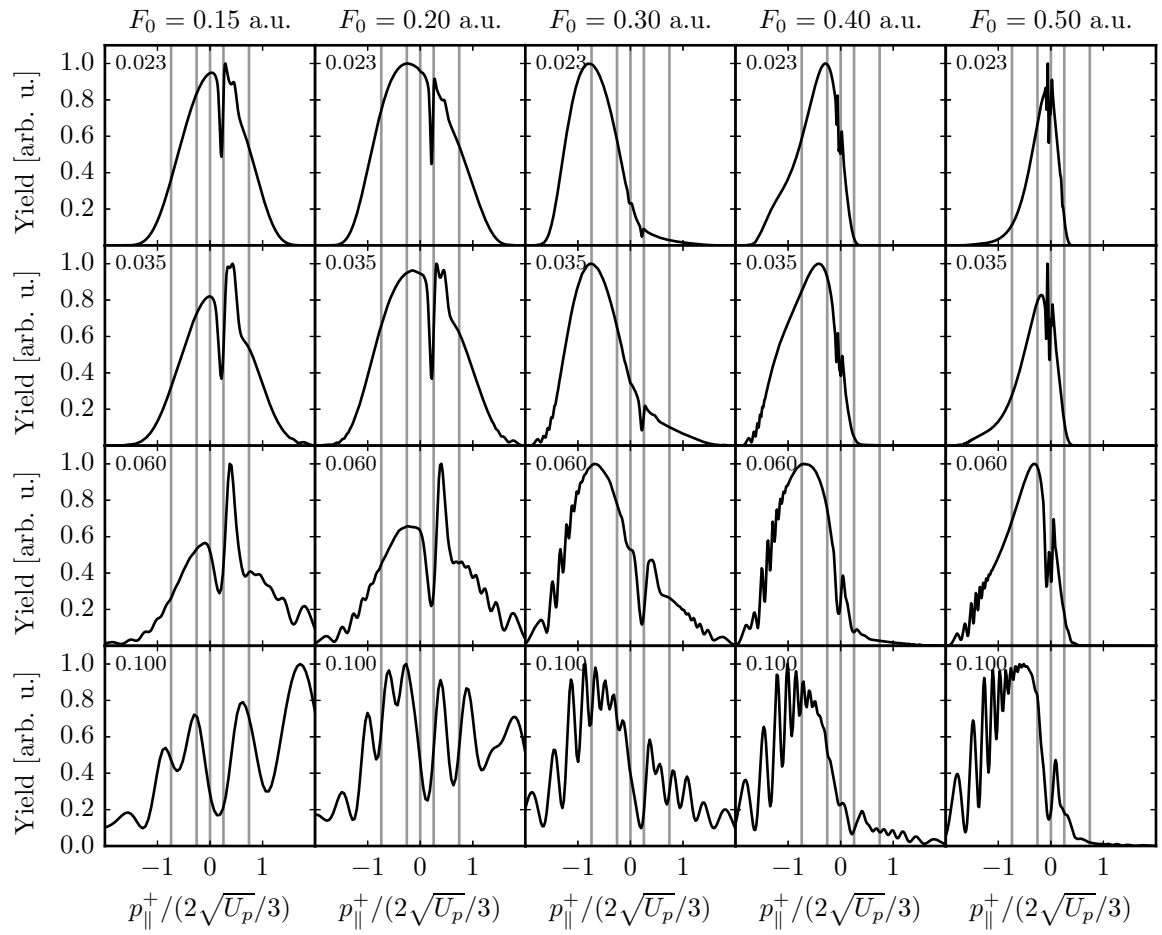

Figure 4.11. SAE Ne^+ ion momentum distributions (black curves) for $n_c = 2$ and (from top to bottom) $\omega_0 = 0.023$ a.u., $\omega_0 = 0.035$ a.u., $\omega_0 = 0.06$ a.u. and $\omega_0 = 0.1$ a.u., compared to the classical ion momenta $2A(t_e)/3$ corresponding to electron ejection at the extrema t_e of the field (gray lines).

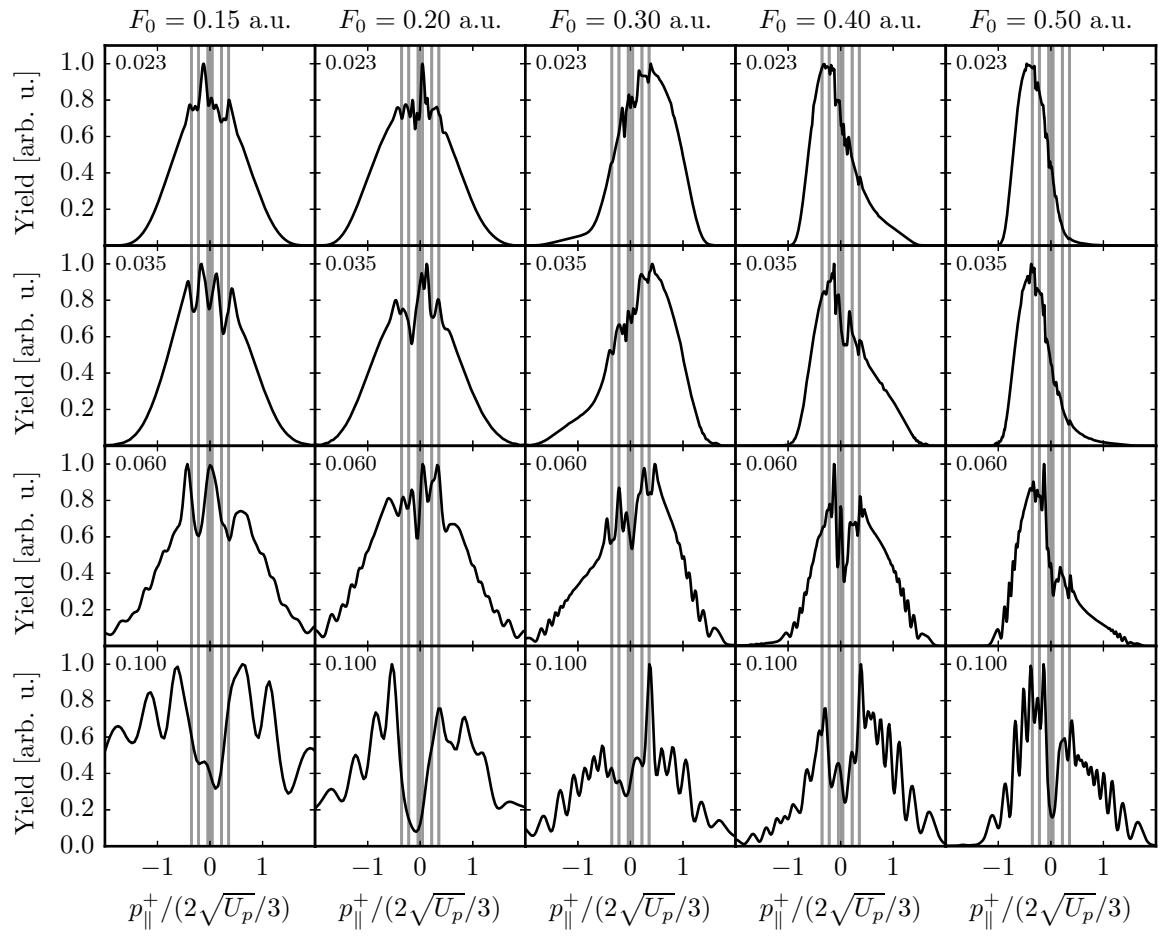

Figure 4.12. Same as Fig. 4.11, but for $n_c = 5$.

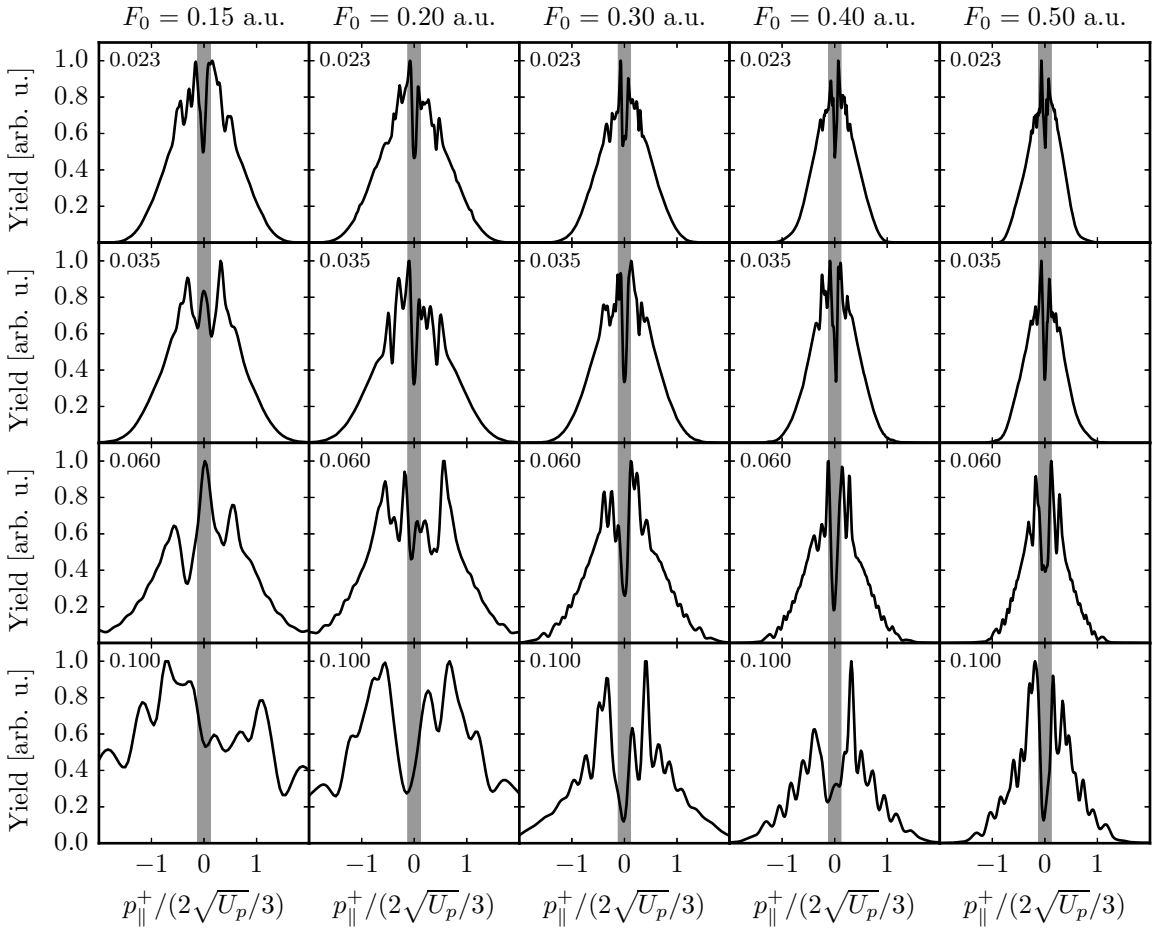

Figure 4.13. Same as Fig. 4.11, but for $n_c = 20$.

distribution and a pronounced minimum at $p_\parallel^+ = 0$. However, there are additional peaks at larger momenta which are not compatible with the notion of direct electron tunneling. The momenta of these peaks seem to scale with $\sqrt{U_p}$, so they probably result from another field-driven effect, e.g. rescattering. However, we do not further investigate this.

Overall, our qualitative interference model allows for an easy understanding of several trends in the momentum distributions of single ionization. However, its present form is clearly not sufficient to explain all of the observed features. The model may be put into a more quantitative form by using Gaussian wave packet dynamics (see the book of Grossmann (2008)) with suitable initial conditions (Yudin and Ivanov, 2001). Gaussian wave packet dynamics is a dynamical method which incorporates rescattering and spreading of the wave packet, i.e. two effects whose influence on the distributions is difficult to assess from the static example (4.72). In addition, completely different explanations of the peaks and dips near $p_\parallel^+ = 0$, e.g. in terms of multiphoton resonances (cf. Section 3.5.2), are possible as well and have been put forward in the last years (see Guo *et al.* (2013) and references therein). Although no definite conclusion regarding the origin of the peaks has been reached until now, most authors emphasize the crucial role of the long-range Coulomb potential for the final electron momenta, regardless of the used approach. The Coulomb potential is not only neglected in the derivation of (4.70), but also in our qualitative interference model. Its inclusion can lead to additional peaks, e.g. through "soft recollisions" of the electrons with the ion (Kästner *et al.*, 2012a,b). The peaks corresponding to these trajectories approximately scale with $\sqrt{U_p}$ and are only weakly dependent on the attractive core potential, demonstrating the universality of the mechanism (Zhang *et al.*, 2016).

Above, we described the ejection of electron wave packets exclusively in terms of tunnel ionization. However, we showed in Chapter 3 that classical over-the-barrier ionization (OBI) significantly contributes to the Ne^+ yield if the field amplitude is increased beyond $F_{OBI}^{SI} = 0.22$ a.u. In the two- and five-cycle distributions for $F_0 \geq 0.3$ a.u., OBI manifests itself in a pronounced asymmetry with respect to $p_\parallel^+ = 0$, indicative of a strong unilateral ejection of electron wave packets. The left-right asymmetry vanishes if the pulse duration is increased (Fig. 4.8). As a result, the distributions cannot be distinguished from the tunneling case (Krainov, 1997).

Using equation (4.40), we can express the momentum distributions of single ionization as a function of the kinetic energy, but this does not yield new insights, at least not on a linear scale. However, if we leave out the Gaussian smoothing and consider the electron energy distributions on a semilogarithmic scale, we notice peaks beyond the tunneling cut-off $|p_\parallel^+| = 2 \cdot 2\sqrt{U_p}/3$ which are separated by the photon energy. This is a key property of above-threshold ionization where an electron absorbs more than the minimum number of photons needed to escape. Since the distributions beyond the cut-off are very small in magnitude, it is not easy to disentangle physical and numerical effects there. This would require a detailed investigation of the numerical issues on small scales which is beyond the scope of this work. Therefore, we only show the energy distributions in Appendix A.3.

4.2.2. Double ionization

Now we consider double ionization. Fig. 4.14 shows the electron momentum distribution of double ionization and the corresponding longitudinal and transversal Ne^{2+} ion momentum distribution for the five-cycle pulse with $\omega_0 = 0.06$ a.u. as a function of the field amplitude. We start by discussing the distribution of the electron momenta shown in the first row. For the lowest two field amplitudes, the maxima of the distribution are located near the diagonal in the first and third quadrant, indicating that the two electrons typically escape in the same direction and with similar, nonzero momenta. As the field amplitude is increased, this momentum correlation is lost, all quadrants get populated and the distribution peaks near $p_1 = p_2 = 0$. The corresponding longitudinal Ne^{2+} ion momentum distribution (second row) evolves from a function with a double-maximum structure into a smooth distribution of distinct Gaussian shape. The transversal distribution (third row), on the other hand, always exhibits a maximum at $p_\perp^{2+} = 0$. All of the described features are in qualitative agreement with experiments (see e.g. Weber *et al.* (2000b); Moshammer *et al.* (2000); Staudte *et al.* (2007); Rudenko *et al.* (2007, 2008b)) and persist if the frequency of the laser field is changed to $\omega_0 = 0.1$ a.u. (Fig. 4.15).

Due to the indistinguishability of the electrons, their momentum distribution is invariant under the operation $p_1 \leftrightarrow p_2$, i.e. mirror symmetric with respect to the diagonal. As a consequence, the transversal ion momentum distribution is invariant under the operation $p_\perp^{2+} \to -p_\perp^{2+}$, i.e. an even function. The longitudinal distribution, on the other hand, exhibits a left-right asymmetry since we use a few-cycle pulse with a fixed carrier-envelope phase (Liu *et al.*, 2004; Rottke *et al.*, 2006). A symmetric longitudinal distribution can be obtained by either using a long pulse or averaging over a uniform distribution of carrier-envelope phases (Prauzner-Bechcicki *et al.*, 2008).

As shown in Fig. 4.16, the structural change of the momentum distribution with increasing F_0 coincides with the change of slope in the Ne^{2+} yield curve, i.e. it indicates the transition from simultaneous (0-2) to sequential double ionization (0-1-2). For field amplitudes in the last regime, we can quantitatively confirm the assumption of two independent ionization steps as follows. First, we calculate the one-dimensional single ionization momentum distributions $g_{SAE}^+(p_1)$ and $g_{SAE,+}^+(p_2)$ of the neutral atom and the singly-charged ion, respectively. Taking indistinguishability into account, the two-dimensional electron momentum distribution is the symmetrized product

$$g_{SS}^{2+}(p_1, p_2) := \frac{1}{2}\left[g_{SAE}^+(p_1) g_{SAE,+}^+(p_2) + g_{SAE}^+(p_2) g_{SAE,+}^+(p_1)\right]. \tag{4.74}$$

Secondly, we express g_{SS}^{2+} as a function of the longitudinal and the transversal ion momentum and integrate over one of them. This yields the blue curves shown in Fig. 4.14 and 4.15 which are in very good agreement with the momentum distributions of the three-electron model.

The transition from simultaneous to sequential double ionization not only manifests itself in the shape, but also in the width of the distributions. By combining (4.19b) with (4.69), we find that the classical maximum of $p_\parallel^{2+}$ is $4 \cdot 2\sqrt{U_p}/3$ (Feuerstein *et al.*,

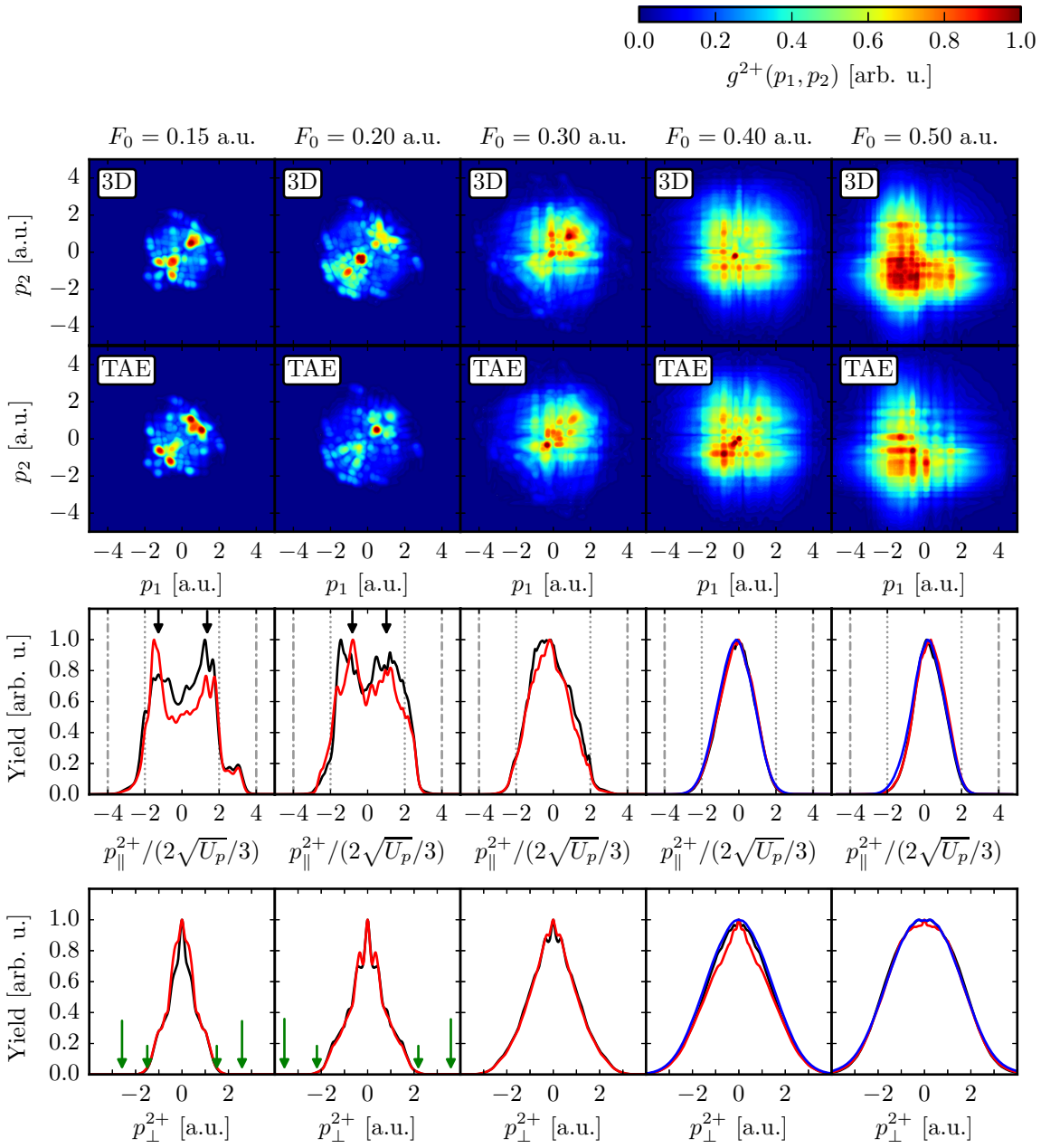

Figure 4.14. Electron momentum distributions of double ionization (first row) and corresponding longitudinal and transversal Ne^{2+} ion momentum distributions (second and third row, respectively) for $n_c = 5$ and $\omega_0 = 0.06$ a.u., calculated from the three-dimensional model (black curves), the two-dimensional TAE approximation (red curves) and a product of two one-dimensional SAE approximations (blue curves). The vertical lines indicate the classical momentum limits $p_\parallel^{2+} = \pm 2n \cdot 2\sqrt{U_p}/3$ of single ionization ($n = 1$, dotted) and double ionization ($n = 2$, dashed dotted). The black and green arrows indicate the most probable longitudinal ion momenta of the pathway 0-2 predicted by the simple man's model (see also Fig. 4.17) and the maximum transversal excess momentum, respectively.

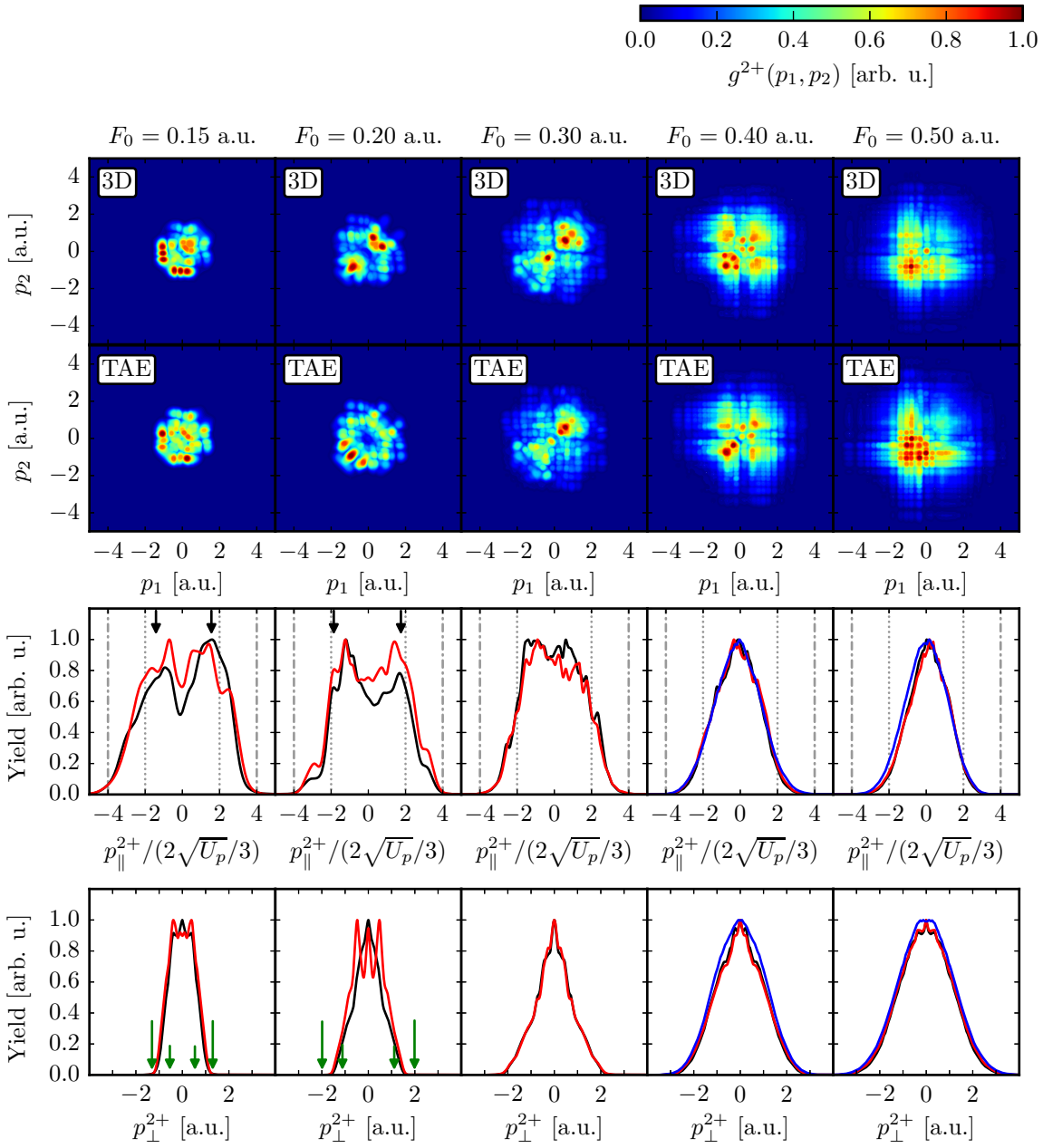

Figure 4.15. Same as Fig. 4.14, but for $\omega_0 = 0.1$ a.u.

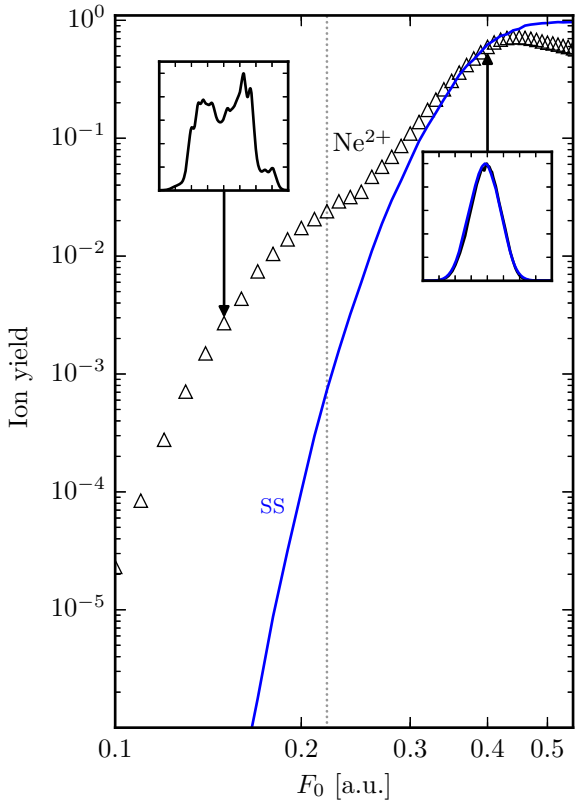

Figure 4.16. Ne^{2+} yield as a function of F_0 (triangles) and selected longitudinal Ne^{2+} ion momentum distributions (insets) for $n_c = 5$ and $\omega_0 = 0.06$ a.u. The saturation field amplitude of single ionization ($F_{sat}^{SI} = 0.22$ a.u.) is indicated by the dotted line. In the nonsequential regime ($F_0 < F_{sat}^{SI}$), the ion momentum distribution has two maxima, indicative of electron rescattering leading to simultaneous double ionization (0-2). In the sequential regime ($F_0 > F_{sat}^{SI}$), the prevalent double ionization pathway is 0-1-2, i.e. the electrons escape independently of each other. Therefore, both the yield and the momentum distribution of the Ne^{2+} ion can be expressed in terms of a SAE product (blue curves).

2000), corresponding to two electrons escaping parallel to the field axis at a zero-crossing of the field, each with the maximum kinetic energy of $2 \cdot 2U_p/3$. As indicated by the dashed dotted lines in Fig. 4.14 and 4.15, the distributions in the simultaneous regime are bounded by $\pm 4 \cdot 2\sqrt{U_p}/3$. In the sequential regime, however, the two electrons tunnel out independently, so the distributions are essentially bounded by the maximum classical momentum of single ionization ($2 \cdot 2\sqrt{U_p}/3$, dotted lines).

Since the tunneling probability is zero at a zero-crossing of the field, longitudinal ion momenta on the order of $4 \cdot 2\sqrt{U_p}/3$ can only be reached if the electrons escape *classically*. For this to occur, the sum energy of the two electrons prior to double ionization, i.e. near the zero-crossing of the field, has to exceed the ground state energy of the doubly-charged ion. The only possibility to fulfill both the time and the energy constraints is a recollision reaction, namely two-electron ROBI. Therefore, the preva-

lence of nonzero longitudinal ion momenta for small field amplitudes, first observed in the famous COLTRIMS experiments of Weber *et al.* (2000a,b) and Moshammer *et al.* (2000), is seen as the ultimate confirmation of the rescattering mechanism being responsible for nonsequential ionization[6].

Using the simple man's model and assuming maximum recollision energy (see Section 3.6.1), one can derive approximate bounds (or "kinematical constraints") for the ROBI ion momenta (Feuerstein *et al.*, 2000, 2001; Moshammer *et al.*, 2000). We will now show that this estimate can be improved if the tunneling probability and the time dependence of the recollision energy are taken into account. Suppose that the first electron tunnels out at a time t_0 with zero momentum and recollides at a later time $t_{rec}(t_0)$ with kinetic energy $2E_{rec}(t_{rec})/3$ so that the excess energy of the recollision reaction

$$E_{exc}(t_{rec}) = \frac{2}{3}E_{rec}(t_{rec}) - E_I^+ - V_s^{SI,+}(t_{rec}) \tag{4.75}$$

is positive, thus allowing for ROBI. Here, $E_I^+ > 0$ is the ionization energy of the singly-charged ion, $V_s^{SI,+} < 0$ is the energy of the single ionization saddle (see Section 3.6.3) and the factor $2/3$ is due to the geometry of our model. Generally, the excess energy is distributed arbitrarily among the two electrons and the ion momentum components,

$$2E_{exc}(t_{rec}) = p_1^2 + p_2^2 = \frac{3}{4}(p_\parallel^{2+})^2 + 2(p_\perp^{2+})^2. \tag{4.76}$$

However, based on the observation that the electron momenta at the end of the pulse are similar ($p_1 \approx p_2 \Leftrightarrow p_\perp^{2+} \approx 0$), we may assume symmetric recollision energy sharing, i.e. the typical longitudinal ion momentum induced by the excess energy is

$$p_{\parallel,exc}^{2+} = \sqrt{\frac{8}{3}E_{exc}(t_{rec})}. \tag{4.77}$$

Since $E_{exc} > 0$ for $t = t_{rec}$, the electrons can ionize classically. Consequently, the longitudinal ion momentum for $t > t_{rec}$ is determined by Newton's equation

$$\dot{p}_\parallel^{2+}(t) = 2\frac{2}{3}F(t) \tag{4.78}$$

with initial condition $p_\parallel^{2+}(t_{rec}) = \pm p_{\parallel,exc}^{2+}$. The sign is found as follows: Since the energy transfer is fast compared to the variation of the laser field, the two electrons escape in the direction defined by the recolliding electron, i.e. the drift momentum received by the ion is diminished by the excess momentum of the recollision. Integration of (4.78) from t_{rec} to T_p yields, with $A(T_p) = 0$, the longitudinal ROBI ion momentum at the

[6]Other mechanisms, such as shake-off and collective tunneling, predict a maximum at zero momentum.

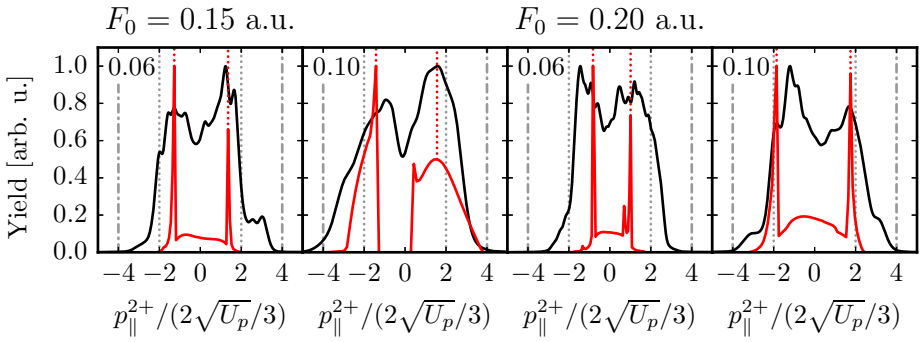

Figure 4.17. Longitudinal Ne^{2+} ion momentum distributions for $n_c = 5$, calculated from the quantum mechanical wave function of the three-dimensional model (black curves) and from the classical trajectories of the one-dimensional simple man's model (red curves). The vertical lines indicate the classical momentum limits $p_\parallel^{2+} = \pm 2n \cdot 2\sqrt{U_p}/3$ of single ionization ($n = 1$, dotted) and double ionization ($n = 2$, dashed dotted).

end of the pulse,

$$p_\parallel^{2+}(T_p) = 2\frac{2}{3}A(t_{rec}) - \mathrm{sgn}(A(t_{rec}))p_{\parallel,exc}^{2+} \tag{4.79a}$$

$$= 4\frac{2}{3}\sqrt{U_p}(-1)^{n_c}\sin^2\left(\frac{\pi t_{rec}}{T_p}\right)\sin(\omega_0 t_{rec}) - \mathrm{sgn}((-1)^{n_c}\sin(\omega_0 t_{rec}))\sqrt{\frac{8}{3}\left[\frac{2}{3}E_{rec}(t_{rec}) - E_I^+ - V_s^{SI,+}(t_{rec})\right]}. \tag{4.79b}$$

To obtain the momentum distribution for fixed pulse parameters, we use the values of E_{rec} and t_{rec} already calculated in Section 3.6.1 and weight each recolliding trajectory with the ADK tunneling probability (3.71). The results for both frequencies and the two smallest field amplitudes are shown in Fig. 4.17, together with the respective quantum momentum distributions. We find that the simple man's model predicts the large-scale maxima of the distributions quite well, demonstrating that ROBI is indeed responsible for the two maxima. If the symmetric recollision energy sharing is abandoned but the sign of the excess momentum is retained, the maxima of the classical distributions are shifted towards the $4 \cdot 2\sqrt{U_p}/3$ limit (dashed dotted vertical lines). Changing the sign of $p_{\parallel,exc}^{2+}$ in equation (4.79) completely destroys the agreement, so our assumption of the double ionization direction relative to the recolliding electron is justified. The positions of the maxima, i.e. the most probable longitudinal ion momenta, are also included in Fig. 4.14 and 4.15 as black arrows.

The above approach to determine the most probable longitudinal ion momenta is not limited to our model. Leaving out the geometrical factors and restoring the singular Coulomb potential of the ion by taking $\lim_{\varepsilon\to 0} V_s^{SI,+}$, the excess energy of the recollision reduces to

$$E_{exc}(t_{rec}) = E_{rec}(t_{rec}) - E_I^+ + 2\sqrt{2|F(t_{rec})|}. \tag{4.80}$$

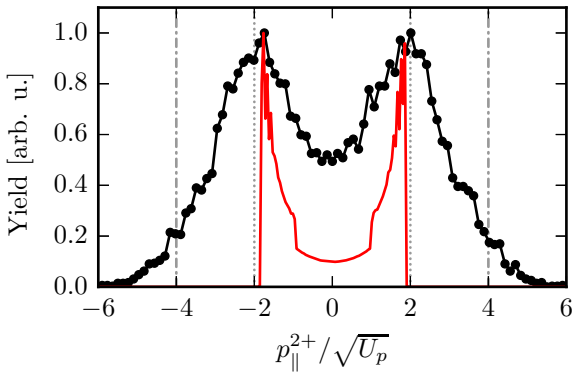

Figure 4.18. Longitudinal Ne^{2+} ion momentum distribution for $n_c = 26$, $\omega_0 = 0.057$ a.u. and $F_0 = 0.17$ a.u. measured by Rudenko *et al.* (2008b) (black markers), compared to the distribution of the longitudinal ROBI ion momentum (4.82) calculated with the simple man's model using the same pulse parameters (red curve). The vertical lines indicate the classical momentum limits $p_\parallel^{2+} = \pm 2n \cdot \sqrt{U_p}$ of single ionization ($n = 1$, dotted) and double ionization ($n = 2$, dashed dotted).

Using the relation between the ion momentum components and the excess energy

$$(p_\parallel^{2+})^2 + (p_\perp^{2+})^2 = 2E_{exc}(t_{rec}), \tag{4.81}$$

equation (4.79) takes the form

$$p_\parallel^{2+}(T_p) = 2A(t_{rec}) - \mathrm{sgn}(A(t_{rec}))\sqrt{2\left[E_{rec}(t_{rec}) - E_I^+ + 2\sqrt{2|F(t_{rec})|}\right]}. \tag{4.82}$$

This equation is a time-dependent version of an expression given by Feuerstein *et al.* (2000) and should be applicable to a real noble gas atom. As an example, we consider a longitudinal ion momentum distribution of neon ($E_I^+ = 1.51$ a.u.) which was measured experimentally by Rudenko *et al.* (2008b) for $I_0 = 10^{15}$ W/cm^2 ($F_0 = 0.17$ a.u.), $\lambda = 795$ nm ($\omega_0 = 0.057$ a.u.) and $T_{1/2,I}^{exp} = 25$ fs ($n_c = 26$). The long duration of the pulse has several consequences. First, the influence of the envelope is marginal since most ionization events occur near the pulse maximum where the envelope is close to one. Therefore, we can use the electric field and the vector potential of our model pulse to approximate the unknown temporal profile of the experimental pulse. Secondly, the field modification $V_s^{SI,+}$ of the ionization energy is small compared to the recollision energy, so neglecting it does not significantly change the ROBI ion momenta. For the sake of consistency, we include it nevertheless. Comparing the experimental distribution and the simple man's result in Fig. 4.18, we observe excellent agreement of the maxima.

Having discussed the longitudinal ion momentum distributions, we now briefly consider the transversal ones which are shown in the bottom row of Fig. 4.14 and 4.15. We restrict the discussion to the simultaneous regime where the transversal ion momentum distribution is assumed to provide information on the recollision process (Weber

et al., 2000b; Weckenbrock *et al.*, 2003). The fact that the transversal ion momentum is not influenced by the acceleration in the laser field after recollision (Feuerstein *et al.*, 2001) has two consequences. First, the transversal distributions are much narrower than the longitudinal ones (even if $p_{\parallel}^{2+}$ is plotted in a.u.). Secondly, the distributions are bounded by the largest transversal ion momentum which can be received during the recollision. According to equation (4.76), this momentum is given by the maximum value of

$$p_{\perp,exc}^{2+} = \sqrt{E_{exc}(t_{rec})} \tag{4.83}$$

during the pulse. For the smaller frequency, the distributions are indeed bounded by $\pm\max(p_{\perp,exc}^{2+})$, as evidenced by the short green arrows in the figure. For the larger frequency, the distributions extend to larger momenta, especially for the smallest field amplitude. A possible explanation for this is the attractive soft-core Coulomb potential of the nucleus which leads to larger recollision energies (see Section 3.6.2), but is not included in the simple man's model. The influence of the Coulomb potential is particularly strong for small field amplitudes and large frequencies, i.e. small ponderomotive energies. Taking the Coulomb potential into account (long green arrows) resolves the discrepancy[7].

In the simultaneous regime, the transversal distributions exhibit pronounced shoulders. This is in marked contrast to early experiments where the measured distributions always had a Gaussian shape (Weber *et al.*, 2000b; Moshammer *et al.*, 2000; Eremina *et al.*, 2003; Zrost *et al.*, 2006). A Gaussian fit of our numerical distributions yields good agreement only in the sequential regime, i.e. for $F_0 \geq 0.4$ a.u. At first glance, the shoulders might be attributed to the reduced dimensionality of our model which overestimates the Coulomb repulsion between the electrons. However, the high-resolution experiments of Staudte *et al.* (2007) and Rudenko *et al.* (2007) which revealed V-shaped structures in the electron momentum distributions[8] indicate the importance of second-order effects which are not captured by the standard recollision picture, e.g. electron repulsion in the final state, backscattering of the recolliding electron by the ion and asymmetric recollision energy sharing. The role of these effects has been investigated elsewhere (Ye *et al.*, 2008; Zhou *et al.*, 2010a).

In the previous section, we found that the single ionization momentum distributions of the three-electron model can be reproduced semiquantitatively with the SAE approximation (Fig. 4.6). Likewise, the double ionization momentum distributions can be reproduced with the TAE approximation, as shown in Fig. 4.14 and 4.15 (lower part of the first row and red curves). As in the single ionization case, an even better agreement is hampered by the projection technique which is used to extract the doubly-ionized parts from the three-electron wave function. Nevertheless, we observe that the distributions typically peak at very similar momenta, supporting our conclusion that the most probable ion momenta are mainly determined by the laser field and

[7] We explicitly verified that the Coulomb interaction has almost no influence on the positions of the maxima in Fig. 4.17, so it is justified to neglect it for the longitudinal distributions.

[8] Unfortunately, these authors do not show the transversal ion momentum distributions.

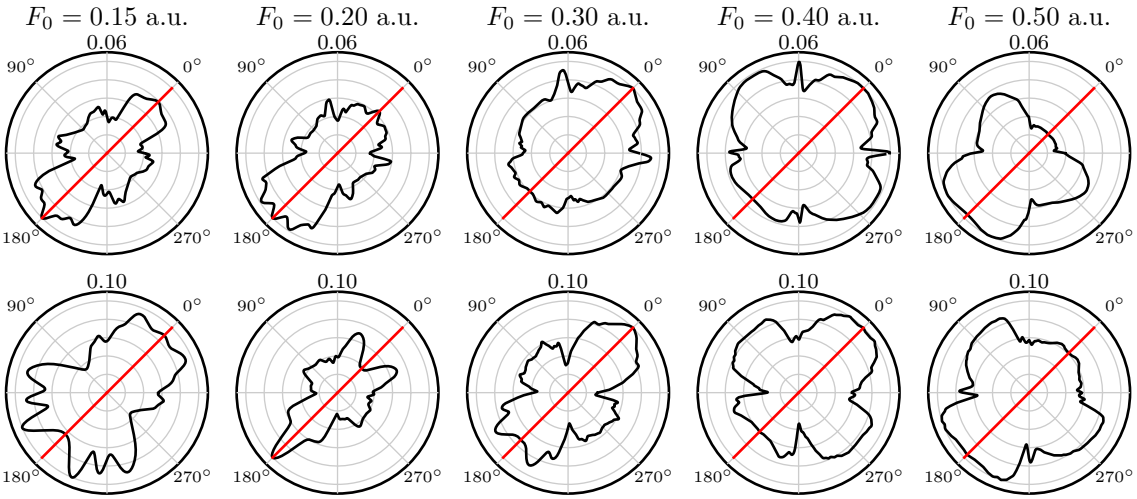

Figure 4.19. Angular distributions of double ionization for $n_c = 5$, $\omega_0 = 0.06$ a.u. (first row) and $n_c = 5$, $\omega_0 = 0.1$ a.u. (second row). The angle is defined with respect to the field axis (red line).

the ionization energy of the singly-charged ion (both of which are retained in the TAE approximation). Only for $\omega_0 = 0.1$ a.u. and $F_0 = 0.2$ a.u. (bottom row of Fig. 4.15), the transversal TAE distribution differs considerably from the three-dimensional result, exhibiting two pronounced side maxima. One may speculate that this is due to a resonance involving an energy level contained in the TAE spectrum but not in the (slightly different) spectrum of the three-dimensional Hamiltonian. However, we do not further investigate this.

To conclude our discussion of double ionization, we present the angular distributions of the two ionized electrons in Fig. 4.19 which illustrate the transition from correlated, unidirectional escape parallel to the field axis (characteristic of simultaneous double ionization) to uncorrelated, omnidirectional escape (characteristic of sequential double ionization). The energy distributions are not shown since they do not yield any new information.

4.2.3. Triple ionization

Finally, we study triple ionization. The distribution of the longitudinal and transversal Ne^{3+} ion momenta $\widetilde{g}^{3+}(p_\perp^{3+}, p_\parallel^{3+})$ obtained for the five-cycle pulse with $\omega_0 = 0.06$ a.u. is shown in the first row of Fig. 4.20 as a function of the field amplitude. The upper half of the distribution is the result of our calculation while the lower half, found by a reflection of the calculated distribution about the $p_\parallel^{3+}$-axis, is shown only for visualization purposes[9]. For the smallest field amplitude, we observe two regions of maximum

[9]On the one hand, the reflection increases the visibility of the structures close to $p_\perp^{3+} = 0$. On the other hand, the resulting distribution looks similar to the experimental distributions obtained by

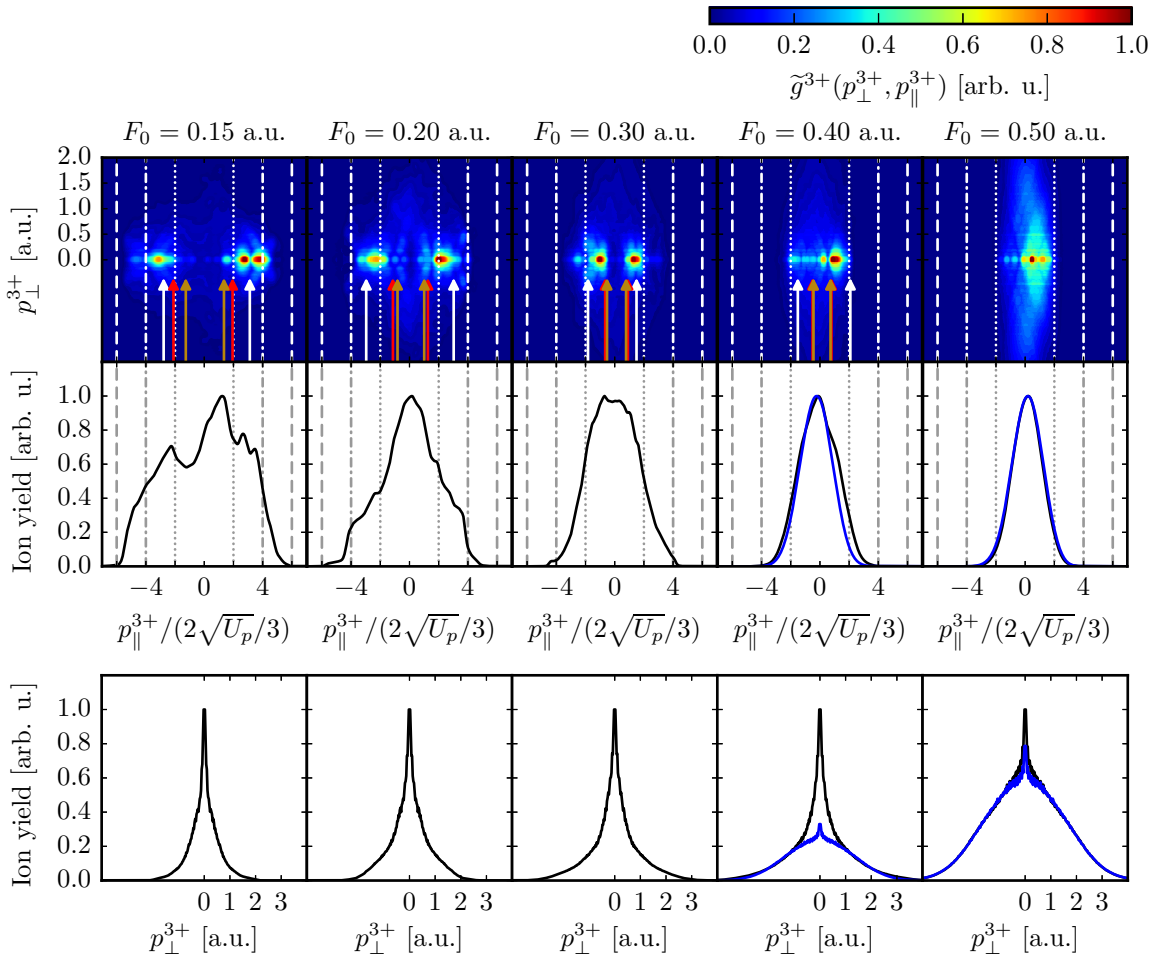

Figure 4.20. Ne^{3+} ion momentum distributions $\widetilde{g}^{3+}(p_\perp^{3+}, p_\parallel^{3+})$ for $n_c = 5$ and $\omega_0 = 0.06$ a.u. (first row), integrated over $p_\perp^{3+}$ (second row, black curves) and integrated over $p_\parallel^{3+}$ (third row, black curves). The distributions calculated from a product of three one-dimensional SAE approximations are shown as blue curves. The vertical lines indicate the classical momentum limits $p_\parallel^{3+} = \pm 2n \cdot 2\sqrt{U_p}/3$ of single ionization ($n = 1$, dotted), double ionization ($n = 2$, dashed dotted) and triple ionization ($n = 3$, dashed), respectively. The arrows indicate the most probable longitudinal ion momenta of the pathways 0-3 (white), 0-1-3 (red) and 0-2-3 (dark orange) predicted by the simple man's model (equations (4.85) and (4.86)).

yield in the distributions, located near $p_\perp^{3+} = 0$ and fairly symmetric in $p_\parallel^{3+}$. As the field amplitude is increased, both the width of the distribution and the separation of the maxima in $p_\parallel^{3+}$ decrease in units of $2\sqrt{U_p}/3$ until only a single maximum near $p_\parallel^{3+} = 0$ is left. This behavior is in agreement with experiments (see e.g. the right-hand side of Fig. 1.5). The longitudinal Ne^{3+} ion momentum distribution (second row of Fig. 4.20) is obtained by integrating $\widetilde{g}^{3+}(p_\perp^{3+}, p_\parallel^{3+})p_\perp^{3+}$ over $p_\perp^{3+}$ (equation (4.36)). The additional factor $p_\perp^{3+}$ assigns a greater weight to the parts of the distribution with $p_\perp^{3+} > 0$. As a result, the decrease of the width survives in the longitudinal distribution but the double-maximum structure does not, in striking contrast to the experiments. Finally, we note that the shape of the transversal Ne^{3+} ion momentum distribution (third row) is nearly independent of F_0 and its width gets only slightly larger as F_0 is increased.

The dependence of the momentum distributions on the field amplitude signifies a change of the prevalent ionization pathway, as expected from the representation of the integral Ne^{3+} yield in terms of the product yields DS, SD and SSS (Fig. 4.21). We start by discussing the distributions for $F_0 = 0.5$ a.u. (rightmost column of Fig. 4.20). This field amplitude lies in the regime where sequential triple ionization (0-1-2-3) dominates, as illustrated by the good agreement of the Ne^{3+} yield with the product yield SSS in Fig. 4.21. Analogous to double ionization, the independence of the ionization steps can be proved by considering the symmetrized product of the single ionization momentum distributions g^+ of the intermediate charge states, i.e.

$$\begin{aligned} g_{SSS}^{3+}(p_1, p_2, p_3) := \frac{1}{6}\Big[& g_{SAE}^{+}(p_1) g_{SAE,+}^{+}(p_2) g_{2+}^{+}(p_3) + g_{SAE}^{+}(p_2) g_{SAE,+}^{+}(p_3) g_{2+}^{+}(p_1) \\ & + g_{SAE}^{+}(p_3) g_{SAE,+}^{+}(p_1) g_{2+}^{+}(p_2) + g_{SAE}^{+}(p_1) g_{SAE,+}^{+}(p_3) g_{2+}^{+}(p_2) \\ & + g_{SAE}^{+}(p_2) g_{SAE,+}^{+}(p_1) g_{2+}^{+}(p_3) + g_{SAE}^{+}(p_3) g_{SAE,+}^{+}(p_2) g_{2+}^{+}(p_1) \Big], \end{aligned} \tag{4.84}$$

expressing it as a function of the longitudinal and the transversal ion momentum and integrating over one of them. This procedure yields the blue curves in Fig. 4.20. Although the separate single ionization momentum distributions g^+ are similar to those of Fig. 4.6, the SSS longitudinal ion momentum distribution for $F_0 = 0.5$ a.u. is a nearly perfect Gaussian and in excellent agreement with the three-dimensional result. The Gaussian shape is expected for a sequence of three independent tunnel ionization steps (Zrost *et al.*, 2006).

Now we turn our attention to the nonsequential regime. For the two smallest field amplitudes, the product yields in Fig. 4.21 considerably underestimate the Ne^{3+} yields, indicating the dominance of a pathway which cannot be represented by product yields, i.e. simultaneous triple ionization (0-3). This pathway is described by the rescattering mechanism (see Section 1.4.1). We focus on the classical scenario, i.e. three-electron ROBI where the energy of the recolliding electron exceeds the first two ionization energies of the singly-charged ion, allowing for a classical escape of all three electrons.

integration over one Cartesian transversal ion momentum coordinate (see e.g. Zrost *et al.* (2006)).

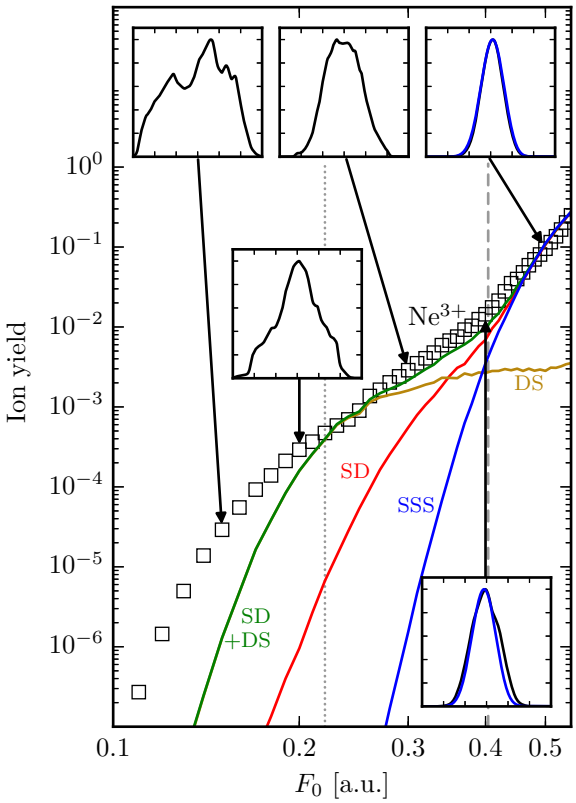

Figure 4.21. Ne^{3+} yield as a function of F_0 (squares) and selected longitudinal Ne^{3+} ion momentum distributions (insets) for $n_c = 5$ and $\omega_0 = 0.06$ a.u. The saturation field amplitudes of single and double ionization $F_{sat}^{SI} = 0.22$ a.u. and $F_{sat}^{DI} = 0.40$ a.u. are indicated by the dotted and dashed line, respectively. In the sequential regime ($F_0 > F_{sat}^{DI}$), the prevalent triple ionization pathway is 0-1-2-3, i.e. the three electrons escape independently of each other. Therefore, both the yield and the momentum distribution can be expressed in terms of a SAE product (blue curves). In the nonsequential regime ($F_0 < F_{sat}^{DI}$), there are three competing pathways, namely 0-2-3 (contained in the product yield DS), 0-1-3 (contained in the product yield SD) and 0-3 (dominating for $F_0 < F_{sat}^{SI}$).

During their motion in the laser field, these electrons receive the same drift momentum (Feuerstein *et al.*, 2001). Since this drift momentum is typically much larger than the excess momentum of the recollision, the final electron momenta will be similar. This has two consequences. On the one hand, the transversal ion momentum (4.24) is close to zero, in agreement with the positions of the maxima in the first two columns of Fig. 4.20. The longitudinal ion momentum, on the other hand, is large and limited only by the kinetic energy of the electrons. If each electron escapes with the maximum energy of $2 \cdot 2U_p/3$ parallel to the field axis, the maximum longitudinal ion momentum $|p_\parallel^{3+}| = 6 \cdot 2\sqrt{U_p}/3$ is reached. As indicated by the dashed vertical lines in Fig. 4.20, the distributions for the two smallest field amplitudes are bounded by this value. However, the observation is not sufficient to establish the dominance of three-electron ROBI in this regime. For this, we need to connect the maxima of the ion momentum distribution in the longitudinal direction to the maxima of a classical ROBI ion momentum distribution, as done for double ionization. Again, we assume that the excess energy of the recollision is distributed equally among the electrons ($p_1 = p_2 = p_3$, i.e. $p_\perp^{3+} = 0$) and that the excess momentum of the recollision (which follows from equation (4.25)) diminishes the ion momentum. Then, the final longitudinal ROBI ion momentum for the pathway 0-3 is given by

$$p_{\parallel,0\text{-}3}^{3+}(T_p) = 3\frac{2}{3}A(t_{rec}) - \mathrm{sgn}(A(t_{rec}))\sqrt{4\left[\frac{2}{3}E_{rec}(t_{rec}) - E_I^+ - E_I^{2+} - V_s^{DI,+}(t_{rec})\right]}. \tag{4.85}$$

As in the previous section, we calculate the distribution of the longitudinal ROBI ion momenta with the simple man's model. The results are similar to the distributions of Fig. 4.17. In Fig. 4.20, the most probable negative and positive longitudinal ion momenta, i.e. the positions of the highest maxima in the classical distributions, are indicated by the white arrows. These are in good agreement with the maxima of the two-dimensional ion momentum distribution, not only for $F_0 = 0.15$ a.u. and $F_0 = 0.20$ a.u., but also for $F_0 = 0.30$ a.u. since the increasing excess momentum in (4.85) shifts the maxima of the classical distribution towards $p_\parallel^{3+} = 0$. However, for $F_0 > F_{sat}^{SI} = 0.22$ a.u., rescattering is dramatically reduced due to the onset of OBI. This suppression effect is not incorporated in the simple man's model. Based on the yields (Fig. 4.21), we conclude that 0-3 is prevalent for $F_0 = 0.15$ a.u. and $F_0 = 0.2$ a.u., but of minor relevance for $F_0 = 0.3$ a.u.

Having identified the sequential and the simultaneous triple ionization pathways (0-1-2-3 and 0-3, respectively) in the distributions, we now focus on the two-step pathways 0-1-3 and 0-2-3. According to the qualitative theory of Feuerstein *et al.* (2000) described in Section 1.5, 0-1-3 dominates in the regime of field amplitudes between 0-3 and 0-1-2-3 while 0-2-3 is suppressed. These expectations hinge on the single-electron tunneling step contained in the two pathways (0-1 and 2-3, respectively): Due to the smaller ionization energy, tunneling from the ground state of the neutral atom (0) is much more probable than from the ground state of the doubly-charged ion (2). However, in Section 3.4.5, we found that the product yield SD containing 0-1-3 strongly

underestimates the Ne^{3+} yields in the regime of interest (red curve in Fig. 4.21). Emphasizing the interaction of the electrons during the recollision, we argued that the third electron in 0-2-3 tunnel ionizes from an *excited* state of the doubly-charged ion. In this case, the tunneling probability in the final step is much larger and the contribution of 0-2-3 is comparable to (or even larger than) the contribution of 0-1-3. Following this proposition, we approximated the yield of 0-2-3 (DS, dark orange curve in Fig. 4.21) as the simultaneous double ionization yield (available through the flux integration method) times the single ionization yield of the first excited state of the doubly-charged ion (available from a separate calculation) times a constant (determined empirically). The sum of SD and DS (green curve in Fig. 4.21) fits the Ne^{3+} yields in the intermediate regime of field amplitudes quite well.

How can 0-1-3 and 0-2-3 be distinguished in the ion momentum distributions? First of all, we note that a product description of the momentum distributions, analogous to the sequential regime, is not possible since the double ionization part of the product yield (SD and DS, respectively) not only contains a simultaneous contribution (1-3 and 0-2, respectively) but also a sequential contribution (1-2-3 and 0-1-2, respectively) which cannot be removed. Therefore, the only remaining option is a classical description in terms of the rescattering mechanism. For both 0-1-3 and 0-2-3, the electron which leaves via tunnel ionization (0-1 and 2-3, respectively) will not transfer a significant momentum to the ion[10] (see the introduction of Section 4.2.1). Therefore, the final ion momentum is largely determined by the simultaneous double ionization step. With equation (4.77) and the same assumptions as above, we obtain the longitudinal ROBI ion momenta

$$p^{3+}_{\parallel,\text{0-1-3}}(T_p) = 2\frac{2}{3}A(t_{rec}) - \operatorname{sgn}(A(t_{rec}))\sqrt{\frac{8}{3}\left[\frac{2}{3}E_{rec}(t_{rec}) - E_I^{2+} - V_s^{SI,2+}(t_{rec})\right]}, \tag{4.86a}$$

$$p^{3+}_{\parallel,\text{0-2-3}}(T_p) = 2\frac{2}{3}A(t_{rec}) - \operatorname{sgn}(A(t_{rec}))\sqrt{\frac{8}{3}\left[\frac{2}{3}E_{rec}(t_{rec}) - E_I^{+} - V_s^{SI,+}(t_{rec})\right]}. \tag{4.86b}$$

Note that the second equation is equal to (4.79). The respective classical distributions peak at momenta which are indicated in Fig. 4.20 by red arrows (for 0-1-3) and dark orange arrows (for 0-2-3). The arrows lie nearly on top of each other, illustrating that the drift term $2 \cdot 2A(t_{rec})/3$ is dominating in (4.86). Therefore, a distinction of 0-1-3 and 0-2-3 based on the rescattering mechanism is not possible for our results. Nevertheless, the distributions for $F_0 = 0.3$ a.u. and $F_0 = 0.4$ a.u. show that at least one of the two-step pathways is at work in our model: On the one hand, the distributions are bounded by $|p_\parallel^{3+}| = 4 \cdot 2\sqrt{U_p}/3$ (dashed dotted lines) which is the maximum longitudinal ion momentum for both 0-1-3 and 0-2-3. On the other hand, the maxima of the quantum and the classical distributions agree rather well. For

[10] Without further explanation, Feuerstein *et al.* (2000) assumed that all singly-ionizing electrons are rescattered and transfer a momentum equal to the maximum recollision energy to the ion.

$F_0 = 0.2$ a.u., i.e. close to saturation of single ionization where the transition from 0-3 to 0-2-3 occurs, we even see some evidence for the four-maximum structure expected by Feuerstein *et al.* (see Fig. 1.4).

From the classical perspective, it is difficult to distinguish the simultaneous and the two-step triple ionization pathways in Fig. 4.20 since the most probable longitudinal ROBI ion momenta (indicated by the arrows) are not sufficiently separated. This is due to the few-cycle pulse which we used in our simulations. In a few-cycle pulse, the recollision parameters strongly depend on the pulse shape. In particular, the typical recollision energy is reduced compared to the periodic case and the typical recollision time is further away from a zero-crossing of the field (see Section 3.6.1). As a consequence, the typical drift momentum is smaller in equations (4.85) and (4.86). At the same time, the larger field modification of the ionization energy compensates the smaller recollision energy to some extent so that the typical excess momentum is less affected by the few-cycle pulse. Overall, the effect for each pathway is a smaller ROBI ion momentum. The above situation changes when the pulse duration is increased (see Table 3.6): The most probable recollision energy converges to $3.17U_p$ and the corresponding recollision time moves closer to a field zero (although it never reaches it) so that the drift term in the ROBI ion momentum dominates. For this reason, the pulse shape is of minor relevance. To demonstrate this, we compare two experimental momentum distributions obtained with a long pulse of unknown shape to the longitudinal ROBI ion momentum distributions of the three nonsequential pathways, calculated with the simple man's model for the laser pulse (2.28). Without the geometrical factors and for $\varepsilon \to 0$, the ROBI ion momenta read

$$p^{3+}_{\parallel,\text{0-3}}(T_p) = 3A(t_{rec}) - \text{sgn}(A(t_{rec}))\sqrt{2\left[E_{rec}(t_{rec}) - E_I^+ - E_I^{2+} + 2\sqrt{10|F(t_{rec})|}\right]}, \tag{4.87a}$$

$$p^{3+}_{\parallel,\text{0-1-3}}(T_p) = 2A(t_{rec}) - \text{sgn}(A(t_{rec}))\sqrt{2\left[E_{rec}(t_{rec}) - E_I^{2+} + 2\sqrt{3|F(t_{rec})|}\right]}, \tag{4.87b}$$

$$p^{3+}_{\parallel,\text{0-2-3}}(T_p) = 2A(t_{rec}) - \text{sgn}(A(t_{rec}))\sqrt{2\left[E_{rec}(t_{rec}) - E_I^{+} + 2\sqrt{2|F(t_{rec})|}\right]}. \tag{4.87c}$$

As in the double ionization case, the influence of the field modification terms turns out to be negligible for a long pulse, but we include them nevertheless. In Fig. 4.22, we plot the longitudinal momentum distributions of triply-charged neon ($E_I^+ = 1.51$ a.u., $E_I^{2+} = 2.33$ a.u.) measured by Rudenko *et al.* (2008a) for $\omega_0 = 0.057$ a.u. and $T^{exp}_{1/2,I} = 25$ fs ($n_c = 26$), i.e. a rather long pulse, together with the distributions of the momenta (4.87) obtained with the same pulse parameters. For $F_0 = 0.24$ a.u. (left panel), the maxima of the measured distribution are in excellent agreement with the maxima of the 0-3 distribution (blue curve). For $F_0 = 0.34$ a.u. (right panel), in contrast, the maxima coincide with the distribution maxima of the two-step pathways (red and dark orange curves). In both cases, the maxima of the distributions for 0-3 and 0-1-3/0-2-3 are well separated so that the change of the prevalent ionization pathway

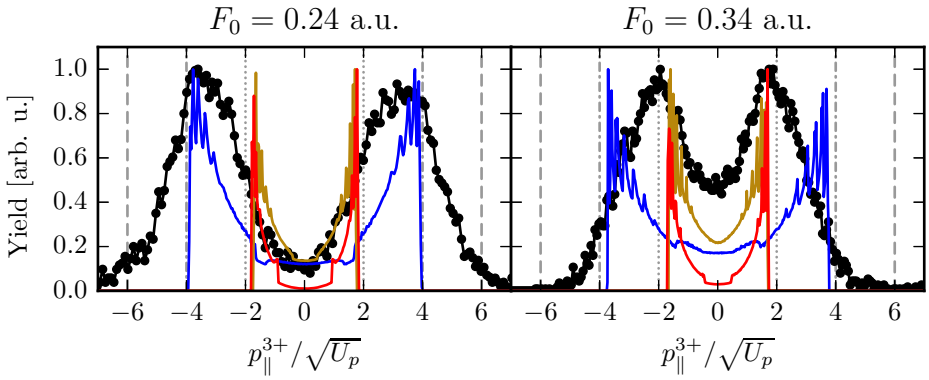

Figure 4.22. Longitudinal Ne^{3+} ion momentum distributions for $n_c = 26$, $\omega_0 = 0.057$ a.u., $F_0 = 0.24$ a.u. and $F_0 = 0.34$ a.u. measured by Rudenko *et al.* (2008a) (black markers), compared to the distribution of longitudinal ROBI ion momenta (4.87) of the pathways 0-3 (blue curve), 0-1-3 (red curve) and 0-2-3 (dark orange curve) calculated with the simple man's model using the same pulse parameters. The vertical lines indicate the classical momentum limits $p_\parallel^{3+} = \pm 2n \cdot \sqrt{U_p}$ of single ionization ($n = 1$, dotted), double ionization ($n = 2$, dashed dotted) and triple ionization ($n = 3$, dashed), respectively.

is clearly visible. However, it is again not possible to distinguish 0-1-3 and 0-2-3 in the distributions. Ultimately, this means that the evidence for the importance of 0-2-3 which we found in Chapter 3 does not contradict the experiments.

Now we return to our simulation results. In Fig. 4.23, we show the Ne^{3+} ion momentum distributions as a function of the Cartesian transversal ion momenta $p_{\perp,x}^{3+}$ and $p_{\perp,y}^{3+}$ (equation (4.37)). All distributions exhibit a threefold rotational symmetry around $p_{\perp,x}^{3+} = p_{\perp,y}^{3+} = 0$ which results from the geometry of our model (see Fig. 2.1). It can be shown that, if the electron momentum distribution of triple ionization is invariant under the inversion operation $(p_1, p_2, p_3) \to (-p_1, -p_2, -p_3)$, the corresponding longitudinal Ne^{3+} ion momentum distribution is an even function of $p_\parallel^{3+}$ and the Cartesian transversal distribution has a sixfold rotational symmetry. For $F_0 = 0.5$ a.u., i.e. in the sequential regime, both properties are nearly realized. This is not surprising since the electron momentum distribution can be approximated by a product of single ionization momentum distributions (equation (4.84)) each of which is sufficiently symmetric. Generally, an inversion symmetry of the electron momentum distribution can be achieved either by using a periodic electric field or by averaging momentum distributions obtained for a uniform distribution of carrier-envelope phases, as done by Prauzner-Bechcicki *et al.* (2008) for double ionization.

We have also calculated the Ne^{3+} ion momentum distributions for $\omega_0 = 0.1$ a.u. which are shown in Fig. 4.24 and Fig. 4.25. The results are very similar to those for $\omega_0 = 0.06$ a.u. but the structural changes, especially in the longitudinal Ne^{3+} ion momentum distribution, are shifted to larger field amplitudes. For example, the longitudinal distribution for $(F_0, \omega_0) = (0.2$ a.u., 0.1 a.u.) is similar to that for (0.15 a.u., 0.06 a.u.). The shift in the field amplitude can be traced back to the change of the

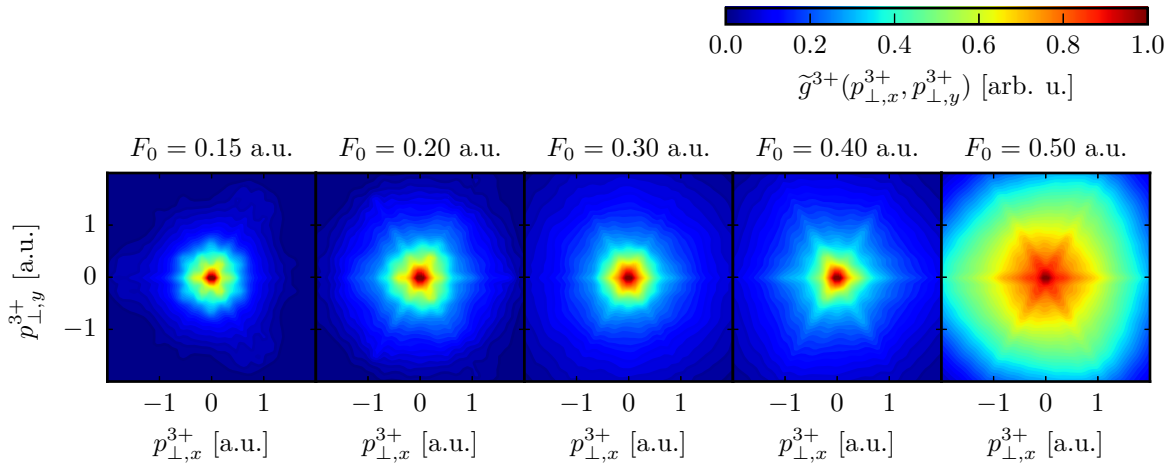

Figure 4.23. Ne^{3+} ion momentum distributions for $n_c = 5$ and $\omega_0 = 0.06$ a.u., integrated over $p^{3+}_{\parallel}$.

classical momentum scale $F_0/\omega_0 \propto \sqrt{U_p}$. This is illustrated in Fig. 4.26 where we plot the distributions with similar momentum scales (e.g. $F_0/\omega_0 = 0.15/0.06$ a.u. $= 2.5$ a.u. versus $F_0/\omega_0 = 0.2/0.1$ a.u. $= 2$ a.u.) on top of each other. In the sequential regime, the three electrons tunnel out one by one. Each of them transfers a longitudinal momentum proportional to $\sqrt{U_p}$ (equation (4.69)) to the ion. Therefore, the width of the longitudinal momentum distribution scales with $\sqrt{U_p}$ and the results for the two frequencies nearly coincide (rightmost panel). For smaller field amplitudes, triple ionization pathways involving a rescattering step are significant. The longitudinal ion momenta of these pathways (equations (4.85) and (4.86)) contain a term due to the excess energy of the recollision which does not scale with $\sqrt{U_p}$. Therefore, it is not surprising that the corresponding distributions do not coincide albeit they are similar in shape.

Now we consider the momentum distributions for $F_0 = 0.15$ a.u. and $\omega_0 = 0.1$ a.u. shown in the leftmost column of Fig. 4.24. For these pulse parameters, the maximum recollision energy ($E_{rec} = 3.04 \cdot 2U_p/3 = 1.14$ a.u.) is much smaller than the sum of the two ionization energies of the singly-charged ion ($E_I^+ + E_I^{2+} = 3.83$ a.u.), even if the field modification is taken into account. As a consequence, three-electron ROBI is energetically forbidden. Its absence is illustrated by the fact that the longitudinal momentum distribution for $F_0 = 0.15$ a.u. is notably narrower than the one for $F_0 = 0.2$ a.u., i.e. Ne^{3+} ions with momenta larger than $4 \cdot 2\sqrt{U_p}/3$ are less probable. Since three-electron ROBI cannot occur, the triply-charged ions may result from three-electron RESI. In this recollision scenario, the kinetic energy of the rescattered electron is only sufficient to promote the other two electrons to an excited state of the singly-charged ion (see Section 1.4.1). For our model, the energy difference between the ground state of the neutral atom and the lowest excited state of the singly-charged ion is $\Delta E = 1.58$ a.u. (see Fig. 2.4), i.e. smaller than the maximum recollision energy. However, if the time-dependent field modification of the first ionization energy is in-

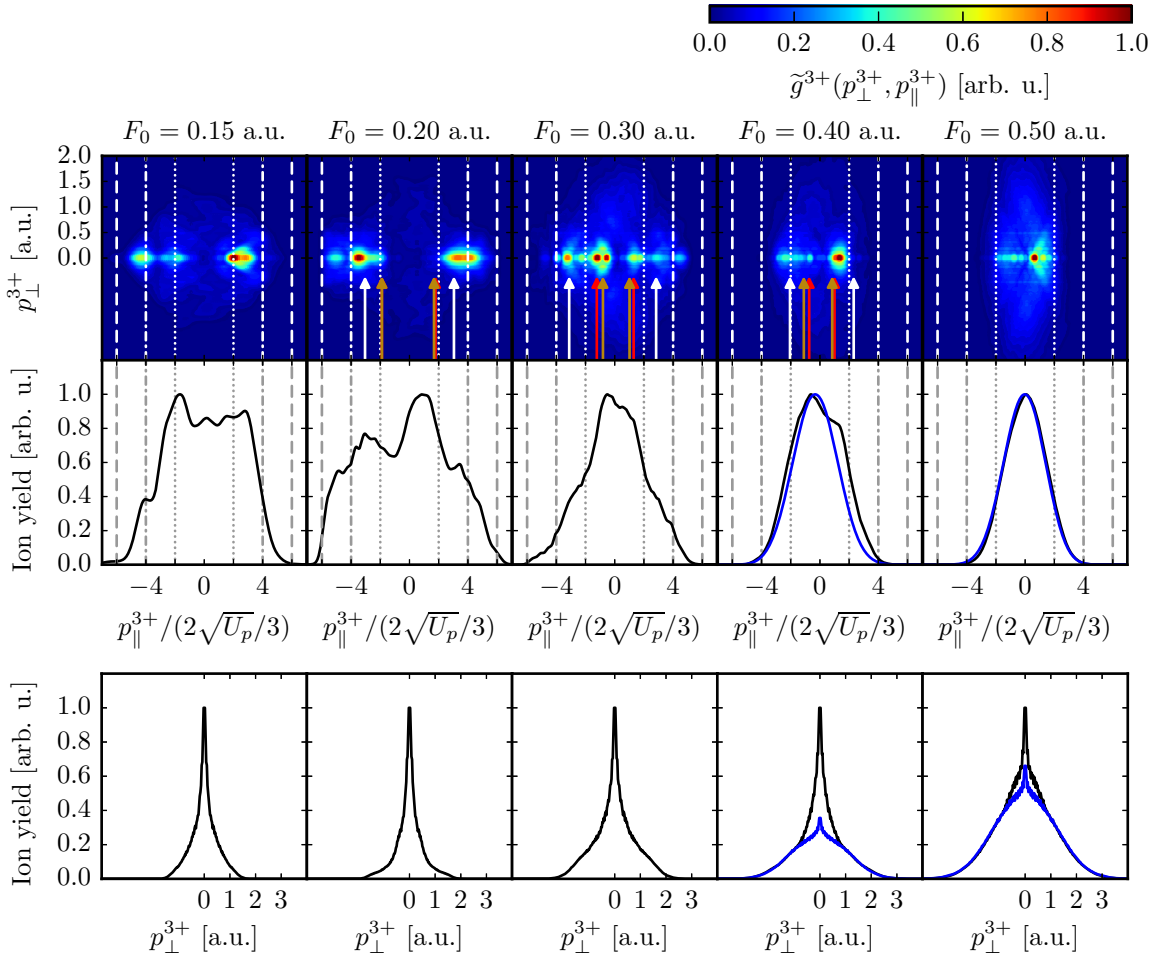

Figure 4.24. Same as Fig. 4.20, but for $\omega_0 = 0.1$ a.u.

cluded, there are recollision times for which a promotion of the two electrons to the first or even the second excited state ($\Delta E = 1.64$ a.u.) is possible.

In three-electron RESI, the rescattering electron ionizes immediately after the recollision while the excited electrons ionize later in the pulse. The time delay implies that the electron momenta at the end of the pulse will differ in both sign and magnitude (Feuerstein *et al.*, 2001; Rudenko *et al.*, 2004), in contrast to three-electron ROBI. This can be seen as follows. Leaving aside the (small) excess momentum retained by the first electron, the final electron momenta are determined only by the drift momentum gained in the laser field (we only consider the longitudinal direction). The first electron leaves the ion after the recollision, i.e. close to a zero-crossing of the laser field, and can thus gain a longitudinal drift momentum on the order of the maximum value $\pm 2 \cdot 2\sqrt{U_p}/3$. The momenta of the other two electrons depend on the ionization mechanism of the excited state. If the electrons simultaneously tunnel ionize at the field extremum following the moment of recollision, as expected from a generalization of the double ionization case (see Fig. 1.3), they essentially gain zero drift momentum.

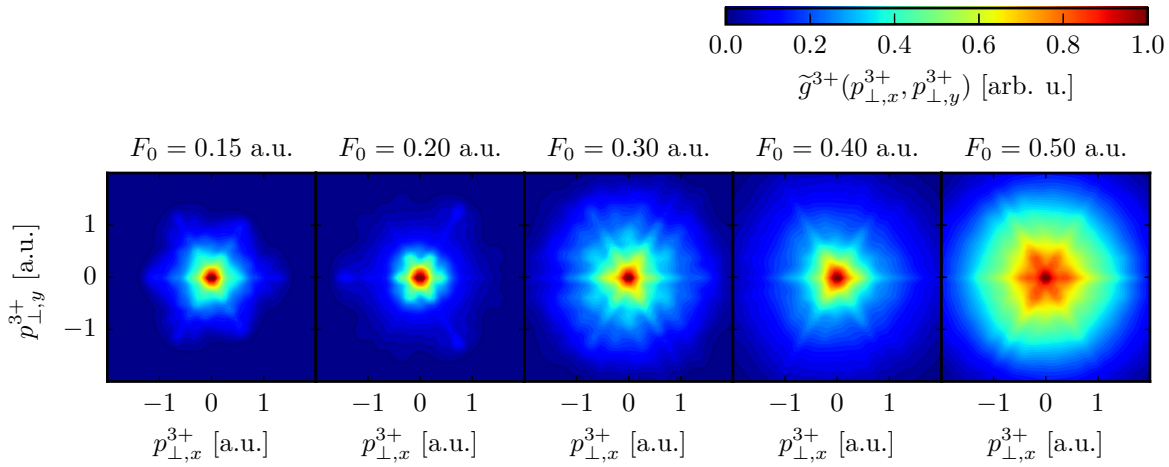

Figure 4.25. Same as Fig. 4.23, but for $\omega_0 = 0.1$ a.u.

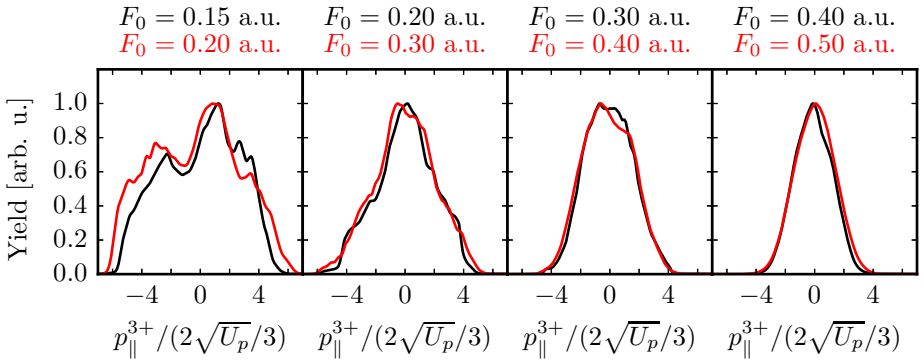

Figure 4.26. Longitudinal Ne^{3+} ion momentum distributions for $n_c = 5$ and $\omega_0 = 0.06$ a.u. (black curves), compared to the distributions for $\omega_0 = 0.1$ a.u. (red curves).

The same holds true for sequential tunnel ionization. In both cases, at least one electron ionizes in the direction opposite to that of the first electron. Simultaneous double ionization by rescattering, on the other hand, would yield electrons with nonzero drift momenta. However, for the pulse parameters under consideration, both two-electron ROBI and RESI from the excited state are energetically forbidden. In the longitudinal Ne^{3+} ion momentum distribution, the first electron produces well-pronounced maxima near $\pm 2 \cdot 2\sqrt{U_p}/3$. Tunnel ionization of the other electrons (either simultaneously or sequentially) "fills the valley" between the maxima and broadens the distribution (Rudenko *et al.*, 2004). This structure is in qualitative agreement with our result for $F_0 = 0.15$ a.u. and $\omega_0 = 0.1$ a.u.

In view of the above arguments, three-electron RESI might be the reason for the general lack of a pronounced minimum near $p^{3+}_{\parallel} = 0$ in our nonsequential longitudinal Ne^{3+} ion momentum distributions. To investigate whether the reduced dimensionality of our model entails a larger contribution of three-electron RESI, we compare our distribution for $F_0 = 0.15$ a.u., $\omega_0 = 0.06$ a.u. and $n_c = 5$ to the results of classical

simulations (Ho and Eberly, 2007; Zhou *et al.*, 2010b; Tang *et al.*, 2013) which were performed with the full-dimensional three-electron Hamiltonian

$$H = \sum_{i=1}^{3} \left(\frac{\boldsymbol{p}_i^2}{2} - \frac{3}{\sqrt{\boldsymbol{r}_i^2 + \varepsilon_1^2}} - F(t) z_i \right) + \sum_{\substack{i,j=1 \\ i<j}}^{3} \frac{1}{\sqrt{(\boldsymbol{r}_i - \boldsymbol{r}_j)^2 + \varepsilon_2^2}} \tag{4.88}$$

with $\varepsilon_1^2 = 1$ a.u. and a trapezoidal pulse (two-cycle turn on and turn off and $n_c - 4$ cycles at full strength). In all cases, the three-electron ground state was represented by a microcanonical ensemble with energy -4.63 a.u. (independent of the cut-off parameter ε_2) which is close to the quantum mechanical ground state energy of our model (-4.69 a.u.). We first consider the results of Ho and Eberly (2007). These authors calculated the longitudinal triply-charged ion momentum distribution for $\varepsilon_2^2 = 0.0625$ a.u. with $3 \cdot 10^6$ trajectories and pulse parameters very similar to our work ($F_0 = 0.15$ a.u., $\omega_0 = 0.058$ a.u., $n_c = 8$). Despite the use of the full-dimensional Hamiltonian, their distribution is similar to ours: On the one hand, it exhibits two maxima near $p_\parallel^{3+} = \pm 2\sqrt{U_p}$ and extends to about $p_\parallel^{3+} = \pm 6\sqrt{U_p}$. On the other hand, the minimum near $p_\parallel^{3+} = 0$ is quite shallow, i.e. the ratio r of the maximum yield to the yield of the minimum is close to one ($r \approx 1.2$). A detailed analysis of the distribution revealed that the shallow minimum is due to two types of recollision-induced triple ionization trajectories occurring with roughly the same probability. For the first type, the electrons leave the atom in the same direction, i.e. their longitudinal momentum components have the same sign. The corresponding longitudinal ion momentum distribution is broad and has two pronounced maxima near $p_\parallel^{3+} = \pm 4\sqrt{U_p}$, similar to the experiments. The second type of trajectories produces electrons with positive *and* negative longitudinal momenta so that the longitudinal ion momentum distribution only has a single maximum near $p_\parallel^{3+} = 0$. Superposition of the two trajectory types yields a distribution with a shallow minimum. Studying the details of the underlying recollision reactions, Ho and Eberly found that the first (second) type of trajectories requires a large (small) recollision energy and that the three electrons are ejected nearly simultaneously (with a significant time delay). Therefore, the first (second) type can be associated with three-electron ROBI (RESI). Accordingly, an increase of the recollision energy scale, e.g. the use of a larger field amplitude or a smaller frequency (or both), should induce a larger probability for ROBI trajectories and therefore lead to a deeper minimum in the momentum distribution. This expectation is corroborated by the simulations of Zhou *et al.* (2010b) ($F_0 = 0.17$ a.u., $\omega_0 = 0.057$ a.u., $n_c = 10$, $\varepsilon_2^2 = 0.01$ a.u., $4 \cdot 10^6$ trajectories) and Tang *et al.* (2013) ($F_0 = 0.17$ a.u., $\omega_0 = 0.028$ a.u., $n_c = 10$, $\varepsilon_2^2 = 0.01$ a.u., 10^7 trajectories) which yield $r \approx 2$ and $r \approx 4$, respectively. However, a rigorous comparison of the three classical simulations is not possible due to the differences in F_0, n_c, ε_2 and the ensemble size.

The full-dimensional classical simulations suggest that the reduced dimensionality of our model *alone* is not responsible for the shallow minima in the longitudinal Ne^{3+} ion momentum distributions. To further investigate this (and to enable a more rigorous comparison with the full-dimensional results), one has to calculate classical momentum

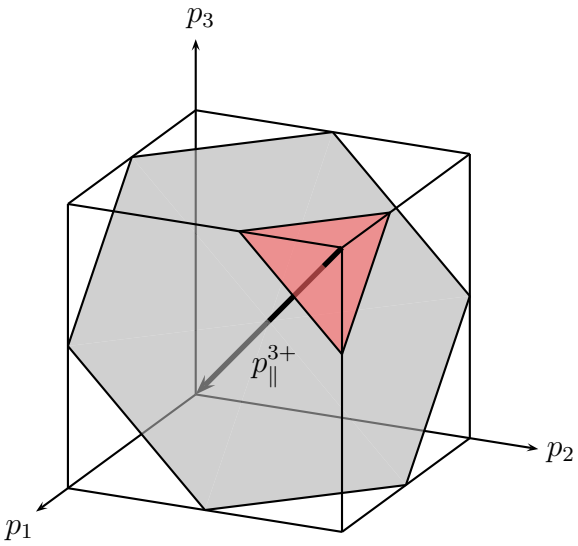

Figure 4.27. Schematic calculation of the longitudinal Ne^{3+} ion momentum distribution. The electron momentum distribution $g^{3+}(p_1, p_2, p_3)$ of triple ionization is calculated on a cube-shaped grid with the numerical method described in Section 4.1.4. By integrating $g^{3+}(p_1, p_2, p_3)$ over the planes perpendicular to the diagonal of the cube (thick black line), the longitudinal Ne^{3+} ion momentum distribution $\widetilde{g}^{3+}(p_\parallel^{3+}) = \widetilde{g}^{3+}(-\sqrt{2/3}(p_1 + p_2 + p_3))$ is obtained. The area of the cube-plane intersection for fixed $p_\parallel^{3+}$ is a measure for the number of grid points contributing to $\widetilde{g}^{3+}(p_\parallel^{3+})$. Therefore, the number of grid points is largest for $p_\parallel^{3+} = 0$ (gray plane) and reduced for $p_\parallel^{3+} < 0$ and $p_\parallel^{3+} > 0$ (red plane).

distributions for the three-electron Hamiltonian (2.7) and systematically vary the relevant parameters, most importantly the pulse shape and the cut-off parameters ε_1 and ε_2 which smooth the nuclear attraction and the electron repulsion, respectively[11]. The role of the cut-off parameters is of special interest since they influence the dynamics of the system close to the nucleus and, therefore, the efficiency of the recollision-induced multiple ionization pathways. However, such classical simulations require a numerical and conceptual effort which is way beyond the scope of this work.

The physical arguments of the previous paragraphs notwithstanding, the shallow or nonexistent minima in our longitudinal Ne^{3+} ion momentum distributions might also have a numerical origin as we will show now. According to equation (4.36), the longitudinal Ne^{3+} ion momentum distribution $\widetilde{g}^{3+}(p_\parallel^{3+})$ is found by calculating the two-dimensional distribution $\widetilde{g}^{3+}(p_\perp^{3+}, p_\parallel^{3+})$, taking it times $p_\perp^{3+}$ and integrating the product over $p_\perp^{3+}$. Mathematically, this is equivalent to integrating the electron momentum distribution $g^{3+}(p_1, p_2, p_3)$ over the planes $p_1 + p_2 + p_3 = \text{const.}$ which are perpendicular to the diagonal of momentum space. Due to the finite position grid spacing Δr, only electron momenta from the interval $[-\pi/\Delta r, \pi/\Delta r]$ are possible, i.e. the numerical momentum space is a cube with side length $2\pi/\Delta r$ (Fig. 4.27). As a consequence, the

[11] Note that we have chosen $\varepsilon_1 = \varepsilon_2 = \varepsilon$ in (2.7) and in all quantum calculations.

extension of momentum space in the $p_\perp^{3+}$-direction, i.e. the upper limit $p_{\perp,max}^{3+}$ of the integral

$$\widetilde{g}^{3+}(p_\parallel^{3+}) = \int_0^{p_{\perp,max}^{3+}} \widetilde{g}^{3+}(p_\perp^{3+}, p_\parallel^{3+}) p_\perp^{3+} \mathrm{d}p_\perp^{3+}, \tag{4.89}$$

is a function of $p_\parallel^{3+}$. In particular, this means that more grid points contribute to $\widetilde{g}^{3+}(p_\parallel^{3+} = 0)$ than to $\widetilde{g}^{3+}(p_\parallel^{3+} \ll 0)$ and $\widetilde{g}^{3+}(p_\parallel^{3+} \gg 0)$, thus filling the minimum in the longitudinal Ne^{3+} ion momentum distribution. However, there are two facts which contradict this conclusion. First, we showed in Fig. 4.3 that decreasing Δr from 0.39 a.u. to 0.2 a.u., i.e. increasing the maximum electron momentum from 8 a.u. to 16 a.u, does not change the distribution[12]. Secondly, for $F_0 \leq 0.4$ a.u. and both frequencies, 8 a.u. is larger than the maximum momentum of a classical, rescattering electron ($\sqrt{2 \cdot 3.17 \cdot 2U_p/3} = \sqrt{3.17/3}(F_0/\omega_0)$), i.e. all significant electron momenta should be contained in the numerical momentum space. Ultimately, the question whether the unpronounced minima are a numerical effect can only be answered by re-calculating the above distributions for a spatial grid spacing which is so small that a cut-off of significant contributions can be excluded. This is not possible with the computational resources available for this work.

To conclude this section, we briefly consider the angular distribution of triple ionization which is calculated from the electron momentum distribution using trilinear interpolation. The angular distribution for both frequencies is shown in Fig. 4.28 as a function of the field amplitude, with the direction of the field axis indicated by black circles. The eight octants of the Cartesian electron momentum distribution can be located in the angular distribution by using the map shown in Fig. 4.29. In essence, the angular distributions are a restatement of our previous results. In the nonsequential regime, the ionized electrons cluster around the field axis, i.e. they are mainly located in the octants I (all electron momenta positive) and VII (all electron momenta negative), illustrating electron momentum correlation. In the sequential regime (rightmost column), the electron correlation is lost and the ionized electron are located in all octants. Regardless of the field amplitude, all distributions exhibit a threefold rotational symmetry around the field axis which is somewhat distorted due to the projection from the unit sphere to the plane. Due to the definition of the longitudinal Ne^{3+} ion momentum ($p_\parallel^{3+} \propto -(p_1 + p_2 + p_3)$), the preferential direction of electron emission, i.e. the global maximum of the angular distribution, is opposite to the preferential direction of the ion ejection. For example, the maximum of the angular distribution for $F_0 = 0.15$ a.u. and $\omega_0 = 0.06$ a.u. is located in octant VII (where all electron momenta are negative) while the corresponding longitudinal Ne^{3+} ion momentum distribution peaks at a positive value of $p_\parallel^{3+}$.

[12]Due to the limited computational resources, this could only be verified for a position grid length of $L = 300$ a.u. However, in view of the weak dependence of the distribution on L for $L \geq 300$ a.u. (third column of Fig. 4.4), we expect that the results of this section (which were obtained for $L = 500$ a.u.) are also insensitive to a decrease of Δr.

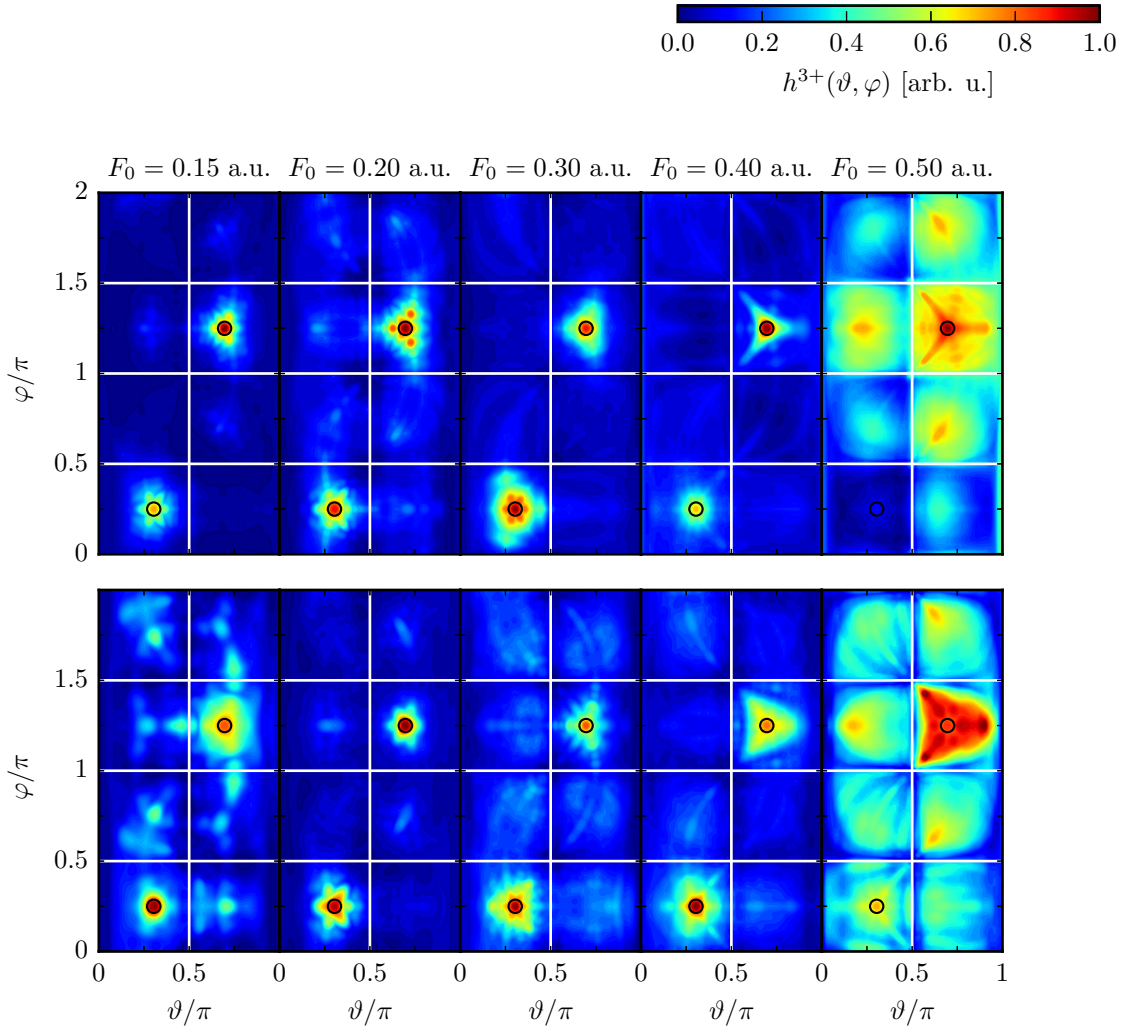

Figure 4.28. Angular distributions of triple ionization for $n_c = 5$, $\omega_0 = 0.06$ a.u. (first row) and $n_c = 5$, $\omega_0 = 0.1$ a.u. (second row). The white lines separate the eight octants of the momentum space grid (see Fig. 4.29). The direction of the field axis is indicated by the black circles.

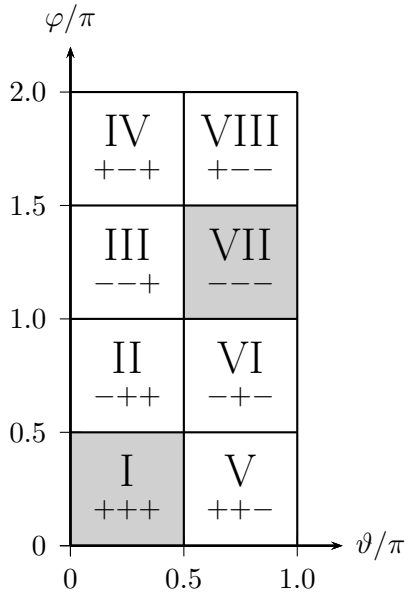

Figure 4.29. Location of the octants I-VIII of the Cartesian electron momentum distribution $g^{3+}(p_1, p_2, p_3)$ in the angular distribution of triple ionization. The symbols indicate the signs of the electron momenta in the respective octant (e.g. $-+-$: $p_1 < 0$, $p_2 > 0$, $p_3 < 0$). The octants containing the field axis are shaded.

5. Conclusions and outlook

In this thesis, we studied laser-induced multiple ionization quantum mechanically in a reduced-dimensionality model, with the main focus on triple ionization. In particular, we were concerned with the relative importance of the four triple ionization pathways from the neutral atom to the triply-charged ion (0-3, 0-1-3, 0-2-3 and 0-1-2-3). Being able to change the parameters of the laser pulse and to access the time- and momentum-resolved ionization probabilities, we could analyze the pathways and the underlying mechanisms in great detail and gain more insights than would be possible in an experiment.

We started by investigating the ion yields at the end of a two-cycle pulse with Ti:sapphire frequency as a function of the field amplitude F_0 (Fig. 3.15). In agreement with experiments, the triply-charged ion yield increases strongly with F_0 and exhibits a knee structure near the saturation field amplitude of double ionization F_{sat}^{DI}. We found that the triply-charged ion yield above F_{sat}^{DI} agrees very well with a product of the single ionization yields of the charge states 0, 1 and 2, all calculated within a single-active-electron approximation. This shows that the prevalent triple ionization pathway above F_{sat}^{DI} is 0-1-2-3, corresponding to sequential, independent ionization of the three electrons. Below F_{sat}^{DI}, however, the product yield of 0-1-2-3 strongly underestimates the triply-charged ion yield, indicating the prevalence of other, i.e. nonsequential, pathways. This transition is reflected in the knee structure in the triply-charged ion yield.

To understand the triple ionization processes below F_{sat}^{DI}, we first considered the pathways 0-1-3 and 0-2-3. Analogous to 0-1-2-3, their ionization yields were represented by products of the yields of the intermediate ionization steps. We found that if the electrons in each step are initially in the ground state, the product yields of both pathways considerably underestimate the triply-charged ion yield below F_{sat}^{DI} (Fig. 3.16a). However, if the electron in the last step of 0-2-3 is initially in the first excited state of the doubly-charged ion and the product yield is multiplied with an empirical "excitation probability" $P_{exc} < 1$, the sum yield of 0-1-3 and 0-2-3 fits the triply-charged ion yield very well between F_{sat}^{SI} (the saturation field amplitude of single ionization) and F_{sat}^{DI}. Moreover, a local maximum and a local minimum in the yield ratio of triple to double ionization can be reproduced this way (Fig. 3.16b). We explained the excitation of the third electron by the fact that the charge state 2 in 0-2-3 is created through recollision-induced double ionization. Due to the electron-electron interaction, the rescattered electron not only ionizes a second electron, but also promotes the third electron to an excited state of the doubly-charged ion from which ionization occurs with a much larger probability than from the ground state. Based on our findings, we conclude that

the prevalent triple ionization pathways between F_{sat}^{SI} and F_{sat}^{DI} are 0-1-3 (with 1 in the ground state) and 0-2-3 (with 2 in an excited state). Below F_{sat}^{SI}, the sum of 0-1-3 and 0-2-3 still underestimates the triply-charged ion yield, with the remaining contribution originating from simultaneous triple ionization (0-3).

Increasing the pulse duration from two to five cycles, we found that the product yield description of the triply-charged ion yield remains valid above F_{sat}^{SI} (Fig. 3.19). However, the relative contribution of the pathway 0-3 below F_{sat}^{SI} is larger than for the two-cycle pulse and accompanied by a pronounced plateau in the yield ratio of triple to single ionization. The analogy to the total ion yield (where the plateau signifies the onset of classical over-the-barrier ionization) suggests that the plateau results from the crossing of a classical threshold, namely of electron recollision leading to classical simultaneous triple ionization. To verify this hypothesis, we first calculated the threshold field amplitude of 0-3 by studying the dynamics of electron rescattering with the simple man's model. This threshold field amplitude was found to coincide very well with the onset of the plateau (Fig. 3.32). Secondly, we calculated the rescattering yield from the time-dependent single ionization yield and showed that their ratio at the end of the pulse depends only weakly on F_0, i.e. it is more or less flat (Fig. 3.35). Combining the two approaches, we conclude that the plateau in the ratio of triple to single ionization signifies the onset of classical simultaneous triple ionization.

The above conclusions are further supported by the momentum distribution of the triply-charged ion (Fig. 4.20). Above F_{sat}^{DI}, the momentum distribution has a single maximum in the longitudinal direction and can be approximated very well by a (suitably integrated) product of the single ionization momentum distributions of the charge states 0, 1 and 2, confirming the prevalence of 0-1-2-3 in this regime. Below F_{sat}^{DI}, the ion momentum distribution has two maxima in the longitudinal direction, indicating simultaneous ionization of several electrons. Plotting the longitudinal ion momentum in units of $F_0 \propto \sqrt{U_p}$ (where U_p is the ponderomotive energy), we found that the distribution above F_{sat}^{SI} is considerably narrower than the distribution below F_{sat}^{SI}. Furthermore, the separation of the maxima is smaller. According to the rescattering mechanism, these observations indicate that the number of simultaneously ejected electrons is smaller in the first than in the second regime of field amplitudes, i.e. two electrons ionize simultaneously above F_{sat}^{SI} (corresponding to the pathways 0-1-3 and 0-2-3) and three below F_{sat}^{SI} (corresponding to the pathway 0-3). By calculating the energy transfer in the recollision reaction, we could approximately reproduce the positions of the maxima with the simple man's model. The momentum distributions confirm our previous conclusion that the pathway 0-3 dominates the production of triply-charged ions below F_{sat}^{SI} and a two-step pathway (0-1-3, 0-2-3) takes over for larger field amplitudes. However, we found that 0-1-3 and 0-2-3 cannot be distinguished within the rescattering mechanism.

In summary, it can be stated that we have achieved our goal of understanding the triple ionization pathways in the different regimes of field amplitudes. The dependence of the yield and the momentum distribution of the triply-charged ion on F_0 is in good agreement with the qualitative description of Feuerstein *et al.* (2000) (Fig. 1.4).

However, there are two important differences. First, in agreement with experiments, the knee structure in the triply-charged ion yield near F_{sat}^{SI} suggested in their paper is not present, although the corresponding transition from 0-3 to a two-step pathway does show up in the yield ratio of triple to single ionization and in the momentum distribution. Secondly, our results indicate significant contributions from *both* 0-1-3 and 0-2-3 between F_{sat}^{SI} and F_{sat}^{DI} whereas Feuerstein *et al.* suggested that only 0-1-3 is significant in this regime. To clarify the role of 0-2-3 for triple ionization, a more quantitative investigation of this ionization pathway (including rescattering, impact ionization and impact excitation) is desirable. As a first step in this direction, one could calculate the impact ionization and excitation cross sections of the doubly-charged ion for our model. This would not only provide information on the importance of excitation, but also eliminate the need for an empirical factor in our 0-2-3 product yields. Moreover, such a calculation does not need the restriction to a low-dimensional model and could be attempted in the full three-dimensional setting, thereby providing information about the relevance of the pathway 0-2-3 in the full system.

In this work, the momentum distributions of the triply-charged ion were calculated only for a five-cycle pulse. Decreasing or increasing the pulse duration may help to answer some questions which remained open in this thesis, e.g. the role of recollision-induced excitation for the pathway 0-3 and the lack of a pronounced minimum in the longitudinal ion momentum distribution. Qualitatively, we expect that a shorter pulse yields a momentum distribution with less structure (due to the reduced number of recollision events) while a longer pulse should give a more symmetric distribution (due to the decreasing influence of the pulse shape and the carrier-envelope phase). Both features considerably simplify the interpretation of the results. However, since the three-electron wave function spreads with time, an increase of the pulse duration requires an increase of the numerical grid size which in turn increases the computation time and the memory requirements. Therefore, it depends on the available computational resources and the degree of parallelization whether a simulation with a certain pulse duration can be realized or not.

The single and double ionization yields used for the product yields in this work were calculated from one- and two-dimensional Hamiltonians. These were derived from the three-dimensional Hamiltonian of the Eckhardt-Sacha model, i.e. the restriction of the electron motion to the field-dependent *triple* ionization saddle. As a result, the representation of single and double ionization within the model differs from that in full space, i.e. the electrons move at a larger angle with respect to the field axis and the effective field amplitude felt by the electrons is therefore smaller. However, given the success of the product yield description, it is worthwhile to investigate whether the "master Hamiltonian" can be abandoned, i.e. if every ionization step in the product yields can be described within the model derived from the corresponding saddle in *full space*. Accordingly, the yields of the steps 0-2 and 0-1-3 would be calculated within the two-dimensional Eckhardt-Sacha model (Eckhardt and Sacha, 2006) while the yields of 0-1, 1-2 and 2-3 would be calculated within the one-dimensional Eckhardt-Sacha model (which is equal to a restriction of the electron motion to the field axis).

The model used in the present work is based on the geometrical electron escape configuration near the first energy threshold of simultaneous triple ionization, i.e. three electrons moving on the vertices of an equilateral triangle perpendicular to the field axis. However, the analysis of possible escape configurations shows that there is a second threshold at a slightly higher energy where the three electrons escape in a plane (one along the field axis and two symmetrically with respect to it). For the planar configuration, a reduced-dimensionality model can be defined in the same way as for the triangular configuration (see Appendix B.4.2). In a quantum mechanical description, the electron on the field axis can be distinguished from the outer ones. Nevertheless, calculating ion yields and momentum distributions for the planar version of the model seems promising for at least two reasons. First, the different form of the reduced potential implies different electron dynamics, especially close to the nucleus where the efficiency of the nonsequential ionization pathways is determined in a recollision reaction. Comparing the momentum distributions of the planar and the triangular model (which reflect the properties of the recollision) should yield more insights on how the atomic structure influences triple ionization in the nonsequential regime. Secondly, both models are subspaces (and therefore, in a way, limiting cases) of the full-dimensional Hamiltonian, so comparing the model results should also lead to a deeper understanding of triple ionization in the full system. The implementation of the planar model in the ion yield program has already been carried out and preliminary simulations are currently performed. For the momentum distribution program, the implementation is more difficult and yet to be undertaken.

Finally, we describe how the results of this work can be generalized to ionization of four electrons. There are eight pathways from the neutral atom to the quadruply-charged ion, namely simultaneous quadruple ionization (0-4), sequential quadruple ionization (0-1-2-3-4), two combinations of simultaneous triple ionization and single ionization (0-3-4, 0-1-4), three combinations of simultaneous double ionization and two single ionization steps (0-2-3-4, 0-1-3-4, 0-1-2-4) and a sequence of two simultaneous double ionization steps (0-2-4). Studying the competition between these pathways as a function of the field amplitude requires a model with four indistinguishable electrons, each of them with at least one degree of freedom. In four dimensions, indistinguishability can only be realized with the aligned-electron model where all electrons are confined to the field axis. Considering the already high computational cost of the three-dimensional simulations, a quantum mechanical study of such a four-dimensional model is not yet within numerical reach. However, with the modified product yield approach described above, the yields of all pathways (except for 0-4) can be calculated with the Eckhardt-Sacha models for one, two and three electrons (all symmetric with respect to electron exchange), using the programs developed for this work. Thus, the results obtained for the pathways of triple ionization can be easily extended to more electrons.

A. Supplementary material

This appendix collects raw data and additional results whose discussion is beyond the scope of this thesis, but may provide starting points for future investigations.

A.1. Ion yield tables

In this section, we show the end-of-the-pulse ion yields of the three-electron Eckhardt-Sacha model which were graphically presented in Sections 3.4, 3.5 and 3.6 in tabular form, with the format of the numbers chosen so as to allow for a quick import of the data points from the document. The tables are complete in the sense that all yield plots of this work may be reproduced from them. The product yields introduced in Section 3.4 which are based on one- and two-dimensional Hamiltonians can be rapidly calculated on a standard personal computer and are therefore not shown here.

All yields were obtained by integrating the time-dependent probability flux across boundaries in the three-dimensional position space, as described in Section 3.3.1. The fact that a partial separation of different ionization pathways is possible with this method was only used in the case of the simultaneous double ionization yield P_{02}. Therefore, only this yield and the total yields of each charge state (P_1, P_2 and P_3) are shown in the tables. Using probability conservation, the population of neutral atoms can be calculated from the total yields as $P_0 = 1 - (P_1 + P_2 + P_3)$.

Since the ion yields are calculated from a wave function represented on a position-space grid, their numerical accuracy is mainly determined by the grid length L and the grid step Δr. For small F_0, the wave function is confined to a small volume around the nucleus. Therefore, Δr has to be small enough so that the small-scale variations of the wave function can be resolved. For large F_0, on the other hand, the wave function can spread over a large volume around the nucleus which requires a value of L large enough to capture all significant contributions to the yield integrals (see Fig. 3.4). The number of possible combinations of Δr and L is limited by the computational effort which scales with the number of grid points $N^3 = (L/\Delta r)^3$. Comparing the results of various test calculations, we settled for $L = 600$ a.u. and $\Delta r = 0.39$ a.u. ($N = 1536$) as the standard grid parameters. At the lower end of the field interval, we decreased Δr by a factor of two by decreasing L to 200 a.u. and N to 1024. To verify that the smaller value of L does not significantly change the results in this regime, F_0 was increased until the yields overlapped with the ones obtained with the standard parameters in the log-log plot. Towards the upper end of the field interval, we increased L to 800 a.u. while keeping Δr constant. Due to the computational effort induced by the very large

number of grid points ($N^3 = 2048^3 = 8.6 \cdot 10^9$), the yields were only calculated for one frequency, two pulse durations and some selected values of F_0.

Most of the calculated yields are listed in the tables, with the values of L and Δr shown in the sixth and seventh column, respectively. All other numerical parameters were kept constant and are shown in Table A.1. Since a rigorous study of convergence is not possible, the yields used for the plots (indicated by shaded cells) were selected based on our experience from double ionization which, for example, tells us that the slope of the yields in the log-log plot does not decrease with decreasing F_0. Since the yields of the three charge states usually differ by orders of magnitude, there are cases where the large yields could be used, but the smaller ones could not, i.e. not all cells in a row are shaded. Furthermore, due to the conservation of probability enforced by the flux integration method, the single ionization yield P_1 becomes negative if the double ionization P_2 is close to one. These values of P_1 are nonphysical and are therefore put in parentheses.

In Section 3.4.5, we discussed the triple ionization pathway 0-2-3 and approximated its yield as P_{02} times the ion yield $P_1^{2+,1}$ of the first excited state of the doubly-charged ion times an empirical excitation probability P_{exc}. The values of P_{exc} used for the plots are listed in Table A.2.

Parameter	Symbol	Value
Time step	Δt	0.05 a.u.
Number of time steps	N_t	$\left\lceil \frac{2\pi(n_c+1)}{\omega_0 \Delta t} \right\rceil$
Space partitioning parameters	r_a	5 a.u.
	r_b	7 a.u.
	r_c	12.5 a.u.
Position of absorbing boundary	r_{abs}	$L/2 - 50$ a.u.
Strength of absorbing potential	η	10^{-5} a.u.

Table A.1. Numerical parameters used for the calculation of the ion yields shown in this section. $\lceil x \rceil = \min\{n \in \mathbb{Z} \mid n \geq x\}$ is the ceiling function.

	P_{exc}	
n_c	$\omega_0 = 0.06$ a.u.	$\omega_0 = 0.10$ a.u.
2	0.030	0.035
5	0.070	0.090
7	0.090	0.110

Table A.2. Empirical excitation probabilities P_{exc} used for the calculation of the 0-2-3 product yields DS.

F_0 [a.u.]	P_1	P_2	P_{02}	P_3	L [a.u.]	Δr [a.u.]	N
0.10	8.113E-04	6.158E-06	2.357E-06	3.413E-08	600	0.39	1536
	6.910E-04	4.891E-07	2.750E-07	5.528E-10	200	0.20	1024
0.11	2.081E-03	7.711E-06	2.952E-06	5.233E-08	600	0.39	1536
	2.026E-03	1.704E-06	1.035E-06	1.625E-09	200	0.20	1024
0.12	5.347E-03	1.485E-05	7.354E-06	7.359E-08	600	0.39	1536
	5.208E-03	8.353E-06	5.101E-06	7.728E-09	200	0.20	1024
0.13	1.139E-02	4.504E-05	2.314E-05	1.183E-07	600	0.39	1536
	1.163E-02	3.552E-05	1.968E-05	3.832E-08	200	0.20	1024
0.14	2.273E-02	1.397E-04	8.180E-05	2.477E-07	600	0.39	1536
	2.327E-02	1.206E-04	7.111E-05	1.269E-07	200	0.20	1024
0.15	4.046E-02	2.851E-04	1.712E-04	5.825E-07	600	0.39	1536
	4.218E-02	2.651E-04	1.602E-04	3.691E-07	200	0.20	1024
0.16	6.622E-02	5.981E-04	3.706E-04	1.274E-06	600	0.39	1536
0.17	1.023E-01	1.088E-03	6.761E-04	2.676E-06	600	0.39	1536
0.18	1.491E-01	1.756E-03	1.030E-03	5.167E-06	600	0.39	1536
0.19	2.057E-01	2.578E-03	1.499E-03	9.219E-06	600	0.39	1536
0.20	2.711E-01	3.567E-03	2.049E-03	1.551E-05	600	0.39	1536
0.21	3.425E-01	4.617E-03	2.594E-03	2.558E-05	600	0.39	1536
0.22	4.154E-01	5.782E-03	3.108E-03	4.136E-05	600	0.39	1536
0.23	4.921E-01	7.427E-03	3.913E-03	6.272E-05	600	0.39	1536
0.24	5.622E-01	9.014E-03	4.635E-03	9.401E-05	600	0.39	1536
0.25	6.261E-01	1.159E-02	5.740E-03	1.322E-04	600	0.39	1536
0.26	6.784E-01	1.481E-02	6.859E-03	1.836E-04	600	0.39	1536
0.27	7.222E-01	1.993E-02	8.708E-03	2.614E-04	600	0.39	1536
0.28	7.536E-01	2.650E-02	1.055E-02	3.247E-04	600	0.39	1536
0.29	7.745E-01	3.607E-02	1.297E-02	4.166E-04	600	0.39	1536
0.30	7.824E-01	4.891E-02	1.569E-02	5.186E-04	600	0.39	1536
	7.823E-01	4.899E-02	1.569E-02	5.369E-04	800	0.39	2048
0.31	7.749E-01	6.576E-02	1.874E-02	6.341E-04	600	0.39	1536
0.32	7.649E-01	8.694E-02	2.200E-02	7.886E-04	600	0.39	1536
0.33	7.439E-01	1.127E-01	2.523E-02	9.564E-04	600	0.39	1536
0.34	7.142E-01	1.433E-01	2.854E-02	1.159E-03	600	0.39	1536
0.35	6.803E-01	1.784E-01	3.152E-02	1.398E-03	600	0.39	1536
	6.805E-01	1.781E-01	3.152E-02	1.510E-03	800	0.39	2048
0.36	6.406E-01	2.179E-01	3.438E-02	1.694E-03	600	0.39	1536
0.37	5.979E-01	2.613E-01	3.687E-02	2.067E-03	600	0.39	1536
0.38	5.572E-01	3.070E-01	3.888E-02	2.554E-03	600	0.39	1536
0.39	5.107E-01	3.555E-01	4.060E-02	3.188E-03	600	0.39	1536
0.40	4.641E-01	4.053E-01	4.203E-02	4.069E-03	600	0.39	1536
	4.643E-01	4.049E-01	4.203E-02	4.297E-03	800	0.39	2048
0.41	4.183E-01	4.555E-01	4.302E-02	5.265E-03	600	0.39	1536
0.42	3.726E-01	5.050E-01	4.374E-02	6.859E-03	600	0.39	1536
0.43	3.272E-01	5.534E-01	4.425E-02	9.021E-03	600	0.39	1536
0.44	2.836E-01	5.999E-01	4.465E-02	1.192E-02	600	0.39	1536
0.45	2.409E-01	6.434E-01	4.506E-02	1.588E-02	600	0.39	1536
	2.392E-01	6.446E-01	4.506E-02	1.633E-02	800	0.39	2048
0.46	2.001E-01	6.830E-01	4.551E-02	2.072E-02	600	0.39	1536
0.47	1.610E-01	7.187E-01	4.615E-02	2.716E-02	600	0.39	1536
0.48	1.230E-01	7.500E-01	4.692E-02	3.595E-02	600	0.39	1536
0.49	8.906E-02	7.753E-01	4.827E-02	4.619E-02	600	0.39	1536
0.50	6.081E-02	7.919E-01	4.958E-02	5.829E-02	600	0.39	1536
	5.561E-02	7.958E-01	4.958E-02	5.951E-02	800	0.39	2048
0.51	3.698E-02	8.007E-01	5.199E-02	7.323E-02	600	0.39	1536
0.52	5.774E-03	8.139E-01	5.437E-02	9.156E-02	600	0.39	1536
0.53	(−1.113E-02)	8.078E-01	5.673E-02	1.113E-01	600	0.39	1536
0.54	(−2.286E-02)	7.959E-01	5.833E-02	1.331E-01	600	0.39	1536
0.55	(−3.176E-02)	7.799E-01	6.105E-02	1.556E-01	600	0.39	1536
	(−5.181E-02)	7.935E-01	6.105E-02	1.620E-01	800	0.39	2048

Table A.3. Ion yields for $n_c = 2$, $\omega_0 = 0.06$ a.u. and $\varphi_0 = 0$.

F_0 [a.u.]	P_1	P_2	P_{02}	P_3	L [a.u.]	Δr [a.u.]	N
0.07	8.174E-06	1.603E-07	9.895E-08	2.075E-10	200	0.20	1024
0.08	3.579E-05	8.235E-07	4.521E-07	4.839E-10	200	0.20	1024
0.09	1.802E-04	4.892E-06	2.491E-06	3.083E-09	200	0.20	1024
0.10	7.548E-04	2.312E-05	1.150E-05	3.629E-08	600	0.39	1536
	8.453E-04	2.418E-05	1.251E-05	2.689E-08	200	0.20	1024
0.11	2.479E-03	8.425E-05	4.542E-05	2.707E-07	600	0.39	1536
	2.888E-03	8.929E-05	4.947E-05	1.923E-07	200	0.20	1024
0.12	7.290E-03	2.768E-04	1.406E-04	1.446E-06	600	0.39	1536
	8.385E-03	2.789E-04	1.474E-04	1.109E-06	200	0.20	1024
0.13	1.731E-02	7.091E-04	3.643E-04	4.972E-06	600	0.39	1536
	1.897E-02	6.766E-04	3.483E-04	3.829E-06	200	0.20	1024
0.14	3.490E-02	1.496E-03	7.371E-04	1.382E-05	600	0.39	1536
	4.039E-02	1.221E-03	5.845E-04	1.013E-05	200	0.20	1024
0.15	6.014E-02	2.700E-03	1.371E-03	2.907E-05	600	0.39	1536
	7.515E-02	2.018E-03	9.832E-04	1.961E-05	200	0.20	1024
0.16	1.048E-01	4.350E-03	2.031E-03	5.521E-05	600	0.39	1536
0.17	1.723E-01	7.420E-03	3.250E-03	9.245E-05	600	0.39	1536
0.18	2.533E-01	1.044E-02	4.499E-03	1.389E-04	600	0.39	1536
0.19	3.318E-01	1.387E-02	5.942E-03	2.112E-04	600	0.39	1536
0.20	4.429E-01	1.731E-02	7.470E-03	2.916E-04	600	0.39	1536
0.21	5.334E-01	2.059E-02	8.410E-03	3.673E-04	600	0.39	1536
0.22	6.046E-01	2.404E-02	9.635E-03	4.722E-04	600	0.39	1536
0.23	7.022E-01	2.915E-02	1.226E-02	5.849E-04	600	0.39	1536
0.24	7.148E-01	3.170E-02	1.281E-02	6.972E-04	600	0.39	1536
0.25	7.918E-01	3.513E-02	1.369E-02	8.997E-04	600	0.39	1536
0.26	8.230E-01	4.705E-02	1.768E-02	1.369E-03	600	0.39	1536
0.27	8.200E-01	5.724E-02	1.952E-02	1.640E-03	600	0.39	1536
0.28	8.099E-01	6.955E-02	2.105E-02	2.025E-03	600	0.39	1536
0.29	8.016E-01	8.601E-02	2.172E-02	2.409E-03	600	0.39	1536
0.30	7.654E-01	1.096E-01	2.328E-02	2.879E-03	600	0.39	1536
	7.613E-01	1.136E-01	2.328E-02	3.048E-03	800	0.39	2048
0.31	7.508E-01	1.372E-01	2.518E-02	3.514E-03	600	0.39	1536
0.32	7.112E-01	1.739E-01	2.730E-02	4.055E-03	600	0.39	1536
0.33	6.701E-01	2.125E-01	2.925E-02	4.778E-03	600	0.39	1536
0.34	6.250E-01	2.599E-01	3.343E-02	5.927E-03	600	0.39	1536
0.35	5.734E-01	3.065E-01	3.315E-02	6.751E-03	600	0.39	1536
	5.332E-01	3.460E-01	3.315E-02	7.542E-03	800	0.39	2048
0.36	5.230E-01	3.604E-01	3.296E-02	7.574E-03	600	0.39	1536
0.37	4.688E-01	4.178E-01	3.797E-02	9.257E-03	600	0.39	1536
0.38	4.103E-01	4.748E-01	3.584E-02	1.033E-02	600	0.39	1536
0.39	3.510E-01	5.356E-01	3.874E-02	1.251E-02	600	0.39	1536
0.40	2.923E-01	5.951E-01	3.818E-02	1.441E-02	600	0.39	1536
	2.241E-01	6.608E-01	3.818E-02	1.685E-02	800	0.39	2048
0.41	2.375E-01	6.492E-01	4.053E-02	1.755E-02	600	0.39	1536
0.42	1.997E-01	6.855E-01	4.073E-02	2.132E-02	600	0.39	1536
0.43	1.719E-01	7.079E-01	4.296E-02	2.789E-02	600	0.39	1536
0.44	1.540E-01	7.180E-01	4.152E-02	3.524E-02	600	0.39	1536
0.45	1.474E-01	7.190E-01	4.350E-02	3.979E-02	600	0.39	1536
	4.478E-02	8.117E-01	4.350E-02	4.968E-02	800	0.39	2048
0.46	1.476E-01	7.095E-01	4.080E-02	4.814E-02	600	0.39	1536
0.47	1.470E-01	6.977E-01	4.337E-02	5.917E-02	600	0.39	1536
0.48	1.484E-01	6.822E-01	4.087E-02	7.010E-02	600	0.39	1536
0.49	1.552E-01	6.621E-01	4.231E-02	8.060E-02	600	0.39	1536
0.50	1.527E-01	6.463E-01	4.071E-02	9.526E-02	600	0.39	1536
	(−2.817E-02)	7.801E-01	4.071E-02	1.422E-01	800	0.39	2048
0.51	1.420E-01	6.367E-01	4.450E-02	1.150E-01	600	0.39	1536
0.52	1.326E-01	6.225E-01	4.428E-02	1.362E-01	600	0.39	1536
0.53	1.193E-01	6.052E-01	4.627E-02	1.654E-01	600	0.39	1536
0.54	9.529E-02	5.936E-01	4.903E-02	2.025E-01	600	0.39	1536
0.55	6.593E-02	5.794E-01	5.072E-02	2.492E-01	600	0.39	1536
	(−6.903E-02)	6.224E-01	5.071E-02	3.412E-01	800	0.39	2048

Table A.4. Ion yields for $n_c = 5$, $\omega_0 = 0.06$ a.u. and $\varphi_0 = 0$.

F_0 [a.u.]	P_1	P_2	P_{02}	P_3	L [a.u.]	Δr [a.u.]	N
0.07	9.982E-06	1.951E-07	1.134E-07	2.198E-10	200	0.20	1024
0.08	4.973E-05	1.446E-06	8.274E-07	1.118E-09	200	0.20	1024
0.09	2.854E-04	9.393E-06	4.729E-06	1.396E-08	200	0.20	1024
0.10	1.166E-03	5.439E-05	2.953E-05	2.356E-07	600	0.39	1536
	1.053E-03	4.520E-05	2.574E-05	1.125E-07	200	0.20	1024
0.11	4.318E-03	2.139E-04	1.204E-04	1.458E-06	600	0.39	1536
	4.226E-03	2.066E-04	1.194E-04	7.584E-07	200	0.20	1024
0.12	9.991E-03	4.134E-04	1.907E-04	5.255E-06	600	0.39	1536
	1.116E-02	4.124E-04	1.967E-04	3.045E-06	200	0.20	1024
0.13	2.318E-02	1.269E-03	6.270E-04	1.823E-05	600	0.39	1536
	2.631E-02	1.093E-03	5.212E-04	9.861E-06	200	0.20	1024
0.14	5.265E-02	2.923E-03	1.530E-03	4.434E-05	600	0.39	1536
0.15	1.025E-01	6.075E-03	2.944E-03	9.679E-05	600	0.39	1536
0.16	1.566E-01	9.387E-03	4.203E-03	1.668E-04	600	0.39	1536
0.17	2.313E-01	1.261E-02	5.563E-03	2.644E-04	600	0.39	1536
0.18	3.642E-01	2.242E-02	9.925E-03	4.612E-04	600	0.39	1536
0.19	4.728E-01	2.644E-02	1.187E-02	6.127E-04	600	0.39	1536
0.20	5.743E-01	3.299E-02	1.508E-02	8.658E-04	600	0.39	1536
0.21	6.392E-01	3.868E-02	1.647E-02	1.086E-03	600	0.39	1536
0.22	7.557E-01	4.276E-02	1.870E-02	1.374E-03	600	0.39	1536
0.23	7.649E-01	4.778E-02	2.118E-02	1.648E-03	600	0.39	1536
0.24	7.881E-01	5.039E-02	2.077E-02	1.945E-03	600	0.39	1536
0.25	8.414E-01	5.763E-02	2.319E-02	2.364E-03	600	0.39	1536
0.26	8.261E-01	6.367E-02	2.317E-02	2.606E-03	600	0.39	1536
0.27	8.072E-01	7.663E-02	2.471E-02	3.238E-03	600	0.39	1536
0.28	8.048E-01	9.445E-02	2.814E-02	3.640E-03	600	0.39	1536
0.29	7.770E-01	1.166E-01	2.947E-02	4.162E-03	600	0.39	1536
0.30	7.512E-01	1.418E-01	3.056E-02	5.100E-03	600	0.39	1536
0.31	7.169E-01	1.762E-01	3.375E-02	5.734E-03	600	0.39	1536
0.32	6.737E-01	2.149E-01	3.207E-02	6.499E-03	600	0.39	1536
0.33	6.254E-01	2.625E-01	3.700E-02	7.806E-03	600	0.39	1536
0.34	5.787E-01	3.062E-01	3.256E-02	8.482E-03	600	0.39	1536
0.35	5.287E-01	3.566E-01	3.698E-02	1.021E-02	600	0.39	1536
0.36	4.794E-01	4.064E-01	3.754E-02	1.142E-02	600	0.39	1536
0.37	4.285E-01	4.546E-01	3.913E-02	1.309E-02	600	0.39	1536
0.38	3.867E-01	4.978E-01	3.764E-02	1.471E-02	600	0.39	1536
0.39	3.416E-01	5.404E-01	4.020E-02	1.654E-02	600	0.39	1536
0.40	2.984E-01	5.840E-01	3.802E-02	1.860E-02	600	0.39	1536
0.41	2.670E-01	6.128E-01	4.122E-02	2.160E-02	600	0.39	1536
0.42	2.342E-01	6.427E-01	3.757E-02	2.562E-02	600	0.39	1536
0.43	2.024E-01	6.700E-01	4.196E-02	3.179E-02	600	0.39	1536
0.44	1.817E-01	6.874E-01	3.886E-02	3.611E-02	600	0.39	1536
0.45	1.601E-01	6.978E-01	4.175E-02	4.773E-02	600	0.39	1536
0.46	1.509E-01	6.999E-01	3.987E-02	5.549E-02	600	0.39	1536
0.47	1.385E-01	7.009E-01	4.345E-02	6.764E-02	600	0.39	1536
0.48	1.410E-01	6.862E-01	3.953E-02	7.903E-02	600	0.39	1536
0.49	1.359E-01	6.730E-01	4.219E-02	9.695E-02	600	0.39	1536
0.50	1.378E-01	6.526E-01	4.006E-02	1.151E-01	600	0.39	1536
0.51	1.420E-01	6.253E-01	4.142E-02	1.366E-01	600	0.39	1536
0.52	1.386E-01	6.000E-01	4.058E-02	1.645E-01	600	0.39	1536
0.53	1.372E-01	5.570E-01	4.086E-02	2.086E-01	600	0.39	1536
0.54	1.312E-01	5.346E-01	4.121E-02	2.350E-01	600	0.39	1536
0.55	1.171E-01	5.083E-01	4.172E-02	2.758E-01	600	0.39	1536

Table A.5. Ion yields for $n_c = 7$, $\omega_0 = 0.06$ a.u. and $\varphi_0 = 0$.

F_0 [a.u.]	P_1	P_2	P_{02}	P_3	L [a.u.]	Δr [a.u.]	N
0.10	1.865E-03	5.651E-06	2.235E-06	3.563E-08	600	0.39	1536
	1.818E-03	1.943E-06	1.018E-06	7.133E-10	200	0.20	1024
0.11	4.270E-03	8.809E-06	3.578E-06	4.274E-08	600	0.39	1536
	4.222E-03	5.284E-06	2.239E-06	8.677E-10	200	0.20	1024
0.12	8.797E-03	1.783E-05	8.064E-06	4.908E-08	600	0.39	1536
	8.768E-03	1.483E-05	6.537E-06	1.166E-09	200	0.20	1024
0.13	1.583E-02	3.894E-05	2.004E-05	5.379E-08	600	0.39	1536
	1.592E-02	3.831E-05	1.861E-05	2.144E-09	200	0.20	1024
0.14	2.575E-02	7.701E-05	4.199E-05	7.235E-08	600	0.39	1536
	2.625E-02	8.037E-05	4.111E-05	1.270E-08	200	0.20	1024
0.15	4.045E-02	1.649E-04	9.773E-05	1.875E-07	600	0.39	1536
	4.162E-02	1.666E-04	9.335E-05	9.811E-08	200	0.20	1024
0.16	6.335E-02	3.662E-04	2.202E-04	6.049E-07	600	0.39	1536
	6.522E-02	3.646E-04	2.086E-04	4.563E-07	200	0.20	1024
0.17	9.662E-02	5.760E-04	3.423E-04	1.670E-06	600	0.39	1536
	9.933E-02	5.576E-04	3.148E-04	1.434E-06	200	0.20	1024
0.18	1.269E-01	1.240E-03	7.937E-04	4.122E-06	600	0.39	1536
	1.306E-01	1.230E-03	7.340E-04	3.752E-06	200	0.20	1024
0.19	1.632E-01	1.574E-03	9.498E-04	8.695E-06	600	0.39	1536
0.20	2.129E-01	3.197E-03	2.047E-03	1.629E-05	600	0.39	1536
0.21	2.778E-01	3.686E-03	2.248E-03	3.016E-05	600	0.39	1536
0.22	3.194E-01	6.769E-03	4.407E-03	5.142E-05	600	0.39	1536
0.23	3.738E-01	7.291E-03	4.417E-03	8.403E-05	600	0.39	1536
0.24	4.508E-01	1.182E-02	7.769E-03	1.282E-04	600	0.39	1536
0.25	4.888E-01	1.362E-02	8.056E-03	1.959E-04	600	0.39	1536
0.26	5.392E-01	1.862E-02	1.171E-02	2.783E-04	600	0.39	1536
0.27	6.094E-01	2.471E-02	1.477E-02	4.029E-04	600	0.39	1536
0.28	6.228E-01	3.008E-02	1.650E-02	5.402E-04	600	0.39	1536
0.29	6.568E-01	3.973E-02	2.235E-02	7.225E-04	600	0.39	1536
0.30	6.986E-01	5.111E-02	2.650E-02	9.814E-04	600	0.39	1536
0.31	7.010E-01	6.307E-02	3.055E-02	1.234E-03	600	0.39	1536
0.32	7.115E-01	7.905E-02	3.722E-02	1.527E-03	600	0.39	1536
0.33	6.942E-01	9.982E-02	4.385E-02	1.946E-03	600	0.39	1536
0.34	6.906E-01	1.208E-01	4.987E-02	2.410E-03	600	0.39	1536
0.35	6.740E-01	1.460E-01	5.607E-02	2.908E-03	600	0.39	1536
0.36	6.584E-01	1.731E-01	6.277E-02	3.461E-03	600	0.39	1536
0.37	6.303E-01	2.046E-01	6.956E-02	4.085E-03	600	0.39	1536
0.38	6.015E-01	2.375E-01	7.590E-02	4.876E-03	600	0.39	1536
0.39	5.642E-01	2.746E-01	8.148E-02	5.813E-03	600	0.39	1536
0.40	5.298E-01	3.110E-01	8.631E-02	6.900E-03	600	0.39	1536
0.41	4.877E-01	3.509E-01	9.153E-02	8.219E-03	600	0.39	1536
0.42	4.517E-01	3.902E-01	9.507E-02	9.814E-03	600	0.39	1536
0.43	4.081E-01	4.302E-01	9.858E-02	1.175E-02	600	0.39	1536
0.44	3.745E-01	4.677E-01	1.008E-01	1.415E-02	600	0.39	1536
0.45	3.326E-01	5.069E-01	1.033E-01	1.714E-02	600	0.39	1536
0.46	3.028E-01	5.375E-01	1.048E-01	2.079E-02	600	0.39	1536
0.47	2.709E-01	5.693E-01	1.057E-01	2.528E-02	600	0.39	1536
0.48	2.403E-01	5.971E-01	1.062E-01	3.066E-02	600	0.39	1536
0.49	2.150E-01	6.204E-01	1.067E-01	3.709E-02	600	0.39	1536
0.50	1.908E-01	6.402E-01	1.064E-01	4.467E-02	600	0.39	1536
0.51	1.674E-01	6.567E-01	1.061E-01	5.365E-02	600	0.39	1536
0.52	1.511E-01	6.665E-01	1.060E-01	6.394E-02	600	0.39	1536
0.53	1.334E-01	6.747E-01	1.062E-01	7.584E-02	600	0.39	1536
0.54	1.162E-01	6.798E-01	1.060E-01	8.918E-02	600	0.39	1536
0.55	1.034E-01	6.796E-01	1.070E-01	1.042E-01	600	0.39	1536

Table A.6. Ion yields for $n_c = 2$, $\omega_0 = 0.10$ a.u. and $\varphi_0 = 0$.

F_0 [a.u.]	P_1	P_2	P_{02}	P_3	L [a.u.]	Δr [a.u.]	N
0.07	4.524E-05	2.011E-07	1.423E-07	2.389E-10	200	0.20	1024
0.08	1.496E-04	1.437E-06	1.237E-06	2.976E-10	200	0.20	1024
0.09	6.967E-04	9.726E-06	6.736E-06	1.131E-09	200	0.20	1024
0.10	1.526E-03	4.556E-05	2.573E-05	1.315E-08	600	0.39	1536
	1.699E-03	4.868E-05	2.770E-05	1.354E-08	200	0.20	1024
0.11	4.211E-03	1.198E-04	6.503E-05	1.064E-07	600	0.39	1536
	4.681E-03	1.283E-04	6.992E-05	1.049E-07	200	0.20	1024
0.12	1.006E-02	3.304E-04	1.808E-04	4.972E-07	600	0.39	1536
	1.118E-02	3.540E-04	1.944E-04	4.790E-07	200	0.20	1024
0.13	2.238E-02	8.904E-04	5.127E-04	2.336E-06	600	0.39	1536
	2.488E-02	9.515E-04	5.518E-04	2.276E-06	200	0.20	1024
0.14	3.850E-02	1.455E-03	7.342E-04	6.544E-06	600	0.39	1536
	4.278E-02	1.553E-03	7.893E-04	6.190E-06	200	0.20	1024
0.15	5.944E-02	3.098E-03	1.730E-03	1.713E-05	600	0.39	1536
	6.598E-02	3.335E-03	1.860E-03	1.626E-05	200	0.20	1024
0.16	9.852E-02	4.230E-03	2.191E-03	3.592E-05	600	0.39	1536
0.17	1.483E-01	8.974E-03	5.496E-03	8.365E-05	600	0.39	1536
0.18	1.897E-01	9.065E-03	4.291E-03	1.387E-04	600	0.39	1536
0.19	2.635E-01	1.788E-02	1.076E-02	2.510E-04	600	0.39	1536
0.20	3.394E-01	1.949E-02	1.069E-02	3.661E-04	600	0.39	1536
0.21	4.516E-01	2.600E-02	1.423E-02	5.555E-04	600	0.39	1536
0.22	4.521E-01	2.975E-02	1.478E-02	7.479E-04	600	0.39	1536
0.23	5.482E-01	3.444E-02	1.727E-02	1.009E-03	600	0.39	1536
0.24	6.004E-01	4.187E-02	2.165E-02	1.336E-03	600	0.39	1536
0.25	6.453E-01	4.568E-02	2.064E-02	1.632E-03	600	0.39	1536
0.26	7.356E-01	6.095E-02	3.056E-02	2.149E-03	600	0.39	1536
0.27	7.507E-01	7.034E-02	3.342E-02	3.122E-03	600	0.39	1536
0.28	7.520E-01	8.317E-02	3.752E-02	4.092E-03	600	0.39	1536
0.29	7.519E-01	9.926E-02	4.025E-02	4.448E-03	600	0.39	1536
0.30	7.113E-01	1.218E-01	4.906E-02	5.066E-03	600	0.39	1536
0.31	7.185E-01	1.426E-01	5.207E-02	6.092E-03	600	0.39	1536
0.32	6.723E-01	1.656E-01	5.127E-02	7.630E-03	600	0.39	1536
0.33	6.454E-01	2.064E-01	6.252E-02	8.959E-03	600	0.39	1536
0.34	5.986E-01	2.442E-01	6.462E-02	1.030E-02	600	0.39	1536
0.35	5.719E-01	2.820E-01	6.481E-02	1.165E-02	600	0.39	1536
0.36	5.156E-01	3.247E-01	6.946E-02	1.390E-02	600	0.39	1536
0.37	4.860E-01	3.710E-01	7.519E-02	1.616E-02	600	0.39	1536
0.38	4.314E-01	4.132E-01	7.759E-02	1.936E-02	600	0.39	1536
0.39	3.659E-01	4.834E-01	8.054E-02	2.201E-02	600	0.39	1536
0.40	3.288E-01	5.274E-01	8.918E-02	2.564E-02	600	0.39	1536
0.41	2.881E-01	5.648E-01	8.882E-02	2.961E-02	600	0.39	1536
0.42	2.334E-01	6.200E-01	8.944E-02	3.266E-02	600	0.39	1536
0.43	1.735E-01	6.686E-01	8.884E-02	3.665E-02	600	0.39	1536
0.44	1.641E-01	6.742E-01	8.420E-02	4.253E-02	600	0.39	1536
0.45	1.200E-01	7.177E-01	8.882E-02	4.990E-02	600	0.39	1536
0.46	1.042E-01	7.273E-01	8.934E-02	5.861E-02	600	0.39	1536
0.47	6.027E-02	7.550E-01	8.781E-02	7.273E-02	600	0.39	1536
0.48	6.166E-02	7.382E-01	8.881E-02	8.802E-02	600	0.39	1536
0.49	5.399E-02	7.345E-01	9.082E-02	1.005E-01	600	0.39	1536
0.50	2.907E-02	7.378E-01	8.817E-02	1.195E-01	600	0.39	1536
0.51	2.008E-02	7.288E-01	8.837E-02	1.361E-01	600	0.39	1536
0.52	1.611E-02	7.129E-01	8.930E-02	1.563E-01	600	0.39	1536
0.53	1.000E-02	6.925E-01	9.271E-02	1.821E-01	600	0.39	1536
0.54	1.396E-03	6.714E-01	9.262E-02	2.107E-01	600	0.39	1536
0.55	(−1.104E-02)	6.492E-01	9.373E-02	2.425E-01	600	0.39	1536

Table A.7. Ion yields for $n_c = 5$, $\omega_0 = 0.10$ a.u. and $\varphi_0 = 0$.

F_0 [a.u.]	P_1	P_2	P_{02}	P_3	L [a.u.]	Δr [a.u.]	N
0.07	4.853E-05	3.527E-07	2.801E-07	2.267E-10	200	0.20	1024
0.08	1.926E-04	3.000E-06	2.513E-06	4.303E-10	200	0.20	1024
0.09	1.090E-03	2.159E-05	1.572E-05	6.833E-09	200	0.20	1024
0.10	1.916E-03	8.508E-05	4.862E-05	1.434E-07	600	0.39	1536
	1.925E-03	8.546E-05	4.638E-05	1.052E-07	200	0.20	1024
0.11	7.225E-03	2.681E-04	1.607E-04	6.978E-07	600	0.39	1536
	7.195E-03	2.489E-04	1.455E-04	4.923E-07	200	0.20	1024
0.12	1.783E-02	8.524E-04	5.141E-04	2.594E-06	600	0.39	1536
	1.830E-02	8.188E-04	4.821E-04	2.018E-06	200	0.20	1024
0.13	2.727E-02	1.353E-03	7.467E-04	8.415E-06	600	0.39	1536
	2.828E-02	1.316E-03	7.148E-04	6.883E-06	200	0.20	1024
0.14	6.804E-02	3.909E-03	2.379E-03	2.930E-05	600	0.39	1536
	6.992E-02	3.914E-03	2.244E-03	2.242E-05	200	0.20	1024
0.15	7.949E-02	6.268E-03	3.636E-03	6.041E-05	600	0.39	1536
0.16	1.479E-01	9.531E-03	5.194E-03	1.182E-04	600	0.39	1536
0.17	2.184E-01	1.707E-02	1.052E-02	2.437E-04	600	0.39	1536
0.18	2.905E-01	2.489E-02	1.476E-02	4.265E-04	600	0.39	1536
0.19	3.783E-01	2.886E-02	1.503E-02	7.040E-04	600	0.39	1536
0.20	4.500E-01	3.846E-02	2.164E-02	9.597E-04	600	0.39	1536
0.21	4.902E-01	4.222E-02	2.335E-02	1.413E-03	600	0.39	1536
0.22	5.472E-01	3.936E-02	1.944E-02	1.715E-03	600	0.39	1536
0.23	6.563E-01	6.939E-02	3.844E-02	2.608E-03	600	0.39	1536
0.24	7.000E-01	7.115E-02	3.759E-02	3.300E-03	600	0.39	1536
0.25	7.054E-01	7.787E-02	3.821E-02	4.210E-03	600	0.39	1536
0.26	7.670E-01	7.876E-02	3.895E-02	4.245E-03	600	0.39	1536
0.27	7.306E-01	9.708E-02	4.676E-02	5.133E-03	600	0.39	1536
0.28	6.768E-01	1.204E-01	5.487E-02	7.805E-03	600	0.39	1536
0.29	7.234E-01	1.407E-01	6.065E-02	8.369E-03	600	0.39	1536
0.30	6.857E-01	1.710E-01	6.805E-02	1.051E-02	600	0.39	1536
0.31	6.727E-01	1.965E-01	7.409E-02	1.257E-02	600	0.39	1536
0.32	6.374E-01	2.177E-01	6.118E-02	1.280E-02	600	0.39	1536
0.33	6.058E-01	2.581E-01	6.894E-02	1.433E-02	600	0.39	1536
0.34	5.403E-01	2.989E-01	7.561E-02	1.696E-02	600	0.39	1536
0.35	4.941E-01	3.523E-01	8.507E-02	2.244E-02	600	0.39	1536
0.36	4.321E-01	4.248E-01	7.846E-02	2.291E-02	600	0.39	1536
0.37	3.724E-01	4.802E-01	7.745E-02	2.616E-02	600	0.39	1536
0.38	3.124E-01	5.389E-01	7.599E-02	2.727E-02	600	0.39	1536
0.39	2.775E-01	5.766E-01	9.270E-02	3.655E-02	600	0.39	1536
0.40	2.351E-01	6.112E-01	8.960E-02	3.910E-02	600	0.39	1536
0.41	1.943E-01	6.515E-01	9.153E-02	4.245E-02	600	0.39	1536
0.42	1.288E-01	7.132E-01	8.888E-02	4.523E-02	600	0.39	1536
0.43	8.337E-02	7.522E-01	9.509E-02	5.625E-02	600	0.39	1536
0.44	1.038E-01	7.245E-01	9.090E-02	6.468E-02	600	0.39	1536
0.45	5.680E-02	7.617E-01	8.683E-02	7.194E-02	600	0.39	1536
0.46	5.138E-02	7.520E-01	9.492E-02	9.011E-02	600	0.39	1536
0.47	3.544E-02	7.553E-01	8.909E-02	1.011E-01	600	0.39	1536
0.48	2.176E-02	7.509E-01	9.285E-02	1.193E-01	600	0.39	1536
0.49	1.460E-02	7.398E-01	9.146E-02	1.385E-01	600	0.39	1536
0.50	1.293E-02	7.143E-01	8.827E-02	1.618E-01	600	0.39	1536
0.51	1.142E-02	6.889E-01	9.141E-02	1.907E-01	600	0.39	1536
0.52	1.357E-02	6.677E-01	8.878E-02	2.095E-01	600	0.39	1536
0.53	5.959E-03	6.428E-01	8.533E-02	2.403E-01	600	0.39	1536
0.54	(−6.718E-04)	6.178E-01	9.245E-02	2.728E-01	600	0.39	1536
0.55	(−6.889E-03)	5.829E-01	9.282E-02	3.140E-01	600	0.39	1536

Table A.8. Ion yields for $n_c = 7$, $\omega_0 = 0.10$ a.u. and $\varphi_0 = 0$.

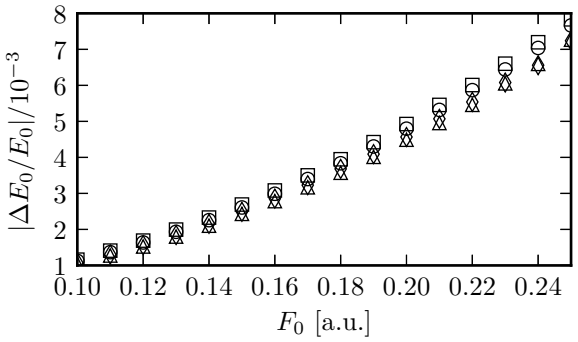

Figure A.1. Relative AC Stark shift of the ground state energy level of the Hamiltonian (2.7) with $\varepsilon^2 = 1.05$ a.u. for the laser field (2.28) with $\omega_0 = 0.06$ a.u., $n_c = 2$ (circles), $\omega_0 = 0.06$ a.u., $n_c = 5$ (triangles), $\omega_0 = 0.1$ a.u., $n_c = 2$ (squares) and $\omega_0 = 0.1$ a.u., $n_c = 5$ (diamonds).

A.2. AC Stark shift

In several parts of this work, especially in Section 3.6.3, we have implicitly assumed that the AC Stark shift of the ground state energy levels of the neutral atom and the ions is negligibly small. For the neutral atom described by the Hamiltonian (2.7), we show that this assumption is correct by calculating the net energy shift of the ground state ϕ_0 in the laser field $F(t)$. This shift is given by (Langhoff *et al.*, 1972)

$$\begin{aligned}\Delta E_0 &= \mathrm{Re}\left(\frac{1}{T_p}\int_0^{T_p}\frac{\langle\phi_0|H_{int}|\psi(t)\rangle}{\langle\phi_0|\psi(t)\rangle}\mathrm{d}t\right)\\ &= \mathrm{Re}\left(\frac{1}{T_p}\int_0^{T_p}\frac{\langle\phi_0|\sum_{i=1}^{3}\sqrt{\frac{2}{3}}F(t)r_i|\psi(t)\rangle}{\langle\phi_0|\psi(t)\rangle}\mathrm{d}t\right).\end{aligned} \tag{A.1}$$

Without the laser field, the ground state energy of (2.7) is $E_0 = -4.69$ a.u. for $\varepsilon^2 = 1.05$ a.u. The relative shift $|\Delta E_0/E_0|$ in the laser field is shown in Fig. A.1 as a function of the field amplitude. We see that the shift increases with F_0 but is almost independent of ω_0, as expected for frequencies which are small compared to the energy difference between the ground state level and the first excited state (Delone and Krainov, 1999). Since $|\Delta E_0/E_0|$ is on the order of 10^{-3} for the field interval of interest, the neglection of the AC Stark shift is justified.

A.3. Energy distributions of single ionization

The energy distributions of single ionization (4.40), calculated within the three-electron Eckhardt-Sacha model for the five-cycle pulse, are shown in Fig. A.2 (for $\omega_0 = 0.06$ a.u.) and A.3 (for $\omega_0 = 0.1$ a.u.) as black curves. We also calculated the distributions within the one-dimensional SAE approximation for the same numerical

parameters (blue curves) and for a larger grid length $L = 1600$ a.u. with a smaller spacing $\Delta r = 0.05$ a.u. (red curves). In contrast to Chapter 4, Gaussian smoothing was not applied to the distributions.

First, we note that the distributions have a fairly uniform shape: Each of them exhibits pronounced large-scale peaks at low energies, followed by a steep decrease beyond $E = E_c := 2 \cdot 2U_p/3$ and a plateau-like regime at even higher energies. The electrons with energies $E < E_c$ ("direct electrons") result from tunnel ionization while the ones with $E > E_c$ ("hot electrons") result from tunnel ionization with subsequent rescattering (Paulus *et al.*, 1994a,b). $E = E_c$, i.e. the final classical energy of an electron tunneling exactly at a zero-crossing of the field, represents the cut-off of the direct electrons since the corresponding tunneling probability is zero. The classical cut-off energy of the hot electrons is $E = 10 \cdot 2U_p/3$, corresponding to elastic backscattering of a rescattered electron by the ion (Paulus *et al.*, 1994a).

In the distributions of the two smallest field amplitudes, we observe a series of peaks near the tunneling cut-off which are separated by the photon energy. This is a characteristic property of above-threshold ionization (ATI) where an electron absorbs more than the minimum number of photons needed to overcome the ionization threshold. As shown by de Bohan *et al.* (2002), the ATI peaks result from the interference of electron wave packets which are ejected in the same direction in every field cycle. Therefore, the peaks become more pronounced if the pulse duration is increased. This is illustrated in Fig. A.4 for the SAE distribution of $\omega_0 = 0.1$ a.u. and $F_0 = 0.15$ a.u. The properties of ATI energy spectra have been thoroughly explored in the last decades (for a recent review, see Milošević *et al.* (2006)), so we do not further investigate this topic here.

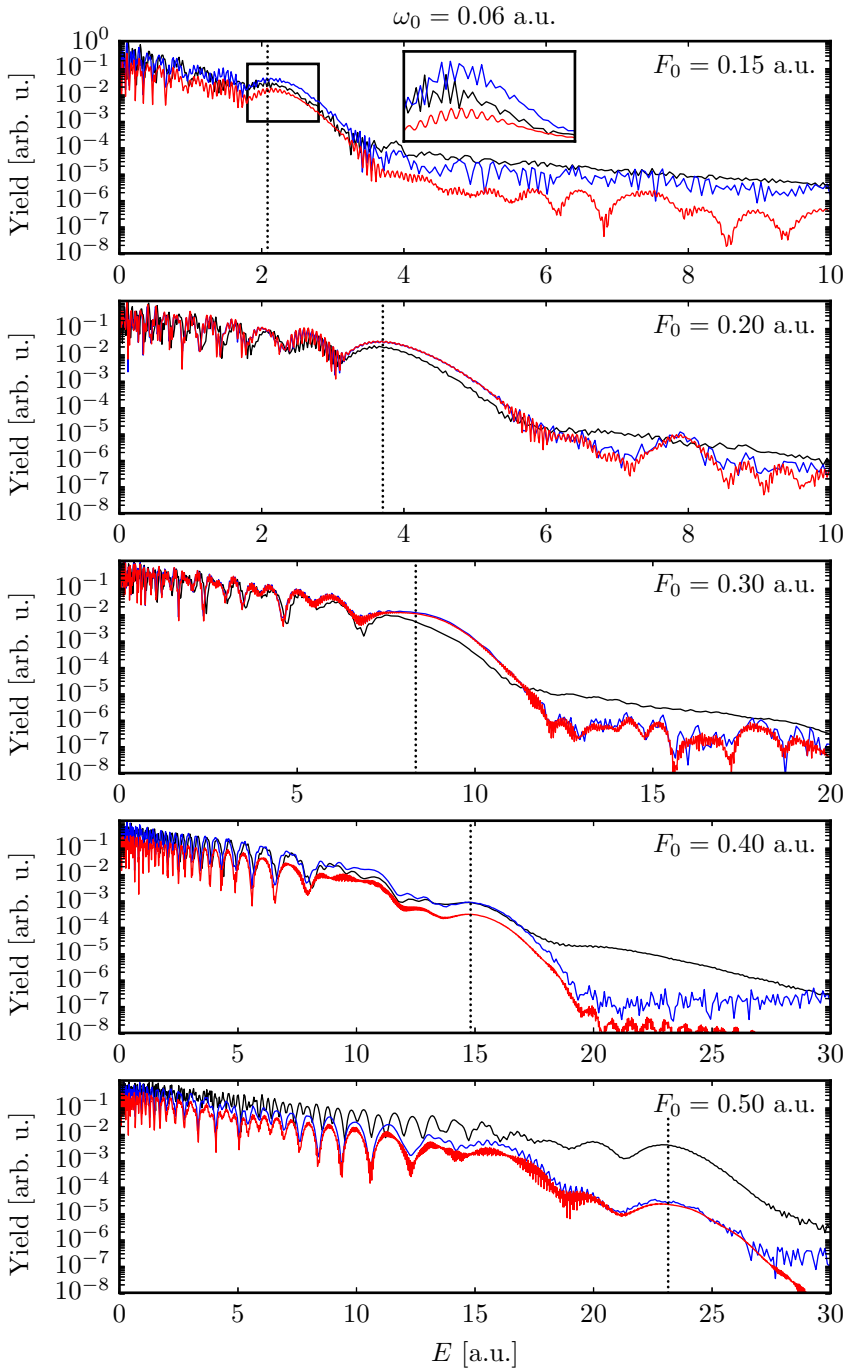

Figure A.2. Energy distribution of single ionization for $n_c = 5$ and $\omega_0 = 0.06$ a.u., calculated from the three-dimensional wave function (black curves), from the one-dimensional SAE wave function with the same numerical parameters (blue curves) and with a smaller grid spacing Δr (red curves). No Gaussian smoothing was applied to the distributions. For each field amplitude, the classical cut-off energy of $E = 2 \cdot 2U_p/3$, corresponding to an electron tunneling at a zero-crossing of the field, is indicated by the dotted line.

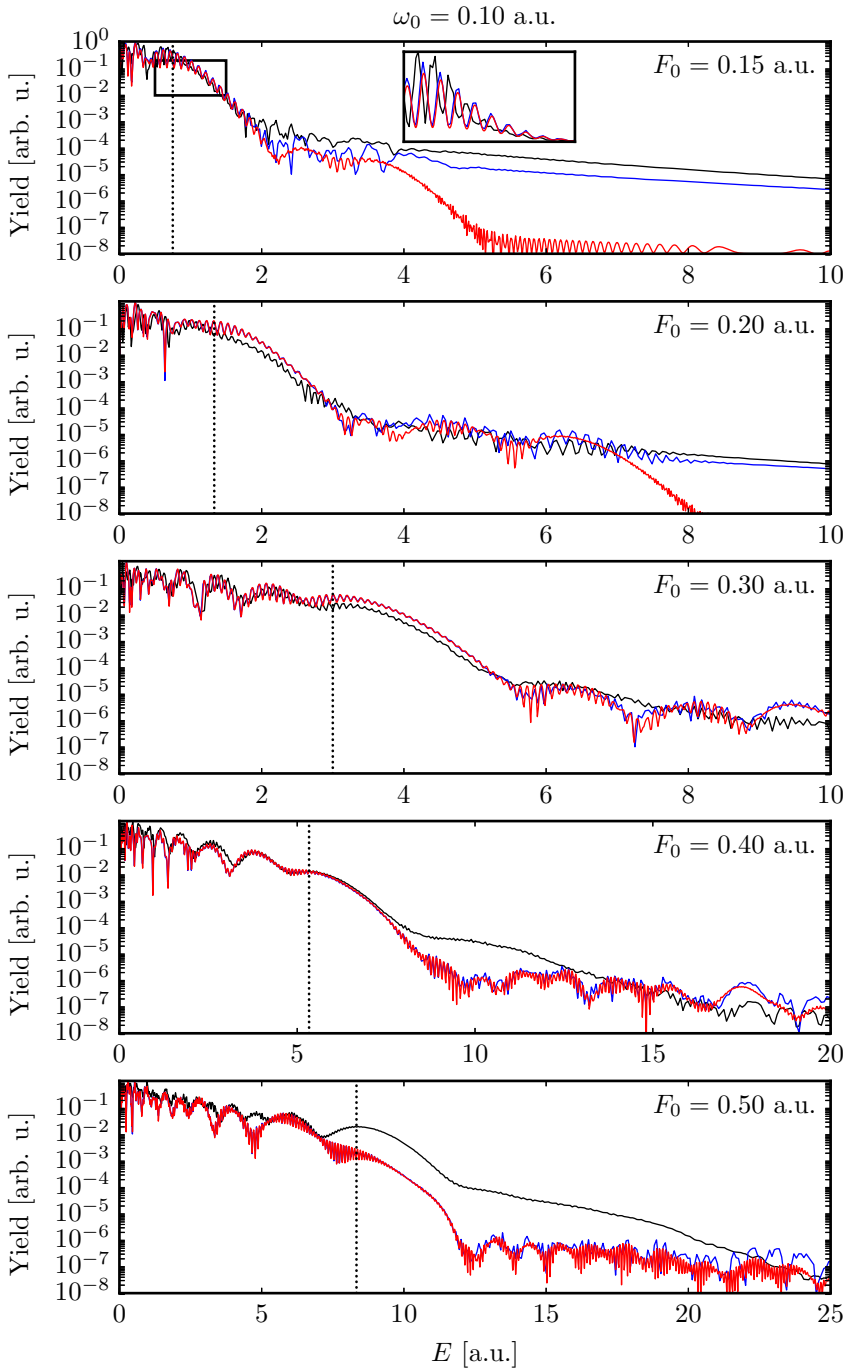

Figure A.3. Same as Fig. A.2, but for $\omega_0 = 0.1$ a.u.

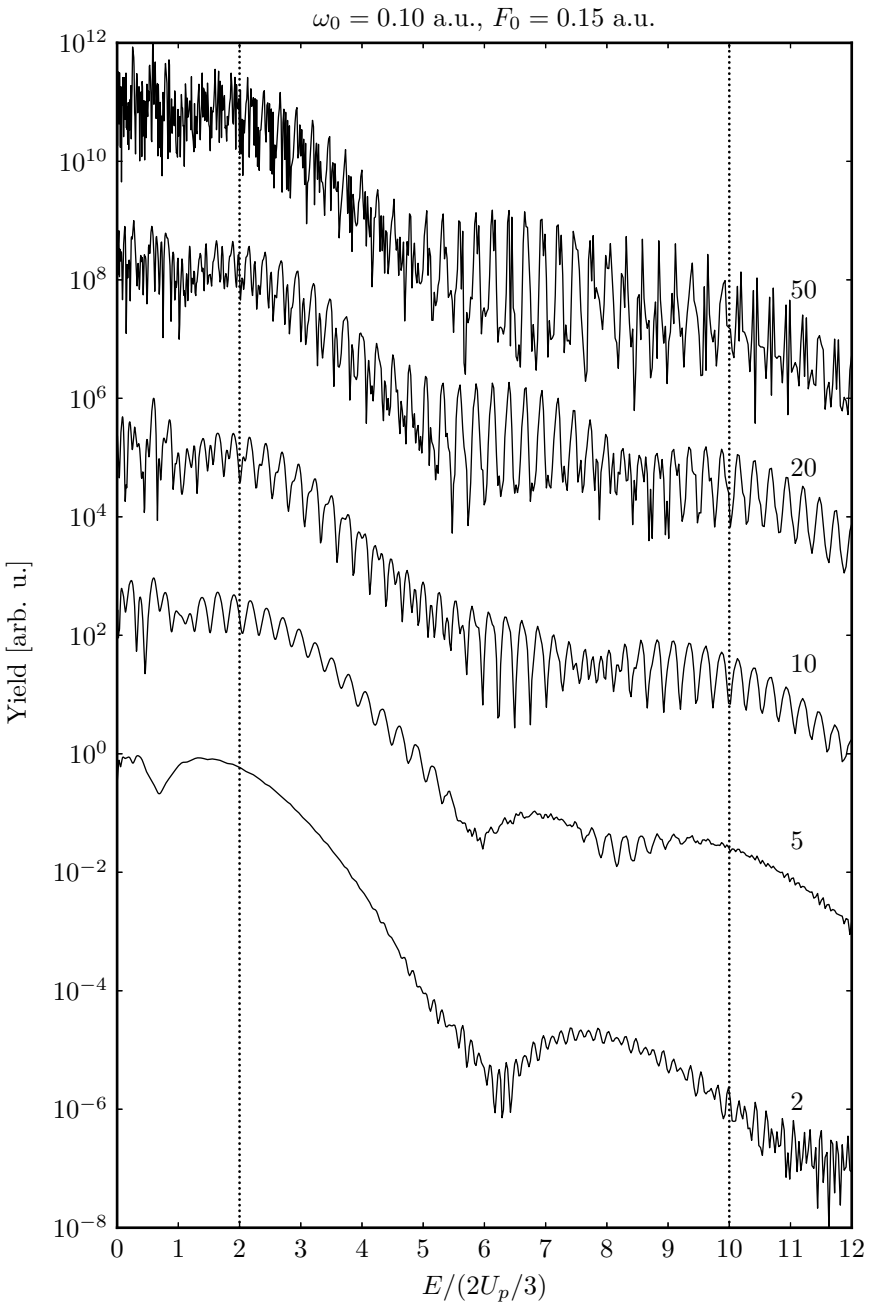

Figure A.4. Energy distribution of single ionization for $\omega_0 = 0.1$ a.u., $F_0 = 0.15$ a.u. and n_c as indicated, calculated within the one-dimensional SAE approximation. No Gaussian smoothing was applied to the distributions. For better visibility, the distributions are scaled apart by a factor of 1000. The classical cut-off energies of an electron tunneling at a zero-crossing of the field ($E = 2 \cdot 2U_p/3$) and elastic backscattering of a recolliding electron ($E = 10 \cdot 2U_p/3$) are indicated by the dotted and dashed lines, respectively.

B. Wannier theory of threshold multiple ionization in a laser field

In this appendix, we investigate the behavior of the N-fold ionization cross section for a constant laser field near the energy threshold of simultaneous escape. The analysis of the geometrical electron escape configurations at this threshold suggests a computationally accessible model to study multiple ionization.

B.1. Survey of Wannier theory without a laser

Consider an atom without an external field. In the classical theory of ionization, the only possibility for N electrons to *simultaneously* reach an infinite distance from each other (simultaneous N-fold ionization (SNI) of the atom) is that their total kinetic energy T exceeds the potential energy V of their Coulomb interaction with each other and the nucleus. Therefore, the cross section of the SNI reaction

$$\sigma_N(E) = \Theta(E) f_N(E) \tag{B.1}$$

is zero for $E = T + V < 0$ and some function of energy $f_N(E)$ for $E > 0$, with $E = 0$ representing an *energy threshold*. Unless $f_N(E) \to 0$ for $E \to 0$, the threshold is accompanied by an abrupt change of the cross section, indicating that a quantum mechanical description is required.

Due to the electron repulsion, there is no universal analytic expression for $f_N(E)$. Perturbation theory gives satisfactory results only for large E where the repulsion is small compared to the kinetic energy (Loughan, 2000). For $E \gtrsim 0$, on the other hand, all energy contributions (kinetic, attractive, repulsive) are of equal importance and a full quantum mechanical solution of the problem seems inevitable. However, it was shown by Wigner (1948) that the details of the reaction *preparing* the highly-excited complex with $E \gtrsim 0$ are unimportant for the energy dependence of the *decay* reaction. For the SNI reaction considered here, this means that $f_N(E)$ only depends on the long-range Coulomb interaction of the product particles, but not on how the complex acquired the small positive energy. Therefore, a solution of the Schrödinger equation is not necessary to determine $f_N(E)$ near threshold, at least not in the region of space where all particles are close together and interact strongly. For single ionization which corresponds to the fragmentation of an atom into an electron and an ion, Wigner found that $f_1(E) \propto 1$, i.e. the cross section sets in with a finite value at threshold.

In a groundbreaking paper, Wannier (1953) extended Wigner's ideas to double ionization[1]. Using hyperspherical coordinates where the radii of the two electrons r_1, r_2 are combined in the hyperradius $R = \sqrt{r_1^2 + r_2^2}$, he identified three zones of the electronic motion. In the reaction zone ($0 < R < a$ with a on the order of the Bohr radius), the interactions between the ion and the electrons are strong and solving the Schrödinger equation is absolutely necessary to describe the processes. For $a < R < b \propto (4Z-1)/E$, in the Coulomb zone, the Coulomb interactions of the electrons are comparable with their kinetic energies. Finally, in the free zone ($R > b$), the energy of the electrons is dominated by the kinetic contribution. Wannier argued that the electronic motion is quasiclassical in the last two zones since the de Broglie wavelength of an escaping electron is much smaller than the radial change of the Coulomb interaction there. Using classical mechanics, he then found that $f_2(E)$ near threshold is determined by the phase space volume containing the trajectories of simultaneous two-electron escape. In the limit $E \to 0$, this volume shrinks to a single trajectory (the so-called Wannier ridge or Wannier orbit) which contains all states where the two electrons have equal momenta and are located at the same distance from the nucleus, but on opposite sides of it. Dynamically, the escape configuration corresponds to two collinear electrons moving "back to back". As clarified by Richter and Wintgen (1990), the Wannier orbit itself does not lead to double escape since it is unstable. In other words, an asymmetry in the electron positions or momenta at $E = 0$, no matter how small, will lead to one electron being pushed back to the nucleus and to single rather than double ionization. For small positive energies, however, small deviations from the back-to-back configuration still lead to double ionization. These trajectories cluster around the Wannier orbit (Grujić, 1983). Mathematically speaking, the phase space volume of initial conditions leading to simultaneous double ionization has finite measure above threshold, but measure zero at threshold.

The energy dependence of the simultaneous double ionization cross section at threshold, known as the Wannier threshold law, reads

$$\sigma_2(E) \propto E^{\alpha_2} \tag{B.2}$$

with the Wannier threshold exponent

$$\alpha_2 = \frac{1}{4}\left(\sqrt{\frac{100Z-9}{4Z-1}} - 1\right) \tag{B.3}$$

that only depends on the charge Z of the residual ion. Some numerical values of α_2 are collected in Table B.2. Equation (B.3) emphasizes that ionization at threshold is a competition between nuclear attraction – which depends on Z – and electron repulsion (Rau, 1984). Wannier's purely classical result could later be rederived both semiclassically (Peterkop, 1971) and fully quantum mechanically (Rau, 1971) since the ideas of Wigner and Wannier are not limited to classical mechanics.

[1]Extensive reviews of Wannier theory are given by Rau (1984), Loughan (2000) and others.

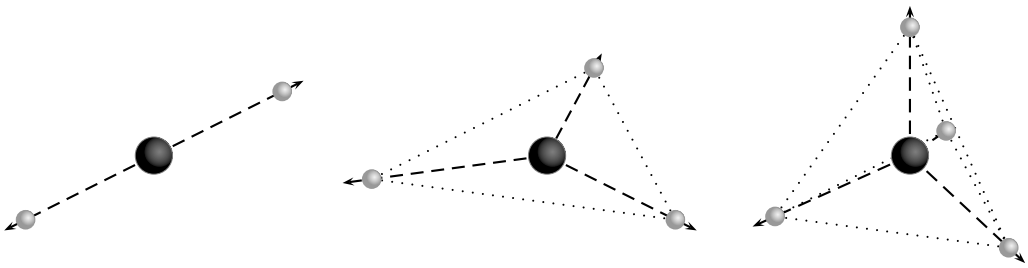

Figure B.1. Threshold escape configurations for simultaneous ionization of two, three and four electrons without a laser field, as predicted by Wannier (1953), Klar and Schlecht (1976) and Grujić (1983).

We discuss two important special cases of the power law (B.2). Single ionization of a neutral atom by slow electron impact ($Z = 1$) – which was the original inspiration for Wannier's analysis – has a threshold exponent of $\alpha_2 \approx 1.127$. This value was confirmed experimentally for hydrogen (McGowan and Clarke, 1968) and helium (Cvejanovic and Read, 1974). For hydrogen, Rost (1994) also provided a semiclassical numerical confirmation. Double photoionization of a neutral atom ($Z = 2$) has the exponent $\alpha_2 \approx 1.056$ which was confirmed for helium, both experimentally (Kossmann *et al.*, 1988; Wehlitz *et al.*, 1999) and numerically (Bouri *et al.*, 2007). Since the Wannier exponent only depends on Z but not on the mechanism that lead to the formation of the initial excited complex, $\alpha_2 \approx 1.056$ is also expected for single ionization of a singly-charged ion by slow electron impact (Müller, 1991).

In his original publication, Wannier considered two escaping electrons. His work was later generalized to three electrons (Klar and Schlecht, 1976), four electrons (Grujić, 1983) and five electrons (Dimitrijević *et al.*, 1990). However, an analytical formula for the threshold exponent was only derived for three electrons. It reads

$$\alpha_3 = \frac{1}{2}\left(\sqrt{\frac{13\sqrt{3}Z - 11 + 12\sqrt{3Z^2 + 1/36}}{\sqrt{3}Z - 1}} - 1\right). \tag{B.4}$$

The most important three-electron ionization reactions whose cross sections are proportional to E^{α_3} near threshold are double ionization of a neutral atom by slow electron impact ($Z = 2$, $\alpha_3 \approx 2.270$) and triple photoionization of a neutral atom ($Z = 3$, $\alpha_3 \approx 2.162$). The second exponent was confirmed experimentally for atomic oxygen and neon (Samson and Angel, 1988) and numerically for lithium with a mixed quantum-classical approach (Emmanouilidou and Rost, 2006).

For the general case of N electrons, Klar and Schlecht (1976) conjectured that the escape configuration at threshold (the N-electron Wannier orbit) has maximum symmetry, with the ionic core at the center of the electronic charge. As shown in Fig. B.1, three electrons are expected to escape on the vertices of an equilateral triangle and four on the vertices of a regular tetrahedron. The conjecture was later refined by Kuchiev and Ostrovsky (1998): In the case of four or more electrons, several competing escape

configurations exist[2] whose threshold exponents are nearly equal, but the aforementioned three-dimensional configurations always yield the smallest value of α_N. As the smallest value of α_N governs the threshold law, this configuration is called the leading configuration (Grujić, 1983).

The SNI cross section near threshold was studied by Rost (2001). Using hyperspherical coordinates, he found that a SNI escape configuration always corresponds to a fixed point (more specifically, a saddle) of Hamilton's equations of motion. Stability analysis of the fixed point revealed that the threshold exponent is given by

$$\alpha_N = \frac{1}{\lambda_R} \sum_{j=1}^{N-1} \lambda_{\Omega_j}. \tag{B.5}$$

Here, $\lambda_R > 0$ is the Lyapunov exponent of the unstable radial normal mode, i.e. the rate at which an initial small perturbation in the hyperradius $R = \sqrt{r_1^2 + \cdots + r_N^2}$ is exponentially amplified, and λ_{Ω_j} are the Lyapunov exponents of the unstable angular normal modes (in the limit $R \to \infty$) which are the rates at which the system, under a small perturbation in the hyperangles Ω_j, departs from the fixed point configuration in angular directions[3]. Equation (B.5) thus illustrates that the energy dependence near threshold is determined by a competition between the radial separation of the electrons (leading to simultaneous N-fold ionization) and the increasing angular deviation from the fixed point configuration (leading, at best, to ionization of $M < N$ electrons). As the number of electrons N is increased, the number of unstable angular modes increases as well, meaning that there are more and more possibilities for partial fragmentation. In (B.5), the increasing number of terms in the sum increases α_N and thus lowers the cross section as a whole. In summary, Rost's analysis suggests the following strategy for finding the threshold exponent of a certain SNI reaction in a given system. First, one determines the corresponding fixed point of the equations of motion in suitably chosen coordinates. Secondly, one linearizes the equations of motion with respect to a small perturbation about the fixed point. The positive eigenvalues of the stability matrix give the Lyapunov exponents and hence the threshold exponent.

The escape of interacting electrons at threshold is characterized by a delicate balance between nuclear attraction and electron repulsion. Without the latter, the process is considerably simpler: Each electron has to overcome the attraction of the ion, independent of the others, and can escape in any direction. With a simple phase space argument, Wannier (1955) predicted the threshold exponent for the escape of N noninteracting electrons to be $\alpha_N = N-1$. Mathematically, turning off the electron repulsion is equal to taking the limit $Z \to \infty$ of the threshold exponent α_N (Rau, 1984). In (B.3) and (B.4), one can easily verify that $\alpha_2 \to 1$ and $\alpha_3 \to 2$ as $Z \to \infty$. For N electrons, Kuchiev and Ostrovsky (1998) convincingly argued that indeed $\alpha_N \to N - 1$.

[2]Consider four escaping electrons. Apart from the tetrahedral configuration shown in Fig. B.1, there exists a plane configuration where the electrons escape on the vertices of a square.

[3]For single ionization, the Coulomb force between the ion and the electron always acts along the interparticle axis (Amusia *et al.*, 2003), so there are no unstable angular modes. As a consequence, we have $\alpha_1 = 0$, i.e. $\sigma_1(E) \propto E^0 = 1$ at threshold. This is equal to the result of Wigner (1948).

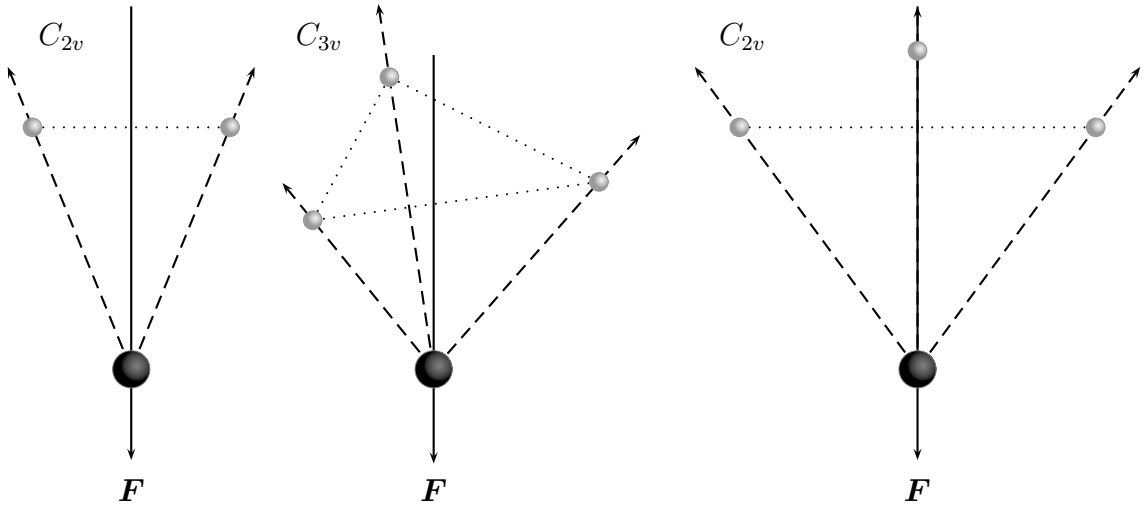

Figure B.2. Threshold escape configurations for simultaneous ionization of two and three electrons in a linearly polarized laser field $\boldsymbol{F}$, as predicted by Sacha and Eckhardt (2003).

B.2. Threshold escape with a nonzero laser field

The threshold properties change dramatically when the atom is exposed to a laser field F. First of all, the field introduces a preferential direction into the system, thus breaking the rotational symmetry of the N-electron Hamiltonian. As a consequence, the electron escape configurations for $F = 0$ (Fig. B.1) do not persist for $F \neq 0$. However, we expect that the new escape configurations will be symmetric with respect to the field polarization axis. Secondly, the SNI saddle has an energy $E_s(F) < 0$ and corresponds to the electrons being located at finite distances from the nucleus, in contrast to the case without a laser field where $E_s = 0$ and the electrons are infinitely far apart (Rost, 2001).

The study of threshold escape in a laser field is motivated by the phenomenon of nonsequential multiple ionization (NSMI) observed with strong linearly polarized laser pulses. Based on the rescattering mechanism of NSMI, Sacha and Eckhardt (2001b) put forward the idea that the recolliding electron is recaptured by the ion and a highly-excited two-electron complex with negative energy E is formed. Since the electron recollides close to a zero-crossing of the electric field, the energy of the double ionization saddle is comparable with E and a connection to Wannier's threshold theory is established. Furthermore, the time scale of the electron motion is much shorter than the one of the laser field for near-infrared frequencies so that F and $E_s(F)$ can be considered as constant during the ionization process. The threshold law for a nonzero laser field thus takes the form

$$\sigma_N(E) \propto (E - E_s(F))^{\beta_N} \tag{B.6}$$

with a new threshold exponent $\beta_N \neq \alpha_N$.

Within the adiabatic assumption $F = \text{const.}$, Eckhardt and Sacha (2001; 2001a; 2003) identified the escape configurations for $N \geq 8$ electrons and calculated the cor-

responding threshold exponents β_N. They found one escape configuration for two electrons and two escape configurations for three electrons (Fig. B.2). As the number of electrons is increased, more and more escape configurations emerge, with 26 configurations already present for $N = 8$. Despite the increasing complexity of the escape configurations, they are all symmetric with respect to the field axis as expected. Furthermore, for any number of electrons, there is a C_{Nv} configuration where the electrons escape on the vertices of a regular N-gon around the field axis. Since all electrons are at an equal distance from each other and the nucleus, the C_{Nv} configuration has maximum symmetry with respect to the field axis. Remarkably, however, the C_{Nv} configuration is the leading configuration, i.e. the one with the smallest Wannier threshold exponent, only for $N < 5$. This is in contrast to field-free Wannier theory where the most symmetric configuration is expected to be the leading one for all N (Klar and Schlecht, 1976).

The Hamiltonian of an N-electron atom with nuclear charge Z in a constant laser field F which is linearly polarized along the z-direction is given by

$$H = \sum_{i=1}^{N} \left(\frac{\boldsymbol{p}_i^2}{2} - \frac{Z}{|\boldsymbol{r}_i|} - F z_i \right) + \sum_{\substack{i,j=1 \\ i<j}}^{N} \frac{1}{|\boldsymbol{r}_i - \boldsymbol{r}_j|} = \sum_{i=1}^{N} \frac{\boldsymbol{p}_i^2}{2} + V(\boldsymbol{r}_1, \ldots, \boldsymbol{r}_N) \tag{B.7}$$

where the position and momentum of the ith electron is given by $\boldsymbol{r}_i = (x_i, y_i, z_i)$ and $\boldsymbol{p}_i = (p_{x_i}, p_{y_i}, p_{z_i})$, respectively. From the fact that the electric field can be scaled out of the Hamiltonian using the transformation

$$\boldsymbol{r}_i = |F|^{-1/2} \boldsymbol{r}_i', \tag{B.8a}$$

$$\boldsymbol{p}_i = |F|^{1/4} \boldsymbol{p}_i', \tag{B.8b}$$

$$H = |F|^{1/2} H', \tag{B.8c}$$

some important conclusions regarding the threshold behavior can already be drawn before the escape configurations are calculated.

- If $\boldsymbol{r}_{i,s} = (x_{i,s}, y_{i,s}, z_{i,s})$ is the position of the ith electron in a given escape configuration, the ratios $x_{i,s}/y_{i,s}$, $x_{i,s}/z_{i,s}$, $y_{i,s}/z_{i,s}$ are constant, i.e. the electron positions in the escape configuration move along straight lines as F is varied.

- The threshold exponent of any escape configuration is independent of F. This is seen as follows. According to equation (B.5), the threshold exponent is given by a ratio of Lyapunov exponents $\lambda_j = \sqrt{-\mu_j}$ where the μ_j are the negative eigenvalues of the Hessian of (B.7). Since the Hessian is a homogeneous function of degree -3 in $\boldsymbol{r}_i$, we have $\mu_j \propto |F|^{3/2}$ and therefore $\lambda_j \propto |F|^{3/4}$.

- As a consequence of the previous property, the field-free threshold exponent α_N is not recovered by "turning off" the field, i.e.

$$\alpha_N \neq \lim_{F \to 0} \beta_N. \tag{B.9}$$

In this sense, the electric field represents a discontinuous perturbation which only vanishes if F is *exactly* zero. However, as discussed by Eckhardt and Sacha (2001), the exponent α_N is expected to govern the threshold behavior if the N-fold ionization saddle induced by the laser field lies outside the Coulomb zone.

Due to the scaling (B.8), we can set $F = 1$ in the following.

B.3. C_{Nv} configuration

In this section, we derive the position of the SNI saddle for the C_{Nv} configuration, discuss its stability properties and calculate the threshold exponents for simultaneous ionization of two, three, four and five electrons. Based on the variation of the saddle with the field amplitude, we then develop the N-electron generalization of the two-electron model for double ionization introduced by Eckhardt and Sacha (2006). The threshold exponents within this model are calculated for arbitrary N and the influence of a cut-off parameter ε in the Coulomb potentials is discussed.

B.3.1. Full-dimensional description

In the C_{Nv} escape configuration, the N electrons are located on the vertices of a regular N-gon with the field axis in the center. In other words, the electrons are distributed evenly on a circle ($\rho_i = \rho\ \forall i$, $\varphi_i = 2\pi i/N$) in a plane perpendicular to the field axis ($z_i = z\ \forall i$). The configuration has C_{Nv} symmetry since the field axis is an N-fold rotation axis and there are N mirror planes containing it. With the coordinate restrictions, the Hamiltonian (B.7) takes the form (Sacha and Eckhardt, 2003)

$$H_{C_{Nv}} = \frac{p_\rho^2 + p_z^2}{2N} - \frac{NZ}{\sqrt{\rho^2 + z^2}} + \frac{W_N}{2\rho} - Nz \tag{B.10}$$

where we have set $F = 1$ and defined[4]

$$W_N := \sum_{k=1}^{N-1} \frac{N-k}{\sin\left(\frac{\pi k}{N}\right)} = \frac{N}{2} \sum_{k=1}^{N-1} \frac{1}{\sin\left(\frac{\pi k}{N}\right)}. \tag{B.11}$$

In Table B.1, the first few values are listed. Unfortunately, a closed-form expression for W_N does not exist (Chen, 2010). However, for large N, one can derive the asymptotic formula (Watson, 1916, 1923)

$$W_N \approx \frac{N^2}{\pi}\left(\log N + \gamma + \log\frac{2}{\pi}\right) \tag{B.12}$$

with Euler's constant $\gamma \approx 0.57721$. The leading term was confirmed numerically by Sacha and Eckhardt (2003). We see from the table that the asymptotic formula gives a good estimate already for small N.

[4]The second equality is proved as follows. One splits the sum into two sums, performs an index shift $k = N - j$ in the second sum, uses $\sin(\pi - x) = \sin(x)$ and finally solves the equation for W_N.

	W_N		
N	ana.	num.	asym.
1	0	0.000	0.040
2	1	1.000	1.043
3	$2\sqrt{3}$	3.464	3.507
4	$2\left(1+2\sqrt{2}\right)$	7.657	7.700
5	$2\sqrt{5\left(5+2\sqrt{5}\right)} = 2\left(\frac{\sqrt{5}+5}{2}\right)^{3/2}$	13.764	13.807
6	$15+4\sqrt{3} = 2+\left(1+2\sqrt{3}\right)^2$	21.928	21.972
7		32.267	32.310
8	$4\left(1+2\sqrt{2}+4\sqrt{2+\sqrt{2}}\right)$	44.878	44.921

Table B.1. W_N for different numbers of electrons N. The prediction of the asymptotic formula (B.12) is shown in the last column. Expressing W_7 analytically in terms of radicals is not possible.

The Hamiltonian (B.10) has a saddle point which corresponds to the SNI saddle in full space. Defining the parameter[5]

$$a := \left(\frac{2NZ}{W_N}\right)^{2/3} \tag{B.13}$$

which is essentially the ratio of the electrons' total nuclear attraction strength $(N \cdot Z)$ to the interelectronic repulsion strength $(W_N/2)$, the saddle is located at

$$\rho_s = \sqrt{\frac{W_N}{2N}}(a-1)^{1/4}, \tag{B.14a}$$

$$z_s = \sqrt{\frac{W_N}{2N}}(a-1)^{3/4} \tag{B.14b}$$

with energy

$$H_{C_{Nv}}(0,0,\rho_s,z_s) = -\sqrt{2NW_N}(a-1)^{3/4}. \tag{B.15}$$

In the full configuration space, the positions of the ith electron on the SNI saddle is

$$x_{i,s} = \rho_s \cos\left(\frac{2\pi i}{N}\right), \tag{B.16a}$$

$$y_{i,s} = \rho_s \sin\left(\frac{2\pi i}{N}\right), \tag{B.16b}$$

$$z_{i,s} = z_s = \rho_s\sqrt{a-1}. \tag{B.16c}$$

[5]Compared to the parameter a defined by Eckhardt and Sacha (2001) for $N = 2$, our version lacks a prefactor of 1/2.

Note that for neutral atoms ($Z = N$), the saddle only exists if $a = (W_N/2N^2)^{2/3} \leq 1$ or, using the asymptotic formula (B.12),

$$N \leq \frac{\pi}{2} \mathrm{e}^{2\pi-\gamma} \approx 472, \tag{B.17}$$

in agreement with the result of Sacha and Eckhardt (2003). For $Z > N$ ($Z < N$), the number is larger (smaller). Clearly, such a large number of electrons is not encountered in a real atom.

In order to understand how small deviations from the escape configuration (B.16) amplify in the full $6N$-dimensional phase space, we make a linear stability analysis of the SNI saddle. To this end, we substitute

$$x_i = x_{i,s} + \Delta x_i, \tag{B.18a}$$
$$y_i = y_{i,s} + \Delta y_i, \tag{B.18b}$$
$$z_i = z_{i,s} + \Delta z_i, \tag{B.18c}$$
$$p_{x_i} = p_{x_{i,s}} + \Delta p_{x_i} = \Delta p_{x_i}, \tag{B.18d}$$
$$p_{y_i} = p_{y_{i,s}} + \Delta p_{y_i} = \Delta p_{y_i}, \tag{B.18e}$$
$$p_{z_i} = p_{z_{i,s}} + \Delta p_{z_i} = \Delta p_{z_i} \tag{B.18f}$$

into the equations of motion

$$\dot{\boldsymbol{r}}_i = \boldsymbol{p}_i, \tag{B.19a}$$
$$\dot{\boldsymbol{p}}_i = -\frac{Z\boldsymbol{r}_i}{|\boldsymbol{r}_i|^3} + F\boldsymbol{e}_{z_i} + \sum_{\substack{j=1 \\ i\neq j}}^{N} \frac{\boldsymbol{r}_i - \boldsymbol{r}_j}{|\boldsymbol{r}_i - \boldsymbol{r}_j|^3} \tag{B.19b}$$

and linearize them with respect to the deviations from the saddle point. With

$$\Delta\boldsymbol{r} := (\Delta x_1, \ldots, \Delta x_N, \Delta y_1, \ldots, \Delta y_N, \Delta z_1, \ldots, \Delta z_N)^\top, \tag{B.20a}$$
$$\Delta\boldsymbol{p} := (\Delta p_{x_1}, \ldots, \Delta p_{x_N}, \Delta p_{y_1}, \ldots, \Delta p_{y_N}, \Delta p_{z_1}, \ldots, \Delta p_{z_N})^\top, \tag{B.20b}$$

the equations of motion for the deviations take the compact form

$$\frac{\mathrm{d}}{\mathrm{d}t}\begin{pmatrix}\Delta\boldsymbol{p} \\ \Delta\boldsymbol{r}\end{pmatrix} = \begin{pmatrix}0_{3N} & -V_s'' \\ 1_{3N} & 0_{3N}\end{pmatrix}\begin{pmatrix}\Delta\boldsymbol{p} \\ \Delta\boldsymbol{r}\end{pmatrix} =: M\begin{pmatrix}\Delta\boldsymbol{p} \\ \Delta\boldsymbol{r}\end{pmatrix} \tag{B.21}$$

where we defined the stability matrix M of the stationary point, consisting of the $3N \times 3N$ zero matrix 0_{3N}, the $3N \times 3N$ identity matrix 1_{3N} and the Hessian V_s'' of the potential V evaluated at (B.16). The eigenvectors $\Delta\boldsymbol{u}_i$ of the stability matrix are called normal modes and have the explicit time dependence (Rost, 2001)

$$\Delta\boldsymbol{u}_i(t) = \mathrm{e}^{\lambda_i t}\Delta\boldsymbol{u}_i(0) \tag{B.22}$$

where λ_i is the eigenvalue belonging to $\Delta\boldsymbol{u}_i$. To calculate the λ_i, we make use of elementary linear algebra and express the characteristic polynomial of M as

$$\begin{aligned}
\chi_M(\lambda_i) &= \det(M - \lambda_i 1_{6N}) = \det\begin{pmatrix} -\lambda_i 1_{3N} & -V_s'' \\ 1_{3N} & -\lambda_i 1_{3N} \end{pmatrix} \\
&= (-1)^{3N} \det\begin{pmatrix} 1_{3N} & -\lambda_i 1_{3N} \\ -\lambda_i 1_{3N} & -V_s'' \end{pmatrix} \\
&= (-1)^{3N} \det\begin{pmatrix} 1_{3N} & -\lambda_i 1_{3N} \\ 0_{3N} & -(V_s'' + \lambda_i^2 1_{3N}) \end{pmatrix} \\
&= (-1)^{3N} \det(1_{3N}) \det(-1_{3N}) \det(V_s'' + \lambda_i^2 1_{3N}) \\
&= \det(V_s'' + \lambda_i^2 1_{3N}) = \chi_{V_s''}(-\lambda_i^2) = \chi_{V_s''}(\mu_i). \qquad \text{(B.23)}
\end{aligned}$$

This shows that the $6N$ eigenvalues λ_i of the stability matrix are determined by the $3N$ eigenvalues μ_i of the Hessian through $\lambda_i = \pm\sqrt{-\mu_i}$. As a symmetric matrix, the Hessian V_s'' is not only devoid of complex eigenvalues, but also diagonalizable with a full set of eigenvectors. Therefore, the relation (B.23) implies several things.

- Eigenvalues of the stability matrix occur in pairs $-\lambda$, $+\lambda$, i.e. the sum of all eigenvalues is zero. This is a consequence of Liouville's theorem for conservative Hamiltonian systems which states that the phase space volume is conserved along a trajectory. For the sake of simplicity, we will only discuss the positive eigenvalues in the following.

- If $\boldsymbol{v}$ is an eigenvector of the Hessian with eigenvalue $\mu = -\lambda^2$, $\boldsymbol{u}_\pm = (\pm\lambda\boldsymbol{v}, \boldsymbol{v})^\top$ is an eigenvector of the stability matrix with eigenvalue $\pm\lambda$.

- Since μ is real, three cases can occur.
  - $\mu < 0$, i.e. λ is real. These eigenvalues λ are called Lyapunov exponents. Due to the exponential time dependence in (B.22), the corresponding normal modes are called hyperbolic. For $\lambda < 0$ ($\lambda > 0$), deviations are exponentially damped (amplified) and the corresponding normal mode is stable (unstable). In the following, we will focus on the positive Lyapunov exponents of the stability matrix since they determine the Wannier threshold exponent, as shown by Rost (2001).
  - $\mu = \lambda = 0$. In this case, $\Delta\boldsymbol{u}(t) = \Delta\boldsymbol{u}(0)$ is a constant vector for all times. This defines a neutral mode.
  - $\mu > 0$, i.e. $\lambda = i\omega$ is purely imaginary. Since (B.22) describes an oscillation in this case, $\omega = \sqrt{\mu}$ is called normal mode frequency of oscillation. The normal mode is stable and also referred to as elliptic.

Using the above properties, it is sufficient to calculate the eigenvalues and eigenfunctions of the Hessian at the saddle point (B.16). Another simplification is found by noticing that the Coulomb part of the potential V in (B.7) is a homogeneous function

of degree -1. Since the non-homogeneous field interaction part $\propto z_i$ is eliminated by differentiating twice, the Hessian V'' is a homogeneous function of degree -3 and we have

$$\begin{aligned} V_s'' &= V''\left(\dots, \rho_s \cos\left(\frac{2\pi i}{N}\right), \rho_s \sin\left(\frac{2\pi i}{N}\right), z_s, \dots\right) \\ &= \frac{1}{\rho_s^3} V''\left(\dots, \cos\left(\frac{2\pi i}{N}\right), \left(\frac{2\pi i}{N}\right), \sqrt{a-1}, \dots\right). \end{aligned} \tag{B.24}$$

With the auxiliary function

$$Y_N := \sum_{k=1}^{N-1} \frac{1}{\sin^3\left(\frac{\pi k}{N}\right)}, \tag{B.25}$$

the elements of V_s'' can be written as

$$\rho_s^3 \frac{\partial^2 V}{\partial x_i \partial x_j} = \begin{cases} \frac{1}{4}\left[Y_N - \frac{W_N}{N}\right] + 3\cos^2\left(\frac{2\pi i}{N}\right)\left[\frac{W_N}{2N}\left(\frac{a-1}{a}\right) - \frac{Y_N}{8}\right], & i = j \\ -\frac{2-3\cos^2(\pi(i+j)/N)}{8\sin^3(\pi|i-j|/N)}, & i \neq j \end{cases} \tag{B.26a}$$

$$\rho_s^3 \frac{\partial^2 V}{\partial y_i \partial y_j} = \begin{cases} \frac{1}{4}\left[Y_N - \frac{W_N}{N}\right] + 3\sin^2\left(\frac{2\pi i}{N}\right)\left[\frac{W_N}{2N}\left(\frac{a-1}{a}\right) - \frac{Y_N}{8}\right], & i = j \\ -\frac{2-3\sin^2(\pi(i+j)/N)}{8\sin^3(\pi|i-j|/N)}, & i \neq j \end{cases} \tag{B.26b}$$

$$\rho_s^3 \frac{\partial^2 V}{\partial z_i \partial z_j} = \begin{cases} -\frac{W_N}{2N}\left[3\left(\frac{a-1}{a}\right) - 1\right] - \frac{Y_N}{8}, & i = j \\ \frac{1}{8}\frac{1}{\sin^3(\pi|i-j|/N)}, & i \neq j \end{cases} \tag{B.26c}$$

$$\rho_s^3 \frac{\partial^2 V}{\partial x_i \partial y_j} = \begin{cases} 3\sin\left(\frac{2\pi i}{N}\right)\cos\left(\frac{2\pi i}{N}\right)\left[\frac{W_N}{2N}\left(\frac{a-1}{a}\right) - \frac{Y_N}{8}\right], & i = j \\ \frac{3}{16}\frac{\sin(2\pi(i+j)/N)}{\sin^3(\pi|i-j|/N)}, & i \neq j \end{cases} \tag{B.26d}$$

$$\rho_s^3 \frac{\partial^2 V}{\partial x_i \partial z_j} = -\frac{3W_N}{2N}\frac{\sqrt{a-1}}{a}\cos\left(\frac{2\pi i}{N}\right)\delta_{ij}, \tag{B.26e}$$

$$\rho_s^3 \frac{\partial^2 V}{\partial y_i \partial z_j} = -\frac{3W_N}{2N}\frac{\sqrt{a-1}}{a}\sin\left(\frac{2\pi i}{N}\right)\delta_{ij}. \tag{B.26f}$$

The Hessian has a block structure if it is arranged as

$$V_s'' = \begin{pmatrix} \frac{\partial^2 V}{\partial x_i \partial x_j} & \frac{\partial^2 V}{\partial x_i \partial y_j} & \frac{\partial^2 V}{\partial x_i \partial z_j} \\ \frac{\partial^2 V}{\partial x_i \partial y_j} & \frac{\partial^2 V}{\partial y_i \partial y_j} & \frac{\partial^2 V}{\partial y_i \partial z_j} \\ \frac{\partial^2 V}{\partial x_i \partial z_j} & \frac{\partial^2 V}{\partial y_i \partial z_j} & \frac{\partial^2 V}{\partial z_i \partial z_j} \end{pmatrix}. \tag{B.27}$$

Although there is an explicit formula which expresses the determinant of a 3×3 block matrix in terms of its blocks (Silvester, 2000; Powell, 2011), it is of little use here since no simple part of the matrix decouples from the rest. Hence, for arbitrary N, an explicit calculation of all eigenvalues seems impossible. However, one can guess the structure of some eigenvectors

$$\boldsymbol{v} = (\dots, v_{x_i}, \dots, \dots, v_{y_i}, \dots, \dots, v_{z_i}, \dots)^\top. \tag{B.28}$$

For example, the ansatz $v_{x_i} = u\cos(2\pi i/N)$, $v_{y_i} = u\sin(2\pi i/N)$, $v_{z_i} = Cu$ yields a quadratic equation for C which has two solutions. One yields the stable mode

$$\boldsymbol{v}_1(a) = \sum_{i=1}^{N}\left[\cos\left(\frac{2\pi i}{N}\right)\boldsymbol{e}_{x_i} + \sin\left(\frac{2\pi i}{N}\right)\boldsymbol{e}_{y_i} + \left(-\frac{a}{6}\frac{\sqrt{25-24/a}+1}{\sqrt{a-1}} + \sqrt{a-1}\right)\boldsymbol{e}_{z_i}\right] \tag{B.29}$$

with frequency

$$\omega_1(a) = \left(\frac{N}{2W_N}\right)^{1/4}\frac{\sqrt{\sqrt{25-24/a}+1}}{(a-1)^{3/8}}, \tag{B.30}$$

one the unstable mode

$$\boldsymbol{v}_r(a) = \sum_{i=1}^{N}\left[\cos\left(\frac{2\pi i}{N}\right)\boldsymbol{e}_{x_i} + \sin\left(\frac{2\pi i}{N}\right)\boldsymbol{e}_{y_i} + \left(\frac{a}{6}\frac{\sqrt{25-24/a}-1}{\sqrt{a-1}} + \sqrt{a-1}\right)\boldsymbol{e}_{z_i}\right] \tag{B.31}$$

with Lyapunov exponent

$$\lambda_r(a) = \left(\frac{N}{2W_N}\right)^{1/4}\frac{\sqrt{\sqrt{25-24/a}-1}}{(a-1)^{3/8}}. \tag{B.32}$$

In view of (B.22), $\boldsymbol{v}_r$ corresponds to a simultaneous and perfectly symmetric motion of the N electrons away from the nucleus. Using terminology from chemical physics, the subspace spanned by $\boldsymbol{v}_r$ is called the reaction coordinate of simultaneous N-fold ionization. For $Z = N$, (B.32) agrees with the numerical results published by Sacha and Eckhardt (2003). Note that we have $\boldsymbol{v}_1 \cdot \boldsymbol{v}_r = 0$, i.e. the stable and unstable mode are perpendicular to each other.

The alternative ansatz $v_{z_i} = 0$ for all i leads to

$$v_{x_i}\cos\left(\frac{2\pi i}{N}\right) + v_{y_i}\sin\left(\frac{2\pi i}{N}\right) = 0 \ \forall i. \tag{B.33}$$

An obvious solution to this equation is $v_{x_i} = -u\sin(2\pi i/N)$, $v_{y_i} = u\cos(2\pi i/N)$ which gives the neutral mode

$$\boldsymbol{v}_0 = \frac{1}{\sqrt{N}}\sum_{i=1}^{N}\left[-\sin\left(\frac{2\pi i}{N}\right)\boldsymbol{e}_{x_i} + \cos\left(\frac{2\pi i}{N}\right)\boldsymbol{e}_{y_i}\right] \tag{B.34}$$

with eigenvalue

$$\lambda_0 = 0. \tag{B.35}$$

The neutral mode results from the rotational symmetry of the system around the z-axis. For i odd, $v_{x_i} = u\sin(2\pi i/N)$, $v_{y_i} = u(-1)^i\cos(2\pi i/N)$ is another solution of (B.33). For $i = 2j$ even, it is a solution if

$$2\sin\left(\frac{4\pi j}{N}\right)\cos\left(\frac{4\pi j}{N}\right) = \sin\left(\frac{8\pi j}{N}\right) = 0\ \forall j \Leftrightarrow \frac{8}{N} \in \mathbb{Z}. \tag{B.36}$$

This can only be true if $N \in \{2, 4, 8\}$. For these cases, the system has the stable mode

$$\boldsymbol{v}_2 = \frac{1}{\sqrt{N}}\sum_{i=1}^{N}\left[\sin\left(\frac{2\pi i}{N}\right)\boldsymbol{e}_{x_i} + (-1)^i\cos\left(\frac{2\pi i}{N}\right)\boldsymbol{e}_{y_i}\right] \tag{B.37}$$

with frequency

$$\omega_2(a) = \left(\frac{2N}{W_N}\right)^{3/4}\frac{C_N}{(a-1)^{3/8}} \tag{B.38}$$

where $C_2 = 1/2$, $C_4 = \sqrt{3}/2^{1/4}$ and $C_8 = (274 + 17\sqrt{2})^{1/4}$. With different ansatzes, it should be possible to construct the other eigenvectors. An inspection of the cases $N = 2, 3, 4$ suggests that all of them fulfill $\sum_{i=1}^{N} v_{z_i} = 0$. This less restrictive ansatz yields, after some lengthy algebra,

$$\sum_{i=1}^{N}\left[v_{x_i}\cos\left(\frac{2\pi i}{N}\right) + v_{y_i}\sin\left(\frac{2\pi i}{N}\right)\right] = 0. \tag{B.39}$$

This equation may be used as a starting point if an explicit calculation of more eigenvalues is attempted in the future.

Since we were not able to derive all Lyapunov exponents, an analytical expression of the threshold exponent β_N for arbitrary N cannot be given. However, if N is small, the missing eigenvalues of the Hessian (B.27) can either be calculated manually or with a computer algebra system. Moreover, in the limit $a \to \infty$ (or $Z \to \infty$), the exponents for $N < 6$ can be found rather easily. For growing Z, the electrons have to move further away from the nucleus in order to maintain the saddle configuration, i.e. the regular N-gon moves outwards along the field axis and its diameter grows ($z_s, \rho_s \to \infty$). However, the ratio $\rho_s/z_s = 1/\sqrt{a-1}$ tends to zero, so the distance to the nucleus grows more quickly than the diameter. Hence, if one scales out z_s (or, equivalently, ρ_s^3), the electron positions approach the field axis for $a \to \infty$, as expected for vanishing electron repulsion. Since

$$\lim_{a\to\infty}\rho_s^3\frac{\partial^2 V}{\partial x_i \partial z_j} = \lim_{a\to\infty}\rho_s^3\frac{\partial^2 V}{\partial y_i \partial z_j} = 0 \tag{B.40}$$

for all i and j, the Hessian becomes partially block diagonal, with the $z_i z_j$-block decoupled from the rest. As a result, the N eigenvalues μ_i of the $z_i z_j$-block are also

eigenvalues of the full Hessian. The $z_i z_j$-block is symmetric and has the structure of a circulant matrix (Davis, 1979), i.e.

$$\lim_{a\to\infty} \rho_s^3 \frac{\partial^2 V}{\partial z_i \partial z_j} = \begin{pmatrix} \nu_0 & \nu_{N-1} & \dots & \nu_2 & \nu_1 \\ \nu_1 & \nu_0 & \nu_{N-1} & \ddots & \nu_2 \\ \vdots & \nu_1 & \nu_0 & \ddots & \vdots \\ \nu_{N-2} & \ddots & \ddots & \ddots & \nu_{N-1} \\ \nu_{N-1} & \nu_{N-2} & \dots & \nu_1 & \nu_0 \end{pmatrix}. \tag{B.41}$$

The eigenvalues of a real-valued symmetric circulant matrix are

$$\mu_i = \nu_0 + \sum_{j=1}^{N} \nu_{N-j} \cos\left(\frac{2\pi i j}{N}\right) \tag{B.42}$$

and the eigenvectors

$$\boldsymbol{w}_i = \left(1, \cos\left(\frac{2\pi i}{N}\right), \cos\left(\frac{4\pi i}{N}\right), \dots, \cos\left(\frac{2\pi (N-1) i}{N}\right)\right) \tag{B.43}$$

where $i = 0, \dots, N-1$. We find

$$\mu_0 = -\frac{W_N}{N}, \tag{B.44a}$$

$$\mu_i = -\left(\frac{W_N}{N} + \frac{1}{4}\sum_{j=1}^{N-1} \frac{\sin^2\left(\frac{\pi i j}{N}\right)}{\sin^3\left(\frac{\pi j}{N}\right)}\right). \tag{B.44b}$$

All eigenvalues are negative, so each one belongs to an unstable direction with a corresponding Lyapunov exponent $\lambda_i = \sqrt{-\mu_i}$. μ_0 belongs to the reaction coordinate of simultaneous N-electron escape since $\boldsymbol{w}_0 = (1, \dots, 1)$. The asymptotic threshold exponent finally reads

$$\lim_{a\to\infty} \beta_N(a) = \sum_{i=1}^{N-1} \sqrt{\frac{\mu_i}{\mu_0}} = \sum_{i=1}^{N-1} \sqrt{1 + \frac{N}{4W_N} \sum_{j=1}^{N-1} \frac{\sin^2\left(\frac{\pi i j}{N}\right)}{\sin^3\left(\frac{\pi j}{N}\right)}}. \tag{B.45}$$

This formula is only valid for $N < 6$. For $N \geq 6$, the number of unstable directions of the saddle is larger than N (Sacha and Eckhardt, 2003), so not all Lyapunov exponents entering the threshold exponent are contained in the $z_i z_j$-block of the Hessian.

To conclude this section, we summarize the normal mode frequencies, Lyapunov exponents and (asymptotic) threshold exponents β_N for $N < 6$. A comparison of the threshold exponents for ionization of two and three electrons, obtained with and without the laser field, is shown in Table B.2.

Z	β_2	α_2 [W53]	β_3	α_3 [KS76]
1	1.3507	1.1269	3.0971	2.8262
2	1.2918	1.0559	2.7079	2.2704
3	1.2730	1.0358	2.6226	2.1620
4	1.2634	1.0264	2.5834	2.1156
5	1.2574	1.0209	2.5604	2.0899
6	1.2532	1.0173	2.5450	2.0735
7	1.2502	1.0147	2.5340	2.0622
8	1.2478	1.0128	2.5256	2.0539
9	1.2460	1.0114	2.5190	2.0476
10	1.2444	1.0102	2.5136	2.0426
⋮	⋮	⋮	⋮	⋮
∞	1.2247	1.0000	2.4495	2.0000

Table B.2. Threshold exponents for simultaneous ionization of two and three electrons in a laser field (first and third row, respectively), compared to the zero-field results of Wannier (1953) and Klar and Schlecht (1976) (second and fourth row, respectively). Some of the values for β_2 were first published by Eckhardt and Sacha (2001).

- **One electron ($N = 1$).** We excluded the single-electron case in the above discussion, so we briefly consider it here. For $N = 1$, the saddle point lies on the field axis at $\rho_s = 0$, $z_s = \sqrt{Z}$. Since there is no electron repulsion, $W_1 = 0$ and hence $a = \infty$, independent of Z. The Hessian is diagonal with two eigenvalues $1/\sqrt{Z} > 0$ and one eigenvalue $-2/\sqrt{Z} < 0$. Since there is no unstable direction other than the field axis, we have $\beta_1 = 0$ and the cross section at threshold is a Heaviside step function (Wigner, 1948).

- **Two electrons ($N = 2$).** With

$$a = \left(\frac{4Z}{W_2}\right)^{2/3} = 2(2Z^2)^{1/3}, \tag{B.46}$$

we obtain the normal mode frequencies

$$\omega_1(a) = \sqrt{2}\frac{\sqrt{\sqrt{4 - 3/a} - 1}}{(a-1)^{3/8}}, \tag{B.47a}$$

$$\omega_2(a) = \frac{\sqrt{\sqrt{25 - 24/a} + 1}}{(a-1)^{3/8}}, \tag{B.47b}$$

$$\omega_3(a) = \frac{\sqrt{2}}{(a-1)^{3/8}} \tag{B.47c}$$

and the Lyapunov exponents

$$\lambda_\perp(a) = \sqrt{2}\frac{\sqrt{\sqrt{4-3/a}+1}}{(a-1)^{3/8}}, \tag{B.47d}$$

$$\lambda_r(a) = \frac{\sqrt{\sqrt{25-24/a}-1}}{(a-1)^{3/8}}, \tag{B.47e}$$

$$\lambda_0 = 0. \tag{B.47f}$$

Numerical values of the above eigenvalues for $a = 4$ ($Z = 2$) are given by Haller *et al.* (2011). The threshold exponent is

$$\beta_2(a) = \sqrt{2}\sqrt{\frac{\sqrt{4-3/a}+1}{\sqrt{25-24/a}-1}} \tag{B.48}$$

with

$$\beta_2(4) = \sqrt{\frac{\sqrt{13}+2}{\sqrt{19}-1}} \approx 1.2918. \tag{B.49}$$

Both results were first derived by Eckhardt and Sacha (2001) although the authors did not arrive at the compact expression (B.48). Analogous to Wannier's field-free result (B.3), β_2 diverges for $Z = 1/4$ ($a = 1$). The limit of the exponent (B.48) for large Z is

$$\lim_{a\to\infty} \beta_2(a) = \sqrt{\frac{3}{2}} \approx 1.2247. \tag{B.50}$$

- **Three electrons ($N = 3$).** We have

$$a = \left(\frac{6Z}{W_3}\right)^{2/3} = (3Z^2)^{1/3}. \tag{B.51}$$

The expressions (B.30), (B.32) and (B.35) yield

$$\omega_1(a) = \frac{3^{1/8}}{\sqrt{2}}\frac{\sqrt{\sqrt{25-24/a}+1}}{(a-1)^{3/8}}, \tag{B.52a}$$

$$\lambda_r(a) = \frac{3^{1/8}}{\sqrt{2}}\frac{\sqrt{\sqrt{25-24/a}-1}}{(a-1)^{3/8}}, \tag{B.52b}$$

$$\lambda_0 = 0. \tag{B.52c}$$

By factorizing the characteristic polynomial of the Hessian, we find that the six remaining eigenvalues occur in pairs (Sacha and Eckhardt, 2001a). The three independent eigenvalues fulfill a cubic equation which can be solved with Cardano's method (see Appendix C.1). We obtain

$$\mu_i(a) = \frac{\sqrt{73-\frac{45}{a}}\cos\left(\frac{1}{3}\arccos\left(\frac{1190-1107/a}{2(73-45/a)^{3/2}}\right)-\frac{\pi}{3}(2i-1)\right)-\frac{1}{2}}{3^{3/4}(a-1)^{3/4}} \tag{B.53}$$

with $i = 1, 2, 3$. The two positive solutions yield the normal mode frequencies

$$\omega_1(a) = \sqrt{\mu_1(a)} = \frac{\sqrt{\sqrt{73-\frac{45}{a}}\cos\left(\frac{1}{3}\arccos\left(\frac{1190-1107/a}{2(73-45/a)^{3/2}}\right)-\frac{\pi}{3}\right)-\frac{1}{2}}}{3^{3/8}(a-1)^{3/8}}, \tag{B.54a}$$

$$\omega_2(a) = \sqrt{\mu_3(a)} = \frac{\sqrt{\sqrt{73-\frac{45}{a}}\cos\left(\frac{1}{3}\arccos\left(\frac{1190-1107/a}{2(73-45/a)^{3/2}}\right)-\frac{5\pi}{3}\right)-\frac{1}{2}}}{3^{3/8}(a-1)^{3/8}}, \tag{B.54b}$$

the negative one the Lyapunov exponent

$$\lambda_\perp(a) = \sqrt{-\mu_2(a)} = \frac{\sqrt{\sqrt{73-\frac{45}{a}}\cos\left(\frac{1}{3}\arccos\left(\frac{1190-1107/a}{2(73-45/a)^{3/2}}\right)\right)+\frac{1}{2}}}{3^{3/8}(a-1)^{3/8}}. \tag{B.54c}$$

The threshold exponent is

$$\beta_3(a) = 2\frac{\lambda_\perp}{\lambda_r} = \frac{2^{3/2}}{\sqrt{3}}\frac{\sqrt{\sqrt{73-\frac{45}{a}}\cos\left(\frac{1}{3}\arccos\left(\frac{1190-1107/a}{2(73-45/a)^{3/2}}\right)\right)+\frac{1}{2}}}{\sqrt{\sqrt{25-24/a}-1}}. \tag{B.55}$$

Analogous to Klar and Schlecht's field-free result (B.4), β_3 diverges for $Z = 1/\sqrt{3}$ ($a = 1$). For $a = Z = 3$, we find

$$\lambda_r(3) = \frac{3^{1/8}}{2^{7/8}}\sqrt{\sqrt{17}-1} \approx 1.1054, \tag{B.56a}$$

$$\lambda_\perp(3) = \frac{\sqrt{\sqrt{58}\cos\left(\frac{1}{3}\arccos\left(\frac{821}{2(58)^{3/2}}\right)\right)+\frac{1}{2}}}{6^{3/8}} \approx 1.4496, \tag{B.56b}$$

$$\beta_3(3) = 2\sqrt{\frac{2}{3}}\frac{\sqrt{\sqrt{58}\cos\left(\frac{1}{3}\arccos\left(\frac{821}{2(58)^{3/2}}\right)\right)+\frac{1}{2}}}{\sqrt{\sqrt{17}-1}} \approx 2.6226, \tag{B.56c}$$

confirming the results of Sacha and Eckhardt (2001a). Since

$$\begin{aligned}
&\lim_{a\to\infty} \cos\left(\frac{1}{3}\arccos\left(\frac{1190-1107/a}{2(73-45/a)^{3/2}}\right)\right)\\
&= \cos\left(\frac{1}{3}\arccos\left(\frac{595}{(73)^{3/2}}\right)\right)\\
&= \cos\left(\frac{1}{3}\arccos\left(4\left(\frac{17}{2\sqrt{73}}\right)^3 - 3\left(\frac{17}{2\sqrt{73}}\right)\right)\right)\\
&= \cos\left(\frac{1}{3}\arccos\left(\cos\left(3\arccos\left(\frac{17}{2\sqrt{73}}\right)\right)\right)\right) = \frac{17}{2\sqrt{73}},
\end{aligned} \tag{B.57}$$

the asymptotic threshold exponent is

$$\lim_{a\to\infty} \beta_3(a) = 2\sqrt{\frac{3}{2}} = \sqrt{6} \approx 2.4494. \tag{B.58}$$

Although the discrete nature of Z does not permit arbitrary values of a, the function β_3 is continuous for $a \in (1,\infty)$. We note the interesting results

$$\beta_3\left(\frac{8}{7}\right) = 4, \tag{B.59a}$$

$$\beta_3\left(\frac{3}{2}\right) = \sqrt{2\left(1+\sqrt{13}\right)}. \tag{B.59b}$$

- **Four electrons ($N = 4$).** The formulas for the Lyapunov exponents and frequencies and are too long to fit the page, so we just give the asymptotic threshold exponent

$$\lim_{a\to\infty} \beta_4(a) = \sqrt{6} + \sqrt{\frac{1+4\sqrt{2}}{1+2\sqrt{2}}} \approx 3.7681. \tag{B.60}$$

- **Five electrons ($N = 5$).** Again, we only give the asymptotic threshold exponent

$$\lim_{a\to\infty} \beta_5(a) = \sqrt{6} + \sqrt{12-2\sqrt{5}} \approx 5.1932. \tag{B.61}$$

B.3.2. Eckhardt-Sacha model for N electrons

For a qualitative study of multiple ionization, it is sufficient to consider a model system with a reduced number of degrees of freedom, provided that it contains the electron repulsion to allow for nonsequential escape. Extending the ideas of Eckhardt and Sacha from two to N electrons, such a model can be based on the escape configurations of simultaneous N-fold ionization.

Consider the C_{Nv} escape configuration. For fixed a, the position of the ith electron ($i = 1, \ldots, N$) only depends on the field amplitude F (the time dependence of the field is suppressed in this section for the sake of compactness) and is given by

$$\boldsymbol{r}_{i,s}(F) = \frac{\rho_s}{\sqrt{|F|}} \begin{pmatrix} \cos\left(\frac{2\pi i}{N}\right) \\ \sin\left(\frac{2\pi i}{N}\right) \\ \mathrm{sgn}(F)\sqrt{a-1} \end{pmatrix}. \tag{B.62}$$

As F is varied, the distance from the origin $|\boldsymbol{r}_{i,s}| = \rho_s\sqrt{a/|F|}$ changes, but the angles with respect to the coordinate axes stay the same. In other words, the "saddle track" of the ith electron, i.e. the image of $\mathbb{R} \cup \{\pm\infty\}$ under the function (B.62), is a straight line through the origin that can be parametrized by a single coordinate $r_i \in \mathbb{R}$. We define the Eckhardt-Sacha model for N electrons as the restriction of the electrons to the C_{Nv} saddle tracks, i.e. we set the position of the ith electron to

$$\boldsymbol{r}_i = r_i(a_i, b_i, c_i). \tag{B.63}$$

with the coefficients

$$a_i = \frac{1}{\sqrt{a}} \cos\left(\frac{2\pi i}{N}\right), \tag{B.64a}$$

$$b_i = \frac{1}{\sqrt{a}} \sin\left(\frac{2\pi i}{N}\right), \tag{B.64b}$$

$$c_i = \sqrt{\frac{a-1}{a}}. \tag{B.64c}$$

The configuration space spanned by the new coordinates $r_1, \ldots, r_N$ is N-dimensional. From the above choice of coefficients, it follows that $|\boldsymbol{r}_i| = |r_i|$. This normalization ensures that the squared momenta $\boldsymbol{p}_i^2$ do not acquire prefactors, neither in the classical nor in the quantum mechanical description of the system.

For the electron repulsion terms in the new Hamiltonian, we need to calculate

$$|\boldsymbol{r}_i - \boldsymbol{r}_j| = \sqrt{r_i^2 + r_j^2 - 2r_i r_j(a_i a_j + b_i b_j + c_i c_j)} \tag{B.65}$$

for $i \neq j$. Simplification of the term in parentheses yields

$$2(a_i a_j + b_i b_j + c_i c_j) = 2 - \frac{4}{a}\sin^2\left(\frac{\pi(i-j)}{N}\right) =: h_{|i-j|}(a). \tag{B.66}$$

The helping function $h_k(a)$ is periodic in k with period N, i.e. $h_{k+N}(a) = h_k(a)$. For $N \leq 3$, it is independent of k. This is geometrically clear (see Fig. B.3) and results in all electron repulsion terms being invariant under permutation of the coordinates r_i. However, this invariance is lost for $N > 3$, so the electrons are not indistinguishable anymore.

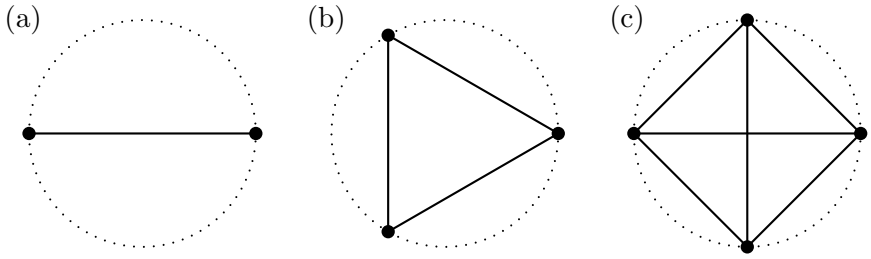

Figure B.3. Circular arrangement of (a) two, (b) three and (c) four electrons. Only in the first two cases, all interelectron distances are equal.

With the coordinates (B.63) and the conjugate momenta p_i, we obtain the N-dimensional Eckhardt-Sacha Hamiltonian

$$H = \sum_{i=1}^{N} \frac{p_i^2}{2} + V(r_1, \ldots, r_N) \tag{B.67}$$

with the potential

$$V(r_1, \ldots, r_N) = -\sum_{i=1}^{N} \left(\frac{Z}{|r_i|} + \sqrt{\frac{a-1}{a}} F r_i \right) + \sum_{\substack{i,j=1 \\ i<j}}^{N} \frac{1}{\sqrt{r_i^2 + r_j^2 - h_{|i-j|}(a) r_i r_j}}. \tag{B.68}$$

The field amplitude felt by the electrons is reduced by a factor of $\sqrt{1-1/a}$ resulting from the tilt of the saddle tracks with respect to the field axis. Another consequence of the tilt is that $h_{|i-j|}$ never equals two, so the subspace of equal electron positions is accessible and the electron repulsion decreases as $1/|r_i|$ there. In the aligned-electron model (Grobe and Eberly, 1993) where all electrons are confined to the field axis, one has $h_{|i-j|} = 2$ for all i, j, so the subspace of equal electron positions is blocked due to the diverging repulsion.

From the classical equations of motion

$$\dot{r}_i = \frac{\partial H}{\partial p_i} = p_i, \tag{B.69a}$$

$$\dot{p}_i = -\frac{\partial H}{\partial r_i} = -\frac{Z}{r_i^2}\mathrm{sgn}(r_i) + \frac{1}{2}\sum_{\substack{j=1 \\ i\neq j}}^{N} \frac{2r_i - h_{|i-j|}(a) r_j}{(r_i^2 + r_j^2 - h_{|i-j|}(a) r_i r_j)^{3/2}} + \sqrt{\frac{a-1}{a}} F, \tag{B.69b}$$

we find that the Hamiltonian (B.67) has a stationary point ($\dot{p}_i = 0\ \forall i$) on the diagonal of the configuration space at

$$r_1 = \cdots = r_N = r_s = \mathrm{sgn}(F) \sqrt{\frac{Z}{|F|}} \left(\frac{a-1}{a} \right)^{1/4} \tag{B.70}$$

with energy

$$E_s = V(r_s, \ldots, r_s) = -2N\sqrt{Z|F|}\left(\frac{a-1}{a}\right)^{3/4} = -\sqrt{2NW_N|F|}(a-1)^{3/4}. \quad \text{(B.71)}$$

It corresponds to the original C_{Nv} configuration with all electrons at an equal distance from the nucleus. By construction, $|r_s|/\sqrt{a}$ is equal to (B.14a) while the energy of the stationary point agrees with (B.15).

The Hessian of the potential (B.68) evaluated at the stationary point (B.70) is

$$\begin{aligned} V''_{ij,s} &= \left(\frac{\partial^2 V}{\partial r_i \partial r_j}\right)(r_s, \ldots, r_s) \\ &= -\frac{1}{r_s^3}\left[2Z\delta_{ij} + \frac{1}{2}\sum_{\substack{k=1 \\ i\neq k}}^{N}\left(\frac{2\delta_{ij} - h_{|i-k|}(a)\delta_{jk}}{(2-h_{|i-k|}(a))^{3/2}} - \frac{3}{2}\frac{\delta_{ij}+\delta_{jk}}{(2-h_{|i-k|}(a))^{1/2}}\right)\right]. \end{aligned} \quad \text{(B.72)}$$

A case analysis reveals that the diagonal elements

$$\begin{aligned} V''_{ii,s} &= -\frac{1}{r_s^3}\left[2Z + \frac{1}{2}\sum_{\substack{k=1 \\ i\neq k}}^{N}\left(\frac{2}{(2-h_{|i-k|}(a))^{3/2}} - \frac{3}{2}\frac{1}{(2-h_{|i-k|}(a))^{1/2}}\right)\right] \\ &= -\frac{1}{r_s^3}\left[2Z - \frac{3Z}{2a} + \sum_{l=1}^{N-1}\frac{1}{(2-h_l(a))^{3/2}}\right] \\ &= -\frac{1}{r_s^3}\left[\frac{Z}{2}\left(4-\frac{3}{a}\right) + \sum_{l=1}^{N-1}\frac{1}{(2-h_l(a))^{3/2}}\right] =: \nu_0 \end{aligned} \quad \text{(B.73)}$$

are all equal and the off-diagonal elements

$$\begin{aligned} V''_{ij,s} &= \frac{1}{2r_s^3}\sum_{\substack{k=1 \\ i\neq k}}^{N}\left(\frac{h_{|i-k|}(a)\delta_{jk}}{(2-h_{|i-k|}(a))^{3/2}} + \frac{3}{2}\frac{\delta_{jk}}{(2-h_{|i-k|}(a))^{1/2}}\right) \\ &= \frac{1}{2r_s^3}\left(\frac{h_{|i-j|}(a)}{(2-h_{|i-j|}(a))^{3/2}} + \frac{3}{2}\frac{1}{(2-h_{|i-j|}(a))^{1/2}}\right) =: \nu_{|i-j|} \end{aligned} \quad \text{(B.74)}$$

only depend on $|i-j|$. Due to $h_l(a) = h_{N-l}(a)$, we have $\nu_l = \nu_{N-l}$, so the Hessian has the structure (B.41) of a circulant matrix with the eigenvalues and eigenvectors given by (B.42) and (B.43), respectively. Since

$$\mu_{N-i} = \nu_0 + \sum_{j=1}^{N}\nu_{N-l}\cos\left(\frac{2\pi(N-i)j}{N}\right) = \nu_0 + \sum_{j=1}^{N}\nu_{N-j}\cos\left(\frac{2\pi ij}{N}\right) = \mu_i, \quad \text{(B.75)}$$

all eigenvalues are doubly degenerate, except μ_0 (and $\mu_{N/2}$ if N is even). The ith eigenvalue can be written as

$$\begin{aligned}\mu_i &= \nu_0 + \sum_{j=1}^{N-1} \nu_{N-j} \cos\left(\frac{2\pi ij}{N}\right) = \nu_0 + \sum_{j=1}^{N-1} \nu_j \cos\left(\frac{2\pi ij}{N}\right) \\ &= \frac{1}{r_s^3}\left[\frac{Z}{2}\left(\frac{3}{a}-4\right) + \frac{3}{4}\sum_{j=1}^{N-1}\frac{\cos\left(\frac{2\pi ij}{N}\right)}{(2-h_j(a))^{1/2}} - \frac{1}{2}\sum_{j=1}^{N-1}\frac{2-h_j(a)\cos\left(\frac{2\pi ij}{N}\right)}{(2-h_j(a))^{3/2}}\right] \\ &= -\frac{1}{r_s^3}\left[2Z\frac{a-1}{a} + \frac{\sqrt{a}}{4}\sum_{j=1}^{N-1}\frac{\sin^2\left(\frac{\pi ij}{N}\right)}{\sin\left(\frac{\pi j}{N}\right)} + \frac{a^{3/2}}{4}\sum_{j=1}^{N-1}\frac{\sin^2\left(\frac{\pi ij}{N}\right)}{\sin^3\left(\frac{\pi j}{N}\right)}\right]. \end{aligned} \tag{B.76}$$

Each of the terms in parentheses is positive, so all eigenvalues μ_i of the stationary point are negative, i.e. the stationary point is a local maximum which has only unstable directions in configuration space. The reaction coordinate of simultaneous N-fold ionization is the subspace spanned by the eigenvector (B.43) whose components are all equal. This only happens if $i = 0$. The corresponding eigenvalue is

$$\mu_0 = \sum_{j=0}^{N-1} \nu_j = -\frac{2Z}{r_s^3}\frac{a-1}{a} \tag{B.77}$$

and we obtain the threshold exponent of simultaneous N-fold ionization within the Eckhardt-Sacha model as

$$\begin{aligned}\beta_N^{(ES)}(a) &= \sum_{i=1}^{N-1}\sqrt{\frac{\mu_i}{\mu_0}(a)} \\ &= \sum_{i=1}^{N-1}\sqrt{1 + \frac{Na}{4W_N(a-1)}\left[\sum_{j=1}^{N-1}\frac{\sin^2\left(\frac{\pi ij}{N}\right)}{\sin^3\left(\frac{\pi j}{N}\right)} + \frac{1}{a}\sum_{j=1}^{N-1}\frac{\sin^2\left(\frac{\pi ij}{N}\right)}{\sin\left(\frac{\pi j}{N}\right)}\right]}. \end{aligned} \tag{B.78}$$

This expression might be simplified some more by using (B.75). The asymptotic threshold exponent

$$\lim_{a\to\infty}\beta_N^{(ES)}(a) = \sum_{i=1}^{N-1}\sqrt{1 + \frac{N}{4W_N}\sum_{j=1}^{N-1}\frac{\sin^2\left(\frac{\pi ij}{N}\right)}{\sin^3\left(\frac{\pi j}{N}\right)}} \tag{B.79}$$

agrees with (B.45). Table B.3 collects the threshold exponents for $N \in \{2, 3, 4\}$.

B.3.3. Eckhardt-Sacha model with cut-off parameter

In order to use the Hamiltonian (B.67) in classical or quantum simulations, one has to remove the Coulomb singularities with a cut-off parameter ε. The length scale

N	$\beta_N^{(ES)}(a)$	$\beta_N^{(ES)}(a)$ $[Z=N]$	$\beta_N^{(ES)}(\infty)$
2	$\sqrt{\frac{3}{2}+\frac{1}{a-1}}$	$\sqrt{\frac{11}{6}} \approx 1.354$	$\sqrt{\frac{3}{2}}$
3	$\sqrt{6+\frac{7}{2}\frac{1}{a-1}}$	$\frac{\sqrt{31}}{2} \approx 2.784$	$2\sqrt{\frac{3}{2}}$
4	$2\sqrt{1+\frac{1}{a-1}\left(\frac{a}{2}+\frac{1+\sqrt{2}}{W_4}\right)}+\sqrt{1+\frac{2\sqrt{2}}{W_4}\left(2+\frac{3}{a-1}\right)}$	4.397	$2\sqrt{\frac{3}{2}}+\sqrt{\frac{1+4\sqrt{2}}{1+2\sqrt{2}}}$

Table B.3. Threshold exponents of the Eckhardt-Sacha model for small numbers of electrons N as a function of the parameter a (second column), for $N = Z$ (third column) and $a \to \infty$ (fourth column). W_N is defined by (B.11). The result $\beta_2^{(ES)}(4) = \sqrt{11/6}$ was first derived by Eckhardt and Sacha (2006).

introduced by ε destroys the $1/\sqrt{|F|}$-scaling in (B.70) and the scaling of the matrix elements of the Hessian. As a consequence, the threshold exponent $\beta_N^{(ES)}$ of the smoothed Hamiltonian not only depends on ε, but also on F.

However, an analytical determination of r_s and $\beta_N^{(ES)}$ is possible for $Z = N < 4$. This can be seen as follows. Using the equations of motion (B.69b) with a cut-off parameter ε, the condition for a stationary point in the symmetric subspace $r_s = r_1 = \cdots = r_N$ takes the form

$$0 = -\frac{Zr_s}{(r_s^2+\varepsilon^2)^{3/2}} + \frac{r_s}{2}\sum_{\substack{j=1\\ i\neq j}}^{N} \frac{2-h_{|i-j|}(a)}{(r_s^2(2-h_{|i-j|}(a))+\varepsilon^2)^{3/2}} + \sqrt{\frac{a-1}{a}}F. \tag{B.80}$$

The helping function $h_{|i-j|}$ is independent of $|i-j|$ for $N < 4$ and equal to one for $Z = N < 4$, so all Coulomb terms in (B.80) collapse into one, leading to the equation

$$\frac{N+1}{2}\frac{r_s}{(r_s^2+\varepsilon^2)^{3/2}} = \sqrt{1-\left(\frac{W_N}{2N^2}\right)^{2/3}}F. \tag{B.81}$$

With the substitution $r_s = \operatorname{sgn}(F)y^{3/2}$, this equation can be solved with Cardano's method (see Appendix C.2). The calculation reveals that two stationary points exist for $|F|$ smaller than the critical field amplitude

$$F_{crit}(\varepsilon) := \frac{N+1}{3^{3/2}\varepsilon^2}\frac{1}{\sqrt{1-\left(\frac{W_N}{2N^2}\right)^{2/3}}} = \begin{cases} \frac{2}{3\varepsilon^2}, & N=2, \\ \frac{2^{3/2}}{3\varepsilon^2}, & N=3. \end{cases} \tag{B.82}$$

One of them,

$$r_s(\varepsilon,F) = \operatorname{sgn}(F)2\varepsilon\sqrt{\frac{F_{crit}(\varepsilon)}{|F|}}\cos^{3/2}\left(\frac{1}{3}\arccos\left(-\frac{|F|}{F_{crit}(\varepsilon)}\right)\right), \tag{B.83}$$

is the ε-dependent counterpart of (B.70) we are looking for. This can be seen by considering the limits $F \to 0$ or $\varepsilon \to 0$ of (B.83). Plugging the stationary point

into the Hessian of the smoothed potential and calculating its eigenvalues, we find the threshold exponents for $N = 2$ and $N = 3$,

$$\beta_2^{(ES)}(\varepsilon, F) = \frac{1}{\sqrt{3}}\sqrt{\frac{11r_s^2(\varepsilon, F) - \varepsilon^2}{2r_s^2(\varepsilon, F) - \varepsilon^2}}, \tag{B.84a}$$

$$\beta_3^{(ES)}(\varepsilon, F) = \frac{1}{\sqrt{2}}\sqrt{\frac{31r_s^2(\varepsilon, F) - 2\varepsilon^2}{2r_s^2(\varepsilon, F) - \varepsilon^2}}. \tag{B.84b}$$

By calculating a large number of trajectories with appropriate initial conditions, the values

$$\beta_2^{(ES)}(1, 0.02) = 1.357, \tag{B.85a}$$

$$\beta_3^{(ES)}(\sqrt{0.6}, 0.02) = 2.787 \tag{B.85b}$$

were confirmed numerically by Eckhardt and Sacha (2006) and Freitag (2014), respectively. In the limit $|F| \to F_{crit}(\varepsilon)$, we have $r_s(\varepsilon, F) \to \varepsilon/\sqrt{2}$, i.e. $\beta_{2/3}^{(ES)}(\varepsilon, F) \to \infty$. This is due to the fact that the minimum and the maximum merge at the critical field amplitude to form a saddle point, i.e. the Lyapunov exponent of the reaction coordinate which describes the stability of the motion across the maximum is zero there. In the limits $\varepsilon \to 0$ or $F \to 0$, the exponents (B.84) converge to the results obtained with the bare Coulomb potentials (which are shown in the third column of Table B.3).

As mentioned in Section 2.2, the three-electron potential (2.8) has additional stationary points if $\varepsilon \neq 0$. There is an index-1 saddle near each coordinate axis and an index-2 saddle near the diagonal of each coordinate plane which can be regarded as transition states of single ionization and of simultaneous double ionization, respectively. Due to the symmetry of the potential, the three saddles of each type are equivalent and their positions are related by a cyclic permutation of the coordinates. The double ionization saddle has two unstable directions, so it has a nonzero threshold exponent $\beta_{3,DI}^{(ES)}(\varepsilon, F)$. As shown in Fig. B.4, $\beta_{3,DI}^{(ES)}(\varepsilon, F)$ is remarkably close to the threshold exponent $\beta_2^{(ES)}(\varepsilon, F)$ of the two-electron Eckhardt-Sacha model for all field amplitudes considered in this work ($F < 0.55$ a.u.). This is due to the fact that the double ionization saddle lies very close to the subspace $r_1 = r_2$, $r_3 = 0$ where the three-electron potential is given by

$$V_{3D}(r_1, r_1, 0) = -\frac{3}{\sqrt{r_1^2 + \varepsilon^2}} - 2\sqrt{\frac{2}{3}}Fr_1 - \frac{3}{\varepsilon}. \tag{B.86}$$

This is very similar to the two-electron potential restricted to the subspace $r_1 = r_2$

$$V_{2D}(r_1, r_1) = -\frac{3}{\sqrt{r_1^2 + \varepsilon^2}} - 2\frac{\sqrt{3}}{2}Fr_1. \tag{B.87}$$

The constant $-3/\varepsilon$ is irrelevant for the position of the maximum.

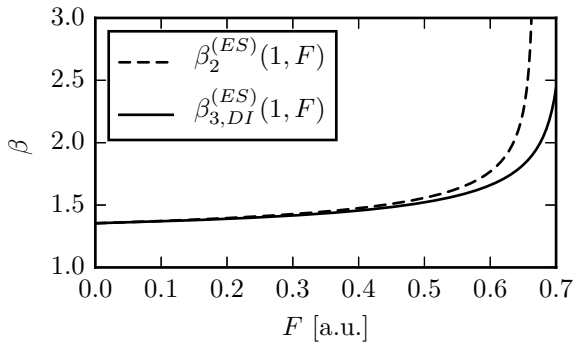

Figure B.4. Threshold exponents of simultaneous double ionization for the two-electron Eckhardt-Sacha model (dashed line) and the three-electron Eckhardt-Sacha model (solid line) as a function of F for $\varepsilon^2 = 1$ a.u.

B.4. C_{2v} configuration

To complete the analysis of threshold escape in a laser field at least for triple ionization, we briefly consider the three-electron C_{2v} escape configuration.

B.4.1. Full-dimensional description

The saddle of simultaneous triple ionization is located in the subspace where two electrons move symmetrically with respect to the field axis in the yz-plane and one electron is confined to the field axis, i.e.

$$\boldsymbol{r}_1 = (0, \quad y, z), \tag{B.88a}$$
$$\boldsymbol{r}_2 = (0, -y, z), \tag{B.88b}$$
$$\boldsymbol{r}_3 = (0, 0, z_3). \tag{B.88c}$$

For $F = 1$, the potential in the subspace is

$$V_{C_{2v}}(y, z, z_3) = -\frac{2Z}{\sqrt{y^2 + z^2}} - \frac{Z}{|z_3|} + \frac{1}{2|y|} + \frac{2}{\sqrt{y^2 + (z - z_3)^2}} - (2z + z_3). \tag{B.89}$$

Unfortunately, the saddle point cannot be found analytically. For $Z = 3$, a numerical calculation (Sacha and Eckhardt, 2001a) yields the saddle in the subspace

$$y_s = 1.1607 =: a_1, \tag{B.90a}$$
$$z_s = 1.1143 =: a_2, \tag{B.90b}$$
$$z_{3s} = 1.4665 \tag{B.90c}$$

and the threshold exponent in full space

$$\beta_3(3) \approx 3.7043 \tag{B.91}$$

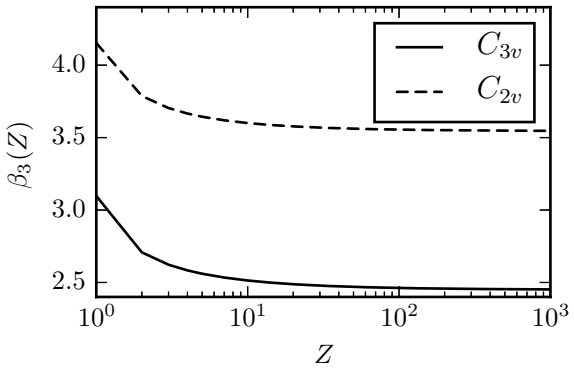

Figure B.5. Threshold exponents β_3 for the C_{3v} escape configuration (solid line) and the C_{2v} escape configuration (dashed line) as a function of the nuclear charge Z.

which is considerably larger than (B.56c). This is not only true for $Z = 3$, but for any value of Z, as shown in Fig. B.5 where the threshold exponents of both configurations are compared. For large Z, the saddle position in the C_{2v} subspace can be found analytically and equals

$$y_s = \left(\frac{5}{4}\right)^{1/3} Z^{1/6}, \tag{B.92a}$$

$$z_s = z_{3s} = \sqrt{Z}. \tag{B.92b}$$

By working through the Hessian matrix, we find the asymptotic threshold exponent

$$\lim_{Z\to\infty} \beta_3(Z) = \sqrt{\frac{3}{2}} + \frac{\sqrt{7}+\sqrt{22}}{\sqrt{10}} \approx 3.5446. \tag{B.93}$$

B.4.2. Saddle-track model

Introducing new coordinates r_1, r_2, r_3 and defining $c := a_1/a_2 = 1.042$ (which is equal to the tangent of the angle between the field axis and the outer saddle tracks), we can again confine the electrons to the saddle tracks, thus obtaining the C_{2v}-version of the three-electron Eckhardt-Sacha model. With the unit vectors of the saddle tracks, the electron positions are given by

$$\boldsymbol{r}_1 = r_1 \left(0, \quad \frac{c}{\sqrt{1+c^2}}, \frac{1}{\sqrt{1+c^2}}\right), \tag{B.94a}$$

$$\boldsymbol{r}_2 = r_2 \left(0, -\frac{c}{\sqrt{1+c^2}}, \frac{1}{\sqrt{1+c^2}}\right), \tag{B.94b}$$

$$\boldsymbol{r}_3 = r_3 \,(0, 0, 1) \tag{B.94c}$$

and the Hamiltonian is

$$H = \frac{p_1^2}{2} + \frac{p_2^2}{2} + \frac{p_3^2}{2} + V(r_1, r_2, r_3) \tag{B.95}$$

with the conjugate momenta p_i and the potential

$$V(r_1,r_2,r_3) = -\frac{3}{|r_1|} - \frac{3}{|r_2|} - \frac{3}{|r_3|} + \frac{1}{\sqrt{r_1^2 + r_2^2 - 2r_1r_2\frac{1-c^2}{1+c^2}}} + \frac{1}{\sqrt{r_1^2 + r_3^2 - \frac{2r_1r_3}{\sqrt{1+c^2}}}} + \frac{1}{\sqrt{r_2^2 + r_3^2 - \frac{2r_2r_3}{\sqrt{1+c^2}}}} - F(t)\left(\frac{r_1+r_2}{\sqrt{1+c^2}} + r_3\right). \tag{B.96}$$

Since (B.96) is not invariant under permutation of the coordinates, the electrons are distinguishable[6]. Consequently, it matters whether one of the outer electrons (1, 2) or the electron on the field axis (3) ionizes first, i.e. there are two distinguishable singly-charged ions described by the Hamiltonians

$$H_{+,1} = \frac{p_2^2}{2} + \frac{p_3^2}{2} - \frac{3}{|r_2|} - \frac{3}{|r_3|} + \frac{1}{\sqrt{r_2^2 + r_3^2 - \frac{2r_2r_3}{\sqrt{1+c^2}}}} - F(t)\left(\frac{r_2}{\sqrt{1+c^2}} + r_3\right), \tag{B.97a}$$

$$H_{+,3} = \frac{p_1^2}{2} + \frac{p_2^2}{2} - \frac{3}{|r_1|} - \frac{3}{|r_2|} + \frac{1}{\sqrt{r_1^2 + r_2^2 - 2r_1r_2\frac{1-c^2}{1+c^2}}} - F(t)\frac{r_1+r_2}{\sqrt{1+c^2}}. \tag{B.97b}$$

Likewise, there are two distinguishable doubly-charged ions described by

$$H_{2+,12} = H_{2+,21} = \frac{p_3^2}{2} - \frac{3}{|r_3|} - F(t)r_3, \tag{B.98a}$$

$$H_{2+,13} = H_{2+,31} = \frac{p_2^2}{2} - \frac{3}{|r_2|} - F(t)\frac{r_2}{\sqrt{1+c^2}}. \tag{B.98b}$$

[6]If c were a free parameter, the indistinguishability could be restored by setting $c = 0$. This corresponds to all electrons on the field axis, i.e. the aligned-electron model (Ho and Eberly, 2006).

C. Mathematics

C.1. Cardano's method to solve cubic equations

The need to solve cubic equations arises in several sections of this thesis, e.g. when determining the extrema of soft-core Coulomb potentials or in the stability analysis of multiple ionization saddles. While it can be safely assumed that the reader is familiar with solving quadratic equations, the cubic case generally represents a much harder task. Here, we briefly review the method of Cardano, as detailed in the handbook of Bronstein *et al.* (2005).

Consider a cubic equation with variable x and constants $a, b, c \in \mathbb{R}$,

$$x^3 + ax^2 + bx + c = 0. \tag{C.1}$$

If one is able to guess a solution[1] of (C.1), polynomial long division and the quadratic formula immediately yield the other two; if not, one has to follow a different path to find the solutions. With the substitution $x = z - a/3$, the quadratic term in (C.1) vanishes and we obtain the reduced (or depressed) cubic equation

$$z^3 + 3pz + 2q = 0 \tag{C.2}$$

where

$$p = \frac{1}{3}\left(b - \frac{a^2}{3}\right), \tag{C.3a}$$

$$q = \frac{1}{2}\left(\frac{2a^3}{27} - \frac{ab}{3} + c\right). \tag{C.3b}$$

Substituting $z = u + v$ (*Cardano's method*) and equating coefficients gives

$$u^3 + v^3 = -2q, \tag{C.4a}$$

$$uv = -p \Leftrightarrow u^3 v^3 = -p^3. \tag{C.4b}$$

Bearing Vieta's formulas in mind, u^3 and v^3 can be seen as solutions to the quadratic equation

$$w^2 - (u^3 + v^3)w + u^3 v^3 = w^2 + 2qw - p^3 = 0, \tag{C.5}$$

[1]The cubic equation (C.1) has at least one real solution. This can be seen as follows. The function $f(x) := x^3 + ax^2 + bx^2 + c$ is continuous $\forall x \in \mathbb{R}$ and tends to $\pm\infty$ as $x \to \pm\infty$, so there are finite $x_0, x_1 \in \mathbb{R}$ with $f(x_0) < 0$ and $f(x_1) > 0$. The intermediate value theorem for continuous functions guarantees the existence of a root in the interval (x_0, x_1).

i.e.

$$w_1 = u^3 = -q + \sqrt{q^2 + p^3} = -q + \sqrt{D}, \tag{C.6a}$$

$$w_2 = v^3 = -q - \sqrt{q^2 + p^3} = -q - \sqrt{D} \tag{C.6b}$$

and hence

$$u = \left(-q + \sqrt{D}\right)^{1/3}, \tag{C.7a}$$

$$v = \left(-q - \sqrt{D}\right)^{1/3} \tag{C.7b}$$

where we defined the discriminant

$$D = q^2 + p^3. \tag{C.8}$$

There is a minor problem in (C.7). If z is a third root of a number y (i.e. $z^3 = y$), $z\exp(2\pi\mathrm{i}/3)$ and $z\exp(-2\pi\mathrm{i}/3)$ are third roots as well, so there would be nine cases to consider. However, the condition $uv = -p$ only holds for three of them, so only these cases remain. Taking u_1 and v_1 as the real cubic roots, we obtain

$$z_1 = u_1 + v_1, \tag{C.9a}$$

$$z_2 = u_1 \mathrm{e}^{2\pi\mathrm{i}/3} + v_1 \mathrm{e}^{-2\pi\mathrm{i}/3} = u_1 \left(-\frac{1}{2} + \frac{\sqrt{3}}{2}\mathrm{i}\right) + v_1 \left(-\frac{1}{2} - \frac{\sqrt{3}}{2}\mathrm{i}\right), \tag{C.9b}$$

$$z_3 = u_1 \mathrm{e}^{-2\pi\mathrm{i}/3} + v_1 \mathrm{e}^{2\pi\mathrm{i}/3} = u_1 \left(-\frac{1}{2} - \frac{\sqrt{3}}{2}\mathrm{i}\right) + v_1 \left(-\frac{1}{2} + \frac{\sqrt{3}}{2}\mathrm{i}\right) = z_2^* \tag{C.9c}$$

with the important property

$$z_1 z_2 z_3 = z_1 |z_2|^2 = u_1^3 + v_1^3 = -2q. \tag{C.10}$$

The discriminant (C.8) determines the number of real solutions. Three cases can occur.

- $D > 0$. There are one real solution and two complex conjugate solutions,

$$z_1 = u_1 + v_1, \tag{C.11a}$$

$$z_{2,3} = -\frac{u_1 + v_1}{2} \pm \frac{u_1 - v_1}{2}\sqrt{3}\mathrm{i}. \tag{C.11b}$$

- $D = 0$. All solutions are real; if $p = q = 0$, the triply degenerate solution is $z_{1,2,3} = 0$. Otherwise, there are two solutions, one of which is doubly degenerate,

$$z_1 = 2u = 2\frac{q}{p}, \tag{C.12a}$$

$$z_{2,3} = -u = -\frac{q}{p}. \tag{C.12b}$$

- $D < 0$. There are three different real solutions,

$$z_1 = 2\sqrt{-p}\cos\left(\frac{1}{3}\arccos\left(-\frac{q}{\sqrt{-p^3}}\right)\right), \tag{C.13a}$$

$$z_2 = 2\sqrt{-p}\cos\left(\frac{1}{3}\arccos\left(-\frac{q}{\sqrt{-p^3}}\right)+\frac{2\pi}{3}\right), \tag{C.13b}$$

$$z_3 = 2\sqrt{-p}\cos\left(\frac{1}{3}\arccos\left(-\frac{q}{\sqrt{-p^3}}\right)+\frac{4\pi}{3}\right). \tag{C.13c}$$

From the above solutions z_i, the solutions x_i of the original cubic equation (C.1) are calculated as $x_i = z_i - a/3$.

C.2. Soft-core Coulomb potential in a laser field

As an application of Cardano's method, we calculate the local extrema of a soft-core Coulomb potential in a laser field, i.e. the function

$$V(x) = -\frac{Z}{\sqrt{x^2+\varepsilon^2}} - CFx \tag{C.14}$$

where C, Z, ε are positive constants and $F \in \mathbb{R}\setminus\{0\}$ is the amplitude of the laser field. The necessary condition for a local extremum reads

$$V'(x) = \frac{Zx}{(x^2+\varepsilon^2)^{3/2}} - CF = 0. \tag{C.15}$$

Since $C, Z > 0$, x and F must have the same sign in order to fulfill the equation. With the substitution

$$x = \operatorname{sgn}(F) y^{3/2}, \tag{C.16}$$

the sign dependence is removed and equation (C.15) is transformed into the depressed cubic equation

$$y^3 - \left(\frac{Z}{C|F|}\right)^{2/3} y + \varepsilon^2 = 0. \tag{C.17}$$

Due to the square root in (C.16), only the real positive solutions of the cubic equation are real solutions of (C.15). With the identification

$$p = -\frac{1}{3}\left(\frac{Z}{C|F|}\right)^{2/3}, \tag{C.18a}$$

$$q = \frac{\varepsilon^2}{2}, \tag{C.18b}$$

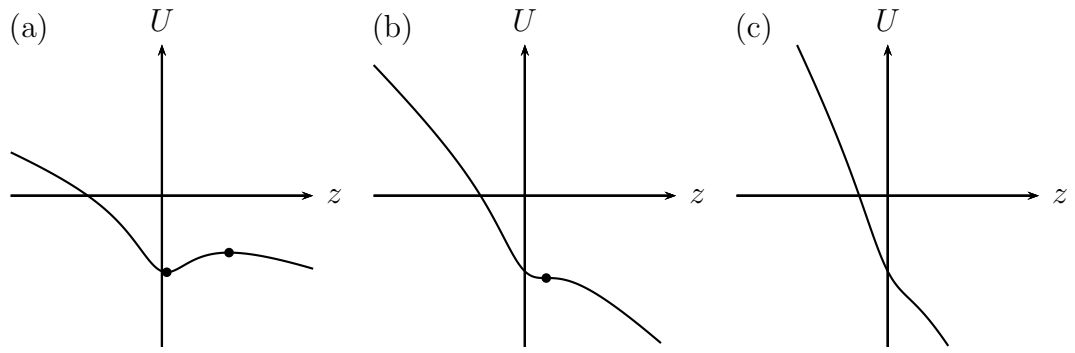

Figure C.1. The potential $U(z)$ for (a) $|F| < F_{crit}$, (b) $|F| = F_{crit}$ and (c) $|F| > F_{crit}$. Points on the curve with $U'(z) = 0$ are indicated by dots.

the discriminant reads

$$\begin{aligned} D = q^2 + p^3 &= \frac{\varepsilon^4}{4} - \frac{1}{27}\left(\frac{Z}{C|F|}\right)^2 \\ &= \frac{\varepsilon^4}{4}\left(1 - \frac{2Z}{3^{3/2}\varepsilon^2 C|F|}\right)\left(1 + \frac{2Z}{3^{3/2}\varepsilon^2 C|F|}\right). \end{aligned} \tag{C.19}$$

Defining the critical field amplitude

$$F_{crit} := \frac{2Z}{3^{3/2}\varepsilon^2 C}, \tag{C.20}$$

we can distinguish three cases which are illustrated in Fig. C.1 for $F = |F| > 0$ and the dimensionless form of the potential (C.14), i.e.

$$U(z) = -\frac{1}{\sqrt{z^2+1}} - \frac{2}{3^{3/2}}\frac{|F|}{F_{crit}}z \tag{C.21}$$

with $z = x/\varepsilon$ and $U = V\varepsilon/Z$.

- $0 < |F| < F_{crit}$, i.e. $D < 0$. Equation (C.17) has the three real solutions (C.13). Since $-q/\sqrt{-p^3} = |F|/F_{crit}$ and $0 < |F|/F_{crit} < 1$, we have

$$\begin{aligned} &\frac{\pi}{3} > \frac{1}{3}\arccos\left(-\frac{|F|}{F_{crit}}\right) > \frac{\pi}{6} \\ \Leftrightarrow &\pi > \frac{1}{3}\arccos\left(-\frac{|F|}{F_{crit}}\right) + \frac{2\pi}{3} > \frac{5\pi}{6} \\ \Rightarrow &\cos\left(\frac{1}{3}\arccos\left(-\frac{|F|}{F_{crit}}\right) + \frac{2\pi}{3}\right) < 0, \end{aligned} \tag{C.22}$$

  so y_2 is negative and must be discarded. The two other solutions are positive.

Inserting them into (C.16), we obtain the solutions of (C.15),

$$x_{min} = \mathrm{sgn}(F) 2\varepsilon \sqrt{\frac{F_{crit}}{|F|}} \cos^{3/2}\left(\frac{1}{3}\arccos\left(-\frac{|F|}{F_{crit}}\right) + \frac{4\pi}{3}\right), \tag{C.23a}$$

$$x_{max} = \mathrm{sgn}(F) 2\varepsilon \sqrt{\frac{F_{crit}}{|F|}} \cos^{3/2}\left(\frac{1}{3}\arccos\left(-\frac{|F|}{F_{crit}}\right)\right) \tag{C.23b}$$

which correspond to a local minimum and a local maximum in the potential, respectively (Fig. C.1a). For $|F| = 0$, $x = 0$ is the only solution of (C.15). Indeed, we have $x_{min} \to 0$ and $|x_{max}| \to \infty$ in the limit $|F| \to 0$.

- $|F| = F_{crit}$, i.e. $D = 0$. The two solutions (C.23) degenerate to the single solution

$$x_{sad} = \mathrm{sgn}(F) 2\varepsilon \cos^{3/2}\left(\frac{\pi}{3}\right) = \mathrm{sgn}(F)\frac{\varepsilon}{\sqrt{2}} \tag{C.24}$$

which corresponds to a saddle point in the potential (Fig. C.1b).

- $|F| > F_{crit}$, i.e. $D > 0$. Equation (C.17) has one real solution y_1 and two complex conjugate ones $y_2 = y_3^*$ that fulfill

$$y_1 y_2 y_3 = y_1 |y_2|^2 = -2q = -\varepsilon^2 < 0 \tag{C.25}$$

which is equivalent to $y_1 < 0$. Consequently, (C.15) has no solution and the potential has neither an extremum nor a saddle point (Fig. C.1c).

C.3. Symmetry group of the three-electron Eckhardt-Sacha model

In this section, we discuss the symmetry group of the three-electron Eckhardt-Sacha Hamiltonian (2.7) and its irreducible representations which determine the degeneracy of the eigenvalues.

We start by recalling some definitions and results from group theory[2] (Welker and Thiede, 2010). A set G with a multiplication $\cdot : G \times G \to G$, $(g_1, g_2) \mapsto g_1 \cdot g_2$ is called a *group* if $\cdot$ is associative ($g_1 \cdot (g_2 \cdot g_3) = (g_1 \cdot g_2) \cdot g_3 \ \forall g_1, g_2, g_3 \in G$), there is a neutral element ($\exists e_G \in G$: $e_G \cdot g = g \cdot e_G = g \ \forall g \in G$) and every element has an inverse ($\forall g \in G \ \exists g^{-1} \in G$: $g \cdot g^{-1} = g^{-1} \cdot g = e_G$). If $\cdot$ is additionally commutative ($g_1 \cdot g_2 = g_2 \cdot g_1 \ \forall g_1, g_2 \in G$), G is called *abelian*. Usually, a group is denoted as $(G, \cdot)$. For the sake of convenience, however, the group multiplication symbol is often left out, $g_1 \cdot g_2$ reduces to $g_1 g_2$ and the group is just denoted by its underlying set G. The number of elements in G, written as $\#G$, is called the

[2]This is a modified version of a collection previously presented in Thiede (2011).

order of G. If $\#G < \infty$ the group is called *finite*, otherwise *infinite*. The invertible $n \times n$-matrices over $\mathbb{R}$ form an infinite group with matrix multiplication, the *general linear group* $\mathrm{GL}_n(\mathbb{R}) = \{A \in \mathbb{R}^{n\times n} | \det A \neq 0\}$. Another important group is the *symmetric group* S_N which contains all permutation operations of N elements. S_N is finite with $\#S_N = N!$ elements. Finally, the coordinate transformations under which a Hamiltonian is invariant also form a group, the *symmetry group* of the Hamiltonian. For a finite group G, all possible products of two group elements can be collected in a *multiplication table*.

Let $(G, \cdot)$, $(H, *)$ be groups. A map $f : G \to H$ with $f(g_1 \cdot g_2) = f(g_1) * f(g_2)\ \forall g_1, g_2 \in G$ is called a *group homomorphism* from G to H. By definition, a group homomorphism preserves the multiplication table of G. A group G is said to be *acting* on a set M by $\circ : G \times M \to M$, $(g, m) \mapsto g \circ m$ if $(g_1 \cdot g_2) \circ m = g_1 \circ (g_2 \circ m)$ and $e_G \circ m = m$ $\forall g_1, g_2 \in G, m \in M$. For $m \in M$, the set $Gm = \{g \circ m | g \in G\} \subseteq M$ is called the *orbit* of m. For example, $\mathrm{GL}_n(\mathbb{R})$ acts on $\mathbb{R}^n$ by matrix-vector multiplication. G acts on itself by *conjugation* $\circ : G \times G \to G$, $(g, h) \mapsto h^g := ghg^{-1}$. The orbits $Gh = \{h^g | g \in G\} \subseteq G$ are called *conjugacy classes*. If G is abelian, each conjugacy class contains only one element.

A group homomorphism $\rho : G \to \mathrm{GL}_n(\mathbb{R})$ is called a *representation* of G on $\mathbb{R}^n$. The *dimension* of ρ is the dimension of the corresponding representation space $\mathbb{R}^n$, i.e. n. The map $\chi_\rho : G \to \mathbb{R}$, $g \mapsto \mathrm{tr}\rho(g)$, where $\mathrm{tr}\rho(g)$ equals the sum of the diagonal elements of the matrix representing g, is called the *character* of ρ. A subspace U of $\mathbb{R}^n$ is called an *invariant subspace* of ρ if $\rho(G)U = \{\rho(g)u | g \in G, u \in U\} \subseteq U$. ρ is called *irreducible* if its only invariant subspaces are the trivial ones $\{0\}$ and $\mathbb{R}^n$. Otherwise, ρ is called *reducible*. Since $\mathrm{GL}_1(\mathbb{R}) = \mathbb{R} \setminus \{0\}$, a one-dimensional representation is always irreducible and equal to its character. For a finite group G, the number of conjugacy classes equals the number of irreducible representations. Furthermore, the sum of the squared dimensions of the irreducible representations is equal to the order of the group. The character of an irreducible representation with respect to a fixed conjugacy class is constant. They are collected in a *character table*.

To apply the above results to our problem, we first define the action of an invertible matrix $A \in \mathrm{GL}_3(\mathbb{R})$ on an arbitrary function $f(r_1, r_2, r_3)$ of the coordinates $(r_1, r_2, r_3)^\top \in \mathbb{R}^3$,

$$Af(r_1, r_2, r_3) := f(A(r_1, r_2, r_3)^\top), \tag{C.26}$$

where the action of A on the vector $(r_1, r_2, r_3)^\top$ is the usual matrix-vector product

$$A(r_1, r_2, r_3)^\top = \begin{pmatrix} a_{11} & a_{12} & a_{13} \\ a_{21} & a_{22} & a_{23} \\ a_{31} & a_{32} & a_{33} \end{pmatrix} \begin{pmatrix} r_1 \\ r_2 \\ r_3 \end{pmatrix} = \begin{pmatrix} a_{11}r_1 + a_{12}r_2 + a_{13}r_3 \\ a_{21}r_1 + a_{22}r_2 + a_{23}r_3 \\ a_{31}r_1 + a_{32}r_2 + a_{33}r_3 \end{pmatrix}. \tag{C.27}$$

Now consider the three-electron Eckhardt-Sacha Hamiltonian (C.28) for $F = 0$,

$$H = -\sum_{i=1}^{3} \left(\frac{1}{2} \frac{\partial^2}{\partial r_i^2} + \frac{3}{\sqrt{r_i^2 + \varepsilon^2}} \right) + \sum_{\substack{i,j=1 \\ i<j}}^{3} \frac{1}{\sqrt{r_i^2 + r_j^2 - r_i r_j + \varepsilon^2}}. \tag{C.28}$$

It is easily verified that (C.28) is invariant under all permutations of the coordinates (r_1, r_2, r_3), the inversion $(r_1, r_2, r_3) \to (-r_1, -r_2, -r_3)$ and all combinations thereof, so the symmetry group of the Hamiltonian is $D_{3d} \cong S_3 \times Z_2$ where Z_2 is the cyclic group of order 2. D_{3d} consists of the twelve elements $\{E, C_3, C_3', S_6, S_6', i, C_2, C_2', C_2'', \sigma_d, \sigma_d', \sigma_d''\}$ which are labeled according to the *Schoenflies notation*: E denotes the neutral operation, C_n an n-fold rotation axis, σ a mirror plane, S_{2n} a $2n$-fold rotation-reflection axis and i a center of inversion. A representation of D_{3d} on $\mathbb{R}^3$ is

$$
\begin{aligned}
E &\mapsto \begin{pmatrix} 1 & 0 & 0 \\ 0 & 1 & 0 \\ 0 & 0 & 1 \end{pmatrix}, & i &\mapsto \begin{pmatrix} -1 & 0 & 0 \\ 0 & -1 & 0 \\ 0 & 0 & -1 \end{pmatrix}, \\
C_3 &\mapsto \begin{pmatrix} 0 & 1 & 0 \\ 0 & 0 & 1 \\ 1 & 0 & 0 \end{pmatrix}, & S_6 &\mapsto \begin{pmatrix} 0 & -1 & 0 \\ 0 & 0 & -1 \\ -1 & 0 & 0 \end{pmatrix}, \\
C_3' &\mapsto \begin{pmatrix} 0 & 0 & 1 \\ 1 & 0 & 0 \\ 0 & 1 & 0 \end{pmatrix}, & S_6' &\mapsto \begin{pmatrix} 0 & 0 & -1 \\ -1 & 0 & 0 \\ 0 & -1 & 0 \end{pmatrix}, \\
\sigma_d &\mapsto \begin{pmatrix} 1 & 0 & 0 \\ 0 & 0 & 1 \\ 0 & 1 & 0 \end{pmatrix}, & C_2 &\mapsto \begin{pmatrix} -1 & 0 & 0 \\ 0 & 0 & -1 \\ 0 & -1 & 0 \end{pmatrix}, \\
\sigma_d' &\mapsto \begin{pmatrix} 0 & 1 & 0 \\ 1 & 0 & 0 \\ 0 & 0 & 1 \end{pmatrix}, & C_2' &\mapsto \begin{pmatrix} 0 & -1 & 0 \\ -1 & 0 & 0 \\ 0 & 0 & -1 \end{pmatrix}, \\
\sigma_d'' &\mapsto \begin{pmatrix} 0 & 0 & 1 \\ 0 & 1 & 0 \\ 1 & 0 & 0 \end{pmatrix}, & C_2'' &\mapsto \begin{pmatrix} 0 & 0 & -1 \\ 0 & -1 & 0 \\ -1 & 0 & 0 \end{pmatrix}.
\end{aligned}
\tag{C.29}
$$

The multiplication table of D_{3d} (Table C.1) is not symmetric, so the group is not abelian. Since $(1,1,1)^\top$ is an eigenvector of all twelve representation matrices, $\{\lambda(1,1,1)^\top | \lambda \in \mathbb{R}\}$ is a nontrivial invariant subspace of $\mathbb{R}^3$, i.e. the representation (C.29) is reducible. Considering all possible conjugations of the group elements, we find that the six conjugacy classes of D_{3d} are $\{E\}$, $\{C_3, C_3'\}$, $\{S_6, S_6'\}$, $\{i\}$, $\{C_2, C_2', C_2''\}$ and $\{\sigma_d, \sigma_d', \sigma_d''\}$, so there are six irreducible representations. The most obvious one is the *trivial representation* which maps every group element to 1,

$$
\begin{array}{llllllll}
E \mapsto & 1, & \sigma_d \mapsto & 1, & i \mapsto & 1, & C_2 \mapsto & 1, \\
C_3 \mapsto & 1, & \sigma_d' \mapsto & 1, & S_6 \mapsto & 1, & C_2' \mapsto & 1, \\
C_3' \mapsto & 1, & \sigma_d'' \mapsto & 1, & S_6' \mapsto & 1, & C_2'' \mapsto & 1.
\end{array}
\tag{C.30}
$$

Since $\det(AB) = \det A \det B$ for arbitrary matrices A, B, it follows that the homomor-

	E	C_3	C_3'	σ_d	σ_d'	σ_d''	i	S_6	S_6'	C_2	C_2'	C_2''
E	E	C_3	C_3'	σ_d	σ_d'	σ_d''	i	S_6	S_6'	C_2	C_2'	C_2''
C_3	C_3	C_3'	E	σ_d''	σ_d	σ_d'	S_6	S_6'	i	C_2''	C_2	C_2'
C_3'	C_3'	E	C_3	σ_d'	σ_d''	σ_d	S_6'	i	S_6	C_2'	C_2''	C_2
σ_d	σ_d	σ_d'	σ_d''	E	C_3	C_3'	C_2	C_2'	C_2''	i	S_6	S_6'
σ_d'	σ_d'	σ_d''	σ_d	C_3'	E	C_3	C_2'	C_2''	C_2	S_6'	i	S_6
σ_d''	σ_d''	σ_d	σ_d'	C_3	C_3'	E	C_2''	C_2	C_2'	S_6	S_6'	i
i	i	S_6	S_6'	C_2	C_2'	C_2''	E	C_3	C_3'	σ_d	σ_d'	σ_d''
S_6	S_6	S_6'	i	C_2''	C_2	C_2'	C_3	C_3'	E	σ_d''	σ_d	σ_d'
S_6'	S_6'	i	S_6	C_2'	C_2''	C_2	C_3'	E	C_3	σ_d'	σ_d''	σ_d
C_2	C_2	C_2'	C_2''	i	S_6	S_6'	σ_d	σ_d'	σ_d''	E	C_3	C_3'
C_2'	C_2'	C_2''	C_2	S_6'	i	S_6	σ_d'	σ_d''	σ_d	C_3'	E	C_3
C_2''	C_2''	C_2	C_2'	S_6	S_6'	i	σ_d''	σ_d	σ_d'	C_3	C_3'	E

Table C.1. Multiplication table of D_{3d}. The element in each cell is obtained by multiplying the row element by the column element.

phism mapping a group element to the determinant of its representing matrix,

$$\begin{aligned} E &\mapsto 1, & \sigma_d &\mapsto -1, & i &\mapsto -1, & C_2 &\mapsto 1, \\ C_3 &\mapsto 1, & \sigma_d' &\mapsto -1, & S_6 &\mapsto -1, & C_2' &\mapsto 1, \\ C_3' &\mapsto 1, & \sigma_d'' &\mapsto -1, & S_6' &\mapsto -1, & C_2'' &\mapsto 1, \end{aligned} \tag{C.31}$$

is another one-dimensional representation, the so-called *parity representation*. To find out if there are other one-dimensional representations ρ of D_{3d}, we consider the multiplication table. It can be shown that D_{3d} is *generated* by C_3, σ_d and i, i.e. all group elements can be written as a product of these three elements. Since

$$E = C_3^3 \Rightarrow 1 = \rho(C_3^3) = \rho(C_3)^3 \Rightarrow \rho(C_3) = 1, \tag{C.32a}$$

$$E = \sigma_d^2 \Rightarrow \rho(\sigma_d^2) = \rho(\sigma_d)^2 = 1 \Rightarrow \rho(\sigma_d) \in \{-1, 1\}, \tag{C.32b}$$

$$E = i^2 \Rightarrow \rho(i^2) = \rho(i)^2 = 1 \Rightarrow \rho(i) \in \{-1, 1\}, \tag{C.32c}$$

we have four choices. $\rho(\sigma_d) = \rho(i) = 1$ yields the trivial representation (C.30) and $\rho(\sigma_d) = \rho(i) = -1$ the parity representation (C.31). The other two one-dimensional representations are determined by $\rho(\sigma_d) = -\rho(i) = 1$,

$$\begin{aligned} E &\mapsto 1, & \sigma_d &\mapsto 1, & i &\mapsto -1, & C_2 &\mapsto -1, \\ C_3 &\mapsto 1, & \sigma_d' &\mapsto 1, & S_6 &\mapsto -1, & C_2' &\mapsto -1, \\ C_3' &\mapsto 1, & \sigma_d'' &\mapsto 1, & S_6' &\mapsto -1, & C_2'' &\mapsto -1 \end{aligned} \tag{C.33}$$

and $\rho(\sigma_d) = -\rho(i) = -1$,

$$\begin{aligned} E &\mapsto 1, & \sigma_d &\mapsto -1, & i &\mapsto 1, & C_2 &\mapsto -1, \\ C_3 &\mapsto 1, & \sigma_d' &\mapsto -1, & S_6 &\mapsto 1, & C_2' &\mapsto -1, \\ C_3' &\mapsto 1, & \sigma_d'' &\mapsto -1, & S_6' &\mapsto 1, & C_2'' &\mapsto -1. \end{aligned} \tag{C.34}$$

respectively. We have thus found four one-dimensional irreducible representations of D_{3d}. The dimensions d_1, d_2 of the two remaining irreducible representations must fulfill $d_1^2 + d_2^2 = 12 - 4 \cdot 1^2 = 8$. The only solution of this equation in $\mathbb{N}$ is $d_1 = d_2 = 2$. Therefore, we look for invertible 2×2 matrices that preserve the multiplication table of D_{3d}. Again, it is sufficient to specify C_3, σ_d and i. With C_3 and σ_d equal to the 120° rotation matrix and the 2×2 exchange matrix, respectively, we find

$$
\begin{aligned}
E &\mapsto \begin{pmatrix} 1 & 0 \\ 0 & 1 \end{pmatrix}, & \sigma_d' &\mapsto \begin{pmatrix} -\frac{\sqrt{3}}{2} & -\frac{1}{2} \\ -\frac{1}{2} & \frac{\sqrt{3}}{2} \end{pmatrix}, & S_6' &\mapsto \begin{pmatrix} -\frac{1}{2} & -\frac{\sqrt{3}}{2} \\ \frac{\sqrt{3}}{2} & -\frac{1}{2} \end{pmatrix}, \\
C_3 &\mapsto \begin{pmatrix} -\frac{1}{2} & \frac{\sqrt{3}}{2} \\ -\frac{\sqrt{3}}{2} & -\frac{1}{2} \end{pmatrix}, & \sigma_d'' &\mapsto \begin{pmatrix} \frac{\sqrt{3}}{2} & -\frac{1}{2} \\ -\frac{1}{2} & -\frac{\sqrt{3}}{2} \end{pmatrix}, & C_2 &\mapsto \begin{pmatrix} 0 & 1 \\ 1 & 0 \end{pmatrix}, \\
C_3' &\mapsto \begin{pmatrix} -\frac{1}{2} & -\frac{\sqrt{3}}{2} \\ \frac{\sqrt{3}}{2} & -\frac{1}{2} \end{pmatrix}, & i &\mapsto \begin{pmatrix} 1 & 0 \\ 0 & 1 \end{pmatrix}, & C_2' &\mapsto \begin{pmatrix} -\frac{\sqrt{3}}{2} & -\frac{1}{2} \\ -\frac{1}{2} & \frac{\sqrt{3}}{2} \end{pmatrix}, \\
\sigma_d &\mapsto \begin{pmatrix} 0 & 1 \\ 1 & 0 \end{pmatrix}, & S_6 &\mapsto \begin{pmatrix} -\frac{1}{2} & \frac{\sqrt{3}}{2} \\ -\frac{\sqrt{3}}{2} & -\frac{1}{2} \end{pmatrix}, & C_2'' &\mapsto \begin{pmatrix} \frac{\sqrt{3}}{2} & -\frac{1}{2} \\ -\frac{1}{2} & -\frac{\sqrt{3}}{2} \end{pmatrix}
\end{aligned}
\tag{C.35}
$$

for i equal to the identity matrix and

$$
\begin{aligned}
E &\mapsto \begin{pmatrix} 1 & 0 \\ 0 & 1 \end{pmatrix}, & \sigma_d' &\mapsto \begin{pmatrix} -\frac{\sqrt{3}}{2} & -\frac{1}{2} \\ -\frac{1}{2} & \frac{\sqrt{3}}{2} \end{pmatrix}, & S_6' &\mapsto \begin{pmatrix} \frac{1}{2} & \frac{\sqrt{3}}{2} \\ -\frac{\sqrt{3}}{2} & \frac{1}{2} \end{pmatrix}, \\
C_3 &\mapsto \begin{pmatrix} -\frac{1}{2} & \frac{\sqrt{3}}{2} \\ -\frac{\sqrt{3}}{2} & -\frac{1}{2} \end{pmatrix}, & \sigma_d'' &\mapsto \begin{pmatrix} \frac{\sqrt{3}}{2} & -\frac{1}{2} \\ -\frac{1}{2} & -\frac{\sqrt{3}}{2} \end{pmatrix}, & C_2 &\mapsto \begin{pmatrix} 0 & -1 \\ -1 & 0 \end{pmatrix}, \\
C_3' &\mapsto \begin{pmatrix} -\frac{1}{2} & -\frac{\sqrt{3}}{2} \\ \frac{\sqrt{3}}{2} & -\frac{1}{2} \end{pmatrix}, & i &\mapsto \begin{pmatrix} -1 & 0 \\ 0 & -1 \end{pmatrix}, & C_2' &\mapsto \begin{pmatrix} \frac{\sqrt{3}}{2} & \frac{1}{2} \\ \frac{1}{2} & -\frac{\sqrt{3}}{2} \end{pmatrix}, \\
\sigma_d &\mapsto \begin{pmatrix} 0 & 1 \\ 1 & 0 \end{pmatrix}, & S_6 &\mapsto \begin{pmatrix} \frac{1}{2} & -\frac{\sqrt{3}}{2} \\ \frac{\sqrt{3}}{2} & \frac{1}{2} \end{pmatrix}, & C_2'' &\mapsto \begin{pmatrix} -\frac{\sqrt{3}}{2} & \frac{1}{2} \\ \frac{1}{2} & \frac{\sqrt{3}}{2} \end{pmatrix}
\end{aligned}
\tag{C.36}
$$

for i equal to the negative identity matrix. We omit the proof of irreducibility.

Having found all irreducible representations ρ of the group D_{3d}, we can set up its character table. It is shown in Table C.2, with the columns corresponding to the conjugacy classes and the rows to the irreducible representations. The irreducible representations are labeled with the symbols introduced by Mulliken (1933): A indicates a one-dimensional representation ($\chi_\rho(E) = 1$) that is even with respect to rotation around the principal axis ($\chi_\rho(C_3) = 1$) and E (german *entartet*) a two-dimensional representation ($\chi_\rho(E) = 2$). An index 1 or 2 signifies $\chi_\rho(C_2) = 1$ and $\chi_\rho(C_2) = -1$, respectively. g and u indicate whether the representation is even (german *gerade*) or odd (german *ungerade*) with respect to inversion, i.e. if $\chi_\rho(i) = \chi_\rho(E)$ or $\chi_\rho(i) = -\chi_\rho(E)$, respectively.

To understand what "even" and "odd" means in the Mulliken notation, one has to consider quantum mechanical wave functions. The outstanding importance of group

D_{3d}	E	$2C_3$	$3C_2'$	i	$2S_6$	$3\sigma_d$
A_{1g}	1	1	1	1	1	1
A_{2g}	1	1	−1	1	1	−1
E_g	2	−1	0	2	−1	0
A_{1u}	1	1	1	−1	−1	−1
A_{2u}	1	1	−1	−1	−1	1
E_u	2	−1	0	−2	1	0

Table C.2. Character table of D_{3d}. The columns correspond to the conjugacy classes and the rows to the irreducible representations of the group, labeled with their Mulliken symbols.

theory for quantum physics was first recognized by Wigner and is extensively discussed in his famous book (Wigner, 1959). Here, we are only interested in the degeneracy[3] of the eigenvalues of the Hamiltonian (C.28). Due to (C.26), the elements R of the symmetry group D_{3d} can be interpreted as linear operators O_R acting on the wave function $\psi(r_1, r_2, r_3)$. Using the matrices (C.29), it can be easily shown that these operators are unitary ($O_R^{-1} = O_R^\dagger = O_R^{\top,*}$), so they conserve the norm of ψ. Most importantly, since H is invariant under all R, the operators O_R and H commute. Therefore, if $\psi_n(r_1, r_2, r_3)$ is a normalized eigenfunction of H with eigenvalue E_n, $O_R\psi_n(r_1, r_2, r_3)$ also is an eigenfunction of H with the same eigenvalue. Now one has to distinguish two cases (Vvedensky, 2001).

- If E_n is nondegenerate, $O_R\psi_n$ must be a constant multiple of ψ_n since ψ_n is the only eigenfunction belonging to E_n. Due to the unitarity of O_R, the constant must lie on the unit circle in the complex plane, i.e.

$$O_R\psi_n = \mathrm{e}^{\mathrm{i}\varphi_R}\psi_n. \tag{C.37}$$

  By the same argument, application of an operator O_S corresponding to another symmetry element S of H gives

$$O_S(O_R\psi_n) = \mathrm{e}^{\mathrm{i}\varphi_R}O_S\psi_n = \mathrm{e}^{\mathrm{i}\varphi_R}\mathrm{e}^{\mathrm{i}\varphi_S}\psi_n. \tag{C.38}$$

  The left-hand side of this equation is equal to applying the operator corresponding to the matrix product SR to ψ_n,

$$O_S(O_R\psi_n) = (O_SO_R)\psi_n = O_{SR}\psi_n = \mathrm{e}^{\mathrm{i}\varphi_{SR}}\psi_n, \tag{C.39}$$

  so we have

$$\mathrm{e}^{\mathrm{i}\varphi_{SR}} = \mathrm{e}^{\mathrm{i}\varphi_S}\mathrm{e}^{\mathrm{i}\varphi_R}. \tag{C.40}$$

[3] An eigenvalue E_n of a Hamiltonian H is called m-fold degenerate if there are m linearly independent, orthonormal functions $\psi_{n,j}$ $(j = 1, \ldots, m)$ which are solutions of the time-independent Schrödinger equation $H\psi_{n,j} = E_n\psi_{n,j}$. Due to the linearity of this equation, any linear combination of the $\psi_{n,j}$ is also an eigenfunction of H with eigenvalue E_n.

This means that the phase factors preserve the multiplication table of the group. Since the neutral operation does not change the wave function, its phase factor must be equal to one,

$$\mathrm{e}^{\mathrm{i}\varphi_E} = 1. \tag{C.41}$$

Moreover, the elements $\{\sigma_d, \sigma_d', \sigma_d'', i, C_2, C_2', C_2''\}$ are self-inverse, i.e. $R^2 = E$ or

$$\left(\mathrm{e}^{\mathrm{i}\varphi_R}\right)^2 = \mathrm{e}^{\mathrm{i}\varphi_E} = 1 \Rightarrow \mathrm{e}^{\mathrm{i}\varphi_R} \in \{-1, 1\}. \tag{C.42}$$

The phase factors of the other elements $\{C_3, C_3', S_6', S_6''\}$ must also be from this set or the group multiplication (C.40) will not be well-defined. Therefore, we have

$$O_R\psi_n = \pm\psi_n, \tag{C.43}$$

for all $R \in D_{3d}$, i.e. the eigenfunction ψ_n is either even (eigenvalue $+1$) or odd (eigenvalue -1) with respect to R. Due to the multiplication table of the group, only the four combinations of 1 and -1 given in the character table are possible. The map $\rho : D_{3d} \to \mathbb{R}\setminus\{0\}$, $R \mapsto \langle\psi_n|O_R|\psi_n\rangle$ is a one-dimensional (and therefore irreducible) representation of D_{3d}. Since $\langle\psi_n|O_R|\psi_n\rangle$ is a matrix element, one says that ψ_n is a *basis function* for the irreducible representation ρ. As stated above, the characters χ_ρ determine the *symmetry type* of the wave function ψ_n which is compactly written in the Mulliken notation. For example, if we have

$$O_E\psi_n = O_{C_3}\psi_n = O_{C_3'}\psi_n = O_{C_2}\psi_n = O_{C_2'}\psi_n = O_{C_2''}\psi_n = \psi_n, \tag{C.44a}$$
$$O_i\psi_n = O_{S_6}\psi_n = O_{S_6'}\psi_n = O_{\sigma_d}\psi_n = O_{\sigma_d'}\psi_n = O_{\sigma_d''}\psi_n = -\psi_n, \tag{C.44b}$$

we say that ψ_n *transforms like* A_{1u}.

- If E_n is m-fold degenerate, $O_R\psi_{n,j}$ (j fixed) will be a linear combination of all $\psi_{n,j}$ ($j = 1, \ldots, m$). This can be written as

$$O_R \begin{pmatrix} \psi_{n,1} \\ \vdots \\ \psi_{n,m} \end{pmatrix} = A_n(R) \begin{pmatrix} \psi_{n,1} \\ \vdots \\ \psi_{n,m} \end{pmatrix} \tag{C.45}$$

where $A_n(R)$ is an $m\times m$ matrix with elements $a_{jk} = \langle\psi_{n,j}|O_R|\psi_{n,k}\rangle$. $A_n(R)$ must be invertible since each symmetry element R has an inverse R^{-1} which undoes the action of R on the wave function. As above, application of a second operator O_S to $\psi_{n,j}$ and equating coefficients yields

$$A_n(RS) = A_n(R)A_n(S), \tag{C.46}$$

so the map $\rho : D_{3d} \to \mathrm{GL}_m(\mathbb{R})$, $R \mapsto A_n(R)$ is an m-dimensional representation of D_{3d}. It can be shown that ρ is irreducible (Wigner, 1959), so we can only have

$m = 2$. Therefore, apart from the nondegenerate eigenvalues, there are doubly degenerate ones whose eigenfunctions transform like E_g and E_u. However, the characters of these irreducible representations are not equal to the eigenvalues of $\psi_{n,j}$ under the operators O_R, but to the traces of the matrices $A_n(R)$.

In summary, we found that the degeneracy of an eigenvalue of (C.28) equals the dimension of the corresponding irreducible representation of the symmetry group D_{3d}. Eigenvalues associated with A_{1g}, A_{2g}, A_{1u} or A_{2u} are nondegenerate while eigenvalues associated with E_g or E_u are doubly degenerate.

D. Numerical methods

D.1. Operator splitting

Let $\boldsymbol{r} := (x, y, z)$ and

$$\nabla^2 := \frac{\partial^2}{\partial x^2} + \frac{\partial^2}{\partial y^2} + \frac{\partial^2}{\partial z^2}. \tag{D.1}$$

The formal solution of the three-dimensional time-dependent Schrödinger equation

$$\mathrm{i}\frac{\partial}{\partial t}\psi(\boldsymbol{r}, t) = -\frac{1}{2}\nabla^2\psi(\boldsymbol{r}, t) + V(\boldsymbol{r}, t)\psi(\boldsymbol{r}, t) = H(\boldsymbol{r}, t)\psi(\boldsymbol{r}, t) \tag{D.2}$$

can be written as

$$\psi(\boldsymbol{r}, t) = U(t, t_0)\psi(\boldsymbol{r}, t_0) \tag{D.3}$$

where $U(t, t_0)$ is the time-evolution operator that advances an initial solution $\psi(\boldsymbol{r}, t_0)$ in time from t_0 to t. For a time-independent potential V, we have

$$U(t, t_0) = \mathrm{e}^{-\mathrm{i}H(\boldsymbol{r})(t-t_0)}. \tag{D.4}$$

The time-evolution operator can be expressed in terms of exponentials even if V is time-dependent. To do this, we divide the interval $[t_0, t]$ into n intervals of length $\Delta t = (t - t_0)/n$. If n is large enough, the potential is approximately constant on the intervals $[t_j, t_j + \Delta t]$ (where $t_j = t_0 + j\Delta t$, $j = 0, \ldots, n-1$) and we can write $U(t, t_0)$ as a product of infinitesimal time-evolution operators (Grossmann, 2008)

$$U(t_j + \Delta t, t_j) = \mathrm{e}^{-\mathrm{i}H(\boldsymbol{r}, t_j)\Delta t} \tag{D.5}$$

which are also referred to as short-time propagators (Heather and Metiu, 1987). In the limit $n \to \infty$, the approximation becomes exact and we arrive at the formula

$$U(t, t_0) = \lim_{n\to\infty} \mathrm{e}^{-\mathrm{i}H(\boldsymbol{r}, t_{n-1})\Delta t}\mathrm{e}^{-\mathrm{i}H(\boldsymbol{r}, t_{n-2})\Delta t} \cdots \mathrm{e}^{-\mathrm{i}H(\boldsymbol{r}, t_1)\Delta t}\mathrm{e}^{-\mathrm{i}H(\boldsymbol{r}, t_0)\Delta t}. \tag{D.6}$$

In a numerical treatment of the Schrödinger equation, n is necessarily finite, but the product (D.6) still represents a good approximation if Δt is small. In position space, the kinetic part of $U(t_j + \Delta t, t_j)$ involves calculating the second derivative of the wave function whereas it only corresponds to a multiplication with a phase factor in momentum space. In order to switch between the appropriate representations of the wave

function via a Fourier transform, we split (D.5) into kinetic and potential operators. The simplest way to do this is the Trotter product (Grossmann, 2008) where the evolution of a wave function by a small time increment Δt is written as

$$\psi(\boldsymbol{r}, t+\Delta t) = U(t+\Delta t, t)\psi(\boldsymbol{r}, t) = \mathrm{e}^{\mathrm{i}\nabla^2 \Delta t/2}\mathrm{e}^{-\mathrm{i}V(\boldsymbol{r},t)\Delta t}\psi(\boldsymbol{r}, t) + \mathcal{O}((\Delta t)^2). \tag{D.7}$$

The symmetric splitting (Feit *et al.*, 1982)

$$\psi(\boldsymbol{r}, t+\Delta t) = \underbrace{\mathrm{e}^{-\mathrm{i}V(\boldsymbol{r},t)\Delta t/2}\mathrm{e}^{\mathrm{i}\nabla^2 \Delta t/2}\mathrm{e}^{-\mathrm{i}V(\boldsymbol{r},t)\Delta t/2}}_{=:U_{SO}(t+\Delta t,t)}\psi(\boldsymbol{r}, t) + \mathcal{O}((\Delta t)^3). \tag{D.8}$$

is superior with respect to accuracy and therefore more popular. By repeatedly applying the operator U_{SO}, the wave function may be evolved for any desired time interval. Moreover, U_{SO} is unitary, so the norm of the wave function is conserved and the method is unconditionally stable (Hermann and Fleck, 1988). Finally, we note that operator splitting is not limited to three spatial dimensions since $U(t, t_0)$ is only split with respect to time.

For a practical application of the operator splitting method, we represent the wave function in position space on a grid with N equally spaced points in each coordinate. The length L and spacing $\Delta x = L/N$ of the position grid determine the spacing and length of the momentum grid as $\Delta p = 2\pi/L$ and $L_p = 2\pi/\Delta x$, respectively. With the positions

$$x = -\frac{L}{2} + j_1 \Delta x, \tag{D.9a}$$

$$y = -\frac{L}{2} + j_2 \Delta x, \tag{D.9b}$$

$$z = -\frac{L}{2} + j_3 \Delta x \tag{D.9c}$$

and the momenta

$$p_x = -\frac{L_p}{2} + k_1 \Delta p, \tag{D.10a}$$

$$p_y = -\frac{L_p}{2} + k_2 \Delta p, \tag{D.10b}$$

$$p_z = -\frac{L_p}{2} + k_3 \Delta p, \tag{D.10c}$$

where $j_i, k_i = 0, \ldots, N-1$, the momentum-space wave function $\widehat{\psi}(p_x, p_y, p_z) =: \widehat{\psi}_{k_1,k_2,k_3}$ is given by the discrete three-dimensional Fourier transform of the position-space wave function $\psi(x, y, z) =: \psi_{j_1,j_2,j_3}$,

$$\widehat{\psi}_{k_1,k_2,k_3} = \sum_{j_1,j_2,j_3=0}^{N-1} \psi_{j_1,j_2,j_3}\mathrm{e}^{-2\pi\mathrm{i}(j_1k_1+j_2k_2+j_3k_3)/N}. \tag{D.11}$$

The backwards transform reads

$$\psi_{j_1,j_2,j_3} = \frac{1}{N^3} \sum_{k_1,k_2,k_3=0}^{N-1} \widehat{\psi}_{k_1,k_2,k_3} \mathrm{e}^{2\pi\mathrm{i}(j_1k_1+j_2k_2+j_3k_3)/N}. \tag{D.12}$$

Note that the choice of the positions (D.9) and momenta (D.10) is slightly asymmetric since neither the wave function value at $x = L/2$ nor the one at $p_x = L_p/2$ is included (the same is true for the other coordinates). However, by definition of the Fourier transform, one has $\psi_{N,j_2,j_3} = \psi_{0,j_2,j_3}$ and $\widehat{\psi}_{N,k_2,k_3} = \widehat{\psi}_{0,k_2,k_3}$, i.e.

$$\psi(-L/2 + N\Delta x, y, z) = \psi(L/2, y, z) = \psi(-L/2, y, z), \tag{D.13a}$$

$$\widehat{\psi}(-L_p/2 + N\Delta p, p_y, p_z) = \widehat{\psi}(L_p/2, p_y, p_z) = \widehat{\psi}(-L_p/2, p_y, p_z). \tag{D.13b}$$

Both (D.11) and (D.12) can be efficiently computed with Fast Fourier transform (FFT) algorithms, e.g. with the popular FFTW software library of Frigo and Johnson (2005). Furthermore, if Δx is chosen small enough so that the wave function is negligible on the grid boundaries of momentum space, the Whittaker-Kotel'nikov-Shannon sampling theorem (Kosloff, 1988) states that the discrete Fourier transform equals the continuous Fourier transform at the discrete grid points (D.9) and (D.10), so performing Fourier transforms in (D.8) does not increase the numerical error. Moreover, the value of Δx which is necessary for an accurate evaluation of the kinetic part in (D.5) is typically much larger than in finite-difference methods.

There are many other methods to solve the time-dependent Schrödinger equation, such as the Crank-Nicolson scheme and finite basis-set techniques. An overview can be found in the book of Grossmann (2008).

D.2. Parallelization with MPI

In the operator splitting method, the time evolution of the wave function is local in position as well as in momentum space, i.e. the wave function at each grid point is multiplied by a phase factor which does not depend on the value of the wave function at other grid points. This allows for an efficient parallelization using the Message Passing Interface (MPI) standard: Instead of evolving the full grid with $N \times N \times N$ points on a single processor, k chunks with $(N/k) \times N \times N$ points are stored on k processors and the evolution of these local grids is performed in parallel. However, for the Fourier transforms, the processors have to exchange data twice per time step. Depending on the quantities that are calculated from the wave function, additional communication operations may be necessary. For a fast calculation, the task is therefore to minimize the amount of communication.

One way to achieve this is to exploit the symmetries of the system. For example, consider the Eckhardt-Sacha Hamiltonian (2.7) with wave function $\psi(\boldsymbol{r}, t) = \psi(r_1, r_2, r_3, t)$ which is distributed on the processors along the r_1-axis. The determination of ion yields

involves the evaluation of surface integrals over the probability current

$$\boldsymbol{j}(\boldsymbol{r},t) = \begin{pmatrix} j_1(\boldsymbol{r},t) \\ j_2(\boldsymbol{r},t) \\ j_3(\boldsymbol{r},t) \end{pmatrix} = \mathrm{Im} \begin{pmatrix} \psi^*(\boldsymbol{r},t)\frac{\partial}{\partial r_1}\psi(\boldsymbol{r},t) \\ \psi^*(\boldsymbol{r},t)\frac{\partial}{\partial r_2}\psi(\boldsymbol{r},t) \\ \psi^*(\boldsymbol{r},t)\frac{\partial}{\partial r_3}\psi(\boldsymbol{r},t) \end{pmatrix} \tag{D.14}$$

which is nonlocal in position space since it contains derivatives. If we approximate them with simple second-order finite differences,

$$\frac{\partial}{\partial r_1}\psi(r_1,r_2,r_3,t) = \frac{\psi(r_1+\Delta r,r_2,r_3,t)-\psi(r_1-\Delta r,r_2,r_3,t)}{2\Delta r} + \mathcal{O}((\Delta r)^2), \tag{D.15}$$

the calculation of j_1 on the boundaries of the local grids requires that the processors exchange the values of the wave function there. In addition, for the integration of $\boldsymbol{j}$ over any plane which is not perpendicular to the r_1-axis, all contributions have to be collected on one processor. These communications can be eliminated by noticing that the Hamiltonian (2.7) is invariant under permutation of the coordinates r_1, r_2 and r_3. As a result, the probability current is also invariant and the surface integral reduces to

$$\begin{aligned} \iint\limits_{\partial R} \boldsymbol{j}\cdot\mathrm{d}\boldsymbol{A} &= \iint_{\partial R\perp r_1} j_1 \mathrm{d}r_2\mathrm{d}r_3 + \iint_{\partial R\perp r_2} j_2 \mathrm{d}r_1\mathrm{d}r_3 + \iint_{\partial R\perp r_3} j_3 \mathrm{d}r_1\mathrm{d}r_2 \\ &= 3\iint_{\partial R\perp r_3} j_3 \mathrm{d}r_1\mathrm{d}r_2. \end{aligned} \tag{D.16}$$

Therefore, each processor can just calculate the integral over j_3 (which is completely local) and take it times three.

Another symmetry-based simplification can be made in the three-dimensional Fourier transform routine of the FFTW package (Frigo and Johnson, 2005) which works as follows. The position-space wave function is first Fourier transformed with respect to the coordinates r_2 and r_3. Afterwards, a global transposition is performed so that the nonlocal coordinate r_1 becomes local. Finally, after the wave function has been Fourier transformed with respect to r_1, it is transposed back. Together with the backward transform, this amounts to four global transpositions of the wave function per time step which, given the typical size of the wave functions ($\approx$ 60 GB), is a very time-consuming communication operation. However, due to the invariance of the phase factor in momentum space with respect to permutation of the momenta p_1, p_2 and p_3, the second (first) transposition can be omitted in the forward (backward) transform.

Bibliography

Alnaser, A. S., Comtois, D., Hasan, A. T., Villeneuve, D. M., Kieffer, J.-C., and Litvinyuk, I. V. *Strong-field non-sequential double ionization: wavelength dependence of ion momentum distributions for neon and argon.* J. Phys. B: At. Mol. Opt. Phys. **41**, 031001 (2008).

Alnaser, A. S., Maharjan, C. M., Wang, P., and Litvinyuk, I. V. *Multi-photon resonant effects in strong-field ionization: origin of the dip in experimental longitudinal momentum distributions.* J. Phys. B: At. Mol. Opt. Phys. **39**, L323 (2006).

Ammosov, M. V., Delone, N. B., and Krainov, V. P. *Tunnel ionization of complex atoms and of atomic ions in an alternating electromagnetic field.* Sov. Phys. JETP **64**, 1191 (1986).

Amusia, M., Krivec, R., and Mandelzweig, V. *Two-electron photoionization cross sections at high energies.* In *Few-Body Problems in Physics '02* (edited by R. Krivec, M. Rosina, B. Golli, and S. Širca), volume 14 of *Few-Body Systems*, 147–152 (Springer Vienna, 2003).

Augst, S., Meyerhofer, D. D., Strickland, D., and Chin, S. L. *Laser ionization of noble gases by Coulomb-barrier suppression.* J. Opt. Soc. Am. B **8**, 858 (1991).

Augst, S., Strickland, D., Meyerhofer, D. D., Chin, S. L., and Eberly, J. H. *Tunneling ionization of noble gases in a high-intensity laser field.* Phys. Rev. Lett. **63**, 2212 (1989).

Augst, S., Talebpour, A., Chin, S. L., Beaudoin, Y., and Chaker, M. *Nonsequential triple ionization of argon atoms in a high-intensity laser field.* Phys. Rev. A **52**, R917 (1995).

Auguste, T., Monot, P., Lompré, L. A., Mainfray, G., and Manus, C. *Multiply charged ions produced in noble gases by a 1 ps laser pulse at* $\lambda = 1053$ *nm.* J. Phys. B: At. Mol. Opt. Phys. **25**, 4181 (1992).

Baier, S., Ruiz, C., Plaja, L., and Becker, A. *Nonsequential double ionization of the hydrogen molecule in a few-cycle laser pulse.* Phys. Rev. A **74**, 033405 (2006).

Bannow, L. C. *Quantum calculations of multiple ionization in diatomic molecules.* Masterarbeit, Philipps-Universität Marburg (2013).

Bauer, D. *Two-dimensional, two-electron model atom in a laser pulse: Exact treatment, single-active-electron analysis, time-dependent density-functional theory, classical calculations, and nonsequential ionization.* Phys. Rev. A **56**, 3028 (1997).

Bauer, D. and Mulser, P. *Exact field ionization rates in the barrier-suppression regime from numerical time-dependent Schrödinger-equation calculations.* Phys. Rev. A **59**, 569 (1999).

Bebb, H. B. and Gold, A. *Multiphoton ionization of hydrogen and rare-gas atoms.* Phys. Rev. **143**, 1 (1966).

Becker, A. and Faisal, F. H. M. *S-matrix analysis of ionization yields of noble gas atoms at the focus of Ti:sapphire laser pulses.* J. Phys. B: At. Mol. Opt. Phys. **32**, L335 (1999).

Becker, W., Liu, X., Ho, P. J., and Eberly, J. H. *Theories of photoelectron correlation in laser-driven multiple atomic ionization.* Rev. Mod. Phys. **84**, 1011 (2012).

Beran, L. *A classical analysis of double ionization of helium in ultrashort laser pulses.* Ph.D. thesis, Philipps-Universität Marburg (2014).

Bergues, B., Kübel, M., Johnson, N. G., Fischer, B., Camus, N., Betsch, K. J., Herrwerth, O., Senftleben, A., Sayler, A. M., Rathje, T., Pfeifer, T., Ben-Itzhak, I., Jones, R. R., Paulus, G. G., Krausz, F., Moshammer, R., Ullrich, J., and Kling, M. F. *Attosecond tracing of correlated electron-emission in non-sequential double ionization.* Nat. Commun. **43**, 813 (2012).

Bhardwaj, V. R., Aseyev, S. A., Mehendale, M., Yudin, G. L., Villeneuve, D. M., Rayner, D. M., Ivanov, M. Y., and *Few cycle dynamics of multiphoton double ionization.* Phys. Rev. Lett. **86**, 3522 (2001).

de Bohan, A., Piraux, B., Ponce, L., Taïeb, R., Véniard, V., and Maquet, A. *Direct and indirect pathways in strong field atomic ionization dynamics.* Phys. Rev. Lett. **89**, 113002 (2002).

Bouri, C., Malegat, L., Selles, P., and Njock, M. G. K. *Numerical test of the Wannier threshold law for double photoionization of helium.* J. Phys. B: At. Mol. Opt. Phys. **40**, F51 (2007).

Brabec, T., Ivanov, M. Y., and Corkum, P. B. *Coulomb focusing in intense field atomic processes.* Phys. Rev. A **54**, R2551 (1996).

Brabec, T. and Krausz, F. *Intense few-cycle laser fields: Frontiers of nonlinear optics.* Rev. Mod. Phys. **72**, 545 (2000).

Bronstein, I. N., Semendjajew, K. A., Musiol, G., and Mühlig, H. *Taschenbuch der Mathematik* (Harri Deutsch, 2005), 6th edition.

Campi, F., Coudert-Alteirac, H., Miranda, M., Rading, L., Manschwetus, B., Rudawski, P., L'Huillier, A., and Johnsson, P. *Design and test of a broadband split-and-delay unit for attosecond XUV-XUV pump-probe experiments.* Rev. Sci. Instrum. **87**, 023106 (2016).

Camus, N., Fischer, B., Kremer, M., Sharma, V., Rudenko, A., Bergues, B., Kübel, M., Johnson, N. G., Kling, M. F., Pfeifer, T., Ullrich, J., and Moshammer, R. *Attosecond correlated dynamics of two electrons passing through a transition state.* Phys. Rev. Lett. **108**, 073003 (2012).

Cervenan, M. and Isenor, N. *Multiphoton ionization yield curves for Gaussian laser beams.* Opt. Comm. **13**, 175 (1975).

Chaloupka, J. L., Rudati, J., Lafon, R., Agostini, P., Kulander, K. C., and DiMauro, L. F. *Observation of a transition in the dynamics of strong-field double ionization.* Phys. Rev. Lett. **90**, 033002 (2003).

Chen, H. *Excursions in Classical Analysis.* Classroom Resource Materials (Mathematical Association of America, 2010).

Chen, S., Ruiz, C., and Becker, A. *Double ionization of helium by intense near-infrared and VUV laser pulses.* Phys. Rev. A **82**, 033426 (2010).

Chin, S. L. *From multiphoton to tunnel ionization.* In *Advances In Multi-Photon Processes And Spectroscopy*, 249–271 (World Scientific, 2004).

Chin, S. L. and Isenor, N. R. *Multiphoton ionization in atomic gases with depletion of neutral atoms.* Can. J. Phys. **48**, 1445 (1970).

Chin, S. L., Yergeau, F., and Lavigne, P. *Tunnel ionisation of Xe in an ultra-intense CO_2 laser field (10^{14} W cm^{-2}) with multiple charge creation.* J. Phys. B: At. Mol. Phys. **18**, L213 (1985).

Chowdhury, E. A. and Walker, B. C. *Multielectron ionization processes in ultrastrong laser fields.* J. Opt. Soc. Am. B **20**, 109 (2003).

Collins, P., Ezra, G. S., and Wiggins, S. *Index k saddles and dividing surfaces in phase space with applications to isomerization dynamics.* J. Chem. Phys. **134**, 244105 (2011).

Corkum, P. B. *Plasma perspective on strong field multiphoton ionization.* Phys. Rev. Lett. **71**, 1994 (1993).

Corkum, P. B., Burnett, N. H., and Brunel, F. *Above-threshold ionization in the long-wavelength limit.* Phys. Rev. Lett. **62**, 1259 (1989).

Corkum, P. B. and Krausz, F. *Attosecond science.* Nat. Phys. **3**, 381 (2007).

Cornaggia, C. and Hering, P. *Laser-induced non-sequential double ionization of small molecules.* J. Phys. B: At. Mol. Opt. Phys. **31**, L503 (1998).

Corso, P. P., Lappas, D. G., and Knight, P. L. *Time-dependent effects in the nonsequential ionization of helium at various wavelengths.* Laser and Particle Beams **18**, 433 (2000).

Cvejanovic, S. and Read, F. H. *Studies of the threshold electron impact ionization of helium.* J. Phys. B: At. Mol. Phys. **7**, 1841 (1974).

Davis, P. J. *Circulant matrices* (Wiley New York, 1979).

Delone, N. B. and Krainov, V. P. *Energy and angular electron spectra for the tunnel ionization of atoms by strong low-frequency radiation.* J. Opt. Soc. Am. B **8**, 1207 (1991).

Delone, N. B. and Krainov, V. P. *Tunneling and barrier-suppression ionization of atoms and ions in a laser radiation field.* Phys.-Usp. **41**, 469 (1998).

Delone, N. B. and Krainov, V. P. *AC stark shift of atomic energy levels.* Phys.-Usp. **42**, 669 (1999).

DiChiara, A. D., Sistrunk, E., Blaga, C. I., Szafruga, U. B., Agostini, P., and DiMauro, L. F. *Inelastic scattering of broadband electron wave packets driven by an intense midinfrared laser field.* Phys. Rev. Lett. **108**, 033002 (2012).

Dietrich, P., Burnett, N. H., Ivanov, M., and Corkum, P. B. *High-harmonic generation and correlated two-electron multiphoton ionization with elliptically polarized light.* Phys. Rev. A **50**, R3585 (1994).

DiMauro, L., Frolov, M., Ishikawa, K. L., and Ivanov, M. *50 years of optical tunneling.* J. Phys. B: At. Mol. Opt. Phys. **47**, 200301 (2014).

Dimitrijević, M., Grujić, P., and Simonović, N. *Fourfold ionization by electrons near the threshold.* Z. Phys. D: At. Mol. Clust. **15**, 203 (1990).

Dong, S., Chen, X., Zhang, J., and Ren, X. *Pulse-duration effect in nonsequential double ionization of Ar atoms.* Phys. Rev. A **93**, 053410 (2016).

Dörner, R., Weber, T., Weckenbrock, M., Staudte, A., Hattass, M., Moshammer, R., Ullrich, J., and Schmidt-Böcking, H. *Multiple ionization in strong laser fields.* volume 48 of *Advances in Atomic and Molecular Physics*, 1–36 (Academic Press, 2002).

Dundas, D., Taylor, K. T., Parker, J. S., and Smyth, E. S. *Double-ionization dynamics of laser-driven helium.* J. Phys. B: At. Mol. Opt. Phys. **32**, L231 (1999).

Eberly, J. H. *Scale variation in a one-dimensional model of an atom interacting with a strong laser field.* Phys. Rev. A **42**, 5750 (1990).

Eckhardt, B., Prauzner-Bechcicki, J. S., Sacha, K., and Zakrzewski, J. *Suppression of correlated electron escape in double ionization in strong laser fields.* Phys. Rev. A **77**, 015402 (2008).

Eckhardt, B., Prauzner-Bechcicki, J. S., Sacha, K., and Zakrzewski, J. *Phase effects in double ionization by strong short pulses.* Chem. Phys. **370**, 168 (2010).

Eckhardt, B. and Sacha, K. *Wannier threshold law for two-electron escape in the presence of an external electric field.* Europhys. Lett. **56**, 651 (2001).

Eckhardt, B. and Sacha, K. *Classical threshold behaviour in a (1+1)-dimensional model for double ionization in strong fields.* J. Phys. B: At. Mol. Opt. Phys. **39**, 3865 (2006).

Eichmann, U., Dörr, M., Maeda, H., Becker, W., and Sandner, W. *Collective multi-electron tunneling ionization in strong fields.* Phys. Rev. Lett. **84**, 3550 (2000).

Einstein, A. *Über einen die Erzeugung und Verwandlung des Lichtes betreffenden heuristischen Gesichtspunkt.* Ann. Phys. **322**, 132 (1905).

Einstein, A. *Zur Quantentheorie der Strahlung.* Physik. Z. **18**, 121 (1917).

Ekanayake, N., Luo, S., Wen, B. L., Howard, L. E., Wells, S. J., Videtto, M., Mancuso, C., Stanev, T., Condon, Z., LeMar, S., Camilo, A. D., Toth, R., Crosby, W. B., Grugan, P. D., Decamp, M. F., and Walker, B. C. *Rescattering nonsequential ionization of Ne^{3+}, Ne^{4+}, Ne^{5+}, Kr^{5+}, Kr^{6+}, Kr^{7+}, and Kr^{8+} in a strong, ultraviolet, ultrashort laser pulse.* Phys. Rev. A **86**, 043402 (2012).

Emmanouilidou, A. and Rost, J. M. *Triple photoionization of lithium near threshold.* J. Phys. B: At. Mol. Opt. Phys. **39**, L99 (2006).

Eremina, E., Liu, X., Rottke, H., Sandner, W., Dreischuh, A., Lindner, F., Grasbon, F., Paulus, G. G., Walther, H., Moshammer, R., Feuerstein, B., and Ullrich, J. *Laser-induced non-sequential double ionization investigated at and below the threshold for electron impact ionization.* J. Phys. B: At. Mol. Opt. Phys. **36**, 3269 (2003).

Feit, M. D., Fleck, Jr., J. A., and Steiger, A. *Solution of the Schrödinger equation by a spectral method.* J. Comput. Phys. **47**, 412 (1982).

Feuerstein, B., Moshammer, R., Fischer, D., Dorn, A., Schröter, C. D., Deipenwisch, J., Crespo Lopez-Urrutia, J. R., Höhr, C., Neumayer, P., Ullrich, J., Rottke, H., Trump, C., Wittmann, M., Korn, G., and Sandner, W. *Separation of recollision mechanisms in nonsequential strong field double ionization of Ar: The role of excitation tunneling.* Phys. Rev. Lett. **87**, 043003 (2001).

Feuerstein, B., Moshammer, R., and Ullrich, J. *Nonsequential multiple ionization in intense laser pulses: interpretation of ion momentum distributions within the classical 'rescattering' model.* J. Phys. B: At. Mol. Opt. Phys. **33**, L823 (2000).

Fittinghoff, D. N., Bolton, P. R., Chang, B., and Kulander, K. C. *Observation of nonsequential double ionization of helium with optical tunneling.* Phys. Rev. Lett. **69**, 2642 (1992).

Freitag, S. *Phase space analysis and threshold behaviour of a model for triple ionization in strong static fields.* Diplomarbeit, Philipps-Universität Marburg (2014).

Friedrich, H. *Theoretical atomic physics* (Springer Berlin Heidelberg, 2006), 3rd edition.

Frigo, M. and Johnson, S. G. *The design and implementation of FFTW3.* Proc. IEEE **93**, 216. Special issue on "Program Generation, Optimization, and Platform Adaptation" (2005).

Gallagher, T. F. *Above-threshold ionization in low-frequency limit.* Phys. Rev. Lett. **61**, 2304 (1988).

Geltman, S. *Strong-field ionization of helium in the independent-electron model.* Phys. Rev. A **52**, 2468 (1995).

Göppert-Mayer, M. *Über Elementarakte mit zwei Quantensprüngen.* Ann. Phys., Lpz. **401**, 273 (1931).

Goulielmakis, E., Schultze, M., Hofstetter, M., Yakovlev, V. S., Gagnon, J., Uiberacker, M., Aquila, A. L., Gullikson, E. M., Attwood, D. T., Kienberger, R., Krausz, F., and Kleineberg, U. *Single-cycle nonlinear optics.* Science **320**, 1614 (2008).

Grobe, R. and Eberly, J. H. *Photoelectron spectra for a two-electron system in a strong laser field.* Phys. Rev. Lett. **68**, 2905 (1992).

Grobe, R. and Eberly, J. H. *One-dimensional model of a negative ion and its interaction with laser fields.* Phys. Rev. A **48**, 4664 (1993).

Grobe, R., Haan, S., and Eberly, J. *A split-domain algorithm for time-dependent multi-electron wave functions.* Comp. Phys. Comm. **117**, 200 (1999).

Grossmann, F. *Theoretical femtosecond physics*, volume 48 of *Springer Series on Atomic, Optical and Plasma Physics* (Springer Berlin Heidelberg, 2008).

Grujić, P. *The fourfold escape threshold law.* Phys. Lett. A **96**, 233 (1983).

Guo, C., Li, M., Nibarger, J. P., and Gibson, G. N. *Single and double ionization of diatomic molecules in strong laser fields.* Phys. Rev. A **58**, R4271 (1998).

Guo, J. and Liu, X.-s. *Lithium ionization by an intense laser field using classical ensemble simulation.* Phys. Rev. A **78**, 013401 (2008).

Guo, L., Han, S. S., Liu, X., Cheng, Y., Xu, Z. Z., Fan, J., Chen, J., Chen, S. G., Becker, W., Blaga, C. I., DiChiara, A. D., Sistrunk, E., Agostini, P., and DiMauro, L. F. *Scaling of the low-energy structure in above-threshold ionization in the tunneling regime: Theory and experiment.* Phys. Rev. Lett. **110**, 013001 (2013).

Hall, R. L., Saad, N., Sen, K. D., and Ciftci, H. *Energies and wave functions for a soft-core Coulomb potential.* Phys. Rev. A **80**, 032507 (2009).

Haller, G., Uzer, T., Palacián, J., Yanguas, P., and Jaffé, C. *Transition state geometry near higher-rank saddles in phase space.* Nonlinearity **24**, 527 (2011).

Heather, R. and Metiu, H. *An efficient procedure for calculating the evolution of the wave function by fast Fourier transform methods for systems with spatially extended wave function and localized potential.* J. Chem. Phys. **86**, 5009 (1987).

Henrichs, K., Waitz, M., Trinter, F., Kim, H., Menssen, A., Gassert, H., Sann, H., Jahnke, T., Wu, J., Pitzer, M., Richter, M., Schöffler, M. S., Kunitski, M., and Dörner, R. *Observation of electron energy discretization in strong field double ionization.* Phys. Rev. Lett. **111**, 113003 (2013).

Hentschel, M., Kienberger, R., Spielmann, C., Reider, G. A., Milosevic, N., Brabec, T., Corkum, P., Heinzmann, U., Drescher, M., and Krausz, F. *Attosecond metrology.* Nature **414**, 509 (2001).

Hermann, M. R. and Fleck, Jr., J. A. *Split-operator spectral method for solving the time-dependent Schrödinger equation in spherical coordinates.* Phys. Rev. A **38**, 6000 (1988).

Ho, P. J. and Eberly, J. H. *Classical effects of laser pulse duration on strong-field double ionization.* Phys. Rev. Lett. **95**, 193002 (2005).

Ho, P. J. and Eberly, J. H. *In-plane theory of nonsequential triple ionization.* Phys. Rev. Lett. **97**, 083001 (2006).

Ho, P. J. and Eberly, J. H. *Argon-like three-electron trajectories in intense-field double and triple ionization.* Opt. Express **15**, 1845 (2007).

Ilkov, F. A., Decker, J. E., and Chin, S. L. *Ionization of atoms in the tunnelling regime with experimental evidence using Hg atoms.* J. Phys. B: At. Mol. Opt. Phys. **25**, 4005 (1992).

Javanainen, J., Eberly, J. H., and Su, Q. *Numerical simulations of multiphoton ionization and above-threshold electron spectra.* Phys. Rev. A **38**, 3430 (1988).

de Jesus, V. L. B., Feuerstein, B., Zrost, K., Fischer, D., Rudenko, A., Afaneh, F., Schröter, C. D., Moshammer, R., and Ullrich, J. *Atomic structure dependence of nonsequential double ionization of He, Ne and Ar in strong laser pulses.* J. Phys. B: At. Mol. Opt. Phys. **37**, L161 (2004).

Kamta, G. L. and Starace, A. F. *Multielectron system in an ultrashort, intense laser field: A nonperturbative, time-dependent two-active-electron approach.* Phys. Rev. A **65**, 053418 (2002).

Kästner, A., Saalmann, U., and Rost, J. M. *Electron-energy bunching in laser-driven soft recollisions.* Phys. Rev. Lett. **108**, 033201 (2012a).

Kästner, A., Saalmann, U., and Rost, J. M. *Energy bunching in soft recollisions revealed with long-wavelength few-cycle pulses.* J. Phys. B: At. Mol. Opt. Phys. **45**, 074011 (2012b).

Keldysh, L. V. *Ionization in the field of a strong electromagnetic wave.* Sov. Phys. JETP **20**, 1307 (1965).

Klar, H. and Schlecht, W. *Threshold multiple ionization of atoms. Energy dependence for double and triple escape.* J. Phys. B: At. Mol. Phys. **9**, 1699 (1976).

Kondo, K., Sagisaka, A., Tamida, T., Nabekawa, Y., and Watanabe, S. *Wavelength dependence of nonsequential double ionization in He.* Phys. Rev. A **48**, R2531 (1993).

Kosloff, R. *Time-dependent quantum-mechanical methods for molecular dynamics.* J. Phys. Chem. **92**, 2087 (1988).

Kossmann, H., Schmidt, V., and Andersen, T. *Test of Wannier threshold laws: Double-photoionization cross section in helium.* Phys. Rev. Lett. **60**, 1266 (1988).

Krainov, V. P. *Ionization rates and energy and angular distributions at the barrier-suppression ionization of complex atoms and atomic ions.* J. Opt. Soc. Am. B **14**, 425 (1997).

Kramida, A., Ralchenko, Y., and Reader, J. *NIST Atomic Spectra Database (Version 5.4).* National Institute of Standards and Technology, Gaithersburg, MD. `http://physics.nist.gov/asd`. Accessed: 2017-10-26 (2016).

Krause, J. L., Schafer, K. J., and Kulander, K. C. *High-order harmonic generation from atoms and ions in the high intensity regime.* Phys. Rev. Lett. **68**, 3535 (1992).

Kübel, M., Betsch, K. J., Kling, N. G., Alnaser, A. S., Schmidt, J., Kleineberg, U., Deng, Y., Ben-Itzhak, I., Paulus, G. G., Pfeifer, T., Ullrich, J., Moshammer, R., Kling, M. F., and Bergues, B. *Non-sequential double ionization of Ar: from the single- to the many-cycle regime.* New J. Phys. **16**, 033008 (2014).

Kübel, M., Burger, C., Kling, N. G., Pischke, T., Beaufore, L., Ben-Itzhak, I., Paulus, G. G., Ullrich, J., Pfeifer, T., Moshammer, R., Kling, M. F., and Bergues, B. *Complete characterization of single-cycle double ionization of argon from the nonsequential to the sequential ionization regime.* Phys. Rev. A **93**, 053422 (2016).

Kuchiev, M. Y. *Atomic antenna.* JETP Lett. **45**, 404 (1987).

Kuchiev, M. Y. and Ostrovsky, V. N. *Threshold laws for the breakup of atomic particles into several charged fragments.* Phys. Rev. A **58**, 321 (1998).

Kulander, K. C. *Time-dependent Hartree-Fock theory of multiphoton ionization: Helium.* Phys. Rev. A **36**, 2726 (1987).

Kulander, K. C. *Time-dependent theory of multiphoton ionization of xenon.* Phys. Rev. A **38**, 778 (1988).

Kulander, K. C., Cooper, J., and Schafer, K. J. *Laser-assisted inelastic rescattering during above-threshold ionization.* Phys. Rev. A **51**, 561 (1995).

Lambropoulos, P. *Topics on multiphoton processes in atoms.* volume 12 of *Advances in Atomic and Molecular Physics*, 87–164 (Academic Press, 1976).

Langhoff, P. W., Epstein, S. T., and Karplus, M. *Aspects of time-dependent perturbation theory.* Rev. Mod. Phys. **44**, 602 (1972).

Lappas, D. G. and van Leeuwen, R. *Electron correlation effects in the double ionization of He.* J. Phys. B: At. Mol. Opt. Phys. **31**, L249 (1998).

Larochelle, S., Talebpour, A., and Chin, S. L. *Non-sequential multiple ionization of rare gas atoms in a Ti:sapphire laser field.* J. Phys. B: At. Mol. Opt. Phys. **31**, 1201 (1998).

Lein, M., Gross, E. K. U., and Engel, V. *Intense-field double ionization of helium: Identifying the mechanism.* Phys. Rev. Lett. **85**, 4707 (2000).

L'Huillier, A., Lompré, L. A., Mainfray, G., and Manus, C. *Multiply charged ions formed by multiphoton absorption processes in the continuum.* Phys. Rev. Lett. **48**, 1814 (1982).

L'Huillier, A., Lompré, L. A., Mainfray, G., and Manus, C. *Laser pulse duration effects in Xe^{2+} ions induced by multiphoton absorption at 0.53 μm.* J. Phys. France **44**, 1247 (1983a).

L'Huillier, A., Lompré, L. A., Mainfray, G., and Manus, C. *Multiply charged ions induced by multiphoton absorption in rare gases at 0.53 μm.* Phys. Rev. A **27**, 2503 (1983b).

L'Huillier, A., Lompré, L. A., Mainfray, G., and Manus, C. *Multiply charged ions induced by multiphoton absorption processes in rare-gas atoms at 1.064 μm.* J. Phys. B: At. Mol. Opt. Phys. **16**, 1363 (1983c).

Li, Y., Yu, B., Tang, Q., Wang, X., Hua, D., Tong, A., Jiang, C., Ge, G., Li, Y., and Wan, J. *Transition of recollision trajectories from linear to elliptical polarization.* Opt. Express **24**, 6469 (2016).

Liu, W.-C. and Clark, C. W. *Closed-form solutions of the Schrödinger equation for a model one-dimensional hydrogen atom.* J. Phys. B: At. Mol. Opt. Phys. **25**, L517 (1992).

Liu, W.-C., Eberly, J. H., Haan, S. L., and Grobe, R. *Correlation effects in two-electron model atoms in intense laser fields.* Phys. Rev. Lett. **83**, 520 (1999).

Liu, X., Rottke, H., Eremina, E., Sandner, W., Goulielmakis, E., Keeffe, K. O., Lezius, M., Krausz, F., Lindner, F., Schätzel, M. G., Paulus, G. G., and Walther, H. *Nonsequential double ionization at the single-optical-cycle limit.* Phys. Rev. Lett. **93**, 263001 (2004).

Liu, Y., Tschuch, S., Dürr, M., Rudenko, A., Moshammer, R., Ullrich, J., Siegel, M., and Morgner, U. *Towards non-sequential double ionization of Ne and Ar using a femtosecond laser oscillator.* Opt. Express **15**, 18103 (2007).

Liu, Y., Tschuch, S., Rudenko, A., Dürr, M., Siegel, M., Morgner, U., Moshammer, R., and Ullrich, J. *Strong-field double ionization of ar below the recollision threshold.* Phys. Rev. Lett. **101**, 053001 (2008a).

Liu, Y., Tschuch, S., Rudenko, A., Dürr, M., Siegel, M., Morgner, U., Moshammer, R., and Ullrich, J. *Strong-field double ionization of Ar below the recollision threshold.* Phys. Rev. Lett. **101**, 053001 (2008b).

Liu, Y., Ye, D., Liu, J., Rudenko, A., Tschuch, S., Dürr, M., Siegel, M., Morgner, U., Gong, Q., Moshammer, R., and Ullrich, J. *Multiphoton double ionization of Ar and Ne close to threshold.* Phys. Rev. Lett. **104**, 173002 (2010).

Liu, Y., Ye, D., Liu, J., Rudenko, A., Tschuch, S., Dürr, M., Siegel, M., Morgner, U., Gong, Q., Moshammer, R., and Ullrich, J. *Electron correlation dynamics of strong-field double ionization of atoms below recollision threshold.* J. Phys.: Conf. Ser. **276**, 012004 (2011).

Loughan, A. M. *Above and below the Wannier threshold.* In *Adv. Chem. Phys.* (edited by I. Prigogine and S. A. Rice), volume 114, 311–418 (John Wiley & Sons, Inc., 2000).

Maiman, T. H. *Stimulated optical radiation in ruby.* Nature **187**, 493 (1960).

Mainfray, G. and Manus, G. *Multiphoton ionization of atoms.* Rep. Prog. Phys. **54**, 1333 (1991).

McGowan, J. W. and Clarke, E. M. *Ionization of H(1s) near threshold.* Phys. Rev. **167**, 43 (1968).

Micheau, S., Chen, Z., Le, A.-T., and Lin, C. D. *Quantitative rescattering theory for nonsequential double ionization of atoms by intense laser pulses.* Phys. Rev. A **79**, 013417 (2009).

Milošević, D. B., Paulus, G. G., Bauer, D., and Becker, W. *Above-threshold ionization by few-cycle pulses.* J. Phys. B: At. Mol. Opt. Phys. **39**, R203 (2006).

Monmayrant, A., Weber, S., and Chatel, B. *A newcomer's guide to ultrashort pulse shaping and characterization.* J. Phys. B: At. Mol. Opt. Phys. **43**, 103001 (2010).

de Morisson Faria, C. F. and Liu, X. *Electron-electron correlation in strong laser fields.* J. Mod. Opt. **58**, 1076 (2011).

Moshammer, R., Feuerstein, B., Schmitt, W., Dorn, A., Schröter, C. D., Ullrich, J., Rottke, H., Trump, C., Wittmann, M., Korn, G., Hoffmann, K., and Sandner, W. *Momentum distributions of Ne^{n+} ions created by an intense ultrashort laser pulse.* Phys. Rev. Lett. **84**, 447 (2000).

Moshammer, R., Ullrich, J., Feuerstein, B., Fischer, D., Dorn, A., Schröter, C. D., Crespo Lopez-Urrutia, J. R., Hoehr, C., Rottke, H., Trump, C., Wittmann, M., Korn, G., and Sandner, W. *Rescattering of ultralow-energy electrons for single ionization of Ne in the tunneling regime.* Phys. Rev. Lett. **91**, 113002 (2003).

Mourou, G. A., Labaune, C. L., Dunne, M., Naumova, N., and Tikhonchuk, V. T. *Relativistic laser-matter interaction: from attosecond pulse generation to fast ignition.* Plasma Phys. Control. Fusion **49**, B667 (2007).

Müller, A. *Ion formation processes: Ionization in ion-electron collisions.* In *Physics of Ion Impact Phenomena* (edited by D. Mathur), volume 54 of *Springer Series in Chemical Physics*, 13–90 (Springer Berlin Heidelberg, 1991).

Mulliken, R. S. *Electronic structures of polyatomic molecules and valence. IV. electronic states, quantum theory of the double bond.* Phys. Rev. **43**, 279 (1933).

Nubbemeyer, T., Gorling, K., Saenz, A., Eichmann, U., and Sandner, W. *Strong-field tunneling without ionization.* Phys. Rev. Lett. **101**, 233001 (2008).

Palaniyappan, S., DiChiara, A., Chowdhury, E., Falkowski, A., Ongadi, G., Huskins, E. L., and Walker, B. C. *Ultrastrong field ionization of Ne^{n+} ($n \leq 8$): Rescattering and the role of the magnetic field.* Phys. Rev. Lett. **94**, 243003 (2005).

Panfili, R. and Liu, W.-C. *Resonances in the double-ionization signal of two-electron model atoms.* Phys. Rev. A **67**, 043402 (2003).

Parker, J. S., Doherty, B. J. S., Meharg, K. J., and Taylor, K. T. *Time delay between singly and doubly ionizing wavepackets in laser-driven helium.* J. Phys. B: At. Mol. Opt. Phys. **36**, L393 (2003).

Parker, J. S., Doherty, B. J. S., Taylor, K. T., Schultz, K. D., Blaga, C. I., and DiMauro, L. F. *High-energy cutoff in the spectrum of strong-field nonsequential double ionization.* Phys. Rev. Lett. **96**, 133001 (2006).

Parker, J. S., Moore, L. R., Meharg, K. J., Dundas, D., and Taylor, K. T. *Double-electron above threshold ionization of helium.* J. Phys. B: At. Mol. Opt. Phys. **34**, L69 (2001).

Paul, P. M., Toma, E. S., Breger, P., Mullot, G., Augé, F., Balcou, P., Muller, H. G., and Agostini, P. *Observation of a train of attosecond pulses from high harmonic generation.* Science **292**, 1689 (2001).

Paulus, G. G., Becker, W., Nicklich, W., and Walther, H. *Rescattering effects in above-threshold ionization: a classical model.* J. Phys. B: At. Mol. Opt. Phys. **27**, L703 (1994a).

Paulus, G. G., Nicklich, W., Xu, H., Lambropoulos, P., and Walther, H. *Plateau in above threshold ionization spectra.* Phys. Rev. Lett. **72**, 2851 (1994b).

Perelomov, A., Popov, V., and Terent'ev, M. *Ionization of atoms in an alternating electric field.* Sov. Phys. JETP **23**, 924 (1966).

Peterkop, R. *WKB approximation and threshold law for electron-atom ionization.* J. Phys. B: At. Mol. Phys. **4**, 513 (1971).

Pindzola, M. S., Griffin, D. C., and Bottcher, C. *Validity of time-dependent Hartree-Fock theory for the multiphoton ionization of atoms.* Phys. Rev. Lett. **66**, 2305 (1991).

Powell, P. D. *Calculating determinants of block matrices.* ArXiv e-prints 1112.4379 (2011).

Prauzner-Bechcicki, J. S., Sacha, K., Eckhardt, B., and Zakrzewski, J. *Time-resolved quantum dynamics of double ionization in strong laser fields.* Phys. Rev. Lett. **98**, 203002 (2007).

Prauzner-Bechcicki, J. S., Sacha, K., Eckhardt, B., and Zakrzewski, J. *Quantum model for double ionization of atoms in strong laser fields.* Phys. Rev. A **78**, 013419 (2008).

Rau, A. R. P. *Two electrons in a Coulomb potential. double-continuum wave functions and threshold law for electron-atom ionization.* Phys. Rev. A **4**, 207 (1971).

Rau, A. R. P. *The Wannier theory for two electrons escaping from a positive ion.* Phys. Rep. **110**, 369 (1984).

Reiss, H. R. *Unsuitability of the Keldysh parameter for laser fields.* Phys. Rev. A **82**, 023418 (2010).

Richter, K. and Wintgen, D. *Analysis of classical motion on the Wannier ridge.* J. Phys. B: At. Mol. Opt. Phys. **23**, L197 (1990).

Rost, J.-M. *Two-electron escape near threshold: A classical process?* Phys. Rev. Lett. **72**, 1998 (1994).

Rost, J. M. *Critical phenomena in atomic physics.* Physica E **9**, 467 (2001).

Rottke, H., Liu, X., Eremina, E., Sandner, W., Goulielmakis, E., Keeffe, K. O., Lezius, M., Krausz, F., Lindner, F., Schätzel, M. G., Paulus, G. G., and Walther, H. *Non-sequential double ionization in a few-cycle laser pulse: the influence of the carrier-envelope phase.* J. Mod. Opt. **53**, 149 (2006).

Rudati, J., Chaloupka, J. L., Agostini, P., Kulander, K. C., and DiMauro, L. F. *Multi-photon double ionization via field-independent resonant excitation.* Phys. Rev. Lett. **92**, 203001 (2004).

Rudek, B., Rolles, D., Son, S.-K., Foucar, L., Erk, B., Epp, S., Boll, R., Anielski, D., Bostedt, C., Schorb, S., Coffee, R., Bozek, J., Trippel, S., Marchenko, T., Simon, M., Christensen, L., De, S., Wada, S.-i., Ueda, K., Schlichting, I., Santra, R., Ullrich, J., and Rudenko, A. *Resonance-enhanced multiple ionization of krypton at an X-ray free-electron laser.* Phys. Rev. A **87**, 023413 (2013).

Rudek, B., Son, S.-K., Foucar, L., Epp, S. W., Erk, B., Hartmann, R., Adolph, M., Andritschke, R., Aquila, A., Berrah, N., Bostedt, C., Bozek, J., Coppola, N., Filsinger, F., Gorke, H., Gorkhover, T., Graafsma, H., Gumprecht, L., Hartmann, A., Hauser, G., Herrmann, S., Hirsemann, H., Holl, P., Homke, A., Journel, L., Kaiser, C., Kimmel, N., Krasniqi, F., Kuhnel, K.-U., Matysek, M., Messerschmidt, M., Miesner, D., Moller, T., Moshammer, R., Nagaya, K., Nilsson, B., Potdevin, G., Pietschner, D., Reich, C., Rupp, D., Schaller, G., Schlichting, I., Schmidt, C., Schopper, F., Schorb, S., Schroter, C.-D., Schulz, J., Simon, M., Soltau, H., Struder, L., Ueda, K., Weidenspointner, G., Santra, R., Ullrich, J., Rudenko, A., and Rolles, D. *Ultra-efficient ionization of heavy atoms by intense X-ray free-electron laser pulses.* Nat. Phot. **6**, 858 (2012).

Rudenko, A., Ergler, T., Zrost, K., Feuerstein, B., de Jesus, V. L. B., Schröter, C. D., Moshammer, R., and Ullrich, J. *From non-sequential to sequential strong-field multiple ionization: identification of pure and mixed reaction channels.* J. Phys. B: At. Mol. Opt. Phys. **41**, 081006 (2008a).

Rudenko, A., Ergler, T., Zrost, K., Feuerstein, B., de Jesus, V. L. B., Schröter, C. D., Moshammer, R., and Ullrich, J. *Intensity-dependent transitions between different pathways of strong-field double ionization.* Phys. Rev. A **78**, 015403 (2008b).

Rudenko, A., de Jesus, V. L. B., Ergler, T., Zrost, K., Feuerstein, B., Schröter, C. D., Moshammer, R., and Ullrich, J. *Correlated two-electron momentum spectra for strong-field nonsequential double ionization of He at 800 nm.* Phys. Rev. Lett. **99**, 263003 (2007).

Rudenko, A., Zrost, K., Schröter, C. D., de Jesus, V. L. B., Feuerstein, B., Moshammer, R., and Ullrich, J. *Resonant structures in the low-energy electron continuum for single ionization of atoms in the tunnelling regime.* J. Phys. B: At. Mol. Opt. Phys. **37**, L407 (2004).

Ruiz, C., Plaja, L., and Roso, L. *Lithium ionization by a strong laser field.* Phys. Rev. Lett. **94**, 063002 (2005).

Ruiz, C., Plaja, L., Roso, L., and Becker, A. *Ab initio calculation of the double ionization of helium in a few-cycle laser pulse beyond the one-dimensional approximation.* Phys. Rev. Lett. **96**, 053001 (2006).

Sacha, K. and Eckhardt, B. *Nonsequential triple ionization in strong fields.* Phys. Rev. A **64**, 053401 (2001a).

Sacha, K. and Eckhardt, B. *Pathways to double ionization of atoms in strong fields.* Phys. Rev. A **63**, 043414 (2001b).

Sacha, K. and Eckhardt, B. *Pathways to non-sequential multiple ionization in strong laser fields.* J. Phys. B: At. Mol. Opt. Phys. **36**, 3923 (2003).

Samson, J. A. R. and Angel, G. C. *Test of the threshold law for triple photoionization in atomic oxygen and neon.* Phys. Rev. Lett. **61**, 1584 (1988).

van de Sand, G. and Rost, J. M. *Semiclassical description of multiphoton processes.* Phys. Rev. A **62**, 053403 (2000).

Schwabl, F. *Quantenmechanik* (Springer Berlin Heidelberg, 2007), 7th edition.

Scrinzi, A., Geissler, M., and Brabec, T. *Ionization above the Coulomb barrier.* Phys. Rev. Lett. **83**, 706 (1999).

Sheehy, B., Lafon, R., Widmer, M., Walker, B., DiMauro, L. F., Agostini, P. A., and Kulander, K. C. *Single- and multiple-electron dynamics in the strong-field tunneling limit.* Phys. Rev. A **58**, 3942 (1998).

Silvester, J. R. *Determinants of block matrices.* Math. Gaz. **84**, 460 (2000).

Singh, D., Varshni, Y. P., and Dutt, R. *Bound eigenstates for two truncated Coulomb potentials.* Phys. Rev. A **32**, 619 (1985).

Staudte, A., Ruiz, C., Schöffler, M., Schössler, S., Zeidler, D., Weber, T., Meckel, M., Villeneuve, D. M., Corkum, P. B., Becker, A., and Dörner, R. *Binary and recoil collisions in strong field double ionization of helium.* Phys. Rev. Lett. **99**, 263002 (2007).

Strickland, D. and Mourou, G. *Compression of amplified chirped optical pulses.* Opt. Commun. **55**, 447 (1985).

Strohaber, J., Kolomenskii, A. A., and Schuessler, H. A. *Reconstruction of ionization probabilities from spatially averaged data in N dimensions.* Phys. Rev. A **82**, 013403 (2010).

Talebpour, A., Chien, C.-Y., Liang, Y., Larochelle, S., and Chin, S. L. *Non-sequential ionization of Xe and Kr in an intense femtosecond Ti:sapphire laser pulse.* J. Phys. B: At. Mol. Opt. Phys. **30**, 1721 (1997a).

Talebpour, A., Larochelle, S., and Chin, S. L. *Non-sequential and sequential double ionization of NO in an intense femtosecond Ti:sapphire laser pulse.* J. Phys. B: At. Mol. Opt. Phys. **30**, L245 (1997b).

Tang, Q., Huang, C., Zhou, Y., and Lu, P. *Correlated multielectron dynamics in mid-infrared laser pulse interactions with neon atoms.* Opt. Express **21**, 21433 (2013).

Taylor, K., Parker, J., Dundas, D., Smyth, E., and Vivirito, S. *Laser-driven helium in full-dimensionality.* Laser Phys. **9**, 98 (1998).

Taylor, K., Parker, J., Meharg, K., and Dundas, D. *Laser-driven helium at 780 nm.* Eur. Phys. J. D **26**, 67 (2003).

Taylor, K., Parker, J., Moore, L., Roy, K., and Edwards, T. *High intensity 800 nm laser simulations.* `http://www.hector.ac.uk/coe/pdf/HELIUM_FinalReport_July2010.pdf`. Accessed: 2017-10-26 (2010).

Taylor, K. T. and Dundas, D. *Multiphoton absorption by multielectron atoms.* Phil. Trans. R. Soc. Lond. A **357**, 1331 (1999).

Thiede, J. H. *Frequency dependence of double ionization in strong laser fields.* Diplomarbeit, Philipps-Universität Marburg (2011).

Tian, J., Wang, X., and Eberly, J. H. *Numerical detector theory for the longitudinal momentum distribution of the electron in strong field ionization.* Phys. Rev. Lett. **118**, 213201 (2017).

Tong, X. M. and Lin, C. D. *Empirical formula for static field ionization rates of atoms and molecules by lasers in the barrier-suppression regime.* J. Phys. B: At. Mol. Opt. Phys. **38**, 2593 (2005).

Ullrich, J., Moshammer, R., Dorn, A., Dörner, R., Schmidt, L. P. H., and Schmidt-Böcking, H. *Recoil-ion and electron momentum spectroscopy: reaction-microscopes.* Rep. Prog. Phys. **66**, 1463 (2003).

Véniard, V., Taïeb, R., and Maquet, A. *Double ionization of excited helium states by an intense laser field: spin and dressing effects.* J. Phys. B: At. Mol. Opt. Phys. **36**, 4145 (2003).

Voronov, G. S. and Delone, N. B. *Many photon ionization of the xenon atom by ruby laser radiation.* Sov. Phys. JETP **23**, 54 (1966).

Vvedensky, D. *Lecture notes in Group theory.* Imperial College London. `http://www.cmth.ph.ic.ac.uk/people/d.vvedensky/groups/Chapter6.pdf`. Accessed: 2017-10-26 (2001).

Walker, B., Mevel, E., Yang, B., Breger, P., Chambaret, J. P., Antonetti, A., DiMauro, L. F., and Agostini, P. *Double ionization in the perturbative and tunneling regimes.* Phys. Rev. A **48**, R894 (1993).

Walker, B., Sheehy, B., DiMauro, L. F., Agostini, P., Schafer, K. J., and Kulander, K. C. *Precision measurement of strong field double ionization of helium.* Phys. Rev. Lett. **73**, 1227 (1994).

Walsh, T. D. G., Decker, J. E., and Chin, S. L. *Tunnel ionization of simple molecules by an intense CO_2 laser.* J. Phys. B: At. Mol. Opt. Phys. **26**, L85 (1993).

Wang, X., Tian, J., and Eberly, J. H. *Extended virtual detector theory for strong-field atomic ionization.* Phys. Rev. Lett. **110**, 243001 (2013).

Wannier, G. H. *The threshold law for single ionization of atoms or ions by electrons.* Phys. Rev. **90**, 817 (1953).

Wannier, G. H. *Threshold law for multiple ionization.* Phys. Rev. **100**, 1180 (1955).

Watson, G. *XVI. The sum of a series of cosecants.* Phil. Mag. Ser. 6 **31**, 111 (1916).

Watson, G. *LVIII. The sum of series of cosecants.* Phil. Mag. Ser. 6 **45**, 577 (1923).

Weber, T., Giessen, H., Weckenbrock, M., Urbasch, G., Staudte, A., Spielberger, L., Jagutzki, O., Mergel, V., Vollmer, M., and Dörner, R. *Correlated electron emission in multiphoton double ionization.* Nature **405**, 658 (2000a).

Weber, T., Weckenbrock, M., Staudte, A., Spielberger, L., Jagutzki, O., Mergel, V., Afaneh, F., Urbasch, G., Vollmer, M., Giessen, H., and Dörner, R. *Recoil-ion momentum distributions for single and double ionization of helium in strong laser fields.* Phys. Rev. Lett. **84**, 443 (2000b).

Weckenbrock, M., Becker, A., Staudte, A., Kammer, S., Smolarski, M., Bhardwaj, V. R., Rayner, D. M., Villeneuve, D. M., Corkum, P. B., and Dörner, R. *Electron-electron momentum exchange in strong field double ionization.* Phys. Rev. Lett. **91**, 123004 (2003).

Weckenbrock, M., Zeidler, D., Staudte, A., Weber, T., Schöffler, M., Meckel, M., Kammer, S., Smolarski, M., Jagutzki, O., Bhardwaj, V. R., Rayner, D. M., Villeneuve, D. M., Corkum, P. B., and Dörner, R. *Fully differential rates for femtosecond multiphoton double ionization of neon.* Phys. Rev. Lett. **92**, 213002 (2004).

Wehlitz, R., Huang, M.-T., Sellin, I. A., and Azuma, Y. *The Wannier threshold law examined by photoelectron satellite measurements.* J. Phys. B: At. Mol. Opt. Phys. **32**, L635 (1999).

Welker, V. and Thiede, J. *Lecture notes in Algebra.* Philipps-Universität Marburg (2010).

Wigner, E. P. *The transition state method.* Trans. Faraday Soc. **34**, 29 (1938).

Wigner, E. P. *On the behavior of cross sections near thresholds.* Phys. Rev. **73**, 1002 (1948).

Wigner, E. P. *Group theory and its application to the quantum mechanics of atomic spectra* (Academic Press, 1959), expanded and improved edition.

Yamakawa, K., Akahane, Y., Fukuda, Y., Aoyama, M., Inoue, N., and Ueda, H. *Ionization of many-electron atoms by ultrafast laser pulses with peak intensities greater than* 10^{19} W/cm^2. Phys. Rev. A **68**, 065403 (2003).

Yanovsky, V., Chvykov, V., Kalinchenko, G., Rousseau, P., Planchon, T., Matsuoka, T., Maksimchuk, A., Nees, J., Cheriaux, G., Mourou, G., and Krushelnick, K. *Ultra-high intensity- 300-TW laser at 0.1 Hz repetition rate.* Opt. Express **16**, 2109 (2008).

Ye, D. F., Liu, X., and Liu, J. *Classical trajectory diagnosis of a fingerlike pattern in the correlated electron momentum distribution in strong field double ionization of helium.* Phys. Rev. Lett. **101**, 233003 (2008).

Yu, C.-X., Liu, S.-B., Shu, X.-F., Song, H.-Y., and Yang, Z. *A modified rate equation for the propagation of a femtosecond laser pulse in field-ionizing medium.* Opt. Express **21**, 5413 (2013).

Yudin, G. L. and Ivanov, M. Y. *Physics of correlated double ionization of atoms in intense laser fields: Quasistatic tunneling limit.* Phys. Rev. A **63**, 033404 (2001).

Zhang, K., Lai, Y. H., Diesen, E., Schmidt, B. E., Blaga, C. I., Xu, J., Gorman, T. T., Légaré, F. m. c., Saalmann, U., Agostini, P., Rost, J. M., and DiMauro, L. F. *Universal pulse dependence of the low-energy structure in strong-field ionization.* Phys. Rev. A **93**, 021403 (2016).

Zhang, Q., Basnayake, G., Winney, A., Lin, Y. F., Debrah, D., Lee, S. K., and Li, W. *Orbital-resolved nonadiabatic tunneling ionization.* Phys. Rev. A **96**, 023422 (2017).

Zhang, Z., Bai, L., and Zhang, J. *Double ionization of Ar below the recollision threshold intensity.* Phys. Rev. A **90**, 023410 (2014).

Zhou, Y., Liao, Q., and Lu, P. *Asymmetric electron energy sharing in strong-field double ionization of helium.* Phys. Rev. A **82**, 053402 (2010a).

Zhou, Y., Liao, Q., and Lu, P. *Complex sub-laser-cycle electron dynamics in strong-field nonsequential triple ionization.* Opt. Express **18**, 16025 (2010b).

Zon, B. A. *Many-electron tunneling in atoms.* J. Exp. Theor. Phys. **89**, 219 (1999).

Zrost, K., Rudenko, A., Ergler, T., Feuerstein, B., de Jesus, V. L. B., Schröter, C. D., Moshammer, R., and Ullrich, J. *Multiple ionization of Ne and Ar by intense 25 fs laser pulses: few-electron dynamics studied with ion momentum spectroscopy.* J. Phys. B: At. Mol. Opt. Phys. **39**, S371 (2006).

Acknowledgments

First of all, I would like to thank Bruno Eckhardt for his infectious interest in the topic of nonsequential ionization and his supervision during my diploma and PhD thesis. It all began as a little post-lecture discussion in Renthof 6 back in early 2010, followed by a Großpraktikum on classical scattering in a two-dimensional potential as an introductory exercise. We climbed the ladder of interpretational complexity together, sometimes slipping, sometimes getting stuck, and mostly falling back to one or two dimensions. In the end, a three-dimensional system is not much different from a one- or two-dimensional one – it is just harder to sketch.

The results presented in this work required reliable and efficient simulation algorithms. During their development, I was supported by several people. First, I am indebted to Lars Bannow without whom the yield program might have never been cleared of that one innocent-looking, but crucial error (N^3 instead of N^2 *in one place*). Furthermore, I want to thank Tobias Kreilos for his concise introduction to MPI parallelization which was vital for all programs. Finally, many thanks to the personnel of the Marburger RechenCluster (MaRC2) for tolerating my large temporary files directory (typically occupying 6-10 TB of disk space) and for providing numerical support. Here, I owe special thanks to René Sitt for carrying out several tests which eventually allowed me to perform calculations on more than 64 processors.

Without the fantastic people working in it, Renthof 6 would be a dreary place. Therefore, thanks to all the past and present members of the AG Komplexe Systeme that I got to know over the years, not only for a great time, but also for invaluable physical, technical and moral support. In particular, I would like to thank Eric Jelli (for some Python tricks), Felix Schmidt (for keeping the PCs running), Martin Lellep (for asking the right questions), Deniz Nitt (for coming up with the best puns), Jonathan Prexl (for the Origin connection and plenty of food), Lars Bannow (for proofreading, criticism and see above) and Marina Pausch (for cheering me up).

Sebastian Freitag deserves a whole paragraph of appreciation since we not only shared the office as co-workers, but also the stage as brothers in six-string arms on numerous occasions. It is also worth mentioning that he was the one to numerically confirm the three-electron Wannier law in a laser field. I miss the days in MG33 – and BS2.

A theoretician sometimes has to see beyond his computer monitor. Therefore, thanks to Robert Moshammer, Thomas Pfeifer and Nicolas Camus from the MPI für Kernphysik for fruitful discussions in Heidelberg (2017) and Riezlern (2012, 2017), the permission to use some of their measured momentum distributions in this work and, last but not least, for the guided tour through the COLTRIMS lab where the femtosecond magic happens.

For the exchange of ideas and the discussion of results via Skype, I am grateful to Jakub Zakrzewski and Krzysztof Sacha from the University of Kraków, Poland. Special thanks to Dmitry Efimov for taking a short trip to Marburg and digging into the programming code with me. Moreover, I would like to express my deep gratitude to Jakub Prauzner-Bechcicki for being a patient listener, a subtle motivator and a skillful yet uncredited supervisor. Over the years, we exchanged countless emails, discussed physical results and numerical issues. I turned his innocent little program for solving the helium-laser Schrödinger equation that he wrote during his own PhD thesis into a parallelized monster which devours a lot of computational resources, makes short work of the calculation, and spits outs amazing results. Let us hope that it will also be fed in the future.

Finally, thanks to my loved ones Susanne, Paul and Lisa for supporting me with and without words, giving me distraction and constantly reminding me that there is a life outside the PhD, even if it is hard to see sometimes. I would be nothing without you.

And now for something completely different.

The unknown future rolls toward us.
I face it, for the first time, with a sense of hope.

Sarah Connor, Terminator 2: Judgment Day

Wissenschaftlicher Werdegang

02/2013 – 07/2017	Wissenschaftlicher Mitarbeiter in der AG Komplexe Systeme Fachbereich Physik, Philipps-Universität Marburg Doktorand bei Prof. Dr. Bruno Eckhardt
02/2012 – 01/2013	Wissenschaftliche Hilfskraft in der AG Komplexe Systeme Fachbereich Physik, Philipps-Universität Marburg
21/12/2011	Diplom Physik
11/2010 – 12/2011	Diplomarbeit bei Prof. Dr. Bruno Eckhardt AG Komplexe Systeme *Frequency dependence of double ionization in strong laser fields*
09/2008	Vordiplom Physik
10/2006 – 12/2011	Studium der Physik (Diplom) Philipps-Universität Marburg